



This is to certify that the

dissertation entitled

PROCESSING AND CHARACTERIZATION OF HIGH-TEMPERATURE  
NICKEL-TITANIUM-HAFNIUM SHAPE MEMORY THIN FILMS

presented by

Jinping Zhang

has been accepted towards fulfillment  
of the requirements for

Ph.D. degree in Materials Science



Major professor

Date 9/20/02

**LIBRARY**  
**Michigan State**  
**University**

**PLACE IN RETURN BOX** to remove this checkout from your record.  
**TO AVOID FINES** return on or before date due.  
**MAY BE RECALLED** with earlier due date if requested.

DATE DUE	DATE DUE	DATE DUE

**PROCESSING AND CHARACTERIZATION OF HIGH-TEMPERATURE  
NICKEL-TITANIUM-HAFNIUM SHAPE MEMORY THIN FILMS**

By

Jinping Zhang

A DISSERTATION

Submitted to  
Michigan State University  
in partial fulfillment of the requirements  
for the degree of

DOCTOR OF PHILOSOPHY

Department of Chemical Engineering and Materials Science

2002

## **ABSTRACT**

### **PROCESSING AND CHARACTERIZATION OF HIGH-TEMPERATURE NICKEL-TITANIUM-HAFNIUM SHAPE MEMORY THIN FILMS**

By

Jinping Zhang

Near-equiatomic TiNi thin films are of interest as robust actuator materials in microelectromechanical systems (MEMS) due to the high mechanical energy density associated with reversible martensitic transformations. High-temperature (Ti+Hf)Ni shape memory thin films have been of particular interest because their high transformation temperatures allows use at higher temperatures at which binary TiNi films become inoperative, and also because they can improve the operation frequency for actuation. In this thesis, (Ti+Hf)Ni films having different hafnium contents were prepared by magnetron sputtering. Crystalline films exhibiting martensitic transformation were obtained either by depositing the films at elevated temperatures or by conducting a post-deposition anneal of as-sputtered amorphous films. Phase transformations, microstructure, mechanical properties and shape memory properties of films obtained by different procedures were investigated in order to find the best way to produce high-temperature shape memory films.

In films obtained by post-deposition annealing, the heating rates during annealing were found to significantly affect mechanical properties. Conventional vacuum annealing with heating rates ranging from 5°C/min to 40°C/min resulted in brittle films even though the as-deposited amorphous films were ductile, but rapid thermal annealing (RTA) with a heating rate of 6000°C/min resulted in ductile films having improved martensitic transformation characteristics. Embrittlement of the films annealed by

conventional annealing occurred at temperatures well below the crystallization temperature. The RTA treated  $\text{Ni}_{49.1}\text{Ti}_{36.2}\text{Hf}_{14.7}$  films had room-temperature ductility of 5.8%, fully recoverable strain of 1.7%, maximum recoverable strain of 1.9%, and maximum stress for full strain recovery 200 MPa.

*In-situ* deposited crystalline  $\text{Ni}_{48.9}\text{Ti}_{36.6}\text{Hf}_{14.5}$  films demonstrated substantially better properties than the RTA treated samples. The transformation temperatures were higher, transformation hysteresis was lower, and most importantly, the mechanical properties and shape-memory properties were significantly improved. *In-situ* deposited crystalline  $\text{Ni}_{48.9}\text{Ti}_{36.6}\text{Hf}_{14.5}$  films had room-temperature ductility of 8.3%, fully recoverable strain of 2.8%, maximum recoverable strain of 3.6%, and maximum stress for full strain recovery of 250 MPa. In addition, the transformation temperatures were effectively increased as more Hf was substituted for Ti. These properties of *in-situ* deposited crystalline Ni-Ti-Hf films put them in a good position for industrial applications where binary TiNi films are not applicable because of their lower transformation temperatures.

## **ACKNOWLEDGMENTS**

I would like to express my profound gratitude to my major advisor, Professor David Grummon, for his continuous guidance and support during this period of my education. His careful reading of the preliminary drafts and critical comments helped in many ways. Also I would like to thank other professors in my Ph.D. guidance committee, Professor Mercouri Kanatzidis, Professor Jun Nogami, and Professor Donnie Reinhard, for their invaluable suggestion and comments.

I am thankful to my employer, Delphi Corporation, for allowing me use the materials obtained at work. Encouragement and support from my supervisors Gregory Rasmussen and Rick Kerr are appreciated. Assistance from Mr. Brian Jones of Delphi Delco Electronics in conducting the RTA experiments is acknowledged.

Special thanks are due to my family for their support and patience, which have been a driving force for me to finish this work.

## TABLE OF CONTENTS

LIST OF TABLES.....	vii
LIST OF FIGURES.....	viii
KEY TO ABBREVIATIONS.....	xiv
CHAPTER 1	
INTRODUCTION .....	1
CHAPTER 2	
LITERATURE REVIEW .....	4
2.1. SHAPE MEMORY EFFECTS AND SHAPE MEMORY ALLOYS .....	4
2.1.1. SME and Thermoelastic Martensitic Transformation.....	5
2.1.2. Transformational Superelasticity .....	8
2.1.3. Two-way Shape Memory Effect .....	9
2.2. NEAR-EQUIATOMIC NI-TI SHAPE-MEMORY ALLOYS.....	10
2.2.1. SME and Displacive Transformation in Near-equiatomic Ni-Ti .....	11
2.2.2. Aging Effect .....	13
2.3. SHAPE-MEMORY ALLOYS WITH HIGH TRANSFORMATION TEMPERATURES.....	17
2.3.1. Ti-Ni-Pd, Ti-Ni-Pt and Ti-Ni-Au alloys .....	19
2.3.2. Ni-Ti-Zr and Ni-Ti-Hf Alloys .....	26
2.3.3. General Comparison of Different HTSMAs .....	32
2.4. SHAPE-MEMORY ALLOY THIN FILMS.....	33
2.4.1. Deposition of Thin Films by Sputtering.....	33
2.4.2. Sputtered Shape Memory Thin Film.....	39
2.4.3. High-Temperature Shape Memory Alloy Thin Films.....	53
CHAPTER 3	
EXPERIMENTAL PROCEDURE .....	59
3.1. THIN FILM FABRICATION.....	59
3.1.1. Thin Film Deposition .....	60
3.1.2. Hot Pressed Powder Target .....	61
3.1.3. Post-Deposition Annealing .....	62
3.2. THIN FILM CHARACTERIZATION .....	64
3.2.1. Transformation Temperatures .....	64
3.2.2. Mechanical Property Measurement.....	65
3.2.3. Shape-Memory Property Evaluation.....	67
3.3. COMPOSITIONAL, STRUCTURAL AND MICROSTRUCTURAL ANALYSES.....	71
3.3.1. Composition Analysis .....	71
3.3.2. Crystallographic Structure Analysis.....	72

3.3.3. Microstructure Observation.....	72
CHAPTER 4	
RESULTS AND DISCUSSION.....	74
4.1. FILMS CRYSTALLIZED BY POST-DEPOSITION ANNEALING.....	75
4.1.1. Crystallization by Conventional Isochronal Heating.....	77
4.1.2. Isothermal Annealing at Low Temperatures.....	85
4.1.3. Isothermal Annealing at High Temperature via Different Ramp Rates.....	87
4.1.4. Discussion on Ni-Ti-Hf Films Crystallized by Post-Deposition Annealing...	93
4.2. IN-SITU CRYSTALLIZED Ni-Ti-Hf FILMS.....	98
4.2.1. Phase Transformations.....	99
4.2.4. Crystallographic and Microstructural Analysis.....	101
4.2.2. Mechanical Properties.....	103
4.2.3. Shape-Memory Properties.....	110
4.2.4. Discussion on In-situ Crystallized Ni-Ti-Hf Films.....	116
CHAPTER 5	
CONCLUSIONS.....	120
BIBLIOGRAPHY.....	126

## LIST OF TABLES

### **Chapter 2.**

Table 2.1. Selected properties of Ni-Ti SMA.....	12
--	----

### **Chapter 3.**

Table 3.1. Composition and porosity of the targets used to deposit Ni-Ti-Hf SMA thin films in this study.....	62
---	----

### **Chapter 4.**

Table 4.1. Target compositions vs. film compositions.....	75
---	----

Table 4.2. Peak temperatures and transformation enthalpies of the peaks on the DSC curves during isochronal annealing of as-sputtered amorphous Ni <sub>49.1</sub> Ti <sub>36.2</sub> Hf <sub>14.7</sub> films at different heating rates.....	78
--	----

Table 4.3. Transformation temperatures and enthalpies of as-crystallized Ni <sub>49.1</sub> Ti <sub>36.2</sub> Hf <sub>14.7</sub> films after isochronal heating at different rates.....	81
--	----

Table 4.4. Comparison of room-temperature ductility of as-deposited amorphous Ni <sub>49.1</sub> Ti <sub>36.2</sub> Hf <sub>14.7</sub> samples before and after isochronal heating from room temperature to 575°C.....	84
--	----

Table 4.5. Comparison of room-temperature ductility of the as-deposited amorphous Ni <sub>49.1</sub> Ti <sub>36.2</sub> Hf <sub>14.7</sub> films before and after 1-hour annealing at 300°C and 350°C.....	86
--	----

Table 4.6. Martensitic transformation temperatures and transformation enthalpies for Ni <sub>49.1</sub> Ti <sub>36.2</sub> Hf <sub>14.7</sub> samples crystallized by isothermal annealing with different heating rates to annealing temperatures.....	89
--	----

Table 4.7. Comparison of room-temperature ductility of as-deposited amorphous Ni <sub>49.1</sub> Ti <sub>36.2</sub> Hf <sub>14.7</sub> films crystallized by isothermal annealing via different ramp rates to the annealing temperatures.....	91
---	----

Table 4.8. Martensitic transformation temperatures vs. sample composition of <i>in-situ</i> crystallized Ni-Ti-Hf SMA films.....	100
--	-----

Table 4.9. Room-temperature tensile testing results of <i>In-situ</i> crystallized Ni-Ti-Hf films with different hafnium content.....	105
---	-----

## LIST OF FIGURES

### **Chapter 1.**

Figure 1.1. Work per volume versus cycling frequency for various microactuators [Krulevitch *et al.* 1996]..... 138

### **Chapter 2.**

Figure 2.1. Schematic showing physical property changes and endothermic/exothermic effects during reversible martensitic phase transformation..... 139

Figure 2.2. Theoretical recoverable strain of single-crystal Ni-Ti SMA as functions of crystal direction developed by (a) Saburi *et al.* [1981], (b) Inoue *et al.* [1996]..... 140

Figure 2.3. Equilibrium phase diagram of Ti-Ni alloy [Massalski 1987]..... 141

Figure 2.4. Schematic showing the dependence of austenite yield stress and reverse transformation peak temperature of Ni-Ti alloy on the composition of the material [Hodgson and Brown 2000]..... 142

Figure 2.5. Isothermal time-temperature-transformation (TTT) diagram for Ti-52at.%Ni alloy [Nishida *et al.* 1986]..... 143

Figure 2.6. Effect of Pd and Hf composition on reverse martensitic transformation temperature of NiTi-base ternary alloys summarized from the literature..... 144

Figure 2.7. Effect of Hf composition on transformation temperature of Ni-Ti-Hf alloys summarized from the literature..... 145

Figure 2.8. Effect of Ni composition on the transformation temperature of Ni-Ti-Hf shape memory alloy..... 146

Figure 2.9. Deformation Behavior of Ni-Ti-Hf alloys at different test temperatures [Olier *et al.* 1995]..... 147

Figure 2.10. A microactuator structure proposed by Johnson *et al.* [1994]... 148

Figure 2.11. A schematic showing realization of vertical cyclic displacement from a horizontal component under an applied force..... 149

Figure 2.12. Shape-memory properties of sputtered Ni-Ti-Pd SMA thin film during thermal cycles under different applies stresses [Miyazaki <i>et al.</i> 1995].....	150
--	-----

**Chapter 3.**

Figure 3.1. Schematic of the sputtering system used to deposit Ni-Ti-Hf SMA thin films in this study.....	151
---	-----

Figure 3.2. Schematic of the apparatus for conducting heating treatment for Ni-Ti-Hf thin film.....	152
---	-----

Figure 3.3. Typical temperature profile of sample in a rapid thermal anneal treatment for crystallization of Ni-Ti-Hf thin films.....	153
---	-----

Figure 3.4. Schematic of the apparatus for measuring resistance of the thin film sample to determine phase transformation temperature in this study.....	154
--	-----

Figure 3.5. Schematic of the experimental setup of semi-quantitatively determining the ductility of Ni-Ti-Hf thin films using bending test.....	155
---	-----

Figure 3.6. Schematic of the method measuring recoverability of a pre-strain put to Ni-Ti-Hf martensite.....	156
--	-----

Figure 3.7. Schematic of the apparatus measuring shape memory properties of Ni-Ti-Hf thin film in constrained thermal cycles.....	157
---	-----

Figure 3.8. Typical hysteresis in a strain-temperature curve for measuring shape memory properties of Ni-Ti-Hf SMA thin films.....	158
--	-----

**Chapter 4.**

Figure 4.1. Composition uniformity of the thin films deposited from an 8”-diameter Ni <sub>48.5</sub> Ti <sub>37.5</sub> Hf <sub>14</sub> target. ....	159
--	-----

Figure 4.2. Composition variation of films at central area with continuous wearing of the Ni <sub>48.5</sub> Ti <sub>35.5</sub> Hf <sub>16</sub> target. ....	160
---	-----

Figure 4.3. DSC curves of as-deposited amorphous Ni <sub>49.1</sub> Ti <sub>36.2</sub> Hf <sub>14.7</sub> films during isochronal heating from room temperature to 575°C at different heating rates.....	161
--	-----

Figure 4.4. Dependence of exothermic peak temperatures and enthalpies on heating rate during heating as-deposited amorphous $\text{Ni}_{49.1}\text{Ti}_{36.2}\text{Hf}_{14.7}$ films in DSC instrument.....	162
Figure 4.5. Estimation of activation energy for crystallization transformation and the transformation associated with the low-temperature exothermic peak using Kissinger's method.....	163
Figure 4.6. DSC curves of $\text{Ni}_{49.1}\text{Ti}_{36.2}\text{Hf}_{14.7}$ films crystallized by isochronal anneal at different heating rates showing reversible martensitic transformation during thermal cycling between 50°C and 250°C.....	164
Figure 4.7. Martensitic transformation temperature of annealed $\text{Ni}_{49.1}\text{Ti}_{36.2}\text{Hf}_{14.7}$ films as functions of heating rates during isochronal heating for crystallization.....	165
Figure 4.8. Room-temperature XRD spectra of as-deposited amorphous $\text{Ni}_{49.1}\text{Ti}_{36.2}\text{Hf}_{14.7}$ films and the samples crystallized by isochronal heating to 575°C at different rates.....	166
Figure 4.9. TEM micrograph and SAED pattern of as-deposited amorphous $\text{Ni}_{49.1}\text{Ti}_{36.2}\text{Hf}_{14.7}$ thin films after crystallized by isochronal heating to 575°C at different rates.....	167
Figure 4.10. Room-temperature XRD of as-deposited amorphous $\text{Ni}_{49.1}\text{Ti}_{36.2}\text{Hf}_{14.7}$ thin films and those for films after annealed at 300°C and 350°C for 1 hour, respectively.....	169
Figure 4.11. TEM micrograph and SAED pattern of as-deposited amorphous $\text{Ni}_{49.1}\text{Ti}_{36.2}\text{Hf}_{14.7}$ films and those for films after annealed at 300°C and 350°C for 1 hour, respectively.....	170
Figure 4.12. DSC curves during thermal cycling between 50°C and 250°C of as-deposited amorphous $\text{Ni}_{49.1}\text{Ti}_{36.2}\text{Hf}_{14.7}$ films after crystallized by isothermal annealing at different ramp rates.....	171
Figure 4.13. Transformation temperatures and transformation enthalpy of $\text{Ni}_{49.1}\text{Ti}_{36.2}\text{Hf}_{14.7}$ films isothermally annealed by different procedures (conventional vacuum anneal and RTA).....	172
Figure 4.14. Room-temperature XRD spectra of as-deposited amorphous $\text{Ni}_{49.1}\text{Ti}_{36.2}\text{Hf}_{14.7}$ thin films after crystallized by isothermal annealing via different ramp rates from room temperature to the annealing temperature.....	173

Figure 4.15. TEM micrograph and SAED patterns of as-deposited amorphous $\text{Ni}_{49.1}\text{Ti}_{36.2}\text{Hf}_{14.7}$ films after crystallized by isothermal annealing via different ramp rates from room temperature to the annealing temperatures.....	174
Figure 4.16. Room-temperature stress-strain curves of as-deposited amorphous $\text{Ni}_{49.1}\text{Ti}_{36.2}\text{Hf}_{14.7}$ films after rapid thermal annealing at 650°C for 20 seconds with heating rate of 6000°C/min.....	178
Figure 4.17. Schematic strain-temperature curve of RTA crystallized $\text{Ni}_{49.1}\text{Ti}_{36.2}\text{Hf}_{14.7}$ films during constrained thermal cycling starting from room temperature (fully martensitic condition).....	179
Figure 4.18. Strain-temperature curves of as-deposited amorphous $\text{Ni}_{49.1}\text{Ti}_{36.2}\text{Hf}_{14.7}$ thin films crystallized by RTA anneal at 650°C for 20 seconds during thermal cycling under different loads.....	180
Figure 4.19. Dependence of strain induced by cooling from austenite to martensite and that recovered by heating from martensite to austenite of RTA treated as-deposited amorphous $\text{Ni}_{49.1}\text{Ti}_{36.2}\text{Hf}_{14.7}$ SMA thin films on applied stress during thermal cycling.....	171
Figure 4.20. DSC curves of <i>in-situ</i> crystallized Ni-Ti-Hf thin films with different hafnium content during thermal cycling between 50°C and 300°C.....	182
Figure 4.21. Dependence of transformation temperatures on hafnium content of <i>in-situ</i> crystallized Ni-Ti-Hf films.....	184
Figure 4.22. Room-temperature XRD of <i>in-situ</i> crystallized $\text{Ni}_{48.9}\text{Ti}_{36.6}\text{Hf}_{14.5}$ SMA film.....	185
Figure 4.23. TEM micrograph and SAED pattern of <i>in-situ</i> crystallized $\text{Ni}_{48.9}\text{Ti}_{36.6}\text{Hf}_{14.5}$ SMA films taken at ambient temperature.....	186
Figure 4.24. Room-temperature stress-strain curves of <i>in-situ</i> crystallized $\text{Ti}_{50.5}\text{Ni}_{49.5}$ SMA thin films.....	189
Figure 4.25. Stress-strain curves of <i>in-situ</i> crystallized binary $\text{Ti}_{50.5}\text{Ni}_{49.5}$ SMA films at different temperatures.....	190
Figure 4.26. Room-temperature stress-strain curves of <i>in-situ</i> crystallized Ni-Ti-Hf thin films with different hafnium content.....	191

Figure 4.27. Dependence of room-temperature yield stress, fracture stress and ultimate elongation on hafnium content in <i>in-situ</i> crystallized Ni-Ti-Hf films.....	192
Figure 4.28. Stress-strain curves of <i>in-situ</i> crystallized Ni <sub>48.9</sub> Ti <sub>36.6</sub> Hf <sub>14.5</sub> SMA thin films at different test temperatures using cooling-down routine. ....	193
Figure 4.29. Dependence of yield stress of <i>in-situ</i> crystallized Ni <sub>48.9</sub> Ti <sub>36.6</sub> Hf <sub>14.5</sub> SMA on tensile test temperatures between 200°C and 140°C using cool-down procedure.....	194
Figure 4.30. Dependence of ultimate elongation and yield stress on test temperature of <i>in-situ</i> crystallized Ni <sub>48.9</sub> Ti <sub>36.6</sub> Hf <sub>14.5</sub> SMA thin films.....	195
Figure 4.31. Stress-strain curves of <i>in-situ</i> crystallized Ni <sub>48.9</sub> Ti <sub>36.6</sub> Hf <sub>14.5</sub> thin films elongated at room-temperature upon loading, unloading and subsequent heating.....	196
Figure 4.32. Recoverable strain and recovery rate of <i>in-situ</i> crystallized Ni <sub>48.9</sub> Ti <sub>36.6</sub> Hf <sub>14.5</sub> films with different amount of pre-strain introduced at room temperature.....	197
Figure 4.33. Stress-strain curves of <i>in-situ</i> crystallized Ni <sub>48.9</sub> Ti <sub>36.6</sub> Hf <sub>14.5</sub> thin films elongated at different temperatures upon loading, unloading and subsequent heating. The strain upon unloading was fixed at about 3%, and the direct-heating routine was used.....	198
Figure 4.34. Dependence of recoverable strain and recovery rate on deformation temperature of <i>in-situ</i> crystallized Ni <sub>48.9</sub> Ti <sub>36.6</sub> Hf <sub>14.5</sub> martensite films at a fixed pre-strain of about 3%.....	199
Figure 4.35. Stress-strain curves of <i>in-situ</i> crystallized Ni <sub>48.9</sub> Ti <sub>36.6</sub> Hf <sub>14.5</sub> elongated at different temperatures (in the initially austenitic condition) during loading and unloading. Before test, samples were heated to 250°C and then cooled down to various test temperatures.....	200
Figure 4.36. Dependence of isothermal strain recovery on deformation temperature for <i>in-situ</i> crystallized Ni <sub>48.9</sub> Ti <sub>36.6</sub> Hf <sub>14.5</sub> SMA thin film at a fixed total tensile strain of 4%.....	201
Figure 4.37. Stress-strain curves of <i>in-situ</i> crystallized Ni <sub>48.9</sub> Ti <sub>36.6</sub> Hf <sub>14.5</sub> thin films loaded and unloaded at 190°C for different amounts of total strain.....	202

Figure 4.38. Dependence of recoverable strain and recovery rate on initial strain of <i>in-situ</i> crystallized Ni <sub>48.9</sub> Ti <sub>36.6</sub> Hf <sub>14.5</sub> SMA thin films when elongation was done at 190°C.....	203
Figure 4.39. Strain-temperature curves of <i>in-situ</i> crystallized Ni <sub>48.9</sub> Ti <sub>36.6</sub> Hf <sub>14.5</sub> thin film during thermal cycling under various constant stresses.....	204
Figure 4.40. Dependence of strain induced by cooling from austenite to martensite and that recovered by heating from martensite to austenite of <i>in-situ</i> crystallized Ni <sub>48.9</sub> Ti <sub>36.6</sub> Hf <sub>14.5</sub> SMA thin films on biasing stress during thermal cycling.....	205
Figure 4.41. Dependence of transformation temperatures on applied stress during thermal cycling of <i>in-situ</i> crystallized Ni <sub>48.9</sub> Ti <sub>36.6</sub> Hf <sub>14.5</sub> SMA thin films.....	206

## KEY TO ABBREVIATIONS

A.....	Austenite phase
A <sub>f</sub> .....	Austenite finish temperature
A <sub>p</sub> .....	Austenite transformation peak temperature
A <sub>s</sub> .....	Austenite start temperature
CTE.....	Coefficient of thermal expansion
DSC.....	Differential scanning calorimetry
EDS.....	Energy-dispersive spectrum
HTSMA.....	High-temperature shape memory alloy(s)
LVDT.....	Linear voltage-displacement transducer
M.....	Martensite phase
M <sub>f</sub> .....	Martensite finish temperature
M <sub>p</sub> .....	Martensite transformation peak temperature
M <sub>s</sub> .....	Martensite start temperature
RTA.....	Rapid thermal anneal
SAED.....	Selected-area electron diffraction
SE.....	Superelasticity (Pseudoelasticity)
SEM.....	Scanning electron microscope (microscopy)
SIM.....	Stress-induced martensite (martensitic transformation)
SMA.....	Shape memory alloy(s)
SME.....	Shape memory effect(s)
TEM.....	Transmission electron microscope (microscopy)
TTR.....	Transformation temperature(s)
TTT diagram.....	Time-temperature-transformation diagram
TWSME.....	Two-way shape memory effect
XRD.....	X-ray diffraction

## Chapter 1

### INTRODUCTION

Shape Memory Alloys (SMAs) undergo a reversible displacive phase transformation between a low-temperature martensite (M) phase and a high-temperature austenite (A) phase [Wayman and Duerig 1990]. Associated with this reversible phase transformation are the shape memory effect (SME) and transformational superelasticity, the two most important properties of SMAs. SME represents the ability to recover a large amount of strain imparted to the low-temperature phase when the alloys are heated to the high-temperature phase. Transformational superelasticity represents isothermal recovery of strain caused by stress-induced  $A \rightarrow M$  transformation when the applied stress is removed. Alloys such as In-Tl, Cu-Zn-Al, Cu-Al-Ni, Au-Cd, Ni-Ti and some ferrous materials have been found to be shape memory alloys.

Near-equiatomic Ni-Ti alloys are the most economically successful shape memory alloys developed so far due to their large recoverable strain (up to 8% in uniaxial mode), large recovery stress (up to 700 MPa), excellent corrosion resistance, and excellent fatigue resistance [Wasilewski 1972, Beuhler and Wang 1968, Mercier and Melton 1979, Miyazaki, Sugaya and Otsuka 1989, Ford and White 1996]. Therefore, a vast majority of current applications related to the shape memory effect and transformational superelasticity makes use of Ni-Ti alloys. Also important is the biocompatibility of Ni-Ti alloys with human body. In fact, Ni-Ti alloys have found as many medical applications as industrial ones [Russell, Hodgson and Basin 1997].

Although they have superior mechanical and shape-memory properties, near-equiatomic Ni-Ti alloys have phase transformation temperature ( $A_f$  temperature) below  $110^\circ\text{C}$ , which is too low for many automotive underhood and aerospace related

applications. Therefore, development of alloys having high transformation temperatures has been actively pursued [Humbeeck 1999]. The most promising are Ni-Ti based psuedo-binary alloy systems, which are formed by substituting Au, Pd or Pt for Ni, or substituting Zr or Hf for Ti in the CsCl-type structure of  $\beta$ -NiTi. It has been found that the transformation temperatures of the psuedo-binary alloys could reach as high as 600°C depending on the atomic percentage of the ternary elements, but the mechanical and shape-memory properties were often degraded by the third element. Among those alloy systems, Ni-Ti-Hf alloys showed better shape-memory properties than Ni-Ti-Zr alloys and were more cost competitive than Ni-Ti-Pt or Ni-Ti-Pd alloys [Humbeeck 1999, Wu and Ma 2000].

Shape-memory thin films have been attracting widespread interest due to their potential usefulness as microactuator materials in microelectromechanical systems in which high energy-density output is desired. In fact, Ni-Ti binary shape-memory thin films have an energy density at least one order of magnitude larger than any other microactuator materials currently available (see Figure 1.1), and it is the only shape-memory alloy thin film that has been successfully developed. The mechanical and shape-memory properties of Ni-Ti alloy thin films are comparable or superior to those of their bulk alloy counterparts [Miyazaki and Ishida 1999]. However, the application of Ni-Ti shape-memory thin films has been limited to relatively low temperatures, and the response time is too long for many applications. Development of high-temperature shape-memory thin films has been considered as a measure to overcome these drawbacks.

Although few and far between, attempts to fabricate shape-memory thin films with high transformation temperatures have been made, and Ni-Ti-Pd or Ni-Ti-Hf thin films have shown some promise [Johnson, Martynov and Minners 1995, Johnson, Martynov and Shahoian 1995, Miyazaki, Hashinoga, Yumikura, Hirikawa, Ueki and Ishida 1995, Quandt, Halene, Holleck, Feit, Kohl and Schloßmacher 1995]. From the limited data on Ni-Ti-Hf thin films, it has been demonstrated that high transformation

temperature can be obtained through composition adjustment, but evaluation of mechanical and shape-memory properties of Ni-Ti-Hf SMA thin film is uncharted territory. No literature exists on optimization of thin film properties by appropriate processing strategies.

In order to acquire shape-memory properties, binary Ni-Ti thin films must be deposited at high substrate temperature [Ikuta, Fujita, Ikeda and Yamashita 1990, Gisser, Busch, Johnson and Ellis 1992, Hou and Grummon 1995], or the thin films must be annealed at high temperature [Miyazaki and Ishida 1994], because alloys sputtered onto substrate at temperatures below 350°C are metallic glasses. Thin film properties may be different according to whether *in-situ* deposition or post-deposition annealing is used. For the post-deposition annealing treatment, annealing time and annealing temperature affect the properties profoundly. This thesis work presents results on fabrication of Ni-Ti-Hf thin films having the shape-memory effect, and shows how process parameters, especially heating rate during annealing, affect their mechanical and shape-memory properties. The result will be useful as a reference for the fabrication of high-temperature shape memory thin films.

The organization of this thesis is as follows: A review on shape-memory alloys, especially high-temperature shape memory alloys, and thin films is presented in the *Literature Survey* chapter; experimental techniques and procedures are detailed in the *Experimental Methods* chapter; the experimental results on mechanical property evaluation and microstructural investigation of both annealed and in-situ deposited films are presented and discussed in the *Results and Discussion* chapter; the major results of this research work are summarized in the *Conclusions* chapter.

## **Chapter 2**

### **LITERATURE REVIEW**

In this chapter, a literature survey is presented on the shape memory effect and shape-memory alloys, particularly near equiatomic Ni-Ti alloys. Ni-Ti-base ternary shape-memory alloys having high transformation temperatures are emphasized. Also, the fabrication and evaluation of Ni-Ti shape memory thin films and Ni-Ti-X (X = Hf, Zr, Pt, Pd, Au) high-temperature thin films are reviewed in detail. Applications of Ni-Ti shape memory thin films are discussed.

#### **2.1. Shape Memory Effects and Shape Memory Alloys**

The shape memory effect (SME) represents the ability of a certain group of materials to recover, upon heating, the plastic deformation sustained at low temperature. It was first found in 1951 by Chang and Read in Au-Cd alloys [Chang and Read 1951]. Since then, a quite number of materials, including metals [Arbuzova and Khandros 1964, Smialek and Hehemann 1973, Schroeder and Wayman 1979, Delaey, Humbeeck, Chandrasederan, Janssen, Andrade and Mwamba, 1981, Miyazaki and Otsuka 1989], ceramics [Muddler and Traill 1994], and even polymers [Hayashi 1993], have been found to be shape memory materials. Metallic shape memory materials, which are also called Shape Memory Alloys (SMAs) display the greatest SME, and the most important SMAs are near-equiatomic Ni-Ti and Cu-base alloys including Cu-Zn-Al and Cu-Al-Ni [Miura, Meada and Nakanishi 1974, Sakamoto, Otsuka and Shimizu 1977]. Between these two alloy systems, Ni-Ti has significantly better mechanical and shape-memory properties and greater thermal stability, while Cu-base alloys hold some economic advantage for heavy sections.

### 2.1.1. SME and Thermoelastic Martensitic Transformation

The shape memory effect originates from the martensitic transformation, a displacive transformation like that in carbon steel [Reed-Hill and Abbaschian 1992]. But the martensitic transformation in SMAs differentiates itself from the one in steel by its reversibility and the highly mobile interfaces [Wayman 1992]. As a result, the transformation in SMAs takes place thermoelastically, meaning that it is thermally reversible<sup>1</sup>. The high-temperature phase is called the ‘parent’ or austenite phase, and the low-temperature phase is called the ‘daughter’ or martensite phase. Because of the displacive nature of the phase transformation, atoms do not need to undergo long-range migration (in contrast to diffusive transformations), and the transformation is independent of time. Rather, the fraction transformed depends on the temperature of the material.<sup>2</sup> Displacive transformations are thus called ‘athermal’ to indicate that they do not depend on thermal activation.

*2.1.1.1. Transformation Temperatures.* On cooling, the austenite phase starts to transform to martensite at  $M_s$  (the martensitic start temperature), and it becomes fully martensitic at  $M_f$  (the martensite finish temperature). On heating, the fully martensitic material starts to transform to austenite  $A_s$  (the austenite start temperature) and becomes fully austenitic at  $A_f$  (the austenite finish temperature). Transformational thermal hysteresis exists between the forward transformation ( $A \rightarrow M$ ) and reverse transformation

---

<sup>1</sup> Although being widely used, the term “thermoelastic” is not very descriptive since both stress and temperature may induce the transformation. Another term “thermotractive” offered by Grummon [Chang and Grummon, 1997] may be a better choice for the description of SMA alloys.

<sup>2</sup> Since the transformation is not time dependent, one may think that it should take place as fast as wanted. In reality, however, heating transfer between the sample and environment may  $A \rightarrow M$  limit the transformation speed. Transformational latent heat may further slow down the temperature change of the sample.

(M → A), which means that the  $A_s$  temperature is always higher than the  $M_f$  temperature, and the  $M_s$  temperature is always lower than the  $A_f$  temperature.

The martensitic transformation is a first-order phase transformation. It is accompanied by a discontinuous non-linear change in physical properties such as electric resistivity and heat capacity. Figure 2.1 schematically illustrates these changes with respect to the transformation temperatures. The martensitic transformation is also accompanied by endothermic and exothermic effects, and Differential Scanning Calorimetry (DSC) is the most common means to determine the transformation temperatures and enthalpies. The transformation temperatures are determined by the tangent-intercept method. In the DSC curve, the exothermic peak during cooling corresponds to martensitic transformation and the peak temperature is defined as  $M_p$ ; the endothermic peak during heating corresponds to reverse martensitic transformation and the peak temperature is defined as  $A_p$ .

*2.1.1.2. Thermoelastic Martensite.* On cooling, the austenite phase of SMAs transforms into martensite with very little volume change (<0.5%) but with large local shear strains. The martensite may be composed of a number of variants that have same crystal structure but different orientations, which is possible because the martensite structure has lower symmetry than the austenite. Although the structures of the austenite phase and martensite are different, martensitic transformation does not result in significant macroscopic shape change if no stress is applied. This is because the martensite variants are accommodated with each other so that lattice distortions are canceled out on macroscopic scale. The interfaces between martensite variants are usually twin boundaries, and the movement of those boundaries results in rearrangement of martensite variants.

The shape memory effect results from the unique plastic deformation mechanism available to the martensite, *i.e.*, the reorientation of martensitic variants effected by

applied stresses, involving preferential growth of some variants at expense of the others [Otsuka and Shimizu 1986]. Ultimately, only one variant may survive, and the surviving variant is the one that gives rise to maximum transformational shear strain with respect to the orientation of the applied stress. The strain appears to be plastic because there is no driving force for the material to return back the original configuration of martensite variants. However, if the deformed material is heated to the  $A_f$  temperature, the martensite will transform into austenite. Due to the displacive nature of the transformation and restriction of the crystal orientation relationship between austenite and martensite imposed by the strongly ordered structure, when the reverse transformation is completed on heating, atoms return to their original positions, thereby the original shape is recovered.

*2.1.1.3. Recoverable Strain and Recovery Stress.* For martensite in shape-memory alloys, there exists a limit of plastic strain that can be recovered upon heating to austenite, which is called maximum recoverable strain. Deformation beyond the maximum recoverable strain may induce permanent strain by dislocation slip, as occurs in ordinary metals. However, a smaller deformation does not guarantee a full recovery upon heating to austenite. This is because slip may occur at the same time or before martensite variants reorient. In order to induce recoverable strain and avoid non-recoverable slip deformation, the stress applied must be higher than the critical stress for inducing rearrangement of martensite variants, but lower than the critical stress for slip in the martensite.

In another consideration, a great deal of stress can be generated against a physical constraint when a constrained SMA recovers from a deformation imparted to the martensite. This stress is called recovery stress. Apparently, this stress is also associated with the critical stress for slip. How to increase the critical stress for slip and decrease that for martensite reorientation is an interesting issue. In this respect, control of the

precipitation of non-equiatomic intermetallic phases (such  $Ti_2Ni$  or  $Ti_3Ni_4$  in NiTi SMAs) is of importance and will be discussed further later.

## 2.1.2. Transformational Superelasticity

*2.1.2.1. Stress Induced Martensitic Transformation.* Martensitic transformation can be induced thermally or induced by stress. This is, even without decreasing the temperature of an austenite down to  $M_s$  temperature, martensitic transformation may still occur with the help of an applied stress. This is because the applied stress can increase the martensitic transformation temperature. The effect can be described by a modified version of the well-known Clapeyron equation [Wollants, DeBonte and Roos 1979, Wollants, Roos and Delaey 1993]:

$$\frac{d\sigma}{dT} = -\frac{\Delta H}{T \cdot V \cdot \Delta \epsilon} \quad (2.1)$$

where  $\sigma$ ,  $T$ ,  $\Delta H$ ,  $V$  and  $\Delta \epsilon$  are the stress, equilibrium transformation temperature, transformation enthalpy, molar volume of the material, and resolved transformation strain in the direction of applied stress, respectively. Because of the multiplicity of shear variants, and the sign of each parameter, the ratio is positive for common SMAs. Therefore,  $M_s$ ,  $M_f$ ,  $A_s$  and  $A_f$  temperatures rise with the absolute value of the applied stress. Martensite is stress induced in an otherwise stable austenite when the stress raises the  $M_s$  to the ambient temperature.

*2.1.2.2. Transformational Superelasticity.* While the thermally induced martensite is self-accommodating and no significant macroscopic deformation occurs, the martensite formed by stress tends to favor particular martensite variants that give the maximum transformational strain in the stress axis. On loading, a macroscopic transformational

strain is thus produced.

The unloading behavior of the SMA material is determined by the deformation temperature. If the deformation temperature is below the  $A_s$  temperature, *i.e.*, an austenite specimen is held at a temperature below the  $A_s$  but above  $M_s$ , the plastic strain remains after unloading, and it can be recovered only when the material is heated to above  $A_f$  temperature. However, if the deformation temperature is above  $A_f$  temperature, the reverse transformation is automatic upon unloading (with the same hysteresis), and isothermal recovery of the strain occurs. The usefulness of transformational superelasticity is not only because the recoverable strain is large, but also because there is very little strain hardening.

It is known that slip deformation mechanisms produce permanent strain and should be avoided in SMA applications. In order to ensure that the strain is caused by stress induced transformation instead of slip, the stress for inducing martensitic transformation has to be lower than the critical stress for slip in the austenite. While the stress for inducing martensitic transformation increases with deformation temperature, as described in Clapeyron's equation, the critical stress for slip decreases with an increase of deformation temperature. For a certain SMA, there exists a characteristic temperature at which those two characteristic stresses are equal, and this temperature, called  $M_d$ , defines the maximum temperature for stress inducing a transformational strain.

### 2.1.3. Two-way Shape Memory Effect

Normally, shape-memory materials have the ability to restore its high-temperature shape upon heating, but can not automatically restore to the low-temperature configuration upon cooling. In many applications, cyclic displacement is of interest, and it can be easily realized by using biasing forces with shape memory alloys.

*2.1.3.1. Cyclic Displacement by Biasing Stress.* External biasing stress such as that implemented by a biasing spring can be used to achieve cyclic displacement in a SMA-spring assembly [Ditman and Bergman 1994]. The temperature change must cover both forward and reverse transformation temperatures. Most critically, the biasing stress should be higher than the critical stress for inducing martensitic transformation, but lower than the critical stress for slip in either martensite or austenite. By doing so, the biasing stress can induce a relatively large deformation in the martensite, but can cause only a negligible elastic deformation of the austenite. As temperature changes, cyclic displacement is generated between martensite and austenite.

*2.1.3.2. Intrinsic Two-way SME.* Even without external biasing stress, cyclic displacement is sometimes still achievable. This is called two-way shape-memory effect, and it is actually caused by the internal biasing stress from defects such as dislocations and precipitate interfaces [Schroeder and Wayman 1977, Perkins and Sponholz 1984, Nishida and Honma 1984, Liu and McCormick 1990]. Under such conditions, martensite formed upon cooling is no longer fully self-accommodating, but adopts a preferred configuration with regard to variant distribution. As a consequence, cyclic shape change results on cooling (to form martensite) as well as heating (to form austenite).

## **2.2. Near-equiatomic Ni-Ti Shape-Memory Alloys**

Near equiatomic NiTi alloy was found to have SME by Beuler and his coworkers in 1961 [Beuhler and Wiley 1961, Buehler and Wang 1968]. Since then, there has been a lot of success in research and development of this material. Ni-Ti has become the most important of the shape-memory alloys. It has superior overall shape-memory properties, the raw material is not prohibitively expensive and sophisticated fabrication techniques have been developed. Presently the overwhelming majority of SMA applications use Ni-Ti materials.

Table 2.1 lists selected properties of polycrystalline NiTi alloy and it shows that the alloy has excellent mechanical and shape memory properties [Hodgson and Brown 2000]. For instance, one-time recoverable strain is up to 8%, stress for fully strain recovery is up to 700 MPa, and room-temperature ultimate elongation is up to 50%. The martensitic transformation temperatures, which are sensitive to composition, can be varied from  $-200^{\circ}\text{C}$  to  $+110^{\circ}\text{C}$  (for  $A_f$ ). In addition, its excellent corrosion resistance makes it viable for working in some harsh environments, and its good biocompatibility allows many clinical applications.

### 2.2.1. SME and Displacive Transformation in Near-equiatomic Ni-Ti

The martensitic transformation in Ni-Ti involves the transformation between the high-temperature austenite phase and the low-temperature martensite phase.<sup>3</sup> The former has the CsCl-type structure (ordered b.c.c.,  $\beta$ - phase or B2 phase) with lattice parameter  $a = 0.3005 \sim 0.3015$  nm; the latter has a monoclinic structure (B19' phase) with lattice parameters  $a = 0.2889$  nm,  $b = 0.4120$  nm,  $c = 0.4622$  nm and  $\gamma = 98.6^{\circ}$  [Matsumoto, Miyazaki, Otuka and Tamira 1987]. According to the lattice correspondence of martensitic transformation, there are 12 different martensite orientations that could possibly form from a single austenite grain, *i.e.*, there are possible 12 martensite lattice-correspondence variants [Otsuka, Sawamura and Shimizu 1971].

Crystallographic information on the martensitic transformation in Ni-Ti makes it possible to calculate the maximum recoverable strain theoretically. The single-variant model proposed by Saburi and Nenno [1981] predicts that the maximum recoverable strain is 11% when the uniaxial stress is applied along the  $[111]_{\text{B2}}$  direction and the least

---

<sup>3</sup> In addition, another displacive transformation, the R-phase transformation, may occur prior to martensitic transformation in Ni-Ti SMA. Shape memory effect associated with R-phase transformation has also been observed but the transformational strain is generally limited within 1%. However, the R-phase transformation has small hysteresis, which is of interest in certain applications such as fast actuation [Miyazaki *et al.* 1986]. Since the R-phase transformation does not occur in Ni-Ti-Hf alloys with Hf over 10at.%, it is not discussed further here.

**Table 2.1. Selected Properties of NiTi SMA**  
[after Hodgson and Brown 2000]

**Transformation Properties**

Transformation Temperatures.....	-200 to +110 °C
Latent Heat of Transformation.....	5.78 cal/g
Transformation Strain for Polycrystalline Material	
for 1 cycle.....	max 8%
for 100 cycles.....	6%
for 100,000 cycles.....	4%
Hysteresis.....	30 to 50 °C

**Physical Properties**

Melting Point.....	1300 °C
Density.....	6.45 g/cm <sup>3</sup>
Thermal Conductivity	
austenite.....	0.18 W/cm·°C
martensite.....	0.08618 W/cm·°C
Coefficient of Thermal Expansion	
austenite.....	11.0 × 10 <sup>-6</sup> /°C
martensite.....	6.6 × 10 <sup>-6</sup> /°C
Specific Heat.....	0.20 cal/g · °C
Corrosion Resistance.....	excellent

**Electrical and Magnetic Properties**

Resistivity	
austenite.....	~ 100 μΩ·cm
martensite.....	~ 80 μΩ·cm
Magnetic Permeability.....	<1.002
Magnetic Susceptibility.....	3.0 × 10 <sup>6</sup> emu/g

**Mechanical Properties**

Young's Modulus (highly nonlinear with temperature)	
austenite.....	83 GPa
martensite.....	28 ~ 41 GPa
Yield Strength	
austenite.....	195 to 695 MPa
martensite.....	70 to 140 MPa
Ultimate Tensile Strength	
fully annealed.....	895 MPa
work hardened.....	1900 MPa
Poisson's Ratio.....	0.33
Elongation at Failure	
fully annealed.....	25 to 50%
work hardened.....	5 to 10%
Hot Workability.....	good
Cold Workability.....	difficult due to rapid work hardening
Machinability.....	difficult, abrasive techniques are preferred

recoverable strain was 2% when the stress axis was [100]B2 (Figure 2.2a). The recoverable strain for a randomly oriented polycrystalline NiTi can be estimated at 8.4%. The multi-variant model proposed by Inoue *et al.* [Inoue, Miwa and Inakazu 1996] yielded similar results for single crystal (Figure 2.2b), but the merit of Inoue's model is its capability to take the texture information, *i.e.*, orientation distribution function, into consideration.

Excellent superelasticity associated with stress induced martensitic transformation was also demonstrated in near-equiatomic Ni-Ti [Miyazaki, Imai, Otsuka and Suzuki 1981]. Lüders-like deformation behaviors were observed when the material was deformed at temperatures above  $A_p$ , indicating strain hardening was almost negligible once the martensite started to form under influence of the applied stress. The relationship between the tensile-test temperature and the critical stress for inducing martensitic transformation obeys Clapeyron's equation. For polycrystalline NiTi, the value of  $d\sigma/dT$  is about 7 MPa/K, meaning the  $M_s$  temperature increases about 14 to 15°C for every 100 MPa increment in applied uniaxial stress [Hodgson and Brown 2000].

### 2.2.2. Aging Effect

Thermal treatments are usually adopted to modify the transformation temperatures, mechanical properties and shape memory properties of near-equiatomic Ni-Ti SMAs. While alloys with off-stoichiometric composition are prone to precipitation reactions during aging, defect structures formed by cold working may also undergo reconfiguration. Such microstructural evolution has a profound effect on the properties of the material.

**2.2.2.1. Second Phases in Ti-rich Ni-Ti.** The second phase in Ti-rich Ni-Ti alloys is relatively simple. The phase diagram by Massalski indicates that the solubility of excess Ti into  $\beta$ -NiTi is less than 0.5at.% (reaching a maximum at 984 °C, see Figure 2.3).

Therefore, when Ni-Ti alloys have Ti-rich composition,  $Ti_2Ni$  precipitates are almost inevitable.<sup>4</sup>  $Ti_2Ni$  phases have an f.c.c. structure with lattice parameters  $a = 1.127 \text{ nm} \sim 1.132 \text{ nm}$  [Rostoker 1952, Yurko, Barton and Parr 1959, Mueller and Knott 1963]. They have particulate morphology, and preferentially appear near grain boundaries.

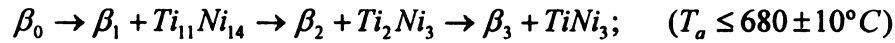
Transformation temperatures of Ti-rich melt-solidified Ni-Ti alloy are relatively consistent because the matrix composition is relatively consistent. In addition, the Ti-rich material has higher transformation temperature than Ni-rich one. However, due to second phases around grain boundaries, the mechanical properties of Ti-rich alloys solidified from the melt usually are unsatisfactory, especially for alloys with large  $Ti_2Ni$  particles. Figure 2.4 shows the relationship between the alloy composition and austenite yield stress of Ni-Ti alloys. It indicates that the more Ti in the composition is, the less the austenite yield stress will be. This will, in turn, limit the maximum stress during constrained recovery.

**2.2.2.2. Diffusive Transformations in Ni-rich Ni-Ti.** Second-phase formation is more complicated in Ni-rich Ni-Ti alloys than in Ti-rich ones. According to the equilibrium phase diagram, solubility of excess Ni in  $\beta$ -NiTi is strongly temperature dependent. Ni solubility decreases from about 7at.% at 1118°C to zero at 630°C. Therefore, it is easy to obtain over-saturated nickel in the matrix by quenching the material since excess Ni is readily solutionized. Although Massalski suggested that the only possible second phase was  $Ni_3Ti$  in Ni-rich Ni-Ti alloys, more detailed study by Nishida *et al.* [Nishida, Wayman and Honma 1986] using TTT (Temperature - Time - Transformation) diagram (Figure 2.5) revealed that there may be other metastable phases such as  $Ni_3Ti_2$  and or  $Ni_4Ti_3$ .

---

<sup>4</sup> Oxide  $Ti_4Ni_2O_x$  is easy to form in Ti-Ni alloys when oxygen exists in the system. It has a similar effect on material properties as  $Ti_2Ni$  precipitates. What is different for the two precipitates is that while  $Ti_2Ni$  usually exist only in Ti-rich Ti-Ni alloys,  $Ti_4Ni_2O_x$  may be able to form in equiatomic composition or even in Ni-rich composition. However, Because  $Ti_4Ni_2O_x$  and  $Ti_2Ni$  are isomorphous phases (with very similar lattice parameters), it is generally difficult to distinguish between them using structure analysis.

Nishida *et al.* [Nishida, Wayman and Honma 1986, 1987] also determined the crystal structures of those precipitates and the annealing condition for each precipitate to appear:



Where  $\beta_0$  is the original supersaturated Ti-52Ni alloy,  $\beta_1$  is the composition of the matrix in equilibrium with  $Ti_{11}Ni_{14}$  precipitates. The same role applies to  $\beta_2$ ,  $\beta_3$ ,  $\beta_1'$ ,  $\beta_2'$  and  $\beta_1''$ .

Transformation temperatures, mechanical properties and shape memory properties of Ni-rich Ni-Ti alloys are affected by the formation of second phases. Both matrix composition and interfacial stress conditions of the precipitates change as the annealing proceeds, and they both affect the transformation temperatures. For the effect of matrix composition, 1at.% excess nickel in the matrix will decrease  $M_s$  temperature by about 100°C [Hodgson and Brown 2000]. The more complete the precipitation reaction is, the closer the matrix composition will be to equiatomic stoichiometry. Therefore, transformation temperatures tend to increase as annealing proceeds. Stress field from fine and coherent particles tends to suppress martensitic transformation, while incoherent phase boundaries may be preferential sites for martensite nucleation. From this aspect, extended annealing should also raise transformation temperatures. The mechanical properties of Ni-Ti alloys are also affected by the formation of second phases during annealing. Fine and coherent precipitates are much desired for improving the critical stress for slip, and therefore improve shape memory properties of the alloy.

Due to lack of interfacial coherency with the matrix,  $Ni_3Ti_2$  and  $Ni_3Ti$  precipitates generally do not have significant influence on the shape memory properties of Ni-rich Ni-

Ti alloys [Nishida and Wayman 1987]. On the contrary,  $\text{Ni}_4\text{Ti}_3$  precipitates, which may have perfectly coherent, semi-coherent, or incoherent interfaces with the B2 matrix at different growth stages, are very useful to modify the SME properties by appropriate annealing procedure [Nishida and Honma 1984, Nishida, Wayman, Kainuma and Honma 1986, Xie, Zhao and Lei 1990]. When Ni-Ti alloys with over-saturated Ni composition are annealed,  $\text{Ni}_4\text{Ti}_3$  precipitates start to appear at annealing temperatures as low as  $300^\circ\text{C} \sim 350^\circ\text{C}$  [Ishida, Sato, Takei, Nomura and Miyazaki 1996]. At the beginning,  $\text{Ni}_4\text{Ti}_3$  precipitates are small and densely distributed in the matrix, and they have perfect interfacial coherency with the B2 matrix. As a result, martensitic transformation temperature is greatly depressed. At the same time, the critical stress for slip is the highest but it also needs more stress to activate the movement of variant boundaries. Continued annealing allows the precipitates grow, resulting in larger precipitates, less dense spatial distribution, and partial loss of interfacial coherency with the B2 matrix. Therefore, the depression effect on the  $M_s$  temperature becomes weaker, the transformation temperatures move up, and the mechanical strength of the material decreases accordingly. When the precipitates grow sufficiently large so that interfacial coherency is totally lost, the precipitates promote martensitic transformation by providing site for heterogeneous martensite nucleation.

Xie *et al.* [1990] found that very fine precipitates encourage the growth of certain martensite variants, and Li and Chen [1997] observed similar effect on the R-phase transformation. This result implies that, with presence of fine  $\text{Ni}_4\text{Ti}_3$  precipitates, the configuration of martensite variants formed by cooling is no longer perfectly self-accommodating, but has a preferred set, so the material has a certain macroscopic configuration every time it is cooled. The material can remember both high-temperature and low-temperature shapes without any external aids.<sup>5</sup>

---

<sup>5</sup> Due to the low flow stress of martensite, little mechanical work can be extracted during the  $A \rightarrow M$  transformation on cooling.

### 2.3. Shape-Memory Alloys with High Transformation Temperatures

High-temperature shape memory alloys are defined as those with  $A_s$  temperature above 120°C at the stress-free condition [Humbreeck 1999]. There are quite a few alloys that have been identified as potential high-temperature SMAs including Fe-Mn-Si, Cu-Al-Ni, Ni-Al, Ni-Mn, Cu-Zr, Ni-Ti-Hf, and Ni-Ti-Pd [Wu and Ma 2000]. But the realization of those possibilities has been hampered by various problems such as room-temperature brittleness, phase decomposition, martensite stabilization, small shape-memory strain at high temperature, and long-term instability of transformation temperature. For example, Cu-Al-Ni (or Cu-Al-Ni-Mn-Ti) [Saburi and Nenno 1974, Delaey *et al.* 1981] has potential to reach over 100 °C of  $M_s$  temperature, and the raw material is inexpensive. However, the material has inferior shape memory, and martensite stabilization tends to occur during aging (even at room temperature), leading to gradual loss of SME. The transformation temperatures also shift substantially during thermal cycling. Yet, the biggest problem seems to be the room-temperature brittleness due to large grain size, large elastic anisotropy and the segregation of impurities towards grain boundaries. It was proposed that single-crystal samples may overcome this problem and a prototype actuator using single crystal Cu-Al-Ni has been developed [Yawny, Sade and Lovey 1997, 1999].

Another example is Ni-Al alloys, which are also capable of undergoing martensitic transformation at high temperature. When fabricated and treated appropriately, Ni-Al alloys may have  $M_s$  temperature from room temperature up to 500°C with a small transformational hysteresis [Potapov, Poliakova and Udovenko 1996]. Theoretical calculation as well as experimental data show that single-crystal Ni-Al alloys have the fully recoverable strain nearly 5% if tensile axis is along  $\langle 110 \rangle$ , and as much as 13% if the tensile axis is  $\langle 001 \rangle$  [Enami, Martynov, Tomie, Khandros and Nenno 1981]. Polycrystalline Ni-Al, however, only shows about 0.2% of recoverable strain and it is

very brittle due to the intergranular fracture mechanisms [Kim and Wayman 1992]. Although the high-temperature ductility may be improved by a third element such as Fe or Mn [Chen 1994], problems remain with poor room-temperature ductility and the transformation from martensite (3R or 7R structure) to  $\text{Ni}_3\text{Al}_3$  phase, which hinders the reverse transformation of the martensite to austenite [Yang and Wayman 1993]. So far, it has not been possible to develop polycrystalline Ni-Al SMAs with acceptable SME properties.

There are more potential HTSMAs. Binary Ni-Mn has martensitic transformation temperature between 650°C and 750°C [Adachi and Wayman 1985]. But it is very brittle and prone to tempering at 400°C [Mulder 1995]. The Zr-based intermetallic alloy Cu-Zr has  $M_s$  temperature of 170°C and  $A_s$  temperature of 250°C, and nickel addition to Cu-Zr may be used to modify the transformation temperature [Koval, Firstov and Kotko. 1992]. Fe-Mn-Si alloys show recoverable strain up to 2% and recovery stress up to 350 MPa [Kikuchi, Kajiwara and Tomota 1995, Wang, Cai, Gao, Huang and Zhao 1997]. There are even ultra-high temperature SMAs such as near-equiatomic RuNb and RuTa, which have transformation temperatures from 800°C to over 1000°C [Fonda and Vandermeer 1997]. All those alloys have poor ductility, especially at room temperature.

The most promising and most widely studied HTSMAs are Ni-Ti base ternary alloys, which are obtained by substituting Ni with same atomic percent of Pd, Pt or Au, or substituting Ti with same atomic percent of Zr or Hf. Since the replacement takes place within the same family of the elements, the ternary alloys have phase structures much like Ni-Ti binary alloy, so they are also called pseudo-binary (Ni-Ti) alloys. Because of the importance of these alloy systems and their relevancy to this study, the literature on these alloys is reviewed in detail.

### 2.3.1. Ti-Ni-Pd, Ti-Ni-Pt and Ti-Ni-Au alloys

Substituting Ni in near-equiatomic Ni-Ti SMA with Pd, Pt or Au can greatly increase martensite transformation temperature. At the same time, the shape memory effect and the mechanical properties are modified due to this ternary element substitution. In the following, the effect of ternary composition on phase, phase transformation, shape-memory and mechanical properties will be presented, and because it is most widely studied among these three alloys, Ni-Ti-Pd alloy will be considered in detail.

*2.3.1.1. Phase Transformation and Transformation Temperatures.* Martensitic transformation in Ti-Ni-Pd shape memory alloys has been studied by a number of groups [Donkersloot and van Vucht 1970, Sivokha, Savvinov, Voronin and Khachin 1983, Lapin, Egorushkin, Shabalovshaya and Ivanova 1990, Lo and Wayman 1990, Yi, Moore and Petric 1992, Golberg, Xu, Murakami, Morito, Otsuka, Ueki and Horikawa 1994]. It has been found that the transformation temperatures depend on the content of additional palladium as well as that of titanium. The Ti : (Ni+Pd) ratio has the same critical effect on transformation temperature as found in binary Ni-Ti. When titanium is more than 50at.%, transformation temperatures are nearly the highest and change only slightly with titanium content. But when Ti was less than 50at.%, transformation temperatures decreased dramatically with decreasing Ti content. Therefore, to ensure a high-temperature SMA, titanium had to be at least 50at.%. Palladium affected transformation temperatures in a different way. Figure 2.6 shows the  $M_s$  temperature of Ni-Ti-Pd alloys with different Pd compositions using data obtained in various studies. With palladium content less than about 8 to 10at.%, the transformation temperature is slightly decreased with increasing Pd content. With more palladium than 10at.% added, the transformation temperature markedly increases with increasing Pd content. High  $A_p$  temperature up to 450°C may be obtained when the Pd content is increased to 40at.%. The transformation

hysteresis of Ni-Ti-Pd was lowered to less than 10°C, substantially smaller than binary Ni-Ti. The transformation enthalpy of Ti-Ni-Pd was also increased up to over 1.5 kJ/mol from 1.0 kJ/mol ~ 1.3 kJ/mol for binary Ni-Ti [Lo *et al.* 1990]. The structure of the austenite phase of Ti-Ni-Pd has the same B2 structure (CsCl structure) as binary Ni-Ti, but the lattice parameter was slightly larger. Martensite lattice parameters, as well as structure were also determined by the amount of ternary palladium. When the palladium content is small, martensite has a monoclinic structure (B19' structure) as that in binary Ni-Ti. As palladium content is increased (7 to 15at.%), the martensitic transformation becomes two-stage: a B19 orthorhombic martensite forms first, and as the temperature is continued down, a B19' monoclinic martensite. When the palladium content is over about 15at.%, only B2 to orthorhombic martensite transformation has been observed in normal temperature range [Lotkov, Grishkov and Fadin 1982].

When all the nickel is replaced by palladium in the Ti-Ni binary SMA, an isomorphous Ti-Pd binary intermetallic compound results. Donkersloot and Van Vucht first found the martensitic transformation in this alloy in 1970 [Donkersloot and Van Vucht 1970]. Later on Khachin *et al.* systematically studied the pseudo-binary TiPd-TiNi alloy system, and determined the transformation temperatures and the structures of martensite as a function of composition [Khachin, Matveeva, Sivokha and Chernov 1981]. According to them, the alloys with nearly Ti<sub>50</sub>Pd<sub>50</sub> composition transform from B2 type austenite to the B19 (orthorhombic) martensite. Binary near-equiatomic Ti-Pd alloy had the highest transformation temperature in the TiNiPd system. Otsuka *et al.* [Otsuka, Oda, Ueno and Piao 1993] also studied the phase transformation of the near equiatomic Ti-Pd alloy. It was determined that, after solution treatment followed by water quenching, the material had an M<sub>s</sub> of 817.7 K, M<sub>f</sub> of 812.6 K, A<sub>s</sub> of 847.0 K, and A<sub>f</sub> of 863.8 K.

Aging also affected the transformation temperatures of Ni-Ti-Pd alloys, especially for samples that have non-stoichiometric composition and are quenched after solution

treatment. Shimizu *et al.* [Shimizu, Xu, Okunishi, Tanaka, Otsuka and Mitose 1998] reported that, for Ti-lean compositions, aging at temperatures below 700 K did not result in appreciable change in transformation temperature, but aging at higher temperature resulted in a decrease in  $M_s$  and an increase in  $M_f$  temperature. For Ti-rich compositions, aging the sample between 650 K to 800 K resulted in the lowest transformation temperatures.

Lindquist studied the phase transformation and shape memory properties of Ti-Ni-Pt alloys [Lindquist 1978, Lindquist and Wayman 1990]. He found that platinum substitution could increase the martensitic transformation temperatures in a way more effective than palladium additions, even though less than 10at.% of platinum also slightly decreased the transformation temperatures. With 20at.% of platinum, the  $M_s$  temperature was about 300°C, and when the platinum reached 30at.%, the  $M_s$  temperature increased to about 620°C. Wu and Wayman [1987] reported martensitic transformation in Ni-Ti-Au ternary alloys with Au substituting Ni. The  $M_s$  temperatures of  $Ti_{50}Ni_{10}Au_{40}$  and  $Ti_{50}Au_{50}$  were 440°C and 610°C, respectively.

*2.3.1.2. Shape-Memory Properties.* Shape-memory properties of Ti-Ni-Pd high temperature SMA have been characterized by different research groups, usually in uniaxial tension or bending modes. It was generally found that as palladium content went up, the shape memory properties were degraded. At the same time, the stress for martensite reorientation was increased. Therefore, shape-memory strain is more difficult to obtain. However, depending on palladium composition, the material could still have recoverable strain up to 4%. Khachin *et al.* [1981] also made a high temperature torsion test for a  $Ti_{50}Pd_{37}Ni_{13}$  alloy, and reported that about 4% strain was attained by stress-induced transformation under a uniaxial applied stress of 200 MPa, and it was recovered completely upon reverse transformation. Wu *et al.* [Wu, Liu, March and Tseng 1994] tested Ti-Ni-Pd alloys with different palladium contents in bending and also found the

fully recoverable strain was decreased as Pd content was increased. Partial recovery was observed when the strain exceeded the fully recoverable strain, but the percentage of recovery fell dramatically with excess deformation.

As introduced before, binary  $\text{Ti}_{50}\text{Pd}_{50}$  undergoes martensitic transformation at high temperature. Otsuka *et al.* [1993] also characterized the shape memory properties by deforming the material in uniaxial mode at different temperatures. At room temperature, when the sample was elongated to 3.5% plastic strain, about 60% of the strain was recovered upon heating. As the tensile test temperature was increased to 573 K, while the stress for the same amount of strain decreased to 400 MPa, the recoverable strain became less. When the testing temperature increased to 713 K or above, no recoverable strain was observed. The reason for this phenomenon, as indicated by Otsuka *et al.*, is that the stress for martensite variant reorientation is lower than the critical stress for slip (in both martensite and austenite), especially at elevated temperatures. As a result, slip (which results in permanent strain) occurred before (or at the same time as) reorientation of martensite variants took place. Although this explanation was intended for the shape-memory behavior of  $\text{Ti}_{50}\text{Pd}_{50}$  alloy, it could also be true for that of all Ti-Ni-Pd alloys.

Perfect transformational superelasticity had not been observed in Ti-Ni-Pd or Ti-Pd alloys. The reason may, as indicated by Otsuka *et al.* [1993], be also related to low critical stress for slip at high temperature. In fact, the critical stress for slip in the austenite in Ti-Ni-Pd alloys was lower than that in the martensite, which was just opposite to the situation in Ti-Ni binary alloys [Golberg *et al.* 1994]. Considering that transformational superelastic deformation has to be made at a temperature above  $A_p$ , the stress for inducing martensitic transformation is high. As a result, slip occurs before the applied stress can induce martensitic transformation. Under this circumstance, permanent strain was generated.

The two-way shape memory effect in HTSMAs is more difficult to implement, especially by training processes. This is because at elevated temperature, dislocations are

prone to recover. However, Sun *et al.* reported limited success in developing two-way SME in the Ni-Ti-Pd and Ti-Ni-Pd-B shape memory alloys by mechanical training [Sun and Wu 1994]. The training process that was used included: 1) deforming the material to a given constant strain at room temperature; 2) unloading and heating to  $A_f + 30^\circ\text{C}$ , and finally, 3) quenching the sample into water. The effect of training strain and training number on TWSME was studied. It showed that applying larger training strain and more training numbers increase the strain for TWSME. However, most TWSME strain had been developed in the first five cycles. Sun *et al.* also found that as the palladium content increases, the TWSME was decreased for a fixed training numbers at a fixed training strain. Boron additions did not affect the 2-way SME developed by training. Transformation temperatures were also measured for samples after different training numbers. They seemed to be very stable over thermal cycling.

*2.3.1.3. Improvement of Mechanical Properties of Ti-Ni-Pd SMAs.* Substituting Ni with Pd in Ni-Ti SMAs caused a decrease in the critical stress for slip at high temperature and decreasing ductility in the alloys. While low critical stress is the reason for inferior shape memory properties, brittleness made the material less durable and harder to process. Efforts have been made to improve the ductility of the material and increase the critical stress for slip. As reviewed below, the strategies that have been developed included: 1) increase the critical stress for slip by adding a 4th element; 2), strengthen the austenite by age hardening, 3) strengthen the austenite by a thermomechanical treatment.

Yang and Mikkola, among other research groups, attempted to improve the room-temperature ductility of Ni-Ti-Pd alloys (Tuominen and Biermann 1988, Yang and Mikkola 1993) by adding a small amount of boron. According to them, the room-temperature tensile elongation of as-cast sample that has no boron addition was only 2%. With about 2000 ppm of boron, tensile elongation reached 8%. More boron additions tend to decrease the ductility. The reason for the ductilization by boron addition was

because the grains were refined. Micrographic investigation revealed that the as-cast sample with boron has the grain size 4 times smaller than that without boron. Also, boron additions clearly reduce the rate of grain growth that occurred by subsequent annealing of the as-cast samples. As a result, boron is also effective in increasing the materials ductility at high temperature [Suzuki, Xu, Morito, Otsuka and Mitose 1998]. For example, with the same starting grain size with or without boron in hot rolled  $\text{Ti}_{50}\text{Pd}_{30}\text{Ni}_{20}$ , after annealing at  $900^{\circ}\text{C}$  for 1 hour, the sample with boron had a grain size of less than 50 microns, whereas the sample without boron had a grain size of larger than 120 microns.

Boron is also beneficial to high-temperature ductility and strength of  $\text{Ti}_{50}\text{Pd}_{30}\text{Ni}_{20}$  alloy. The ultimate tensile strength and elongation were about 780 MPa and 16% for  $\text{Ti}_{50}\text{Pd}_{30}\text{Ni}_{19.8}\text{B}_{0.2}$ , respectively, compared to 460 MPa and 8% for  $\text{Ti}_{50}\text{Pd}_{30}\text{Ni}_{20}$  alloy. Boron existed as  $\text{TiB}_2$  precipitates with an average size larger than 1 micron, and these precipitates distributed within grains, rather than on grain boundaries. More importantly, additional boron had no noticeable negative influence on high-temperature shape memory characteristics. Suzuki *et al.* [1998] reported that in  $\text{Ti}_{50}\text{Pd}_{30}\text{Ni}_{20}$  alloy after homogenization at  $1000^{\circ}\text{C}$  for 5 hours followed by hot rolling at 923K and annealing 1 hour at 1173 K, with or without boron, the recoverable strain was over 3%. However, the stress that allows a full strain recovery was only about 100 MPa. It was suggested that if small and densely distributed  $\text{TiB}_2$  borides could be achieved through using proper thermal treatments, it was possible to improve the high-temperature SME by precipitation hardening.

Precipitates, such as  $\text{Ni}_4\text{Ti}_3$  in Ni-rich Ni-Ti binary alloys were useful to improve the shape memory properties because the critical stress for slip was increased. Shimizu *et al.* [1998] investigated an approach for inducing precipitates in non-equiatomic  $\text{Ti}_{50.6}\text{Pd}_{30}\text{Ni}_{19.4}$  alloys. They found that the shape memory characteristics were improved

by aging the alloy at 773K for 1 hour. The recovery rate<sup>6</sup> was about 90% for a total of 6% strain for deformation at 473 K, which was about 10% higher than that for the equiatomic Ti<sub>50</sub>Pd<sub>30</sub>Ni<sub>20</sub> alloy. The reason for the improvement was found to be the hardening effect by homogeneously distributed fine precipitates Ti<sub>2</sub>(Ni+Pd), which had Ti<sub>2</sub>Ni type structure and were produced by aging at 773 K of the Ti-rich alloy. The appearance of fine Ti<sub>2</sub>(Ni+Pd) may suggest that the solubility of excess Ti is greater in ternary alloy than that in binary Ni-Ti.

The third approach to improve the shape-memory property of Ti-Ni-Pd is thermomechanical treatment, as suggested by the success of Ti-Ni binary alloys. Golberg *et al.* reported their work on a Ti<sub>50</sub>Pd<sub>30</sub>Ni<sub>20</sub> composition in this regard [Golberg *et al.* 1994, 1997]. The solution treated sheet was firstly cold rolled to 15 to 25% thickness reduction, then annealed at 673 K for a recovery treatment<sup>7</sup>, and then deformed to a tensile strain of 5.3% at 443 K (20 to 40°C below M<sub>f</sub>). This deformation was fully recovered upon heating to A<sub>f</sub> temperature. In comparison, if the cold rolled material was solution treated at 1173 K, the perfectly recoverable strain was only about 2%, even though the solution treated sample was easier to deform than the recovery treated sample. The reasons for the improvement were because that the critical stress for slip in the martensite was increased to 400 MPa after recovery treatment compared to 200 MPa for the sample having only solution treatment. Superelasticity resulting from stress induced martensitic transformation was also observed in the recovery treated sample, but it was absent in the solution treated sample.

It should be pointed out that, similar to the results for Ti-Ni binary alloys, proper thermal treatment was crucial to a successful implementation. This is because during high-temperature annealing, recrystallization could occur, which would result in

---

<sup>6</sup> The recovery rate is defined as the percentage of the *plastic* strain imparted to martensite that can be recovered when the sample is heated to austenite.

<sup>7</sup> "Recovery" is used here in the classical metallurgical sense, *i.e.*, to represent a process of dislocation annihilation.

substantial grain growth and degraded SME properties. Xu *et al.* systematically studied the recovery and recrystallization behavior of Ti<sub>50</sub>Pd<sub>30</sub>Ni<sub>20</sub> alloys after cold work [Xu, Shimizu, Suzuki, Otsuka, Ueki and Mitose 1997]. Hardness drop was linked to the reverse martensitic transformation, and occurrence of recovery and recrystallization. TEM observation directly revealed that recrystallization took place during annealing at temperature higher than 600°C. This result was useful for the optimization of thermomechanical treatment procedure.

### 2.3.2. Ni-Ti-Zr and Ni-Ti-Hf Alloys

Although Ti-Ni-Pd (Pt, Au) alloys are very promising high-temperature shape memory alloys, they contain considerable amount of expensive noble metals. The other group of Ni-Ti –base alloys, Ni-Ti-Hf and Ni-Ti-Zr, which are obtained by substituting Ti with Zr or Hf, are more economical HTSMA candidates. Also, the tertiary additions are more efficient in raising transformation temperatures in Ni-Ti-Hf and Ni-Ti-Zr alloys. Below, the phases, phase transformations, mechanical properties and shape memory characteristics of Ni-Ti-Hf and Ni-Ti-Zr alloys are reviewed.

*2.3.2.1. Transformation Temperatures.* Similar to Pd (Au, Pt) substituting for Ni in binary NiTi, Zr and Hf substituting for Ti can also effectively increase the martensitic transformation temperatures. Pu *et al.* systematically studied the effect of the amount of Zr [Pu, Tseng and Wu 1995] and Hf [Pu, Tseng and Wu 1994] additions on the martensitic transformation temperatures. For Ni-Ti-Zr alloys with fixed Ni composition at 50at.% and varying Zr composition, the transformation temperatures decreased only slightly with increasing Zr content until Zr reached 10at.%, whereafter the transformation temperatures increased dramatically. With 20at.% of Zr, the A<sub>p</sub> temperature reached about 300 °C and M<sub>p</sub> temperature of reached 260 °C. R-phase transformation was also

observed in the alloy with small amount of Zr additions.

Substituting Hf for Ti raises the transformation temperatures even more efficiently than with Zr. As also reported by Pu *et al.* on solution-treated Ni-Ti-Hf alloys with fixed Ni content at 50at.% and varying Hf content, the transformation temperatures were also decreased slightly for the first few percents of Hf additions, then increased rapidly with further increase of Hf content. Angst *et al.* [Angst, Thoma and Kao 1995] also conducted a study of the effect of composition on the transformation temperatures in as-cast Ni-Ti-Hf samples. According to them, with 50at.% or less of Ni content, the apparent minimum peak transformation temperatures were observed at Hf composition between 0 to 3at.%. Transformation temperatures slightly increased before the Hf reached 8at.%, then increased with a large slope as hafnium continuously increased. When the hafnium reached 30at.%, the  $A_p$  and  $M_p$  temperatures reached 600°C and 535°C, respectively. The transformation energy measured by DSC was in the range of 20 to 25 J/g over the Hf composition range between 0 to 15at.%. Figure 2.7 summarizes the effect of hafnium content on  $M_s$  temperature obtained by different research groups.

Angst *et al.* also studied the transformation temperatures of the as-cast Ni-Ti-Hf alloys with off-stoichiometric compositions. As shown in Figure 2.8, the transformation temperatures did not change with the Ni content changed from 40 to 50at.%. However, once the Ni content exceeded 50at.%, the transformation temperature dropped dramatically. With only 0.5at.% more Ni than stoichiometric, both  $A_p$  and  $M_p$  decreased more than 100°C.

Annealing may change the transformation temperatures of Ni-Ti-Hf alloys too, especially for as-melted-then-quenched samples with off-stoichiometric composition, and cold worked samples. Besseghini *et al.* [Besseghini, Villa and Tuissi 1999] studied the  $Ni_{40}Ti_{50}Hf_{10}$  alloy and found that annealing at 400°C after solution treatment decreased the transformation temperature, but annealing at 600°C raised the transformation temperatures slightly. Besseghini attributed the variation of transformation temperature

to the growth of large amount of second phases (about 50% in volume fraction) that are present in the alloy. Augst *et al.* [1995] found cold work considerably decreased the transformation temperature of Ni-Ti-Hf alloy, but the transformation temperatures were recovered upon annealing at high temperatures.

The stability of transformation temperatures against thermal cycling was evaluated by Besseghini *et al.* [1999] in solution treated Ni<sub>40</sub>Ti<sub>50</sub>Hf<sub>10</sub> alloys. Up to 30°C decrease was observed for the first 20 cycles. But the transformation temperature tended to stabilize after the first 20 cycles. Experiments by Pu *et al.* [1994, 1995] revealed similar phenomenon for Ni-Ti-Zr alloys. But Pu *et al.* also found the thermal stability was improved as more Zr was added. Pu *et al.* also found that Ni-Ti-Hf had better thermal stability against thermal cycling than Ni-Ti-Zr alloys, but neither of them was as good as Ti-Ni-Pd in this respect.

The crystal structure of martensite for Ni<sub>48.5</sub>Ti<sub>36.5</sub>Hf<sub>15</sub> alloys was determined by Han *et al.* [Han, Zou, Jin, Zhang and Yang 1995, Han, Zou, Wang, Zhang, Yang and Wu 1995]. It had the same B19' structure as martensite in Ni-Ti binary alloys with the lattice parameters only changed slightly. However, unlike martensite in Ni-Ti binary alloys, the martensite self-accommodating substructure of Ni<sub>48.5</sub>Ti<sub>36.5</sub>Hf<sub>15</sub> alloy was dominated by (100) compound twins, and Han *et al.* attributed this substructure characteristic to the small recovery strain of the ternary Ni-Ti-Hf alloys.

Second phases may exist in Ni-Ti-Hf alloys, especially for alloys with off-stoichiometric composition. Precipitation and growth of second phases during annealing were mainly responsible for variation in transformation temperatures, and were also the reason for alteration of mechanical and shape-memory properties. (Ti+Hf)<sub>2</sub>Ni precipitates were very common in nickel-lean Ni-Ti-Hf alloys. (Ti+Hf)<sub>4</sub>Ni<sub>2</sub>O<sub>x</sub> precipitates were also present due to inevitable introduction of oxygen. Thoma and Boehm [1999] observed a linear relationship between the nickel composition and volume fraction of the precipitates. With nominal 50at.% of nickel there was 0.3% (in volume) precipitates.

When the nickel was decreased to about 49at.%, the volume fraction of precipitates was increased to 6%.

2.3.2.2. *Shape-memory Properties of Ni-Ti-Zr and Ni-Ti-Hf Alloys.* Shape-memory was observed in both Ni-Ti-Zr and Ni-Ti-Hf alloys with up to 40at.% of Zr or Hf replacing Ti. However, the shape memory properties were evidently inferior to binary Ni-Ti because of the tertiary element replacement. This SME property degradation was primarily manifested in the reduction of fully recoverable strain, reduction of the stress allowing full strain recovery, increase of critical stress for martensite reorientation and decrease of critical stress for slip in austenite at high temperature.

Pu *et al.* [1995] evaluated the one-way SME properties of Ni-Ti-Zr and Ni-Ti-Hf alloys, which was done by pre-straining the material at room temperature then heating the material to 50°C above the  $A_r$  temperature. It was found that with increase of Zr content, the strain recovered by heating was reduced. For  $Ni_{50}Ti_{35}Zr_{15}$  alloys, 1.5% pre-strain that was obtained at room temperature was fully recovered upon heating, and 2.2% of pre-strain could be recovered by 90%. For alloys with 5 to 10at.% of Zr composition, the fully recoverable strain was nearly 2.5%. Fully recoverable strain in the Ni-Ti-Hf alloys was also decreased as more hafnium was added. With 5at.%, 15at.% and 20at.% of hafnium in the alloy, the fully recoverable strain was 3.0%, 2.5% and 1.8%, respectively.

However, if the martensite was pre-deformed at elevated temperature, the recovery rate<sup>8</sup> could be improved. Olier *et al.* [1995] studied the dependence of recovery rate on uniaxial strain in a  $Ni_{50}Ti_{38}Hf_{12}$  at room temperature. It was found that the recovery was poorer for the lower deformation (recovery rate was 60% for prestrain = 1%), and it was increased for the higher deformation (recovery rate was 80% for prestrain = 2.5%). Therefore, there seemed to be a competition between the plastic deformation of

---

<sup>8</sup> In uniaxial deformation mode, the recovery rate is defined as the percentage of strain recovered on heating in the total plastic prestrain (elongation). In bending deformation mode, the recovery rate is measured as the percentage of angle recovered on heating from the initial angle.

the austenite and the reorientation of martensitic variants. Deforming the martensite at higher temperature the recovery was better. For example, a 1% strain deformed at 150°C (35°C below  $A_s$  temperature) recovered 93% upon heating.

The best SME was found in  $Ni_{50}Ti_{38}Hf_{12}$  by deforming the austenite at 150°C,<sup>9</sup> a temperature just above  $M_s$ . The alloy fully recovered as much as 4% strain on heating. Based on this experiment, Olier suggested that the movement of twin boundaries in  $Ni_{50}Ti_{38}Hf_{12}$  appeared more difficult than that in binary Ni-Ti. The accommodation process could be hindered by interface pinning or plastic relaxation, which was in correlation with the increase of the hysteresis of Ni-Ti-Hf alloys.

Wang *et al.* [Wang, Cai, Zhu and Zhao 1997] conducted similar experiments on  $Ni_{50}Ti_{35}Hf_{15}$  alloy. They also found if the tensile test was conducted at 353K, up to 3% strain could be fully recovered. 4% strain could be recovered by 95%, and 6% strain by 83%, upon heating to above  $A_f$  temperature.

Transformational superelasticity has not been reported in Ni-Ti-Hf or Ni-Ti-Zr high-temperature shape memory alloys. As was the case for Ni-Ti-Pd(Pt, Au) alloys, the low critical stress for slip in the high-temperature austenite was thought to be the cause. Although stress induced martensitic transformation was observed at temperature just above  $M_s$  temperature, the superelasticity occurred only when the deformation temperature was above  $A_f$  temperature, which was at least 50°C higher than  $M_s$  due to the wide transformational hysteresis of Ni-Ti-Zr and Ni-Ti-Hf alloys.

Two-way SME acquired by training is generally associated with the establishment of dislocation structures and with local internal stress fields in austenite developed during training, which act to favor the formation of certain variants of martensite during cooling. For HTSMAs, because of its high austenite transformation temperature, the dislocation arrangements formed during thermomechanical cycling are easy to recover, making it

---

<sup>9</sup> Because of the transformation temperatures,  $Ni_{50}Ti_{38}Hf_{12}$  was martensitic if it was heated from a low temperature (below  $M_f$  temperature), and it was austenitic if it was cooled down from a high temperature (above  $A_f$  temperature)

more difficult to train the sample to demonstrate two-way SME. However, Pu *et al.* [1994] demonstrated that two-way SME could be implemented into Ni-Ti-Hf HTSMA by training in a bending mode. Even so, they found the magnitude of TWSME strain was not comparable to binary Ni-Ti, and the TWSME became saturated by only 3 or 4 cycles of training [Pu *et al.* 1994].

**2.3.2.3. Mechanical Properties.** In general, Ni-Ti-Zr and Ni-Ti-Hf alloys had considerably poorer ductility and workability than Ni-Ti binary alloys, especially at room temperature. This was supported by the higher hardness of Ni-Ti-Zr and Ni-Ti-Hf alloys. However, Thoma *et al.* [1999] found it possible to achieve a reduction in area of 27% without cracking when they rolled Ni<sub>50</sub>Ti<sub>40</sub>Hf<sub>10</sub> alloys at room temperature. Continued reductions in area above 27% produced significant edge cracking of the strip. Wang *et al.* [1997] systematically studied the tensile behavior of Ni<sub>50</sub>Ti<sub>40</sub>Hf<sub>10</sub> alloys at different temperatures. Unlike the stress-strain curve of binary Ni-Ti alloys, a plateau (*i.e.*, perfect plasticity) was generally absent. Ultimate elongation, as well as characteristic yield stress  $\sigma_{0.2}$ , was a function of test temperature. After solution treatment at 900°C for 1 hour, the material had an ultimate elongation of ~10% at room temperature. With the increase of tensile testing temperature, the ultimate elongation increased substantially, and it reached over 30% at temperature just above  $A_f$  temperature. The dependence of  $\sigma_{0.2}$  stress with temperature was just the opposite with that of ultimate elongation with testing temperature. At room temperature,  $\sigma_{0.2}$  was 550 MPa. As the temperature decreased, it gradually decreased to the minimum (430 MPa) at 510K (just above  $A_f$  temperature). Then it climbed to 650 MPa at 590 K.

For Ni-Ti-Hf and Ni-Ti-Zr high-temperature shape memory alloys, the critical stress for martensite reorientation is high so that permanent strain is easily introduced when the material is deformed in the martensitic condition. Olier *et al.* [1995] studied the yield stress of Ni<sub>50</sub>Ti<sub>38</sub>Hf<sub>12</sub> SMA alloy (Figure 2.9) and found that the yield stress was

highly temperature dependent. The lowest yielding stress was obtained when the material was deformed just above  $M_s$  in austenite (deformation temperature = 150°C,  $M_s \sim 140^\circ\text{C}$ ). The stress-strain curve exhibited a respective elastic contribution of both austenite and martensite phases, separated by the plateau associated with stress induced martensitic transformation. The SME properties were also the best because loading at this condition led to optimal variant formation. Therefore, the need for reorientation of martensite variant was avoided. This result suggests that Ni-Ti-Hf (Zr) alloys may have optimal performance in some working conditions, such as applying continuous biasing stress while cycling the material between low temperature and high temperature.<sup>10</sup>

### 2.3.3. General Comparison of Different HTSMAs

In comparing Ni-Ti-Zr and Ni-Ti-Hf as high-temperature shape memory alloys, Ni-Ti-Zr has advantages over Ni-Ti-Hf in (1) cost; (2) slightly smaller hysteresis for alloys with same transformation temperature; (3) potentially better SME properties. However, Ni-Ti-Hf alloys hold advantages over Ni-Ti-Zr in the following aspects: (1) it has higher transformation temperatures for the same 3<sup>rd</sup> element content; (2) Hf has lower affinity for oxygen as compared to Zr; (3) it has a larger temperature range for hot working due to the slightly higher peritectic and melting points; and (4) it shows better stability against thermal cycling. In comparison between Ni-Ti-Pd group and Ni-Ti-Hf group, Ni-Ti-Pd has advantages over Ni-Ti-Hf in some areas: (1) it has smaller transformation hysteresis which leads to quick response; and (2) the transformation temperatures are more stable during thermal cycling. Ni-Ti-Hf has advantages over NiTi-Pd on some other areas: (1) it is more cost effective; (2) it needs less third element to be

---

<sup>10</sup> Binary Ni-Ti SMAs also exhibit better shape memory properties in such conditions. For example, substantial transformational strain may be obtained at small biasing stress during cooling down, while the same level of stress may not be enough to produce any shape-memory strain if loaded to the martensite.

added for the same transformation temperature and (3) it has potentially larger recoverable strain.

## **2.4. Shape-memory Alloy Thin Films**

Thin film science and technology plays an important role in modern industry. Major applications of thin films have been found for coatings and microelectronics. Interest in fabrication of shape-memory alloy thin films has arisen due to their potential usefulness in microelectromechanical systems (MEMS). As an actuator material, shape-memory alloys may offer large energy-density output upon reverse martensitic transformation, which may be conveniently activated by Joule heating. In addition, by fabricating the shape-memory alloy in the form of a thin film, the disadvantage of slow response for SMA actuator may be greatly offset. In this section, a brief summary of thin film fabrication by sputtering, and the structure and stress characteristics of sputtered thin films is given first, then shape memory in thin films will be reviewed in detail.

### **2.4.1. Deposition of Thin Films by Sputtering**

There are numerous methods of making thin films, but there basically are two categories: Chemical Vapor Deposition (CVD) and Physical Vapor Deposition (PVD), according to whether chemical reactions are involved during the deposition. Sputtering, usually a PVD method unless reactive working gas is used, has high deposition rate and high flexibility of target material selection, thus is favored in many circumstances. It remains the only method successfully applied to fabrication of SMA films.

*2.4.1.1. Sputtering Processes.* Sputtering a thin film usually takes place in a vacuum chamber in order to avoid contamination from atmosphere and to allow atom transport to the substrate. A voltage, either direct current (d.c.) or radio frequency (r.f.),

is applied between target (cathode) and substrate (anode), and it is the energy source to ionize an inert working gas and accelerate the positive ions to the cathode. Energetic ions strike the target surface, causing the target atoms to eject from the surface and to form continuous thin film on the substrate. Secondary electrons from the target play an important role in maintaining the discharge.

The quality of the films is determined by the sputtering parameters such as power to the target, deposition rate, working gas species, working gas pressure, distance from cathode to substrate, and substrate temperature. Among those parameters, working gas pressure and substrate temperature affect thin film quality most dramatically. In general, lower working gas pressure is more desirable because of three reasons: first, less working gas will be incorporated into the deposit so the deposit will be denser. Second, the deposited atoms arrive onto the substrate with more kinetic energy so they are more likely to further diffuse. Third, more energetic reflected working gas neutrals arrive onto the substrate, providing more energy for films to further densify. However, ordinary sputtering has to be operated at high working gas pressure (>10 mTorr) due to reduced ionization efficiency at low pressure. Modification of the simple diode sputtering source needs to be done in order that the working gas pressure can be reduced. Conventionally there are two methods to do so. The first approach to force the secondary electrons travel spirally by applying magnetic field in front of target (magnetron sputtering). The other is to bring additional supply of electrons by introducing a thermoionic source (triode sputtering). Both magnetron sputtering and triode sputtering can be operated at working gas pressure of 1 mTorr or less.

Another important parameter is substrate temperature. In general higher substrate temperature provides more thermal energy allowing the thin film to densify via diffusion. At very high temperature and slow deposition rate, single-crystal films may even be obtained. However, high substrate temperature is not favorable in industry due to increased complexity of the equipment. Magnetron sputtering, which can produce thin

film with reasonably good quality at low substrate temperature, is very popular among all sputtering methods.

*2.4.1.2. Composition, Structure and Microstructure of Sputtered Films.*      Sputtering

from a single-element target obviously produces single-element film in a PVD process, even though the thickness distribution of thin film may vary across the substrate.

Sputtering from multi-element target, however, may produce thin film with composition deviating from that of the target. Basically, the composition shift may arise from several reasons. First, yield rates for different elemental species are different. Therefore, the flux leaving the substrate may have different composition than the target. This is particularly true during the initial sputtering period of a new target. However, the composition discrepancy resulting from yielding rate difference will diminish after a proper wear-in or burn-in period, because the composition change on the surface of target will offset the yield rate difference.

Second, scattering during transport from target to substrate may also cause a composition discrepancy between the target and the film. This is because the atoms with different size and mass have different mean free paths, so some atoms may be more likely to be scattered away than others due to more probable collisions with the background gas atoms. Third, resputtering after the atoms arrive on the substrate may alter the composition of thin film. Incoming atoms may have enough kinetic energy to dislodge some adatoms on the film. Depending on their atomic mass, bonding strength with others, and ability to move to low-energy trapping sites, some atom species may more likely be knocked away from substrate. Despite these uncertainties, it is still possible to get the desired thin film composition by controlling the target composition. This is because the first cause for discrepancy may be eliminated by proper wear-in procedure, and the second and third causes may be corrected through establishing an empirical

relationship between the target composition and film composition, and making suitable compensation in the target composition accordingly.

The structure of thin films may be amorphous, partially crystalline, or totally crystalline, depending on the sputtering parameters that are used. The microstructure of thin film is also determined by sputtering conditions. Thornton [Thornton 1977, Thornton and Hoffman 1985] developed a zone structure model illustrating the structural and microstructural characteristics a function of substrate temperature for sputtered films. The model illustrated that the microstructure of sputtered films are divided into basically three 'zones' depending on the homologous temperature  $T_s/T_m$  (where  $T_s$  is substrate temperature during deposition,  $T_m$  is the melting temperature of the film):

Zone I ( $T_s/T_m < 0.3$ ): Characteristic microstructure of the films is either amorphous or dendritic. In each case the structure is extended in the growth direction. The films are rather porous, and have very poor mechanical properties.

Zone II ( $0.3 < T_s/T_m < 0.5$ ): The most characteristic feature of the microstructure is a largely uniform columnar morphology with high compactness. The grain diameter,  $d$ , extends throughout the thickness of the film,  $t$ , but the grain aspect ratio  $d/t$  is usually less than 1.

Zone III ( $T_s/T_m > 0.5$ ): Metallic films have a columnar structure with a grain diameter greater than the thickness of the film. Films have very strong texture. At extreme conditions, thin film growth in sputtering behaves like epitaxial growth.

The zone structure can be largely explained in terms of self-shadowing, surface diffusion and bulk diffusion. These three mechanisms, along with adsorption of adatoms, constitute four basic processes of film formation. In the first regime, both adatoms and sub-surface atoms have very poor mobility. Due to the self-shadowing effect, porous structures are usually developed. Intermediate substrate temperature allows sufficient

surface diffusion of the adatoms, but bulk diffusion of sub-surface atoms is still sluggish. A more compact film is formed, but numerous grain boundaries exist. At high substrate temperature both surface diffusion and bulk diffusion are sufficient. Therefore, some grain growth takes place during the sputtering process.

Evidently other sputtering parameters can also affect the zone structure. The most pronounced one is the working gas species and its pressure. The momentum exchange between the incoming species and the adatoms provides more energy for adatoms to diffuse. The kinetic energy of the incoming species diminishes as more collisions with working gas occur. Low working gas pressure decreases the probability of such collisions, and the kinetic energy of the incoming species will be mostly preserved. As a result, lowering working gas is similar in a sense to increase the deposition temperature, making the zone structure move toward lower temperature regime.

**2.4.1.3. Extrinsic Stress and Intrinsic Stress.** Stresses are often introduced from thin film fabrication processes and post-fabrication treatment. Stresses in thin films have important effects on many phenomena such as decohesion, defect generation and surface morphology evolution, and they can substantially modify physical properties of the thin films.

Stresses in thin films can be divided into categories: extrinsic stress and intrinsic stress. Extrinsic stress is thermal stress, and it results from the differential CTEs (Coefficients of Thermal Expansion) between thin film and substrate. Assuming that the thermal stress does not exceed the elastic deformation limit of film, and that the substrate is rigid, thermal stress can be quantitatively predicted as:

$$\sigma_{thermal} = \int_{T_s}^{T_f} \frac{E_f}{1-\nu_f} \cdot (\alpha_s - \alpha_f) dT \quad (2.2)$$

Where  $T_s$  and  $T_f$  are starting temperature and finish temperature, respectively.  $E_f$  is the elastic modulus of thin film,  $\nu_f$  is the Poisson's ratio of the film, and  $\alpha_f$  and  $\alpha_s$  are CTEs of film and substrate, respectively.

While the origin of extrinsic stress is quite clear, that of intrinsic stress is much more complicated. In fact, no single model can explain how intrinsic stress is created. Nevertheless, it has been found that a number of mechanisms, such as nonequilibrium growth, defect evolution, interfacial constraint, *in-situ* phase transformation and *in-situ* stress relaxation are related to the sign (tensile or compressive) and the magnitude of the intrinsic stress. However, the dominant mechanism for intrinsic stress in sputtered film is unique compared to films made by other techniques such as evaporation. In sputtered film, compressive stress was usually observed, while films obtained by evaporation were usually under tensile stress. D'Heurle [D'Heurle, Berenbaum and Rosenberg 1968, d'Heurle 1989] first pointed out that, in evaporation, the deposited atoms are nearly in thermal equilibrium with energy about few  $kT$ . In a sputtering process, a flux of depositing atoms and the neutral gas atoms reflected from the cathode arrive onto the substrate with energy up to several  $eV$ . Adatoms on the film are thus subjected to bombardment which, at the atomic scale, is similar to the 'shot peening' effect, an approach widely used to put material surfaces into compression in metallurgical fabrication. It does not matter so much that the energy is small since the damage is immediately buried under newly deposited layers, but rather that the damage is accumulated. The effect is increased under conditions of negative bias sputtering when the substrate is deliberately bombarded with energetic working gas ions. It is particularly noted that this atomic peening mechanism is predominant only when the working gas pressure is low, since too much background gas tends to thermalize the kinetic energy of the working gas atoms reflected from sputtering target.

#### 2.4.2. Sputtered Shape Memory Thin Film

Since 1990, shape-memory alloy thin films as a potential material for microactuator in MEMS has been investigated by a number of research groups [Busch, Johnson, Lee and Stevenson 1990, Ikata, Fujita, Ikeda and Yamashita 1990, Kuribayashi, Yosaki and Ogawa 1990, Walker, Gabriel and Mehregany 1990, Chang and Grummon 1992, Miyazaki and Ishida 1994, Hua, Su and Wuttig 1995]. However, only Ni-Ti-base alloys were successfully made to be shape-memory thin films. In this part, fabrication and characterization of Ni-Ti shape memory thin films are reviewed, and their potential applications are discussed.

*2.4.2.1. Fabrication of Shape Memory Thin Film.* Targets made by different methods may be used to sputter Ni-Ti SMA thin films. However, because oxygen has very strong affinity for titanium and oxygen is known to have grave effects on SME properties of Ni-Ti alloys [Wu, Khachaturyan and Wayman, 1988, Johnson 1991, Lin, Wu and Lin 1994, Barborini, Pieseri, Mutti, Milani, Biasioli, Iannotta and Gialanella 1998], oxygen contamination is a great concern for the target fabrication. The most widely used targets have been pre-alloyed targets. Oxygen level in sputter targets may be well controlled. Besides pre-alloyed targets, composite targets that are composed of pure - element powders [Quandt, Halene, Holleck, Feit, Kohl and Schloßmacher 1995], or sectored pure nickel and titanium material have been used [Bendahan, Canet, Seguin and Carchano 1995, Tsuchiya and Davies 1998].

The composition of deposited Ni-Ti films is of great concern because it is very important for SME and transformation temperature control. It has been repeatedly reported that the composition of sputtered Ni-Ti films deviate from that of the sputter target. For example, Johnson *et al.* reported that sputtering from an equiatomic Ni-Ti target produced thin film containing 51-54at.% nickel [Johnson, Martynov and Minners,

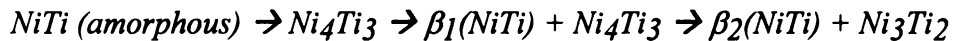
1995]. The major reason for composition discrepancy may be because Ti is a preferentially resputtered species compared to Ni atoms. Sputtering parameters also affect the composition of thin films. Lee [1994] attempted to establish the relationship between film composition and the process parameters in a d.c. magnetron sputtering process. He found that, for a given sputter condition, the film composition varied with the wear history of the target, but steady-state composition of thin film was obtained after the target was worn-in for a period of time. Also, higher deposition power intensifies the preferential loss of Ti, making the film more Ni-rich. However, the composition of film at off-axis position was less prone to change with the deposition power than that at on-axis positions. Bendahan *et al.* [1996] demonstrated that in an r.f. magnetron process, Ni-Ti film composition was sensitive to the product of working gas pressure and working distance ( $P_{Ar} \times D$ ). The lower the value of ( $P_{Ar} \times D$ ) was, the less Ti the sputtered film contained. These results generally point to a resputtering effect dominating the composition shift, but the situation remains uncertain.

Different strategies have been proposed to realize composition control of Ni-Ti film. Bendahan *et al.* [1996] showed that the composition of a plasma could be measured *in-situ* by optical emission spectroscopy, and a small composition change could be realized by changing the working gas pressure. It was also shown that Ni-Ti SMA sputtering may be accomplished by using separate Ni and Ti targets. Almost arbitrary composition of the thin film can be obtained by changing the relative ratio of deposition powers.

Although amorphous Ni-Ti films may be obtained by different methods, they do not possess shape memory properties, and a separate crystallization treatment is needed to confer SME. A crystalline Ni-Ti film may also be obtained at higher substrate temperature (*in-situ* crystallization). Apparently *in-situ* crystallization has certain engineering advantages over the post-deposition annealing, such as shorter processing time. But there are some other issues. Krulevitch *et al.* [Krulevitch, Lee, Ramsey,

Trevino, Hamilton and Northrup 1996] pointed out that the surface smoothness and stress at room temperature needed to be considered. Generally, films sputtered at high temperature have rougher surfaces due to thermal etching and columnar grain growth. Because of the differential CTEs between substrate and the deposit, tensile stress will be developed during cooling down from deposition temperature. This tensile stress may result in delamination of the film from substrate, especially when undercuts exist.

2.4.2.2. *Crystallization of Amorphous NiTi Films.* The amorphous structure is metastable in NiTi at all temperatures below the melting point. When amorphous films are annealed at sufficiently high temperature, crystallization occurs. Crystallization is a first-order exothermic polymorphic phase transformation. Kim *et al.* [Kim, Moire and Steveson 1986] studied the crystallization behaviors of magnetron sputtered Ni<sub>56</sub>Ti<sub>44</sub> amorphous thin film by DSC measurement and TEM investigation, and reported that the crystallization temperature was 791 K and the crystallization sequence was:



Where the  $\beta_1$  and  $\beta_2$  phases were the crystalline B2 matrix when the precipitates were present.

Ishida *et al.* [Ishida, Sato, Takei, Nomura and Miyazaki 1996] observed the microstructure of initially amorphous Ti<sub>51.8</sub>Ti<sub>48.2</sub> films after crystallization annealing. The crystallization sequence was that Guinier-Preston (G.P.) zones formed first, then a fine Ti-rich metastable b.c.t. phase appeared in the matrix, then small spherical Ti<sub>2</sub>Ni uniformly formed in the B2 matrix and at last Ti<sub>2</sub>Ni grows, resulting larger precipitates and more sporadic distribution. While small Ti<sub>2</sub>Ni existed inside the matrix of grains, large Ti<sub>2</sub>Ni preferentially appeared at grain boundaries.

The crystallization temperature of amorphous near-equiatomic NiTi alloys reported by different research groups ranged from 400°C to over 550°C. There are a number of reasons for this inconsistency. First, the crystallization temperature was composition dependent. Ti-rich film had lower crystallization temperature than Ni-rich films. Secondly, the crystallization temperature was related to the heating rate for isochronal heating, such as during DSC measurements. The higher the heating rate, the higher the measured temperature. Thirdly, when the material was held isothermally, the crystallization temperature could be substantially lower if sufficient annealing time was allowed. Zhang [1997] observed the occurrence of crystallization Ni-rich Ni-Ti at 400°C annealing temperature using a wafer curvature measurement. The activation energy for crystallization was 477 kJ/mol.

There have been efforts to decrease crystallization temperature since substrate material may not survive high temperature exposure. Madsen and Jardine [1993] reported that by heavily cold working of the amorphous binary Ni-Ti, the crystallization temperature may be dramatically dropped to as low as 380°C. That was attributed to the large number of defects and stored strain energy introduced by cold working.

*2.4.2.3. Annealing Induced Embrittlement of Amorphous Materials.* Since post-deposition heat treatment is indispensable for as-deposited amorphous Ni-Ti films to become shape memory thin films, the behavior of the amorphous film upon annealing is important. Ishida *et al.* [Ishida, Takei and Miyazaki 1993] found that that volumetric defects in amorphous Ni-Ti films were most likely to survive the subsequent crystallization annealing, therefore, poor-quality amorphous films turned out to be brittle films after crystallized. It was also found that deposition parameters, mainly working gas pressure and deposition power, affected the porosity of amorphous films. At higher deposition power and/or lower Ar pressure, the resulted films appeared featureless (*i.e.*, fully dense) under SEM, suggesting a low-porosity good-quality films. On the contrary,

at lower cathode power and/or high working gas pressure, the resulted films appeared columnar, suggesting porous low-quality films. The results were related to *in-situ* densification which was more complete with the help of energetic bombardment of reflected neutrals.

There have been widespread studies showing that amorphous materials (or metallic glasses) may become brittle during annealing prior to the occurrence of crystallization.<sup>11</sup> The embrittlement was attributed to various structural relaxation phenomena such as phase separation [Haasen 1983, Gruene, Oehring, Wagner and Haasen 1985, Yamasaki and Ogino 1986], element separation [Qu and Xie 1991], formation of microinhomogeneities [Glezer, Molotilov and Utevs kaya, 1984], evolution of short-range order of atoms [Wu and Spaepen 1990, Niikura, Tsai, Inoue and Masumoto 1993] and stress localization [Li, Quan and Hu 1997].

In their study on rapid quenched amorphous  $Ti_{50}Be_{40}Zr_{10}$  and  $Ni_{61}Nb_{39}$  ribbons, Gruene *et al.* [1985] observed spatially extended compositional waves in as-quenched  $Ti_{50}Be_{40}Zr_{10}$  alloys. The amplitudes and wavelengths increased upon aging below the crystallization temperatures. At the same, such compositional variation was not observed in  $Ni_{61}Nb_{39}$  alloys. An embrittlement induced by annealing in  $Ti_{50}Be_{40}Zr_{10}$  alloys was linked to the compositional waves that were aggravated at higher temperatures.

Redistribution of elements along the through-thickness direction was correlated to embrittlement in  $Ni_{80}P_{20}$  metal-metalloid amorphous ribbons. Qu and Xie [1991] detected, by Auger Electron Spectrometry, that P was enriched on the free surface and depleted in the subsurface layers. The amplitude of P enrichment and the thickness of the depletion zone increased with annealing temperature. Planar defects were observed by high-resolution TEM, and these defects were believed to be caused by element redistribution and had a negative impact on the material's ductility.

Glezer *et al.* [1984] observed another form of defects, microinhomogeneities, in a

---

<sup>11</sup> A review on this topic is presented here because it is related to the experimental results.

series of Fe-B-Ni amorphous samples by SEM and TEM. The microinhomogeneities, presumed to have different compositions than the matrix, formed during annealing as a result of structural relaxation. The degree of embrittlement was correlated to the spatial distribution of these defects. Additional elements such as Ce and Sb were introduced to the alloys so the formation of these defects was inhibited, thereby the embrittlement can be alleviated.

Short-range ordering is another possible cause for embrittlement of amorphous materials induced by annealing. There are two kinds of short-range ordering, topological short-range ordering and chemical short-range ordering. Topological short-range ordering is a densification process in which the excess free volume is annealed out [Sonijs, Thijsse and Beukel 1983]. It is an irreversible process and can be kinetically described by a single activation energy [Muraleedharan 1991]. Wu and Spaepen [1990] measured the ductile-to-brittle transition temperature of a Fe-B-Si-C glassy material and correlated the transition temperature with the change in enthalpy due to structure relaxation. They developed a phenomenological model to describe the embrittlement phenomenon based on the change in free volume during relaxation and a minimum free volume for ductility.

In contrast to topological short-range ordering, chemical short-range ordering involves a rearrangement of constituent atoms and may be reversible on temperature changes if atomic mobility is high enough. Kinetic description of chemical short-range ordering requires an activation energy spectrum. Both topological short-range ordering and chemical short-range ordering contribute to the enthalpy change. In general the contribution from chemical short-ordering is overshadowed by that from topological short-range ordering. However, the sensitivity of the enthalpy change on composition may suggest that the occurrence of chemical short-range ordering. For example, Niikura *et al.* [1993] measured the enthalpy change for structural relaxation in two alloy series,  $Mg_{90-x}Cu_xY_{10}$  and  $Mg_{90-x}Cu_{10}Y_x$ , of amorphous ribbons, and the enthalpy change was

correlated to chemical short-range ordering due to a change in bonding state (Mg-Cu and Mg-Y).

In summary, structural relaxation of amorphous materials during annealing can cause a marked loss of ductility and there are numerous mechanisms attributing to the embrittlement phenomenon. Although the atomistic basis of metallic glass embrittlement remains the subject of much debate, empirically, the factors favoring annealing induced embrittlement are well known: a major metallic constituent that has the b.c.c. structure in the crystalline state, a high metalloid content, testing at low temperature or high strain rate, and most importantly, annealing below the crystallization temperature [Wu and Spaepen 1985].

*2.4.2.4. Transformations in Crystalline NiTi Films.* As indicated above, the microstructure of as-crystallized Ni-Ti film is typically a B2 matrix with possible precipitates. Displacive transformations from B2  $\rightarrow$  (R phase)  $\rightarrow$  B19' martensite may take place upon cooling, and reverse transformations take place upon heating, the same way as in bulk Ni-Ti material. The structures of austenite, R-phase and martensite are the same as in bulk material, and the transformation temperatures are also comparable to those of bulk materials.

While the displacive transformations are fundamental for shape memory properties, the second phases have profound effect on the SME properties. However, the possible second phases were distinctively different for Ni-rich and Ti-rich films. For Ni-rich Ni-Ti films, the most important second phase is Ni<sub>4</sub>Ti<sub>3</sub>, which forms at intermediate annealing temperature between 350°C to 600°C. At temperatures higher than 650°C, Ni-rich alloys become solid solutions [Nishida *et al.* 1986]. Rapid quenching from the solution treatment temperature inhibited the formation of Ni<sub>4</sub>Ti<sub>3</sub> and the resulting microstructure was the B2 phase (at temperatures higher than M<sub>s</sub>) with supersaturated Ni. Due to this fact, M<sub>s</sub> was far below room temperature and the R-phase transformation was

absent. Aging at intermediate temperature after solution treatment resulted in the precipitation of  $\text{Ni}_4\text{Ti}_3$ . Ishida *et al.* observed progressive growth of the precipitates at different aging temperatures and times in  $\text{Ni}_{51.3}\text{Ti}_{48.7}$  thin films, then correlated the size of the precipitate with shape memory behaviors. The dependence of transformation temperatures on precipitate size was demonstrated. In general, larger precipitates resulted in higher transformation temperatures, and the effect of precipitate size on martensitic transformation was more evident than on R-phase transformation. In addition, precipitate density in the matrix resulting from different annealing temperatures had an impact on transformation temperatures. This may partly result from composition differences in the matrix, as the over-saturated Ni decreased the  $M_s$  temperature dramatically. Also, the transformation hysteresis ( $A_f - M_s$ ) has a monotonic relationship with the precipitate diameter, *i.e.*, the hysteresis decreases rapidly with the increase of precipitate diameter when the precipitate diameter is smaller than 100 nm, and it is quite stable when the precipitate diameter is larger than 100 nm. This is an indication that the coherency of the precipitates with the matrix is a strong barrier to martensitic transformation.

Bulk (melt-solidified) Ti-rich TiNi binary SMAs are of less industrial interest than the Ni-rich counterpart because of inferior mechanical properties and poorer workability that result from  $\text{Ti}_2\text{Ni}$  second-phase particles that usually appear on grain boundaries. However, Ti-rich thin films behave differently than their bulk counterparts when the former are crystallized from the amorphous condition. Ishida *et al.* studied the effect of heat treatment at annealing temperatures ranging from 500°C to 700°C for different times on an initially amorphous  $\text{Ti}_{51.7}\text{Ni}_{48.3}$  film [Ishida, Sato, Takei and Miyazaki 1995]. After crystallization treatment,  $\text{Ti}_2\text{Ni}$  second phases were formed. Usually the  $\text{Ti}_2\text{Ni}$  phases appeared to be evenly distributed inside the matrix grains, which was distinctively different in the situation for melting-solidified bulk material. Essentially this is because Ti can be super-saturated in amorphous TiNi and caused to precipitate out at low

temperature. Only at extreme annealing conditions (such as high temperature at 700°C, long time at 1000 hrs), do the precipitates grow preferentially at grain boundaries.

Unlike Ti-rich bulk material, crystalline Ti-rich films obtained by annealing of the amorphous phase display an R-phase transformation as well as martensitic transformation during cooling from austenite. Ishida *et al.* [1995] reported that martensitic transformation temperatures increased with the increasing annealing temperature and time with the annealing temperature ranging from 500°C to 700°C. Kawamura *et al.* [Kawamura, Gyobu, Horikawa and Saburi 1996] studied extensively both martensitic transformation temperature and R-phase transformation temperature. They found that R-phase transformation temperature is evidently more stable than the martensitic transformation temperature. In their unpublished work, Zhang and Grummon [1998] studied the effect of heat treatment on the transformation temperatures of originally amorphous Ti-rich films. It was found that the transformation temperatures were increased as the annealing temperatures increased from 500°C to 700°C. In the mean time, the transformation hysteresis was decreased.

Recently, a non-equilibrium phase was found in the Ti-rich thin films when the materials were heat-treated at temperatures a little above the crystallization temperature, which had been never found in the bulk materials. Under transmission electron microscope, the new phase, which was identified as a b.c.t. phase, appeared to be disk-shaped platelets of Ti-rich composition with sub-nanometer thickness and 5 to 10 nm diameter. They strongly suppressed martensitic transformation. High-resolution TEM revealed that they were formed at the interface between crystallized domains during the crystallization process. It was also found that these non-equilibrium phases were formed at low annealing temperature in an initially amorphous film for a fairly long annealing time (for example, 745 K for 1 hour). At relatively high annealing temperature, the very early stage (for example, 773 K for 10 minutes), a platelet second phase can be formed. With increase in annealing time, spherical precipitates started to appear. Those spherical

precipitates were identified as  $Ti_2Ni$ , and the nuclei formed evenly in the sample. As the annealing time increased, they grew preferentially along the grain boundaries.

It is well-known that the crystalline Ni-Ti films are obtainable at higher substrate temperature [Ikuta *et al.* 1990, Gisser *et al.* 1992, Hou and Grummon 1995, Krulevitch *et al.* 1996]. As-deposited films possessed SME without necessity of any additional thermal treatment. Hou [1998] has studied systematically the phase transformation and shape memory behaviors of Ni-rich NiTi binary thin film deposited at elevated substrate temperatures. He developed a model showing the structure/microstructure dependence on the deposition temperature, which was believed to be the dominating parameter. According to Hou, by using a Ni-rich target, magnetron sputtered Ni-rich film was amorphous when the substrate temperature was below 300°C. With increased substrate temperature, very fine grain started to form inside the amorphous matrix. Grains appeared to be columnar, and the diameter of the grains increased as the thickness of thin film continuously grew. Therefore, although the diameter of columnar grains may be relatively large on the growing surface, it was very small at areas adjacent to the substrate. There was a tendency that the thin layer of deposit next to substrate surface was still amorphous even the substrate temperature was high enough to produce crystalline structure elsewhere. Further increasing the substrate temperature resulted in larger columnar grain diameter (on the growing surface) and  $Ni_4Ti_3$  precipitates started to form inside the grain, and the size of precipitates was larger at higher substrate temperature.

One of the important results in Hou's work was that crystalline film could be obtained at substrate temperature considerably lower than the generally reported crystallization temperature. Hou attributed the surface diffusion during deposition to this temperature difference compared to bulk diffusion in the other method. As we know, the activation energy for diffusion is different for different diffusion mechanisms. Because there is less lattice resistance, surface diffusion is easier than bulk diffusion, therefore, the activation energy is smaller, and it leads to a crystalline film growth at lower temperature.

Other mechanisms for thin film growth become operational at higher temperature. Large grains and large precipitates at high substrate temperature were mainly associated with bulk diffusion occurring during the sputtering process.

*2.4.2.5. Mechanical and SME Properties.* The properties of Ni-Ti shape memory thin films are comparable to those of bulk Ni-Ti. The ultimate elongation can reach more than 10% in Ni-rich films and can be as high as 40% for nominally equiatomic composition. The tensile fracture stress is usually over 700 MPa for nominal equiatomic composition and can reach 1.7 GPa for Ni-rich compositions. The recoverable strain associated with martensitic transformation nearly 6%, and the maximum stress for full strain recovery over 500 MPa can be achieved.

Like bulk materials, Ni-rich films are more extensively studied than Ti-rich films. This is because the precipitate in Ni-rich films,  $\text{Ni}_4\text{Ti}_3$ , helps to optimize the shape memory properties. Ishida *et al.* studied effect of  $\text{Ni}_4\text{Ti}_3$  precipitates, particularly the size of the precipitates, on shape-memory characteristics in originally amorphous  $\text{Ni}_{51.3}\text{Ti}_{48.7}$  films [Ishida *et al.* 1996]. Note that the grain size has not been changed appreciably after different aging procedure so this effect was excluded. It was found that when the precipitates were small, the critical stress for slip could be over 500 MPa, but it decreased rapidly to below 300 MPa when the precipitates grew to 100 nm in diameter. Further growth of the precipitates resulted in even lower critical stress, but in a less effective manner. Maximum recoverable strain was also higher for the samples with smaller precipitates, but it also depended on annealing temperature. It was suggested that the dependence of aging temperature is associated with the size and spatial distribution of precipitates.

Mechanical and shape-memory properties of Ti-rich thin films that crystallized from originally amorphous samples were also studied. Surprisingly Ti-rich films were not as brittle as their melt-solidified bulk counterparts. Ductile SMA films were obtained

with titanium as high as 56.1at.%. The reason is because the distribution of second phase  $Ti_2Ni$  was different in bulk material and thin film samples. In thin films, precipitates were evenly distributed inside the grains, while they formed preferentially on grain boundaries in the melt solidified bulk samples, which was the cause for embrittlement. Using thermal cycling at constant load, Ishida *et al.* [1996] demonstrated the annealed  $Ni_{51.3}Ti_{48.7}$  films had recoverable strain over 4% and the maximum stress for full strain recovery up to 400 MPa. Due to the good ductility of Ti-rich films, they are favored over Ni-rich films under some circumstances because both relatively high transformation temperatures and good shape memory properties can be obtained, and Ti-rich films are more tolerant of small errors in composition.

Ogawa *et al.* observed the precipitation sequence of Ti-rich Ni-Ti films and correlated the precipitate characteristics with the shape memory properties [Ogawa, Sato and Miyazaki 1997]. As described in section 2.4.2.3, second phases having morphology of disk-shaped platelets were found in Ti-rich films crystallized at lower temperature, and they evolved into  $Ti_2Ni$  precipitates at higher annealing temperature. Disk-shaped platelets formed inside the matrix during annealing amorphous films for 1 hour at 400°C. The recoverable strain was near 4%, but critical stress for slip was the highest (at 250 MPa). Increasing the annealing temperature to 500°C caused very fine spherical precipitates of  $Ti_2Ni$  to form inside the matrix. Correspondingly, the recoverable strain increased to the maximum at near 6% but the critical stress for slip decreased to about 100 MPa. When the annealing temperature was increased to 600°C, large  $Ti_2Ni$  precipitates formed along the grain boundaries. At that time, the recoverable strain decreased back to 4%. Therefore, annealing temperature higher than 550°C was not recommended because maximum recoverable strain and critical stress for slip were decreased.

Ni-Ti films deposited at elevated substrate temperature showed SME without necessity of crystallization annealing. Hou conducted tensile tests of the Ni-rich films at

different temperatures. He found that at low temperature when the material was martensitic, there was a plateau-like segment on the stress-strain curve and the strain associated with the plateau-like segment was up to 4.3%. At high temperature when the materials were austenitic, superelastic properties were demonstrated.

*2.4.2.6. NiTi SMA Films in MEMS and Related Research.* SMA thin films are regarded as potential materials for microactuators in microelectromechanical systems due to their robustness and large recoverable strain. Busch and Johnson proposed a method to fabricate silicon-base NiTi SMA microactuator/microvalve using a Si etch process [Johnson and Ray 1994]. In their method, thin films of amorphous Ni-Ti were sputtered onto Si wafer and crystallized at high temperature. Photolithography was used to pattern both sides of the wafer and then SMA etching and Si etching were performed. Finally a device having a rectangular Si frame, a narrow NiTi SMA strip running through middle of the frame, and a small Si island at the center of the frame was made. In operating the device, d.c. current is applied to the SMA thin film to heat the material, and on-and-off switching can change the material structure between austenite and martensite. When the SMA is stressed such as by virtue of a small biasing spring located in the middle, the center island can move up and down by supplying on-and-off electrical power (square wave), therefore it can be used as a microactuator or microvalve. The structure of a prototype of NiTi microvalve is shown in Figure 2.10.

The displacement of the center island depends on the length of SMA strip as well as recoverable strain. Assuming that initially the SMA strip does not sag nor under any tension, cyclic displacement due to reversible transformation can be estimated as (Figure 2.11):

$$y = \frac{L}{2} \left( \sqrt{(1 + \varepsilon_0 + \varepsilon)^2 - 1} - \sqrt{(1 + \varepsilon_0)^2 - 1} \right) \quad (2.3)$$

where  $y$  is the vertical displacement,  $L$  is the length of the SMA strip,  $\varepsilon_0$  is the conventional elastic strain resulting from applied force  $F$ ,<sup>12</sup> and  $\varepsilon$  is the recovered strain resulting from reversible martensitic transformation under biasing load  $F$ . It may be noted that, although the force  $F$  is constant, the stresses are different at high-temperature and low-temperature positions due to different deflection angle. The applied force to the sample, which may be converted to uniaxial stress ( $\sigma$ ) if the dimensions of the SMA strip are known, can be calculated using similar triangular principle:

$$\sigma = \frac{1 + \varepsilon_0 + \varepsilon_r}{2 \cdot \sqrt{(1 + \varepsilon_0 + \varepsilon_r)^2 - 1}} \times \frac{F}{t \cdot w} \quad (2.4)$$

where  $F$  is the force applied vertically to the SMA strip,  $t$  and  $w$  are the film thickness and film width, respectively.

Estimation using equation (2.3) tells us that considerable displacement can be realized even when the lateral dimension of the actuator is rather small. For example, assuming the effective length of the thin film strip is 2mm, elastic strain ( $\varepsilon_0$ ) due to applied force  $F$  is 0.5% and the recoverable strain  $\varepsilon$  is 2%, the displacement at the center of the strip is about 124 microns.

Ion-beam sputtering is another way to form Ni-Ti SMA films, and crystalline films can be obtained at relatively low substrate temperature. In a study reported by Tsuchiya *et al.* [1998], near-equiatomic Ni-Ti films were deposited using Kaufman-type gridded ion beam source to bombard a composite sectored Ti/Ni target at a 45° angle through an aperture. During deposition, no external heating was applied to the substrate.

---

<sup>12</sup> The elastic modulus of Ni-Ti SMA is a function of temperature/phase. Therefore, temperature change also results in different elastic strains if the applied force is constant, and this change also causes cyclic displacement of central island in the microactuator assembly. However, the change in elastic strain is typically one order of magnitude less than the transformation strain.

However, due to the energy generated by ion beam bombardment, the substrate temperature increased to 170°C. The as-deposited thin films were crystalline, and they showed R-phase and martensitic transformations as well as shape memory properties. This result, which was in agreement with an earlier experiment conducted by Grummon's group [Walles, Chang and Grummon 1992], suggested that by using ion beam sputter deposition, the as-deposited NiTi thin films possessed SME without additional heating of substrate. Thus, polyimide substrates can be used. However, one of the major restrictions was the low deposition rate comparing to d.c. or r.f. magnetron sputter deposition. At the ion beam current density about 1 mA/cm<sup>2</sup>, the deposition rate was only about 1 micron in 1 hour of deposition.

Grummon *et al.* suggested a novel way to bias the martensite formation to create cyclic displacement in a SMA thin film [Grummon and Gotthardt 2000]. By heavily implanting N<sup>+</sup> ions into a pre-strained martensitic Ni-Ti thin film, the top layer of the material was amorphized. This amorphous layer did not have SME, but could provide biasing force to the martensite formation. Cyclic out-of-plane shape change upon heating and cooling was demonstrated in the ion implanted Ni-Ti SMA thin film bimorph structure.

#### 2.4.3. High-Temperature Shape Memory Alloy Thin Films

High transition temperature SMA thin films have been of great interest due to the limitation of transition temperature of binary NiTi SMAs. However, there have been only a few successful attempts that have been reported. Johnson *et al.* [1995] studied alloy systems that potentially have A<sub>s</sub> temperatures over 100°C. In their study, three kinds of alloy thin films, Cu-Al-Ni, Ni-Al and Ni-Ti-Hf, were sputter deposited at without substrate heating. No martensitic phase transformation was detected in Cu-Al-Ni thin films after traditional annealing treatment. Martensitic phase transformation was

detected in Ni-Al thin films but shape memory was not observed due to brittleness. Ni-Ti-Hf thin films showed some promise because the annealed films were relatively ductile and had high transformation temperatures. Quandt *et al.* [1995] and Miyazaki *et al.* [1995] reported their work on Ti-Ni-Pd SMA thin films. Both had limited success. So far only Ni-Ti-Hf and Ti-Ni-Pd alloys are regarded as promising candidates for high-temperature SMA thin films.

*2.4.3.1. Ni-Ti-Pd SMA Thin Films.* There are only a few reports in the literature concerning Ni-Ti-Pd HTSMA thin films. Quandt *et al.* [1995] obtained the Ni-Ti-Pd thin films by post-deposition annealing of the as-sputtered amorphous films, and the thin films showed two-way shape memory effect. But no data were presented to show phase transformation and detailed shape memory properties of the thin films. Miyazaki *et al.* [Miyazaki, Hashinaga, Yumikura, Horikawa, Ueki and Ishida 1995] also investigated Ni-Ti-Pd SMA films. The transformation temperatures and shape memory properties were studied more extensively.

Miyazaki *et al.* [1995] reported several results that were worthy of mention. First, they found that the composition of the ternary thin films was slightly Ti rich, *i.e.*, the atomic percent of titanium should be between 50% to 51%. By doing this, the transformation temperatures of thin films could be effectively increased by the ternary element while the mechanical properties remained satisfactory. Secondly, transformation temperatures (particularly  $M_s$  temperature) of the 700°C annealed films depended on the atomic percentage of palladium. With increasing Pd content from 0 to 6at.% the  $M_s$  decreased slightly, but with continued increasing Pd content, the  $M_s$  temperature increased rapidly. With 21.8at.% of palladium, the  $M_s$  temperature reached 117°C. Also, the transformation hysteresis was decreased due to additional palladium. With more than 6at.% of palladium, the hysteresis was generally lower than 20°C, and sometimes was below 10°C. These results were generally in agreement with those reported for bulk Ti-

Ni-Pd research [Pu *et al.* 1994]. Thirdly, good shape memory properties were found in those high-temperature thin films treated by secondary annealing. By thermal cycling the thin films under applied stresses that were stepwise increased for different cycles, the shape memory effect was demonstrated at stresses as low as 30 MPa. About 2% strain was produced when the sample was cooled under 150 MPa of applied stress, and maximum recoverable strain was about 2.5%. Due to the solution hardening by palladium, the critical stress for slip was close to 300 MPa (Figure 2.12).

Pre-martensitic transformation and martensite structure in Ni-Ti-Pd thin films were also related to palladium content, as reported by Miyazaki *et al.* [Miyazaki and Ishida 1999]. When the palladium content was less than 6at.% or so, R-phase transformation occurred prior to the martensitic transformation. The martensite was monoclinic in films having 6at.% Pd or less. When the palladium content was higher than 6at.%, R-phase transformation was absent, instead, on cooling, austenite transformed to orthorhombic martensite, which transformed to monoclinic martensite upon further cooling. As Pd content increased above 6at.%, the start temperature for austenite to orthorhombic martensite increased. At the same time, the start temperature for orthorhombic martensite to monoclinic martensite transformation decreased rapidly. At palladium contents more than 15%, the start temperature of monoclinic martensite was lower than -120°C, so normally this transformation was not considered.

Both Miyazaki and Quandt showed that Ti-Ni-Pd had smaller hysteresis than Ti-Ni binary alloys. Winzek and Quandt [1999] also studied the hysteresis of Ti-Ni-Pd films under different constraint conditions<sup>13</sup>, which were realized by depositing the SMA onto substrates (thermal silicon oxide, 50-micron thick molybdenum and Fe<sub>72</sub>Cr<sub>18</sub>Ni<sub>10</sub> alloy) with different coefficients of thermal expansion. SMA films along with their substrates

---

<sup>13</sup> Transformational hysteresis is generally defined as  $A_p - M_p$ . However, in the stress-temperature hysteresis loop or strain-temperature hysteresis loop, the transformation hysteresis is typically measured as the difference in temperatures at which the same stress or strain level is obtained during forward transformation and reverse transformation, respectively (Figure 2.1).

were annealed 1 hour at 700°C for crystallization. Curvature of the composite was measured during thermal cycles to get hysteresis loops. It was found that the hysteresis was smaller under substrate constraint, no matter whether tensile or compressive, than in free-standing form. The smallest hysteresis (nearly none to 3.5°C) was found in a 10at.% Pd film and under compressive stress. However, substrate constraint did not change the temperature difference between  $A_f$  and  $M_f$  temperatures.

Fatigue of Ti-Ni-Pd SMA thin films was also evaluated by Winzek and Quandt [1999] using curvature measurement during thermal cycling. The stress change resulting from transformation continuously decreased due to thermal cycling. It was reduced to half of the initial value after the first 100 cycles, although it became relatively stable upon further cycling. It was noted that the fatigue behavior of Ti-Ni-Cu thin films was much better than that of Ti-Ni-Pd, the former showing no reduction of stress change from transformation for the first 2000 cycles.

**2.4.3.2. Ni-Ti-Hf SMA Thin Films.** Material cost has been a consideration for high temperature alloys containing noble metals such as Au, Pt and Pd. Therefore, alternative ternary alloys that substitute Zr or Hf for Ti have been attractive. Due to the success of making NiTiHf high-temperature shape memory alloy in bulk form, fabrication of Ni-Ti-Hf thin films was studied by a number of research groups. Reportedly, Johnson was the first to fabricate Ni-Ti-Hf high-temperature SMA thin films [Johnson, Martynov and Shahoian 1995]. He sputter deposited amorphous Ni-Ti-Hf films and then acquired SME by a secondary annealing at 520°C and high transformation temperature was obtained. With 19.5at.% hafnium in the thin film, an  $M_s$  temperature of about 100°C was measured. The resulting films appeared ductile, although no quantitative data was presented for comparison. Independently, You *et al.* [You, Chung, Han, and Gu 1997] also successfully obtained moderately high transformation Ni-Ti-Hf SMA thin films by

sputtering amorphous films and then annealing for crystallization. The peak temperature for martensitic transformation was 52°C for 12.5at.% hafnium films and it was increased to 92°C in a film with 20at.% hafnium. Microstructural observation indicated that the grain size was only about 0.1 micron. Mechanical properties and shape memory properties were not evaluated.

Besides sputter deposition, laser ablation was also investigated as a method to fabricate Ni-Ti-Hf high-temperature SMA thin films. In an experiment reported by *Gu et al.*, 6-micron thick Ni-Ti-Hf ternary thin films having Hf content up to 13.3at.% were produced using a KrF excimer laser ablation system with different composite targets in high vacuum. Laser pulses had 10Hz frequency, 248nm wavelength, and 34ns pulse duration. The laser was directed to the surface of polished composite target at an incidence angle of 45°. The circular composite target consisted of three fan-like plates: one Ti<sub>50</sub>Ni<sub>50</sub>, one pure Ni, and one pure Hf. The growth rate was 1µm/hr. The as-deposited film was amorphous and crystallization temperature was 513°C. Annealed film showed R-phase and martensitic transformations on cooling, but the transformation temperatures were quite low: the forward martensitic transformation temperature was only 31°C. Fine grain size and Ni-rich composition were believed to be the reasons for low transformation temperatures.

In spite of the cost advantage, Ni-Ti-Hf ternary SMA films had some drawbacks compared to Ti-Ni-Pd thin films. As shown in Johnson's reports, the hysteresis of Ni-Ti-Hf SMA films was about 60 to 100°C, which was considerably larger than that of Ti-Ni-Pd films. Wide hysteresis results in longer response time for cyclic actuation, and is therefore not favorable for applications in microelectromechanical systems.

Although encouraging, the work by Johnson *et al.*, You *et al.* and Gu *et al.* on development of Ni-Ti-Hf high-temperature SMA thin film was only rudimentary. Johnson demonstrated that high transformation temperatures could be obtained in Ni-Ti-Hf thin films while Gu showed martensitic transformation with low transition

temperatures. Neither group has characterized the microstructure or was able to evaluate the mechanical and shape memory properties of the thin films. In this thesis study, both post-deposition annealing and *in-situ* deposition are used to produce crystalline Ni-Ti-Hf thin films that possess shape memory at high temperatures. Different annealing procedures are investigated to optimize the mechanical properties. Microstructure characterization and mechanical evaluation are conducted to correlate the performance and microstructural features.

## **Chapter 3**

### **EXPERIMENTAL PROCEDURE**

This study concerns preparation of high-temperature shape-memory alloy thin films, characterization of their properties, and correlation of their properties with structural and microstructural features. In SMA thin film preparation, magnetron sputtering has been used, and depending on the microstructure of the as-deposited films, a secondary annealing was carried out to crystallize the samples. Thermal analyses to determine phase transformation, mechanical property tests and shape-memory property evaluation were carried out. Structural and microstructural analyses utilizing X-ray diffraction techniques, electron diffraction and transmission electron microscopy have been conducted. This chapter describes in detail various experimental methods and procedures used in this study.

#### **3.1. Thin Film Fabrication**

Experimental procedures for shape-memory alloy thin film fabrication consist in two parts: thin film deposition, and post-deposition thermal treatment to give the film SME properties if the as-deposited films do not have SME. For film deposition using magnetron sputtering, target preparation is necessary, and the quality of deposit is directly related to that of the target. In this section, procedures of target preparation and thin film deposition are outlined, and thermal treatment is detailed.

### 3.1.1. Thin Film Deposition

Ternary Ni-Ti-Hf thin films were made by planar d.c. magnetron sputtering method in a Perkin-Elmer Ultek sputtering system. A schematic of the sputter system is illustrated in Figure 3.1. As shown, the system was composed of a 29"-diameter vacuum chamber, a Ni-Ti-Hf target (cathode) with magnets behind, substrate (anode) on a substrate holder, a substrate heater, and a d.c. power supply that was connected to target and the substrate. The vacuum chamber, evacuated by an Edwards A6117DC36A mechanical pump and an Ultek-12 cryo-pump, could be pumped to  $10^{-7}$  torr. The target was 8 inches in diameter and 0.25 inch thick. The substrate holder was 3.0mm thick 160mm-diameter circular molybdenum plate which provided sufficient thermal conductivity across the entire plate. The substrate heater was composed of three parallel 500W quartz lamps that were supplied with variable power to achieve different substrate temperatures, which was measured by an ungrounded exposed K type thermocouple located near the center of the substrate. Although the quartz-lamp heater may create non-uniform heating, the massive molybdenum plate helped achieve a temperature uniformity better than  $\pm 5^{\circ}\text{C}$  across 5 inch diameter area. The D.C. power supply had maximum capacity of 5 kW.

Thin film deposition was made after about  $10^{-6}$  torr base vacuum was achieved. 99.999%-purity Kr was introduced during sputtering as working gas, and the pressure of working gas was controlled by MKS 1259B mass flow controller and measured by an MKS 127 Barometer. The composition of gas in vacuum was analyzed by an ion pump backed UTI 100C reduced-pressure RGA (Residual Gas Analyzer) before and after the introduction of the working gas.

Due to the differential sputtering rates of different atomic species, the composition of the deposit is not expected to be at steady-state in the early stage of the sputtering [Lee 1994, George 1992]. Therefore, a fresh target was usually burned in for 20 hours at 1kW

of deposition power to achieve compositional stability. In addition, before each deposition run, preheating was applied to outgas the substrate and vacuum chamber.

The thin film fabrication process is determined by a number of process parameters including base vacuum, working gas species, working gas pressure, deposition power, substrate-to-target distance, and substrate temperature. During this study, base pressure was below  $10^{-6}$  torr, typically  $5 \times 10^{-7}$  torr. The pressure of the working gas krypton 1.0 mTorr. The sputter power, which was defined as the product of the voltage between target (cathode) surface and substrate (anode) and the current, and was set constant at 1 kW during each sputter run.<sup>14</sup> The working distance, the distance from the cathode to the substrate, was set at 81 mm. The substrates were 5-inch diameter thermal oxide passivated (100) single-crystal silicon wafers. The substrate temperature was varied in order to get desired crystallinity of the as-deposited films. Without external substrate heating, the plasma can gradually raise the substrate temperature up to 200°C. At the deposition parameters described above, the sputtering rate was about 15 Å/sec.

### 3.1.2. Hot Pressed Powder Target

The targets for this study were made by hot pressing a mixture of pure metallic powders in the appropriate ratio by the vendor (Pure Tech Co.). There are three steps involved:

- 1). Mixing the pure metallic powders and placing the mixture in a mold;
- 2). In protective environment of Ar, heating the mixture to about 1000°C and then applying pressure of about 100 MPa to 200 MPa to the mixture;

---

<sup>14</sup> As the target is continuously worn in, the voltage decreased slightly and the current increased at constant deposition power.

- 3). Machining the consolidated target material to appropriate dimension and soldering it to a copper backing plate.
- 4). Grinding the surface of the target, and sealing it in Ar until ready to use.

The density of final target piece was measured. The porosity of the target was calculated by comparing the measured density with theoretical value. Table 3.1 is the lists of those data for the targets with different compositions used in this study and shows that the porosity in the targets was between 11.4% and 15.5% of the full density.

**Table 3.1. Composition and Porosity of the Targets Used to Deposit Ni-Ti-Hf SMA Thin Films in This Study.**

Target Composition	Ni <sub>47.5</sub> Ti <sub>32.5</sub> Hf <sub>20</sub>	Ni <sub>47.5</sub> Ti <sub>34.5</sub> Hf <sub>18</sub>	Ni <sub>48.5</sub> Ti <sub>35.5</sub> Hf <sub>16</sub>	Ni <sub>48.5</sub> Ti <sub>37.5</sub> Hf <sub>14</sub>
Theoretical Density (g/cc)	8.83	8.27	8.08	7.83
Measured Density (g/cc)	7.46	7.24	7.16	6.85
Porosity (%)	15.5	12.5	11.4	12.5

### 3.1.3. Post-Deposition Annealing

Although the films deposited at elevated substrate temperature showed SME at the as-deposited state, those deposited without sufficient substrate heating were amorphous, and crystallization annealing was necessary to render a material with SME properties. In this study, conventional vacuum annealing, as well as rapid thermal anneal (RTA), was used to achieve different heating rates in the thermal treatment for crystallization.

Conventional heat treatment was conducted in a custom built vacuum furnace that was equipped with an Edwards ES/ED 200 rotary mechanical pump and a Varian VHS 6" diffusion pump having a pumping capacity 2400 liters/sec. A schematic of the furnace is illustrated in Figure 3.2. As shown, the furnace consisted in two 10 by 12 inch 5 kW

heating plates, which were placed about 2 inches apart. The Ni-Ti-Hf samples, which are in free-standing form, were housed inside 5.5 x 5.5 x 0.5” pure titanium box, which was situated between the two heating plates during the annealing treatment. A K-type thermocouple was placed on each side of the Ti box. Temperature control was accomplished by time proportional cycle, which was realized by an Omega CN3000 temperature dual input/output controller. The vacuum of the chamber was maintained below  $5 \times 10^{-6}$  torr during the annealing process. After annealing was completed, the sample remained as shiny as before annealing, suggesting that the vacuum and protective titanium box were effective to protect the sample from oxidation.

Due to radiative heat loss, the maximum heating rate was limited and was temperature dependent with slower heating rate at higher temperature. For the conventional vacuum annealing system described above, the maximum achievable heating rate was about 40°C/min at 400°C. The RTA technique (radiant type thermal annealing), which provided much higher heating rate, was also used to crystallize the amorphous Ni-Ti-Hf films. During the RTA treatment, the sample was attached to the substrate. A Heatpulse 410 system was used and the procedure included the following steps:

- 1). Program the temperature profile for the annealing treatment;
- 2). Load the wafer sample into the system;
- 3). Purge the system using 99.99% Ar at a flow about 200 cc/min for about 60 seconds;
- 4). Apply power to the quartz lamps and heat the sample according to the program;
- 5). Remove sample from the oven when the reading of sample temperature is below 100°C.

Depending on sample load, the heating rate can be as high as 300°C/min. However, the heating rate for this experiment was chosen at 100°C/sec in order to minimize temperature overshoot. After isothermal annealing, the samples were cooled at 50°C/sec. Only minor discoloration of the sample was observed after the RTA treatment. Figure 3.3 shows a typical temperature profile for an RTA treatment.

### **3.2. Thin Film Characterization**

The properties of the deposited films or annealed films were evaluated for their phase transformation temperature, mechanical properties and shape-memory properties. In the following, the detailed experimental procedure for each category is described.

#### **3.2.1. Transformation Temperatures**

Martensitic transformation is a first-order phase transformation, and is accompanied by enthalpy, entropy, and other physical property changes. Therefore, Differential Scanning Calorimetry (DSC) has been used to measure to endothermic/exothermic effects, and the transformation temperatures can be determined from the endothermic/exothermic peaks. DSC measurements were conducted on a Perkin Elmer 7 Thermal Analysis System. To ensure good resolution, the weight of the sample was at least 10mg. The heating/cooling rate was set to 20°C/min, and the temperature ranges were from ambient temperature up to 350°C. A typical DSC curve for an SMA thin film is shown in Figure 2.1(b). As indicated in the figure, the transformation temperatures were defined by the tangent-intercept method, and they may vary slightly according to the segment that was chosen to extrapolate. However, the endothermic and exothermic peak temperatures ( $M_p$  and  $A_p$ ) were well defined.

Electrical resistivity measurement was also used to determine the transformation temperatures. The experimental set-up is schematically shown in Figure 3.4. The samples, preferably in the form of strips, were connected to a DC power supply (in Constant Voltage mode) with a  $3\text{k}\Omega$  resistor in series, and the potential drop across the sample was recorded by a Data Acquisition System (DAS2000). Because the sample resistance ( $<2\ \Omega$  for typical sample size) is much smaller than  $3\text{k}\Omega$ , the electrical current passing through the sample was virtually constant regardless varying electrical resistivity of the sample resulting from varying temperature<sup>15</sup>. The potential drop across the sample is proportional to the sample resistivity, so variation of the voltage reflects the resistivity change with the temperature. During the test, the sample was put into a 12-inch long circular furnace. The temperature of the sample was measured by a K-type thermocouple placed nearby and it was also recorded by a Data Acquisition System. A CN4800 Omega controller was used to control the temperature of the sample. For a typical set-up, the voltage of the DC power supply was about 10V, heating rate was  $15^\circ\text{C}/\text{min}$ , and temperature ranged from room temperature to  $300^\circ\text{C}$ . During cooling, the furnace was turned off so the sample cooled down naturally. Figure 2.1(a) is the typical resistance-temperature curve. The tangent intercept method was used to determine the transformation temperature.

### 3.2.2. Mechanical Property Measurement

Mechanical properties of the SMA thin films were mostly measured by tensile testing on a 5564 Instron system that is capable of conducting tensile test at temperatures up to  $350^\circ\text{C}$ . Various temperature can be realized by programming an Eurotherm 2408 temperature controller. The load cell has a maximum load capacity of 50 Newtons with

---

<sup>15</sup> In this setup, the current flowing through the sample is about 3.3 mA and the power is about  $22\ \mu\text{W}$ . This level of power is 3 to 4 orders of magnitude less than can cause appreciable Joule heating to the sample. Therefore, there is no sample heating due to the current flow in the resistivity measurement.

an accuracy of 0.025 Newton. The displacement of the cross-head had an accuracy of measurement at about 25 microns. Test samples were free-standing films, obtained by manually peeling from the substrate. The sample was cut into a 70x3 mm strip and loaded onto the tensile testing machine with gauge length set at 50 mm. In order to prevent slipping, the ends of the sample were attached to folded copper foil and then clamped between stainless steel blocks having ridged faces. During the test, the sample was elongated at 1 mm/min, or at strain rate about 0.02 mm/mm/min. Strain measurement was usually taken by the displacement of upper grip, but a video extensometer was also used. In the latter, a gauge length of 20 mm was marked on the sample with black ink. The contrast signal was picked up from video so the distance between black marks can be measured. The resolution of video extensometer was 5  $\mu\text{m}$ .

For tensile tests that were conducted at elevated temperature, the ramp rate was usually set at 10°C/min. In order to ensure temperature uniformity, the sample was held for 5 minutes at the targeted temperature before tensile test started. Most samples were elongated to failure to get the ultimate elongation at different temperatures, and at least 5 samples of the same kind were tested to get the average value. The stress-strain data was collected using Merlin V4.42 software.

In some circumstances where samples were too brittle to be clamped to the clamping fixture, a bending test method was used to semi-quantitatively evaluate the ductility of the sample. A schematic of the test method is shown in Figure 3.5. Basically the minimum curvature radius was measured and the strain (tensile or compressive, depending on which side) at the sample surface was calculated as:

$$\varepsilon_{surface} = t / (D - t)$$

where  $t$  is the thickness of the sample and  $D$  is the curvature diameter of the deformed sample. As shown in Figure 3.5, the distance of the two blocks was adjusted to be slightly wider than the diameter of the metal wire that was used to force the strip into the

gap between the two blocks. The radius of the metal wire was considered to be the bending radius. Samples were deformed at larger bending radius first and then the bending radius was decreased step by step until the sample failed. Because the sample was very thin, it can be deformed to very small curvature radius even when the material has very poor ductility.

### 3.2.3. Shape-Memory Property Evaluation

Shape-memory properties were evaluated by measuring the recoverability of a prestrain, recoverable strain and maximum stress for full recovery during constrained thermal cycling between martensite and austenite. The recoverability of a prestrain can be measured in the following procedure and schematically showed in Figure 3.6:

- 1). load the sample in the 5564 Instron material test system which has capability of varying test temperature;
- 2). bring the sample to the test temperature and allow sufficient time for thermal equilibrium and zero the strain measurement system (making sure that the temperature does not exceed the austenite start temperature);
- 3). apply load to elongate the sample to a predetermined strain ( $\epsilon_{total}$ );
- 4). unload the sample completely, load the sample again very slightly in tension (1 MPa), and then measure the strain ( $\epsilon_p$ );
- 5). slacken the sample sufficiently by lowering the upper grip, and then heat the sample to 50°C above the  $A_f$  temperature, making sure the sample is NOT under stress;
- 6). cool the sample to temperature at which the sample was elongated, allow sufficient time for thermal equilibration;

- 7). bring the sample slightly under tension (1 MPa) and measure the strain of the sample at this time ( $\epsilon_{nr}$ ) (This is the non-recoverable strain).

The strain obtained at Step 4 is the plastic strain in martensite, and the difference between  $\epsilon_{total}$  and  $\epsilon_p$  is the elastic strain of the martensite. Of the plastic strain in martensite  $\epsilon_p$ , recoverable strain is  $\epsilon_r = \epsilon_p - \epsilon_{nr}$ . Therefore, the recovery rate of the plastic strain of martensite is:<sup>16</sup>

$$RR = \frac{\epsilon_r}{\epsilon_p} = \frac{\epsilon_p - \epsilon_{nr}}{\epsilon_p} \times 100\% \quad (3.1)$$

Measuring  $\epsilon_p$  and  $\epsilon_{nr}$  at the same sample temperature eliminates the error from thermal expansion. However, if the strain is measured from the displacement of the upper grip, it is important to make sure that the shafts are at the same temperature when measurement is taken. Otherwise, thermal expansion of shafts of the tensile machine could cause substantial error. To solve this problem, two methods can be used. The first one is to wait enough long time to let the shafts to come to thermal equilibrium. This includes both before the initial elongation (step 3) and before the measurement of residual strain (step 7). In order to establish the waiting time that is necessary for shafts to become thermal equilibrium, a non-SMA dummy sample (such as a strip of copper foil) was loaded on the Instron machine, and was put through every step except step 2 and unloading. If enough elapsed time was allowed,  $\epsilon_p$  and  $\epsilon_{nr}$  should be equal, and the waiting time should be used as reference for SMA film measurement. In the other method, video extensometer can be used to measure the length change of the sample. A

---

<sup>16</sup> Two-way memory effect may be introduced by prestraining the SMA material severely and repeatedly. In this case, when the sample is cooled down from austenite at high temperature, a small amount of elongation may occur, so the measured recovery rate may be lower than the actual one. The error may be minimized by taking two measures: 1) keep pre-strain at small level; and 2) use fresh sample every time.

20 mm gauge length was marked before test started. Gauge length was recorded in step 3, 4, and 7. In doing so, there is no need to wait until the shafts to reach thermal equilibrium if video extensometer is used to measure sample elongation, although it is still desirable to wait sufficient time to allow the sample to reach the deformation temperature.

Measurement of recoverable strain at different applied stresses was determined by thermal cycling at a constant load, which was conducted in a custom built experimental setup that is schematically shown in Figure 3.7. As in the tensile test, sample strips, which usually have dimensions of 40mm x 3mm x 4.5 $\mu$ m, were used in the constant-load test. The sample strip was loaded into the circular furnace by clamping between two pairs of copper grips. Samples were always placed in the middle of the circular furnace to achieve maximum temperature uniformity. Low-CTE molybdenum strips were attached to the copper grips to extend the ends out of furnace. While the upper end of molybdenum strip was fixed, the lower end was attached to the location where the load was applied to the sample. LVDT (Linear Voltage-Displacement Transducer) cores were also attached to the lower end. During thermal cycling, the length of sample changed, the position of the LVDT core was changed accordingly. The LVDT device converted the length change into electrical signal, which was picked up and recorded in a DAS-2000 data acquisition system. Sample temperature was measured by a K-type thermocouple that situated near the middle of the sample, and reading was also recorded. A CN3000 Omega temperature controller is used to realize various iterations of the sample temperature profiles.

The length change of sample reflected the strain of the sample. However, the LVDT could only detect the overall length change resulting from sample length change and fixture length change. If ignored, thermal expansion of the fixture (mainly molybdenum extension strips) during thermal cycle could give a great deal of error. This

is particularly true for short samples, which were usually used to ensure good temperature uniformity. For example, considering a situation that 10-inch molybdenum extension strip was heated up by 250°C uniformly, the elongation resulting from temperature increase is:

$$\Delta l = 5.9 \times 10^{-6} (\text{mm/mm/}^\circ\text{C}) \times 10 \times 25.4 (\text{mm}) \times 250^\circ\text{C} = 0.375 \text{ mm.}$$

this elongation, if mistakenly considered as the elongation of a 50mm sample, would cause an absolute error of 0.75% which would be subtracted from the overall shape memory strain. Although thermal expansion of fixture might be compensated just by calculation, it is very complicated to do that, because it is necessary to know the temperature distribution over the entire length of the molybdenum fixture. The following calibration procedure was used to eliminate the error from the thermal expansion of fixture. It involves three steps:

1. For a certain temperature profile running, record the displacement of the sensing bar in LVDT assembly for a dummy sample (a molybdenum strip with the same length of the SMA sample to be measured) during a thermal cycle;
2. Using the same temperature profile, record the displacement of the LVDT sensing element for a real SMA sample during a thermal cycle;
3. Subtract the data obtained in step 1 from the data obtained in step 2, then add the thermal expansion compensation of the dummy sample.

For certain temperature profile, the displacement of LVDT sensing bar for a dummy sample was measured several times to ensure repeatability. It should be pointed out that, although the displacement for the dummy sample during thermal cycles repeated very well for the same temperature profile, when the temperature profile is changed, the calibration procedure has to be repeated. This is because with different heating/cooling rate, the temperature distribution of the molybdenum fixture (with time) also changes. A

typical strain-temperature curve during a thermal cycle under a constant stress is shown in Figure 3.8, where sample thermal expansion, recoverable strain and residual strain are shown.

### **3.3. Compositional, Structural and Microstructural Analyses**

In order to explore the underlying reason for the mechanical behavior of the material, it is necessary to conduct phase analyses, which involve compositional, structural and microstructural analyses. The following describes each technique used to carry out those experiments.

#### **3.3.1. Composition Analysis**

The composition of thin films was analyzed by a LINK AN-1000 X-ray EDS (Energy Dispersive Spectrum) system mounted on a JEOL S-2500 SEM (scanning Electron Microscope) operating at 20 kV. Gain calibration was made on Co-K $\alpha$  radiation and bulk calibration was done using LINK ZAF-4 code. The analyzed samples were usually 5  $\mu\text{m}$  thick films and were attached to silicon substrates or glass slides. Area scanning mode at 100x magnification was used to illuminate the sample in order to get average compositional data over a relatively large area. It should be pointed that, although composition analysis by EDS is expeditious, considerable error may exist. While the accuracy of the data is usually within  $\pm 2\sigma$  ( $\sigma$  is the standard deviation, usually  $< 0.25\%$ ), The precision is more difficult to tell unless a standard alloy specimen (Ni-Ti-Hf) is measured. However, a careful calibration using pure specimens (Ni, Ti, and Hf) may minimize the errors.

### 3.3.2. Crystallographic Structure Analysis

Crystallographic structure analysis was conducted by X-ray diffraction using a Scintag-2000 diffractometer with accelerating voltage of 35 kV, tube current of 25 mA, Cu-K $\alpha$  radiation and normal scanning mode. The scan step was 0.03°/step, the scan rate was 0.25 to 2°/min and the scan range ( $2\theta$ ) was from 20° to 70°. All the X-ray spectra were taken in free-standing films, and the films was attached to a glass slide (amorphous) during X-ray scanning in order to avoid extraneous peaks. Nevertheless, it was found that with film thickness greater than 3  $\mu\text{m}$ , few X-rays from the substrate were detected.

In indexing of the X-ray diffraction spectra, the interplanar distance ( $d$ ) corresponding to each X-ray peak was calculated by the well-known Bragg equation. Then the measured  $d$  is compared to interplanar distance of possible phases with known structures to find the best match. The tolerance was usually set at 0.01 Å. In case that unknown structures existed, the  $d$  value for each peak was calculated by Debye equation, then the values of  $d^2$  were listed in sequence from small to large, and normalized by dividing all the value by the smallest  $n \times d^2$  ( $n = 1, 2, 3, \dots$ ). If an integral sequence was obtained, then a cubic phase was detected. In cases that more complicated phase structure existed, the measured  $d$  values were listed in Excel spreadsheet, and a structure similar to known structure based on literature was assumed. A list of  $d$  spacings were calculated then compared with the measured values. The lattice parameters were modified until a match between calculated values and measured values was obtained.

### 3.3.3. Microstructure Observation

The in-plane microstructure of the Ni-Ti-Hf thin films was observed on a Hitachi H-800 TEM operated at 200 kV. Free-standing films were obtained by manually peeling the films from substrate. Samples were cut into 3 x 3 mm dimension and then glued with acid-resistant lacquer on 3mm-diameter nickel grids with 2 mm-diameter holes. Electron

transparency was achieved by twin-jet electropolishing method using a fresh electrolyte that contained 20% nitric acid and 80% methanol in volume percent. The electropolishing was done on a Tenupol-3™ (Struers A/S, Denmark) twin jet polisher operated at 8V (which gave a current density of 12mA/mm<sup>2</sup>). The temperature of electrolyte was kept between 233 K and 243 K by continuously introducing liquid nitrogen into the electrolyte.

Selected-Area Electron Diffraction (SAED) was also used to determine phase structure. SAED was done on a Hitachi H-800 Transmission Electron Microscope (TEM) The TEM was operated at 200 kV acceleration voltage and the sample was installed in a double-tilting specimen holder. Indexing of electron diffraction spot/ring was done by comparing the  $d$  value measured on the pattern with those calculated from known structures. Camera length was calibrated from the diffraction pattern of phase determined by X-ray diffraction.

## Chapter 4

### RESULTS AND DISCUSSION

The main purpose of this research is to find a method to produce Ni-Ti-Hf thin films having high transformation temperatures, good shape memory properties and good mechanical properties that are useful for industrial applications. Additional objectives are to correlate the properties of the shape memory thin films with details of the fabrication process, to characterize the microstructure of SMA thin films with different properties, and to improve the material properties through process selection based on the characterization results. Our first goal was to achieve suitable crystallinity of the thin film, and it was accomplished by either sputtering *in-situ* crystallized material, or applying post-deposition thermal treatment to crystallize the as-deposited amorphous material. The *in-situ* crystallized thin films were obtained by choosing proper deposition parameters, particularly by using sufficiently high substrate temperature. Because crystalline phase formed during deposition, this procedure was also called *in-situ* crystallization. The post-deposition thermal treatment for crystallization was a high temperature anneal, either isothermal or isochronal. In this thesis, two classes of deposition technique, one characterized by relatively low substrate temperature and the other by relatively high substrate temperature, were used to control the crystallinity of the as-deposited samples. The as-deposited material was either fully amorphous or fully crystalline<sup>17</sup>. For those having fully amorphous structure, separate annealing was carried for crystallization. In the following, crystalline Ni-Ti-Hf films obtained by post-

---

<sup>17</sup> Partially crystalline samples can be obtained using intermediate substrate heating. In this study, however, the partially crystalline samples were generally brittle, and this prevented us from doing extensive evaluation on their mechanical and shape-memory properties.

deposition annealing and those by *in-situ* crystallization will be discussed separately. Results for each process class will be presented before proceeding to a discussion of their implications.

#### 4.1. Films Crystallized by Post-Deposition Annealing

A number of Ni-Ti-Hf films with different compositions were sputter deposited using different target compositions. With deposition parameters described in Section 3.1.1 (working gas Kr pressure 1.0 mTorr, working distance 81 mm, deposition power 1 kW, and substrate temperature  $200 \pm 15^\circ\text{C}$ ), the composition of the thin films was slightly different than their targets. Table 4.1 shows the composition of films at the central area deposited from different targets. Measurement was taken after the target were worn about (equivalently) 20 hours at 1 kW of deposition power (about 1/5 to 1/6 lifetime of a target). In general, there was more nickel in the films in the central area than in the target and less titanium. Hafnium content was mostly higher in the films than in the target. This composition shift may be related to combined effects of preferential loss of some species of atoms due to collisions with background gases during atom transport from the target to the substrate, and preferential resputtering of the growing film [Fursenko, Galjukov, Makarov, Lutovinov and Ramm 1995].

**Table 4.1. Target Compositions vs. Film Compositions**

Target Composition	Ni <sub>47.5</sub> Ti <sub>32.5</sub> Hf <sub>20</sub>	Ni <sub>47.5</sub> Ti <sub>34.5</sub> Hf <sub>18</sub>	Ni <sub>48.5</sub> Ti <sub>35.5</sub> Hf <sub>16</sub>	Ni <sub>48.5</sub> Ti <sub>37.5</sub> Hf <sub>14</sub>
Film Composition	Ni <sub>48.7</sub> Ti <sub>29.2</sub> Hf <sub>22.1</sub>	Ni <sub>48.8</sub> Ti <sub>33.4</sub> Hf <sub>17.8</sub>	Ni <sub>49.7</sub> Ti <sub>33.9</sub> Hf <sub>16.4</sub>	Ni <sub>49.1</sub> Ti <sub>36.2</sub> Hf <sub>14.7</sub>
ΔNi	+1.2	+1.3	+1.2	+0.6
ΔTi	-3.3	-1.1	-1.6	-1.3
ΔHf	+2.1	-0.2	+0.6	+0.7

The composition uniformity of the thin films (deposited from the  $\text{Ni}_{48.5}\text{Ti}_{37.5}\text{Hf}_{14}$  target) across 5"-diameter wafer was evaluated and the results were shown in Figure 4.1. It can be seen that within 3" diameter, the compositions were very uniform (deviation <0.5%). More deviation was measured at locations outside of 3"-diameter area. Therefore, in order to guarantee the maximum composition uniformity, only films within the 3"-diameter limit were used to conduct further study. The non-uniformity of composition is generally associated with angular distribution of sputtered atoms [Olson, King and Wehner 1979, Fursenko *et al.* 1995].

The composition of films was also varied as the target was continuously consumed. Figure 4.2 shows the composition of films at central area for different time-on-power for the  $\text{Ni}_{48.5}\text{Ti}_{35.5}\text{Hf}_{16}$  target. It can be seen that as the target was continuously worn-in, Ni and Hf contents in the films decreased and Ti content increased. In addition, the composition varied most during the first 20 hours of wear at 1 kW, then a relatively stable period (20 to 80 hr·kW) followed. More variation was observed as the lifetime of the target was approached. This change trend of composition is generally associated with the geometrical change of the target surface since the target was not evenly worn out in a magnetron sputtering process.

Films with  $\text{Ni}_{49.1}\text{Ti}_{36.2}\text{Hf}_{14.7}$  composition were annealed and studied in detail. These films were deposited from a  $\text{Ni}_{48.5}\text{Ti}_{37.5}\text{Hf}_{14}$  target at substrate temperature around 200°C, and crystallized by conventional vacuum annealing. Phase transformations, microstructural characteristics and mechanical properties were analyzed. One of the major findings was that after annealing, the samples became brittle, but using faster heating rate alleviated this problem. In order to clarify the causes of embrittlement, different annealing procedures were conducted. The mechanical properties of as-annealed samples were evaluated and their microstructures were examined. Rapid thermal annealing was also utilized in order to confirm the heating rate effect and to assess the benefit of using high heating rates to crystallize Ni-Ti-Hf films.

#### 4.1.1. Crystallization by Conventional Isochronal Heating

Like binary Ni-Ti alloy thin films, amorphous Ni-Ti-Hf thin films must be crystallized in order to become shape memory materials. Crystallization may take place either by isothermal annealing or isochronal heating, and the annealing parameters must be established experimentally according to the characteristics of crystallization. The most important parameter for crystallization is the crystallization temperature, which is heating-rate dependent, but provides an important guideline for crystallization annealing treatment. In this experiment, the crystallization temperature was determined by DSC analysis.

*4.1.1.1. Crystallization Temperature and Activation Energy.* Figure 4.3 shows the DSC curves of the as-deposited amorphous  $\text{Ni}_{49.1}\text{Ti}_{36.2}\text{Hf}_{14.7}$  thin films during isochronal heating excursion to 575°C at rates of 5°C/min, 10°C/min, 20°C/min and 40°C/min, respectively. Apparently there are two exothermic peaks in the course of isochronal heating. The peak temperatures as well as transformation enthalpies of exothermic peaks of different DSC curves are listed on Table 4.2 (and also in the insets in Figure 4.3). In each curve, the second exothermic peak, which was sharp and located at higher temperature, was associated with amorphous-to-crystalline transformation. Comparing the curves that were obtained using different heating rates, one can see that the peak temperature and transformation enthalpy were heating-rate dependent (Figure 4.4a). With the heating rate changed from 5°C/min to 40°C/min, the crystallization peak temperature monotonically increased from about 513°C to 545°C. At the same time, the transformation enthalpy increased from 12.6 to 17.8 J/g. The peak temperature of the crystallization transformation of  $\text{Ni}_{49.1}\text{Ti}_{36.2}\text{Hf}_{14.7}$  amorphous thin films was higher than has been observed for amorphous near-equiatomic Ni-Ti films [Kim *et al.* 1986, Gong *et al.* 1994, Zhang 1997].

**Table 4.2. Peak Temperatures and Transformation Enthalpies of the Peaks on the DSC Curves During Isochronal Annealing of As-Sputtered Amorphous Ni<sub>49.1</sub>Ti<sub>36.2</sub>Hf<sub>14.7</sub> Films at Different Heating Rates.**

Heating Rate (°C/min)	5	10	20	40
1 <sup>st</sup> Peak Temperature (°C)	342	360	372	382
1 <sup>st</sup> Peak Enthalpy (J/g)	6.2	5.5	3.6	2.5
2 <sup>nd</sup> Peak Temperature (°C)	514	525	533	545
2 <sup>nd</sup> Peak Enthalpy (J/g)	12.6	14.9	16.9	17.8
$\Delta H_1 + \Delta H_2$ (J/g)	18.8	20.4	20.5	20.3

The shift of crystallization temperature during isochronal annealing resulting from different heating rate is well understood, and was observed in other amorphous SMA materials [Chang and Grummon 1997]. The reason is because crystallization is a diffusive process that depends on thermal activation and is controlled by both temperature and time. Lower heating rate may allow more time for diffusion, and the crystallization temperature is lower. The activation energy for crystallization may be calculated based on the shift of crystallization temperature with heating rate using Kissinger's method [1957]:

$$E = -R \frac{d(\ln(\phi / T_m^2))}{d(1/T_m)} \quad (4.1)$$

where  $R$  is the molar gas constant ( $R = 8.314$  J/mol),  $\phi$  is the heating rate, and  $T_m$  is the temperature at which the reaction rate reaches a maximum. It would be a good estimation to consider  $T_m$  as the peak temperature in the DSC measurement (for a certain heating rate). Figure 4.5(a) shows the linear fitting result according to Kissinger's equation. The activation energy was estimated at 347 kJ/mol. That value was slightly smaller than the data (385 kJ/mol) from Chang and Grummon for Ti-rich Ti<sub>51.0</sub>Ni<sub>44.4</sub>Cu<sub>4.6</sub> multi-layered

films [1997] and much lower than that (477 kJ/mol) from Zhang [1997] in Ni-rich Ti-Ni films.

The first exothermic peak locating at temperature between 300°C and 400°C was very shallow compared to the peak at higher temperature. The peak temperature as well as the corresponding heat varied with the heating rate (Figure 4.4b). The peak temperature increased with increasing heating rate, whereas the heat associated with these peaks decreased. That suggests the reaction was suppressed at high heating rate. In addition, although the enthalpies for both the high-temperature peak and low-temperature peak varied evidently with heating rate, their sum was relatively constant, which may suggest that the reaction at the lower temperature have produced a product that would contribute less heat to the crystallization transformation. Unlike the high-temperature sharp peaks that are associated with crystallization transformation, the low-temperature peaks are relatively diffuse. However, estimation of transformation activation energy for those peaks using Kissinger's method was also attempted (Figure 4.5b), and it gave a value of 162 kJ/mol.

*4.1.1.2. Martensitic Transformation Temperatures and Enthalpies.* Samples were thermally cycled between room temperature and 250°C in the DSC system directly after the crystallization annealing<sup>18</sup> to determine the displacive transformation temperatures. Figures 4.6 show the DSC curves for samples crystallized by isochronal heating with different heating rates. In each of those figures, an exothermic peak associated with A → M transformation occurs during cooling at temperatures ranging from about 70°C to about 100°C, and an endothermic peak associated with M → A transformation appears during heating at temperatures ranging from about 120°C to 175°C.

---

<sup>18</sup> The cooling rate from 575°C (end temperature for isochronal heating) to 250°C was 40°C/min, and the scan rate was 20°C/min during thermal cycling between 50°C and 250°C.

Start and finish temperatures of martensitic transformation were obtained from Figures 4.6 using tangent-intercept method, and the results are listed on Table 4.3. The correlation between those temperatures and the heating rate during isochronal heating is illustrated in Figure 4.7. It is indicated that the transformation temperatures, especially the peak temperatures for calorimetric peaks in the DSC curves, did not vary much with the heating rate during isochronal annealing for crystallization. The transformational hysteresis did not seem to change substantially with crystallization heating rate either. However, the transformational enthalpy evidently varied with the heating rate. For the sample annealed at the lowest heating rate (5°C/min), the average value of enthalpies for forward and reverse transformations is 7.2 J/g (0.52 kJ/mol). As the heating rate was increased, the average enthalpy was increased consistently. For sample heated at 40°C/min, the transformation enthalpy increased to 10.2 J/g (0.74 kJ/mol). The variation of transformation enthalpy with heating rate for crystallization anneal may suggest more martensite formed as the material cooled down to the  $M_f$  temperature. In addition, the transformation enthalpies were generally lower even than that for binary Ni-Ti films (which normally had  $\Delta H$  of 1.0 kJ/mol to 1.3 kJ/mol [Lo *et al.* 1990]), just opposite to the prediction that  $H_f$  would increase the transformation enthalpy [Cesari *et al.* 1999]. Therefore, it is suggested that there was a considerable fraction of material did not participate martensitic transformation.

Because the martensitic transformation temperatures and transformation hysteresis did not varied evidently with the heating rate for crystallization, it is likely that the composition of the transforming phase was similar in films crystallized at different rates. Also, the microstructural characteristics are not expected to vary substantially with the heating rate. Evidences to this effect will be sought in next section.

**Table 4.3. Transformation Temperatures and Enthalpies of As-Crystallized  $\text{Ni}_{49.1}\text{Ti}_{36.2}\text{Hf}_{14.7}$  Films After Isochronal Heating at Different Rates.**

Heating Rate (°C/min)	5	10	20	40
$M_i$ (°C)	100	100	100	97
$M_f$ (°C)	70	72	70	78
$A_i$ (°C)	120	110	110	134
$A_f$ (°C)	172	170	173	166
$M_p$ (°C)	85	86	85	87
$A_p$ (°C)	155	153	158	152
Hysteresis (°C)	70	67	73	65
Average Enthalpy (J/g)	7.2	8.3	9.3	10.2
Average Enthalpy (kJ/mol)	0.52	0.60	0.67	0.74

4.2.1.3. *Structure and Microstructure Analyses.* X-ray diffraction and TEM observation were conducted to investigate the crystallography and microstructure of the annealed samples. Spectrum (a) in Figure 4.8 is the X-ray diffraction spectrum of the as-deposited sample taken prior to isochronal annealing for crystallization. Spectra (b) ~ (d) in Figure 4.8 are for samples after isochronal heating from room temperature to 575°C at rates of 5°C/min, 10°C/min, 20°C/min and 40°C/min. The sole wide hump at  $2\theta$  angle ranging from about 34° to 46° in curve (a) in Figure 4.8 confirms the as-deposited sample was totally amorphous. After isochronal heating, the wide hump disappeared and sharp diffraction peaks emerged, verifying that the amorphous structure had transformed to crystalline phase during the heating. In the spectrum of sample annealed at 5°C/min heating rate, the highest peak appears at  $2\theta$  angles of 41.6° ( $d = 2.17\text{Å}$ ), and two minor peaks appear at  $2\theta$  angles of 29.1° ( $d = 3.06\text{Å}$ ) and 60.4° ( $d = 1.53\text{Å}$ ), respectively. In addition, there are two weak peaks at  $2\theta$  angles of 38.4° ( $d = 2.34\text{Å}$ ) and 44.4° ( $d = 2.04\text{Å}$ ). As the heating rate for isochronal annealing was increased, the intensity of the

peak at 41.7°C decreased, while the peaks at 38.4° ( $d = 2.34\text{Å}$ ) and 44.4° ( $d = 2.04\text{Å}$ ) became stronger.

Analysis of the crystalline peaks indicated that three strong peaks (at 41.6°, 29.1° and 60.4°) belong to a cubic structure with lattice parameter of  $a = 3.06\text{Å}$ . Because of the existence of the (001) reflection, the unit cell of the cubic structure is either a simple cubic or an ordered b.c.c. structure (B2 structure). Since the intensity of (001) diffraction peak is very weak compared to that of (110) diffraction, it is likely a superlattice reflection, and the structure is thus ordered. In addition, the measured lattice parameter matched the predicted value of an ordered b.c.c. structure.<sup>19</sup> In fact, the crystal structure is the same as that of the austenite phase in binary Ni-Ti alloy except that the lattice parameter is slightly larger. The weak peaks emerging at higher heating rate belonged to a monoclinic structure with lattice parameters of  $a = 2.63\text{Å}$ ,  $b = 4.01\text{Å}$ ,  $c = 4.77\text{Å}$  and  $\beta = 99.1^\circ$ . This monoclinic structure is similar to B19' martensite in binary Ni-Ti alloy ( $a = 2.889\text{Å}$ ,  $b = 4.120\text{Å}$ ,  $c = 4.622\text{Å}$  and  $\beta = 98.6^\circ$ ) except that the lattice parameters are slightly different. The lattice parameters are close to those of the martensite in  $\text{Ni}_{49}\text{Ti}_{36}\text{Hf}_{15}$  alloy obtained by Han *et al.* from SAED ( $a = 2.63\text{Å}$ ,  $b = 4.11\text{Å}$ ,  $c = 4.73\text{Å}$  and  $\beta = 100.1^\circ$ ). Changes in the relative intensity of the XRD peaks with different heating rate indicate that the phase fraction was strongly affected by the heating rate for crystallization. At higher heating rate during crystallization heating, more cubic structured phase formed and there was less monoclinic martensite phase in the films.

TEM micrographs of as-sputtered amorphous samples after isochronal heating to 575°C at different rates are shown in Figure 4.9 (a) and (b). In the micrograph of the sample heated at 5°C/min rate (Fig.4.9(a)), the grain size was 0.2 microns or less, which varied substantially from one grain to another. Some grains have twin-like substructure

---

<sup>19</sup> Using the known lattice parameters of 3.01 Å for Ni-Ti B2 structure, the covalent radii of Ni, Ti and Hf atoms were modified to 1.214, 1.393 and 1.520 Å, respectively. Assuming Hf taking Ti sites randomly, the effective radius for (Ti, Hf) would be 1.429 Å. Therefore, the expected lattice parameters in Ni(Ti,Hf) B2 structure is  $a \approx 2(R_{\text{Ni}} + R_{\text{Hf,Ti}})/\sqrt{3} = 3.05\text{Å}$ .

while others do not. The twin-like substructure suggests that those grains were martensite at room temperature. Grains without twin-like substructure are presumably the cubic phase that was detected from the X-ray diffraction spectrum. It was noted that the shapes of the grains looked irregular, and the grain growth seemed to be hindered at some points. In the TEM micrograph of the sample heated at 40°C/min (Fig.4.9(b)), there are also both apparent martensite grains and cubic phase grains. There did not seem to be major differences between the TEM micrograph of the sample heated at 5°C/min and that heated at 40°C/min. It is noted that the grains size in annealed Ni-Ti-Hf films was much smaller than that in annealed binary Ni-Ti films. The latter typically was on the order of micron or larger [Ishida *et al.* 1996, Meng and Catalan 1999].

*4.1.1.4. Mechanical and Shape Memory Properties.* Preliminary examination of the as-annealed samples after isochronal crystallization treatment revealed that the samples were very brittle although the amorphous films before crystallization annealing were fairly ductile. Quantitative measurement by tensile test turned out to be very difficult because the as-annealed samples were so brittle that it was almost impossible to clamp the samples without failure at the clamping area. In this experiment, the ductility of the annealed samples was semi-quantitatively evaluated by bending the strip sample to different radii until the smallest bending curvature radius the samples could survive with was found.

The results of room-temperature ductility evaluation for different samples are listed on Table 4.4. The original amorphous samples had ultimate uniaxial tensile elongation of about 2.5%. However, after the samples were crystallized by isochronal annealing with 40°C/min heating rate, the samples became so brittle that tensile test was no longer applicable. In bending tests, most samples survived at 1mm bending diameter (corresponding bending strain is 0.5%) but failed at 0.5mm bending diameter (corresponding bending strain is 1.0%). For the samples crystallized by isochronal

annealing at heating rate of 5°C/min, most failed at 1mm bending diameter (corresponding bending strain is 0.5%) although they survived at 2mm bending diameter (corresponding to 0.25% bending strain). Therefore, it was qualitatively demonstrated that embrittlement had occurred in the isochronal annealing, and but higher heating rate during isochronal annealing may alleviate the embrittlement to some degree.

**Table 4.4. Comparison of Room-Temperature Ductility of As-Deposited Amorphous Ni<sub>49.1</sub>Ti<sub>36.2</sub>Hf<sub>14.7</sub> Samples Before and After Isochronal Heating from Room Temperature to 575°C**

Sample (4 kinds)	Heating Rate (°C/min)	Tensile Elongation (%)	Bending Diameter (mm)	RT Ductility (%)
Amorphous	N/A	2.5	N/A	2.5
Annealed #1	40	N/A	0.5 ~ 1 mm	0.5 ~ 1
Annealed #2	5	N/A	1 ~ 2 mm	0.25 ~ 0.5

Reversible shape change of the as-annealed samples was observed upon heating and cooling. At room temperature, the sample strips were usually curled (radii 5 ~ 10 mm), but when the samples were heated on a hot plate, they usually suddenly became straight at temperatures around 150°C. Reverse shape change occurred when the samples were cooled down to around 90°C. Although thermal expansion may also result in shape change (curling and uncurling), it was not the case because curling/uncurling would happen gradually. In addition, the temperature for shape change seemed to be consistent with the transformation temperatures of the as-annealed samples. Therefore, the curling/uncurling shape change was most likely related to the shape memory effect resulting from reversible martensitic transformation.<sup>20</sup> However, quantitative measurement of SME either by free-recovery method or constrained thermal cycling was impossible to conduct due to the brittleness of the samples.

<sup>20</sup> The shape memory effect described here was two-way SME, which was possible for samples having stress gradient.

#### 4.1.2. Isothermal Annealing at Low Temperatures

The DSC curves of amorphous  $\text{Ni}_{49.1}\text{Ti}_{36.2}\text{Hf}_{14.7}$  films during isochronal heating indicated that there was also shallow exothermic peak in each of those curves (Figure 4.3). The enthalpies associated with those shallow peaks were affected by the isochronal heating rates. Larger enthalpy was measured in the samples that were heated at lower rates. This observation seemed to be linked with the embrittlement which was more severe in the sample heated at the lower rate. Therefore, it was interesting to clarify what caused the shallow exothermic peak and if there was any connection between those shallow peaks and embrittlement of the annealed samples.

To do so, we isothermally annealed the as-deposited amorphous  $\text{Ni}_{49.1}\text{Ti}_{36.2}\text{Hf}_{14.7}$  thin films for 1 hour at 300°C and 350°C in vacuum, respectively. These temperatures covered the range of the shallow peaks in the DSC curves of  $\text{Ni}_{49.1}\text{Ti}_{36.2}\text{Hf}_{14.7}$  films during isochronal heating (Figure 4.3), but substantially lower the corresponding crystallization temperatures (510°C ~ 550°C). In order to minimize the influence from heating rate, fast heating (40°C/min) was used to bring the sample the target temperature. Annealed samples were evaluated for their room-temperature ductility, and crystallographic and microstructural characteristics.

*4.1.2.1. Room-Temperature Ductility.* The ductility of the samples before and after low-temperature isothermal annealing at different temperatures were semi-quantitatively evaluated by tensile or bending tests. The results are shown on Table 4.5. For the original amorphous samples, the room-temperature ductility was measured using tensile tests which showed fair ductility with ultimate elongation at 2.5%. After the sample was annealed for 1 hour at 300°C, the sample remained fairly ductile at room temperature and a tensile test showed ultimate elongation at a similar level as the original amorphous

sample. If tested in bending mode, these two kinds of samples could be bent back without failure (bending curvature radius  $\cong$  film thickness). Samples annealed at higher temperature showed obvious embrittlement. After annealing for 1 hour at 350°C, the sample was too brittle to be loaded on to tensile test machine. Therefore, semi-quantitative measurement using bending test was conducted. It showed that the minimum curvature diameter for the annealed samples to be bent was between 1 mm to 2 mm, which corresponds an elongation (or compression) at the sample surface at about 0.25% ~ 0.5%.

**Table 4.5. Comparison of Room-Temperature Ductility of the As-Deposited Amorphous Ni<sub>49.1</sub>Ti<sub>36.2</sub>Hf<sub>14.7</sub> Films Before and After 1-hour Annealing at 300°C and 350°C.**

Sample (4 kinds)	Annealing Temperature (°C)	Tensile Elongation (%)	Minimum Bending Diameter	RT Ductility (%)
As-deposited	N/A	2.5	~ 10 microns	2.5
Annealed #1	300	2.7	~ 10 microns	2.7
Annealed #2	350	N/A	> 1mm	< 0.5

*4.1.2.2. Crystallographic and Microstructural Characterization.* X-ray diffraction analyses and transmission electron microscopy were conducted for the samples before and after isothermal annealing. The X-ray diffraction spectra for different samples at room temperature are shown in Figure 4.10. It can be seen that the spectrum of the sample annealed at 300°C and that annealed at 350°C have features similar to those of the original amorphous sample, which showed only a wide hump, indicating that the amorphous phase remained after 1 hour annealing at 300°C, and even at 350°C. Therefore, the embrittlement must have occurred while the sample was still amorphous. However, careful examination of the spectra for sample without annealing and those for

samples with 300°C and 350°C annealing indicated some subtle changes. The XRD spectra of as-deposited sample and 300°C annealed sample look very similar, but the XRD spectrum of 350°C annealed sample looks slightly different: the peak is at a higher angle and has broadened, perhaps, indicating the presence of a second peak at 42.2°. Therefore, even though still amorphous, some structural change has taken place when the annealing temperature was increased from 300°C to 350°C.

Microstructure observation was also conducted for the samples annealed at different temperatures to verify the results from X-ray diffraction analyses. The TEM micrographs, as well as SAEDs, are shown in Figure 4.11. Both the as-deposited sample and the one annealed at 300°C show featureless microstructures, and the electron diffraction patterns of the samples showed only diffuse rings, consistent with the TEM and XRD results. However, for the sample annealed at 350°C for 1 hour, a modulated contrast is apparent although the electron diffraction pattern still shows only a diffuse ring. Therefore, after the sample was annealed at 350°C, there was some structural and/or chemistry change within the amorphous structure, but no detectable crystalline structure had formed. The nature of this change will be discussed in later sections.

#### 4.1.3. Isothermal Annealing at High Temperature via Different Ramp Rates

Above, it was shown that the properties of the  $\text{Ni}_{49.1}\text{Ti}_{36.2}\text{Hf}_{14.7}$  thin films depended on the heating rate during the isochronal crystallization anneal. Higher heating rate for crystallization treatment apparently improved the properties of the materials. In this section, amorphous  $\text{Ni}_{49.1}\text{Ti}_{36.2}\text{Hf}_{14.7}$  thin films were crystallized by isothermal annealing at high temperatures, but the heating rates from room temperature to isothermal annealing temperatures were different. Three annealing procedures were chosen. The first two were conventional vacuum annealing at 550°C for 1 hour with ramp rates of 5°C/min and

40°C/min, respectively. The third one was a rapid thermal annealing at 650°C for 20 seconds with ramp rate of 100°C/sec (6000°C/min).<sup>21</sup> The annealed samples were evaluated and characterized for their transformation temperatures, microstructure, mechanical and shape memory properties.

*4.1.3.1. Transformation Temperatures.* The martensitic phase transformation temperatures of the three annealed samples were measured by DSC during thermal cycling between 50°C to 250°C. The DSC curves are shown in Figure 4.12. The transformation temperature data were taken from those DSC curves and are listed on Table 4.6. The difference in transformation temperatures in different annealing process are illustrated in Figure 4.13. In general, reversible martensitic transformations were observed in all three samples, but the transformation temperatures and transformational enthalpy varied, more or less, with different annealing procedures. Between the two vacuum annealed samples, the transformation temperatures did not seem to be strongly affected by the heating rate, but the transformation enthalpy was considerably higher for the sample heated at higher rate. The RTA treated sample (heating rate 6000°C/min) seemed to have slightly higher martensitic transformation temperature ( $M_s$  temperature = 103°C) and slightly smaller transformational hysteresis (= 63°C) than the two vacuum annealed samples. The transformation enthalpy was higher as the heating rate increased. The RTA treated sample had an enthalpy for martensitic transformation of 14.7 J/g, which was considerably higher than that for the sample heated at 40°C/min ( $\Delta H = 10.5$  J/g) and that for the sample heated at 5°C/min ( $\Delta H = 7.8$  J/g). The difference in  $\Delta H$  strongly suggests a larger volume of material underwent martensitic transformation in the RTA treated sample. Therefore, using very high heating rate in an RTA process has

---

<sup>21</sup> The reason that the annealing temperature for RTA treatment is 650°C in stead of 550°C is because 550°C may not be high enough to crystallize amorphous  $Ni_{49.1}Ti_{36.2}Hf_{14.7}$  thin films due to the very high heating rate and short isothermal duration in an RTA process. The crystallization temperature is estimated at 631°C using Kissinger's method if taking the heating rate as 100°C/sec and activation energy as 347 kJ/mol.

clearly improved the transformation characteristics of the Ni-Ti-Hf shape memory thin films crystallized from amorphous samples.

**Table 4.6. Martensitic Transformation Temperatures and Transformation Enthalpies for Ni<sub>49.1</sub>Ti<sub>36.2</sub>Hf<sub>14.7</sub> Samples Crystallized by Isothermal Annealing with Different Heating Rates to Annealing Temperatures.**

Samples	Annealed #1	Annealed #2	Annealed #3
Process	Vacuum Anneal	Vacuum Anneal	RTA
Heating Rate	5°C/min	40°C/min	6000°C/min
Annealing Temperature	550°C	550°C	650°C
Annealing Time	1 hour	1 hour	20 seconds
Martensite Start (°C)	98	97	103
Martensite Finish (°C)	68	78	87
Martensite Peak (°C)	85	87	95
Austenite Start (°C)	132	134	148
Austenite Finish (°C)	170	166	163
Austenite Peak (°C)	152	152	158
Hysteresis (A <sub>p</sub> – M <sub>p</sub> )	67	65	63
Enthalpy (J/g)	7.8	10.5	14.7
Enthalpy (kJ/mol)	0.565	0.760	1.064

**4.1.3.2. Crystallographic and Microstructural Analyses.** X-ray diffraction experiments were conducted and TEM observation was carried out for the samples isothermally annealed in vacuum and for those crystallized by the rapid thermal anneal. Figure 4.14 shows the X-ray spectra for different samples using  $2\theta$  diffraction condition and CuK<sub>α</sub> irradiation. Indexing of the diffraction peaks is also shown in the figure. For samples using ramp rates of 5°C/min and 40°C/min, the result was similar to what has

been found in samples crystallized by isochronal anneal at similar heating rates. The annealed samples were composed of monoclinic martensite and cubic phase. The lattice parameters of the monoclinic phase were  $a = 2.63 \text{ \AA}$ ,  $b = 4.01 \text{ \AA}$ ,  $c = 4.77 \text{ \AA}$  and  $\beta = 99.1^\circ$ , and the lattice parameter of the cubic phase was  $a = 3.06 \text{ \AA}$ . The change in relative peak intensity indicated that the phase fraction of martensite was higher for the sample heated at higher rate. The RTA treated sample showed the highest martensite content, but still contained some of the cubic phase.

TEM micrographs and SAED pattern of the isothermally annealed samples are shown in Figure 4.15(a) and Figure 4.15(b). For samples treated by conventional vacuum annealing with ramp rates of  $5^\circ\text{C}/\text{min}$  and  $40^\circ\text{C}/\text{min}$ , the microstructure looked very similar to those of isochronal annealed Ni-Ti-Hf films at similar heating rates. That is, the microstructure consisted in both martensite and cubic phases with varied grain sizes of  $0.2 \text{ }\mu\text{m}$  or smaller. The shapes of grains were irregular and the grain boundaries seemed to have been pinned locally during grain growth. The microstructure of the RTA treated samples (Figure 4.15(c)) was very different. It was highly uniform with very fine martensite clusters (characterized by twin-like substructure) dominating the microstructure. There were also fine grains not having twin-like substructure which were probably the cubic phases revealed by XRD experiments. The size of the martensite grains was generally about  $50\text{nm}$ , and the width of twin plates was  $10\text{nm}$  to  $20\text{nm}$ , as indicated in Figure 4.15(d). The micrograph also indicated that large grains or large second phases were generally absent in the RTA treated samples.

**4.1.3.3. Mechanical and Shape Memory Properties.** Mechanical properties of the isothermally annealed samples were evaluated at room-temperature by bending deformation or uniaxial tensile tests. The results are shown in Table 4.7. Note that the ultimate elongation for conventional vacuum annealed samples was measured by bending test and that for RTA treated samples was measured by uniaxial tensile test. Again, this

is because the samples annealed in vacuum furnace were not ductile enough for clamping which is necessary in uniaxial tensile test, and the RTA sample was so ductile that it can be bent back (bending curvature radius  $\approx$  film thickness) without failure. The table shows that, the conventionally annealed samples were fairly brittle. The maximum achievable strain at the sample surface was less than 0.5% at room temperature. The RTA treated sample, however, is much more ductile. It has a uniaxial elongation of 5.8% and fracture stress of 1370 MPa (Figure 4.16). Between the two vacuum annealed samples, the one heated by higher heating rate seemed to be more ductile than the one heated at lower rate. The effect of heating rate on ductility observed in this series of samples was in agreement with the results of samples crystallized by isochronal annealing (see Table 4.4).

**Table 4.7. Comparison of Room-Temperature Ductility of As-deposited Amorphous  $\text{Ni}_{49.1}\text{Ti}_{36.2}\text{Hf}_{14.7}$  Films Crystallized by Isothermal Annealing via Different Ramp Rates to the Annealing Temperatures**

Sample	Annealed #1	Annealed #2	Annealed #3
Process	Conventional	Conventional	RTA
Heating Ramp Rate	5°C/min	40°C/min	6000°C/min
Annealing Temperature	550°C	550°C	650°C
Annealing Time	1 hour	1 hour	20 seconds
Min. Bending Diameter	$\geq 1$ mm	0.5 ~ 1 mm	$\sim 10$ $\mu\text{m}$
Tensile Elongation (%)	N/A	N/A	5.8
Ductility (%)	$\leq 0.5$	0.5 ~ 1	5.8

Similar to that in samples crystallized by isochronal heating, the two-way shape memory effect in all the samples was observed, with sudden cyclic shape change upon both heating and cooling. However, no quantitative data was obtained for samples annealed in vacuum furnace due to their brittleness. The RTA treated samples, however, were good enough for quantitative measurement. Thermal cycling under various constant

loads <sup>22</sup> was conducted between 50°C and 250°C, and the applied stresses were up to 350 MPa.

In conducting thermal cycling under different applied stress, the strain recovery path (heating path) on the first half-cycle was markedly different than on subsequent cycles. Figure 4.17 schematically shows such differences. The sample was loaded at room temperature and the load was kept constant throughout subsequent thermal cycles. Under a constant load, the sample was firstly heated to about 250°C (above  $A_f$  temperature), and the corresponding strain-temperature curve was A-B-C. Then the sample was cooled down to 50°C and the strain-temperature curve was C-D-E. Then, the sample was heated up again to 250°C and the corresponding strain-temperature was E-F-G. The two heating curves A-B-C and E-F-G are markedly different. This is because little strain was produced by the initial loading at room temperature (or a temperature substantially lower than the  $M_s$  temperature), but a large recoverable strain was produced during cooling from high temperature (curve D-E-F-G). This phenomena suggested that for RTA crystallized  $Ni_{49.1}Ti_{36.2}Hf_{14.7}$  films, transformation strain can be induced at temperature just above  $M_s$ , whereas the same level of stress was not sufficient to cause substantial martensite variant reorientation when applied to a thermally induced martensite. Therefore, in order to determine the recoverability of shape memory strain, it is important to apply the load to the material in the austenite condition, *i.e.*, thermal cycling should start from high temperature.

Figure 4.18 shows the strain-temperature plots for RTA treated samples during thermal cycling at different fixed loads.<sup>23</sup> It can be seen that an appreciable amount of

---

<sup>22</sup> Although the applied load was constant during thermal cycling, the true applied stress changed slightly due to cross-area change resulting from elongation.

<sup>23</sup> For the same strip, the load started from 100 MPa for the first thermal cycle, and then was gradually increased to 150 MPa, 175 MPa, 200 MPa, and 225 MPa for subsequent cycles (Fig.4.18 and Fig.4.19). Thermal cycling under 250 MPa, 275 MPa, 300 MPa and 350 MPa stresses was conducted using fresh samples because a large number of dislocations could be generated during thermal cycling at those stresses and may have effect on the shape memory characteristics of the materials. Applying stresses greater than 350 MPa usually resulted in film breakage, which often occurred during cooling when transformational strain began to form.

strain ( $\epsilon_c$ ) was obtained by cooling at applied stresses as low as 100 MPa during thermal cycling, and the material could be thermally cycled at biasing stresses as high as 350 MPa without immediate failure. At lower biasing stress ( $\leq 200$  MPa), closed strain-temperature hysteresis loops were obtained, indicating the strain generated on cooling was fully recovered on heating. At higher biasing stress, the hysteresis strain-temperature loops were open, indicating the strain generated on cooling was not fully recovered. Figure 4.19 summarizes the shape memory characteristics from this series of strain-temperature plots. It indicates that the RTA crystallized  $\text{Ni}_{49.1}\text{Ti}_{36.2}\text{Hf}_{14.7}$  samples had fully recoverable strain of 1.8% and the maximum stress for full strain recovery of about 200 MPa. Recovery strain increased slightly at stresses beyond 200 MPa and reached a maximum at 1.9% before decreasing with increasing biasing stress. Residual strain started to develop at biasing stresses higher than 200 MPa, and the higher the biasing stress during thermal cycling, the more residual strain was developed for a complete thermal cycle. The maximum strain induced by cooling may be as high as 3% but almost half of it was not recoverable.

#### 4.1.4. Discussion on Ni-Ti-Hf Films Crystallized by Post-Deposition Annealing

*4.1.4.1. Transformation Temperatures.* Producing Ni-Ti-Hf SMA films using post-deposition crystallization annealing has been attempted by a number of groups [Johnson *et al.* 1995, Gu *et al.* 1995, You *et al.* 1997]. Although there have been reports that indicated the transformation temperatures obtained were higher than those in binary Ni-Ti films, the effectiveness of hafnium in the films in increasing transformation temperatures was disappointing compared to that in melt-solidified materials. Moreover, no literature disclosed the mechanical characteristics of the annealed samples.

In this thesis,  $\text{Ni}_{49.1}\text{Ti}_{36.2}\text{Hf}_{14.7}$  SMA films produced by annealing an amorphous precursor exhibited  $M_p$  temperatures between 80 and 90° and  $A_p$  temperatures between

150°C and 160°C. Although evidently higher than those in binary Ni-Ti films, those temperatures were generally about 80 to 90°C lower than those of melt-solidified bulk Ni-Ti-Hf alloy having similar hafnium content [Han *et al.* 1995], which were about 170°C and 235°C for  $M_p$  and  $A_p$  temperatures, respectively. The results were in general agreement with those reported by others.

*4.2.4.2. Annealing Induced Embrittlement of Amorphous Ni-Ti-Hf Films.* The mechanical behavior of the annealed Ni-Ti-Hf films was one of the major concerns in this study. It was found that common annealing procedures suitable for crystallizing binary Ni-Ti films typically resulted in brittle Ni-Ti-Hf films after annealing, yielding basically unusable product. Further study indicated that embrittlement occurred at temperatures between 340°C ~ 390°C, far below the typical crystallization temperatures (510°C ~ 550°C), when the samples were still amorphous. X-ray diffraction analyses and transmission electron microscopic observation suggested that during this period, the materials underwent structural change even though no major phase transformation had taken place.

The structure change was most likely to be structural relaxation of amorphous material. In fact, structural relaxation has been often observed in amorphous materials and linked to embrittlement reactions [Chen 1976, Haasen 1983, Makino *et al.* 1990, Wu and Spaepen 1990, Qu and Xie 1991, Niikura *et al.* 1993, Barth *et al.* 1997]. The most widely observed phenomenon is the short-range ordering which can be divided into topological short-range ordering and chemical short-range ordering [van den Buekel and Huizer 1985], during which the atoms diffuse or rearrange even though the structure of the material remain amorphous. In the cases of amorphous Ni-Ti-Hf thin films in this study, embrittlement occurred prior to formation of any detectable crystalline phase, leading to a suspicion that the embrittlement was caused by structural relaxation of amorphous films.

In fact, topological short-range ordering or chemical short range ordering was very likely in sputtered Ni-Ti-Hf films during a post-annealing process. This is because that structural relaxation resulting from such processes has been observed in melt-spun amorphous Ni-Hf ribbons [Buschow and Bekmans 1979] and amorphous Ni<sub>50</sub>Ti<sub>50</sub> produced by ion implantation [Bodin, Moine and Eymery 1987], although the effect on mechanical properties was not discussed. It is reasonable to make comparison between sputtered Ni-Ti-Hf amorphous films and melt-spun ribbons, because the sputtered amorphous films, like melt-spun amorphous ribbons, contained a fraction of free volume due to self-shadowing effect of the sputtered films, and it was the free volume that determined the brittleness of the amorphous material [Wu and Spaepen 1990]. It seemed that the free volume in as-sputtered amorphous films was well distributed since the material was fairly ductile. However, post-deposition annealing may change the fraction and distribution of the free volume which would result in embrittlement of the amorphous material.

The occurrence of short-range ordering was supported by experimental results from X-ray diffraction (Figure 4.10) and TEM investigation (Figure 4.11). In the X-ray diffraction spectra, the shift of amorphous peak towards to higher  $2\theta$  angle indicated the average interatomic distance in the amorphous structure decreased, suggesting that densification took place. In the TEM micrograph, the wavelike contrast suggested there may be regions having compositional enrichment or material enrichment (densification), also an indication of occurrence structural relaxation involving short-range ordering [Glezer *et al.* 1984, Loirat *et al.* 2000]. The TEM micrograph indicated that chemical short-range ordering may be a significant factor for embrittlement.

The apparent activation energy of the process associated with the low-temperature exothermic peak also supported the occurrence of short-range ordering. The activation energy was 162 kJ/mol (1.68 eV/atom). It was comparable with the typical activation energy for structural relaxation in amorphous material (For example, 168 ~ 179 kJ/mol

for  $\text{Al}_{89}\text{Fe}_{10}\text{Zr}_1$  [Wang *et al.* 2002], 154 kJ/mol for  $\text{Fe}_{78}\text{B}_7\text{Si}_{15}$  [Takahara 1997], 159 kJ/mol for  $\text{Fe}_{40}\text{Ni}_{38}\text{Mo}_4\text{B}_{18}$  [Keupers *et al.* 1985]). In addition, the value of the activation energy was close to that for Hf diffusion in amorphous  $\text{Ni}_{54}\text{Zr}_{46}$  alloy which was 171 kJ/mol (1.78 eV/atom) [Loirat *et al.* 2000]. It is known that Ni is a faster diffuser in a Ni-Ti (Zr, Hf) system (activation energy for Ni diffusion was 1.33 eV/atom in Zr-Ni amorphous [Gradjean and Limoge 1997]), the fact that the activation energy for the embrittlement reaction was determined by Hf diffusion may suggest that chemical short-range ordering was more significant than topological short-range ordering in the structural relaxation process.

There are some other possible mechanisms for embrittlement such as segregation of impurities and oxidation. While no evidence for impurity segregation was found in the TEM observation, oxidation induced embrittlement can also be ruled out. Although our observation indicated that significant oxidation of Ni-Ti-Hf films on the surface took place at temperature as low as 250°C in extended exposure to atmosphere, the reduction of ductility was fairly moderate. In addition, pure Ti was used as oxygen getter during the annealing seemed to have successfully inhibited oxidation on the surface (no observable discoloration was noted on the surface) even though the vacuum for the annealing in this experiment ( $\sim 5 \times 10^{-6}$  torr) was not considered to be a very hard vacuum. Therefore, oxidation does not seem to be severe enough to cause significant embrittlement of the material. Nevertheless, there may still be oxygen in the films through absorption or incorporation followed by diffusion to the interior via grain boundaries and they may play a role in precipitation which is discussed next.

*4.1.4.3. Have Precipitates Formed At Low Temperatures?* Although have not been directly observed, crystalline phases such as  $(\text{Ti}+\text{Hf})_2\text{Ni}$  or  $(\text{Ti}+\text{Hf})_4\text{Ni}_2\text{O}$  are likely to form prior to the formation of  $(\text{Ti}+\text{Hf})\text{Ni}$  B2 phase. This is because f.c.c.  $\text{Ti}_2\text{Ni}$  crystallized at lower temperature (350°C ~ 400°C) than B2 NiTi phase [Buchwitz,

Adlwarth-Dieball and Ryder 1993] and local fluctuation of composition was very common in amorphous films. Furthermore, the possible presence of oxygen in the interior of films promoted the likelihood of formation of these phases, since oxygen atoms stabilize the  $(\text{Ti+Hf})_2\text{Ni}$  phase and nucleation of  $(\text{Ti+Hf})_2\text{Ni}$  phase could occur without necessity of local Ti enrichment. Although XRD and TEM studies were not able to detect  $(\text{Ti+Hf})_2\text{Ni}$  or  $(\text{Ti+Hf})_4\text{Ni}_2\text{O}$  phases, it was possible that they may still exist in a very fine form and very small volume percentage, since the composition of the films was very close to stoichiometry. It was noted that formation of these phases would lower the Ti content in the matrix. It is likely the matrix composition became Ni rich, thereby the transformation temperatures would be depressed.

The existence of fine  $(\text{Ti+Hf})_2\text{Ni}$  or  $(\text{Ti+Hf})_4\text{Ni}_2\text{O}$  heterostructures in the amorphous matrix was suggested from the shape of grain boundaries after the sample was fully crystallized. Under normal conditions, crystallization formed spherical B2 grains, which evolved into regularly equiaxial grains as the boundaries met with each other. Spherical crystalline grains in the amorphous matrix were observed in melt-spun  $\text{Ti}_{50}\text{Ni}_{25}\text{Cu}_{25}$  alloys [Rösner *et al.* 1999]. That was expected because the surface energy would be minimized in this way. However, the grains in the conventionally annealed Ni-Ti-Hf samples looked irregular, and it seemed that the grain boundaries had been pinned as the grains grew. It was suspected that the irregular grain boundaries may contribute to the brittleness of the crystallized films, since crack initiation and propagation can be easier at these locations.

Formation of  $(\text{Ti+Hf})_2\text{Ni}$  or  $(\text{Ti+Hf})_4\text{Ni}_2\text{O}$  phases was further supported by the relatively low transformation temperature of the crystallized films and residual B2 phases when the samples were cooled to room temperature. As observed by Han *et al.* [1995], the  $(\text{Ti+Hf})_2\text{Ni}$  or  $(\text{Ti+Hf})_4\text{Ni}_2\text{O}$  phases have higher Hf : Ti ratio than in the matrix. Therefore, Ti and Hf in the matrix somehow was depleted due to the formation of  $(\text{Ti+Hf})_2\text{Ni}$  or  $(\text{Ti+Hf})_4\text{Ni}_2\text{O}$  phases, and the transformation temperatures were thus

decreased. Ni-enrichment in the residual B2 phase may also result from depletion of (Ti+Hf) in the matrix, which drove the martensitic temperatures to a very low level (see Figure 2.8).

**4.1.4.4. Suppression of the Embrittlement via Fast Heating.** Although brittle Ni-Ti-Hf films resulted if crystallized by conventional vacuum annealing, using high heating rate such as in an RTA process to get fully crystalline material seemed to minimize or eliminate the embrittlement. This was probably because at high heating rate, the time/temperature window for embrittlement reaction was shortened, allowing the crystalline (Ti+Hf)Ni phase to form before embrittlement could occur due to the difference in incubation time.

Besides making the material more ductile, using high heating rate to crystallize amorphous Ni-Ti-Hf films had another benefit. As shown in Figure 4.8 and Figure 4.14, the as-annealed samples were composed of B19' martensite and B2 phase at room temperature. There was more room-temperature B19' martensite in the samples annealed via higher heating rate. Therefore, the transformation characteristics were improved by using high heating rate for crystallization.

## **4.2. *In-Situ* Crystallized Ni-Ti-Hf Films**

In the first part of this chapter,  $\text{Ni}_{49.1}\text{Ti}_{36.2}\text{Hf}_{14.7}$  SMA films were discussed that had been obtained by post-deposition annealing the originally amorphous films. In this part, Ni-Ti-Hf SMA films are discussed that were produced by sputtering at elevated substrate temperature so that the as-deposited films were crystalline and showed shape memory properties without necessity for further heat treatment. As shown below, it was found that these *in-situ* crystallized Ni-Ti-Hf SMA films showed greatly improved mechanical and shape-memory properties. Samples with different Hf compositions were investigated.

#### 4.2.1. Phase Transformations

As-deposited crystalline Ni-Ti-Hf thin films having different compositions were obtained by sputter deposition from targets with various compositions using the same deposition parameters for depositing amorphous films (*i.e.*, working gas Kr pressure 1.0 mTorr, working distance 81 mm, deposition power 1 kW) except that the substrate temperatures were between 400 to 450°C<sup>24</sup>. DSC curves for these samples during thermal cycling between 50° and 300°C are shown in Figure 4.20. In each of these curves, an endothermic peak occurred during heating, and an exothermic peak occurred during cooling, corresponding to a transformation from austenite to martensite, and martensite to austenite, respectively.

Transformation temperatures including  $M_s$ ,  $M_f$ ,  $M_p$ ,  $A_s$ ,  $A_f$  and  $A_p$  were determined from those DSC curves. Table 4.8 shows those temperatures as well as the transformational hysteresis ( $A_p - M_p$ ). For comparison, the transformation data for the RTA treated  $Ni_{49.1}Ti_{36.2}Hf_{14.7}$  films are listed in the brackets in the last column. It can be seen that substantially higher transformation temperatures than binary Ni-Ti thin films (typically  $M_f < 60^\circ\text{C}$ ,  $A_f < 110^\circ\text{C}$  [Hunbeeck 1999, Hodgson and Brown 2000]) were obtained in the Ni-Ti-Hf thin films. An  $M_f$  up to 200°C was achieved when the hafnium content was about 21.4at.%. As expected, the transformation temperatures depended on the hafnium content, since all films were (Ti+Hf) rich. Figure 4.21 illustrates the transformation temperatures as a function of hafnium content. As the hafnium content increased, transformation temperatures increased monotonically. The peak temperature

---

<sup>24</sup> Because Hf addition tends to increase the crystallization temperature for the same annealing conditions, one may expect that the minimum substrate temperature required for obtaining fully crystalline Ni-Ti-Hf SMA thin film is also composition dependent. The higher hafnium content, the higher the substrate temperature required for obtaining full crystalline structure. In choosing the substrate temperature, it is important to keep the substrate temperature just slightly above the minimum temperature required for fully crystalline structure, because if the substrate temperature is too high, not only will the microstructure change dramatically, but also the surface roughness will become excessive. That could affect the mechanical properties of the thin films substantially.

of martensitic transformation ( $M_p$ ) was 135°C for the sample with 14.5at.% Hf, and it increased to 182°C for the sample having 21.4at.% hafnium. The same effect was found for other transformation temperatures. Also, transformational hysteresis changed considerably with increasing hafnium content. For example, the transformational hysteresis of the sample containing 14.5at.% hafnium was 45°C, and it increased to 63°C when the hafnium content rises to 21.4at.%. The average of enthalpy change for both forward and reverse transformation was about 17 to 18.3 J/g (or 1.231 ~ 1.501 kJ/mol), with higher transformation heat was measured in samples having higher Hf content. These values are generally higher than the transformation enthalpy measured in Ni-Ti binary alloys (1.0 ~ 1.3 kJ/mol, [Lo *et al.* 1990]).

**Table 4.8. Martensitic Transformation Temperatures vs. Sample Composition of *In-Situ* Crystallized Ni-Ti-Hf SMA Films**

Target Composition	Ni <sub>47.5</sub> Ti <sub>32.5</sub> Hf <sub>20</sub>	Ni <sub>47.5</sub> Ti <sub>34.5</sub> Hf <sub>18</sub>	Ni <sub>48.5</sub> Ti <sub>35.5</sub> Hf <sub>16</sub>	Ni <sub>48.5</sub> Ti <sub>37.5</sub> Hf <sub>14</sub>
Film Composition <sup>25</sup>	Ni <sub>48.2</sub> Ti <sub>30.4</sub> Hf <sub>21.4</sub>	Ni <sub>48.0</sub> Ti <sub>33.9</sub> Hf <sub>18.1</sub>	Ni <sub>49.3</sub> Ti <sub>34.5</sub> Hf <sub>16.2</sub>	Ni <sub>48.9</sub> Ti <sub>36.6</sub> Hf <sub>14.5</sub>
$M_s$ (°C)	200	157	150	140 (103) <sup>†</sup>
$M_f$ (°C)	160	143	130	127 (87)
$A_s$ (°C)	213	202	181	172 (148)
$A_f$ (°C)	260	217	202	184 (163)
$M_p$ (°C)	182	150	140	135 (95)
$A_p$ (°C)	245	210	190	180 (158)
Hysteresis (°C)	63	60	50	45 (63)
Enthalpy (J/g)	18.3	17.6	17.4	17.0 (14.7)
Enthalpy (kJ/mol)	1.501	1.345	1.300	1.231 (1.064)

<sup>†</sup> Values at far right in parentheses are for RTA post-deposition annealed Ni<sub>49.1</sub>Ti<sub>36.2</sub>Hf<sub>14.7</sub> films.

<sup>25</sup>It is noted that the compositions on this table are slightly different than those on Table 4.1 even though the same targets were used. This slight disparity mostly resulted from the difference in deposition temperature. The typical trend is, the Ni and Hf contents in films decreased at increasing deposition temperature while the Ti content increased.

Comparing the transformation data of *in-situ* crystallized  $\text{Ni}_{48.9}\text{Ti}_{36.6}\text{Hf}_{14.5}$  and that of the RTA treated  $\text{Ni}_{49.1}\text{Ti}_{36.2}\text{Hf}_{14.7}$  films, the *in-situ* crystallized films had considerably higher transformation temperatures and smaller transformational hysteresis. In addition, the martensitic transformational enthalpy was higher for *in-situ* crystallized films. These results indicated that the *in-situ* crystallized films exhibited improved transformation characteristics.

#### 4.2.4. Crystallographic and Microstructural Analysis

In order to compare the crystallographic and microstructural characteristics of *in-situ* sputtered Ni-Ti-Hf and post-deposition annealed Ni-Ti-Hf films, X-ray diffraction and TEM micrographs of  $\text{Ni}_{48.9}\text{Ti}_{36.6}\text{Hf}_{14.5}$  films were studied and the results are presented below.

**4.2.4.1. X-ray Diffraction.** Figure 4.22 shows X-ray diffraction spectra of *in-situ* crystallized  $\text{Ni}_{48.9}\text{Ti}_{36.6}\text{Hf}_{14.5}$  thin films. These spectra were taken at room temperature using  $\text{CuK}\alpha$  irradiation and  $2\theta$  mode (in-plane position). Three major peaks were found at  $2\theta$  angles  $45.2^\circ$ ,  $41.5^\circ$  and  $38.2^\circ$ . Also there are several minor peaks at other  $2\theta$  positions. All the peaks can be indexed a phase having monoclinic structure with lattice parameters of  $a = 2.63 \text{ \AA}$ ,  $b = 4.01 \text{ \AA}$ ,  $c = 4.77 \text{ \AA}$  and  $\beta = 99.1^\circ$ . The highest peaks are indexed to (020), (11-1) and (200) planes, respectively, and the two minor peaks at  $2\theta$  angle of  $44.42^\circ$  and  $60.29^\circ$  may be indexed as (012) and (022) planes, respectively. The monoclinic phase was the same as that identified in the RTA treated  $\text{Ni}_{48.9}\text{Ti}_{36.6}\text{Hf}_{14.5}$  samples, but the X-ray spectrum looked different. For RTA treated sample the strongest X-ray diffraction peaks for martensite were (002)M and (012)M, but for as-sputtered crystalline sample the strongest peak was (020)M. This may suggest that the texture of

as-sputtered crystalline sample was different with that of crystallized sample by RTA treatment. Also, unlike the RTA treated sample in which there were cubic phases besides the martensite, the as-sputtered crystalline sample did not explicitly show any phases other than martensite. However, because the films are slightly (Ti+Hf)-rich, it is suspected that  $(\text{Ti+Hf})_2\text{Ni}$  or  $(\text{Ti+Hf})_4\text{Ni}_2\text{O}_x$  precipitates may exist in the B19' matrix. X-ray diffraction spectra cannot rule out the existence of those phases because their peaks could be concealed into the high peaks of the martensite because the volume fraction of the second phases could be very small. Therefore, TEM observation is necessary to confirm whether there are second phases or not.

4.2.4.2. *Transmission Electron Microscopy and Electron Diffraction.* Figure 4.23

(a) ~ (c) show the TEM micrographs of in-plane sample of an *in-situ* crystallized  $\text{Ni}_{48.9}\text{Ti}_{36.6}\text{Hf}_{14.5}$  film as well as corresponding electron diffraction patterns. They indicated that the microstructure was composed of grains that had twinned substructure, a typical feature of the martensite of Ni-Ti based shape memory alloy [Otsuka and Wayman 1986]. The grain size was on the order of 100 nm, which was comparable with that of *in-situ* deposited Ni-rich TiNi films in the interior layer, but evidently larger than the fine grains in the layers close to the substrate surface [Hou 1998]. The grain size was also much smaller than typical grain size for melt-solidified Ni-Ti-Hf alloys ( $>1 \mu\text{m}$ ) [Han *et al.* 1995, Olier *et al.* 1995]. In the TEM micrographs (Figure 4.23 (b), (c)) having higher magnification, clear twinned substructure was revealed. The thickness of twin plate was on the order of 10 nm or smaller. Consistent with the X-ray diffraction results, the micrographs did not reveal any second phases.

A selected-area electron diffraction pattern was also taken and it is shown in Figure 4.23. The aperture size was 50 microns so there may be hundreds of grains. The diffraction pattern was composed of a series of rings. The sharpness of those rings is

generally not good because some of the interplanar distances are very close to each other in this low-symmetry structure.

#### 4.2.2. Mechanical Properties

In order to assess the effect of Hf addition on the mechanical behavior of Ni-Ti SMA films,  $\text{Ni}_{49.5}\text{Ti}_{50.5}$  films were prepared using the *in-situ* crystallization technique and were studied as a benchmark. The binary films were deposited from a  $\text{Ni}_{47}\text{Ti}_{53}$  target using the same deposition parameters as for ternary deposition (*i.e.*, working gas Kr pressure 1.0 mTorr, working distance 81 mm, deposition power 1 kW) except that the substrate temperature was about  $380^\circ\text{C} \sim 400^\circ\text{C}$ . The transformation temperatures of the binary films are  $M_s = 55^\circ\text{C}$ ,  $M_f = 37^\circ\text{C}$ ,  $A_s = 78^\circ\text{C}$ , and  $A_f = 90^\circ\text{C}$ . Figure 4.24 showed a room-temperature stress-strain curve which is typical of martensitic NiTi SMA and is composed of a number of deformation stages. The first segment A-B represents a linear elastic deformation of the martensite. The following segment B-C is characterized by low flow stress with negligible strain hardening, and it is associated with martensite variant reorientation. The third segment C-D is a transitional segment, which is followed by another linear elastic one (D-E). Finally, the segment E-F is a plastic deformation as a result of dislocation slip, which is a common mechanism of plastic deformation occurring in ordinary metallic materials. The second elastic segment (D-E) had a smaller Young's modulus than the first elastic segment (A-B). This may result from either a combination of plastic/elastic deformation or elastic anisotropy.

It is well known that the mechanical behavior of SMAs is temperature dependent. Therefore, tensile tests of the *in-situ* crystallized  $\text{Ni}_{49.5}\text{Ti}_{50.5}$  films were conducted at various temperatures. The results are shown in Figure 4.25. Note that all of the curves except curve (f) were obtained for specimens that were heated from room temperature. Therefore, curves (a) (at  $25^\circ\text{C}$ ), (b) (at  $50^\circ\text{C}$ ) and (c) (at  $75^\circ\text{C}$ ) were all obtained when the

samples were fully martensitic. Curve (d) (at 100°C) and curve (f) (at 125°C) were obtained when the samples were fully austenitic. The test temperature for curve (f) was 75°C but the sample was cooled down to this temperature from 150°C, so the sample was fully austenitic before the test started. Comparing curves (a), (b) and (c), one can see that the ductility increased when the tensile test temperature was increased. At the same time, the yield stress, which corresponds to the onset stress for martensite reorientation, decreased as the test temperature approached  $A_s$  temperature. For curve (d) which was obtained at temperature higher than  $A_f$ , only a small strain associated with plateau-type deformation was observed.<sup>26</sup> At higher temperature (125°C) when  $T \gg M_s$ , plateau deformation did not occur and the stress-strain curve looks similar to that of common metallic materials. The test temperature of curve (f) was closer to  $M_s$ , and the plateau segment, which was associated with stress-induced martensitic transformation, gave almost 8% elongation. Plasticity by stress-induced martensite formation will be discussed further below.

The stress-strain curves showed that the strain hardening rates during martensite reorientation or stress-induced martensitic transformation (SIM) were very low. In curves (a), (b) and (c) where the films were elongated in the martensite, the typical strain hardening rates  $d\sigma/d\varepsilon$  were about 0.75, 0.5 and 0.4 GPa respectively. Therefore, when the temperature approached  $A_s$ , the strain hardening rate for deformation associated with martensite reorientation decreased. In curve (f) where the plateau segment was associated with stress induced martensitic transformation, the corresponding strain hardening rate was even lower ( $d\sigma/d\varepsilon = 0.32$  MPa). Therefore, it seemed that transformation strain can be more easily to be created by inducing martensitic transformation than by martensite reorientation.

---

<sup>26</sup> The low stress for the deformation indicated that some martensite was still present at temperature above the nominal  $A_f$ .

**4.2.2.1. Tensile Tests of Ni-Ti-Hf Films at Room Temperature.** Room-temperature mechanical properties are of interest because it is convenient to manipulate the materials at room temperature. Figure 4.26 shows the stress-strain curves of *in-situ* crystallized Ni-Ti-Hf thin films with different Hf compositions. The strain rate was 0.04 mm/mm/min (or 2 mm/min of cross-head speed for 50mm long sample) and the samples were elongated until failure. Yield stress ( $\sigma_y$ ), ultimate elongation ( $\epsilon_{max}$ ) and fracture stresses ( $\sigma_f$ ) of those samples were obtained by averaging the results of five samples and the results are listed in Table 4.9. Typically, samples with different Hf compositions can be elongated to ultimate strains from 5 to 9% at room temperature, and the fracture stresses ranged from 1480 MPa to 1820 MPa. The hafnium content affected the yield stress, ultimate elongation and fracture stresses of the films, which is illustrated in Figure 4.27. As hafnium content increased, the ultimate elongation decreased and the fracture stress increased. Most importantly, hafnium content had a strong effect on room-temperature yield stress of the films. As the hafnium content was increased from 14.5% to 21.4at.%, the yield stress at room temperature was increased from 480 MPa to 770 MPa. This result suggests that solution hardening resulted from substituting Hf for Ti.

**Table 4.9. Room-Temperature Tensile Testing Results of *In-situ* Crystallized Ni-Ti-Hf Films with Different Hafnium Content.**

Film Composition	Ni <sub>48.2</sub> Ti <sub>30.4</sub> Hf <sub>21.4</sub>	Ni <sub>48.0</sub> Ti <sub>33.9</sub> Hf <sub>18.1</sub>	Ni <sub>49.3</sub> Ti <sub>34.5</sub> Hf <sub>16.2</sub>	Ni <sub>48.9</sub> Ti <sub>36.6</sub> Hf <sub>14.5</sub>
Ultimate Elongation (%)	5.1	6.8	7.4	8.2
Fracture Stress (MPa)	1480	1610	1780	1820
Yield Stress (MPa)	770	640	570	480

Comparing the room-temperature tensile curves of binary and ternary films, one may see that the tensile behavior of the martensite in Ni-Ti-Hf thin films, especially the

ones having higher hafnium content, differs from that of martensite in binary Ni-Ti SMA films. The plateau region in tensile curves for ternary films showed much more working hardening than occurred in the binary films. However, considering the large difference in transformation temperatures between binary films and ternary films ( $\Delta A_p = 95^\circ\text{C} \sim 160^\circ\text{C}$ ), difference in stress-strain curves for binary and ternary films was not unexpected, since the mechanical behavior of SMAs depends on the temperature with respect to their transformation temperatures [Miyazaki *et al.* 1986]. Therefore, in order to compare the mechanical behavior of binary and ternary films, it is necessary to conduct tensile tests at elevated temperatures.

**4.2.2.2. Tensile Tests at High Temperatures.** In order to find the temperature effect on the mechanical behavior of Ni-Ti-Hf SMA films, *in-situ* crystallized Ni-Ti-Hf films were tested at various temperatures. Films having composition  $\text{Ni}_{48.9}\text{Ti}_{36.6}\text{Hf}_{14.5}$  were selected to conduct such tests because the post-deposition annealed films discussed previously had a similar composition and thus a direct comparison can be made.<sup>27</sup> The samples were heated to  $250^\circ\text{C}$  (to make them fully austenitic) before cooling down to the test temperature.<sup>28</sup> In doing that, the material can be austenitic at lower temperature so stress induced martensite formation can be more extensively studied.

Figure 4.28 shows a series of stress-strain curves of  $\text{Ni}_{48.9}\text{Ti}_{36.6}\text{Hf}_{14.5}$  films elongated at different test temperatures. Basically the temperature affected the tensile behavior of the  $\text{Ni}_{48.9}\text{Ti}_{36.6}\text{Hf}_{14.5}$  films in a way similar to that for melt-solidified Ni-Ti-Hf

---

<sup>27</sup> Another reason of choosing this film was its transformation temperatures. It was intended to test the material at both martensite and austenite. On one hand, with material having  $M_f$  above  $100^\circ\text{C}$ , test at martensite can be facilitated in heating furnace since cooling down to sub-ambient temperature is not necessary. On the other hand, very high  $A_f$  temperature is troublesome because oxidation of the material can occur rather rapidly. With the material having  $A_f$  temperature below  $200^\circ\text{C}$ , testing at austenite can be done in non-vacuum furnace without significant oxidation problems.

<sup>28</sup> This test procedure is referred as to “cool-down routine” in contrast to a more frequently used procedure “direct-heating routine” in which the sample is heated to the test temperature from room-temperature at which  $\text{Ni}_{48.9}\text{Ti}_{36.6}\text{Hf}_{14.5}$  films are fully martensitic.

materials [Wang *et al.* 1997]. This is, at temperature much higher than  $A_p$ , the film behaved like ordinary metallic material. Plateau-like deformation associated with SIM took place as the test temperatures approached  $M_s$ . The onset stress for SIM reached a minimum as the temperature decreased to about  $M_s$ . As the test temperature was decreased to below  $M_s$ , martensite reorientation replaces SIM as a mechanism for plastic deformation, the yield stress started to increase, and the plateau-like behavior started to diminish. It was also noted that the effect of temperature on ternary films was similar to that on binary films although major differences exist [see Figure 4.25 and Figure 4.28]. The most marked differences are: (1), the strain associated with SIM or martensite reorientation in the ternary films was smaller than that in the binary films (2 ~ 4% for ternary vs. 6 ~ 8% for binary) which indicating that Hf substitutions reduced the transformational strain dramatically; and (2) the strain hardening rate for SIM or martensite reorientation related deformation was higher in ternary films than in the binary films.

In attempting to quantitatively evaluate the plastic deformation associated with SIM or martensite reorientation, we have estimated the corresponding strain hardening rates, and the results are shown in Figure 4.28. The magnitude of the rates ranged from 3.7 to 14.2 GPa, with the maximum at 25°C (the lowest temperature, corresponding to martensite reorientation) and the minimum at 160°C (corresponding to SIM). This behavior indicated SIM related deformation in the  $Ni_{48.9}Ti_{36.6}Hf_{14.5}$  films was easier than the deformation related to martensite reorientation. However, the strain hardening rate for  $Ni_{48.9}Ti_{36.6}Hf_{14.5}$  ternary films was typically an order of magnitude higher than that for binary  $Ti_{50.5}Ni_{49.5}$  films. That means that transformation strain (whether by SIM or by martensite reorientation) in  $Ni_{48.9}Ti_{36.6}Hf_{14.5}$  ternary films is much more difficult to achieve than that in binary films, and the resistance increases as more strain is generated. It is suggested that increasing stress will be likely to activate dislocation generation and movement, resulting in poor strain recovery.

The relationship between the yield stress and tensile temperature was shown in Figure 4.29. The yield stress increases almost linearly with the tensile test temperature, which is consistent with the prediction from Clapeyron's equation. Linear curve fitting gives the slope ( $d\sigma/dT$ ) at about 6.23 MPa/°C, and this is close to the ratio (6.9 MPa/°C) for stress induced martensitic transformation found for binary Ni-Ti alloy [Hodgson and Brown 2000].

Theoretical transformation strain or optimal transformation strain may be estimated using a number of measured data and Clapeyron's equation:

$$\frac{d\sigma}{dT} = -\frac{\Delta H}{T \cdot V \cdot \Delta \varepsilon} \quad (4.2)$$

With  $d\sigma/dT = 6.23$  MPa/K,  $\Delta H = -1.23$  kJ/mol,  $T_0$ , the equilibrium temperature, simplified as  $(A_f + M_s)/2 = 435$  K, and the molar volume  $V = N_A \times a^3 / 2 = 8.63 \times 10^{-6}$  m<sup>3</sup>/mol, ( $N_A$ , the Avogadro's constant, =  $6.022 \times 10^{23}$ /mol, and  $a$ , the lattice parameter of CsCl-type structure of Ni<sub>48.9</sub>Ti<sub>36.6</sub>Hf<sub>14.5</sub> austenite,  $\approx 3.06$  Å), then  $\Delta \varepsilon$  was estimated at 5.2%. This value approaches that for *in-situ* crystallized binary Ni-Ti films [Hou 1998]. However, the strain associated with the plateau-like deformation was about 2 ~ 4%, which was considerably lower than the expected value from Clapeyron's equation. The disparity suggests that not all the martensite variants formed from stress induced martensitic transformation were optimal for generating transformation strain. Grain boundaries in fine-grain microstructure may force the formation of variants less favorable for strain generation due to continuity restriction [Inoue *et al.* 1996].

In Figure 4.29, it is interesting to note that the yield stress at  $M_s$  (140 °C for Ni<sub>48.9</sub>Ti<sub>36.6</sub>Hf<sub>14.5</sub>) was 325 MPa, because, theoretically, zero yield stress at  $M_s$  temperature is expected by linear regression using Clapeyron's equation, as observed by Hou in *in-situ* crystallized Ni-Ti films. It seemed that there existed a threshold stress to prevent

SIM from happening, and this threshold stress may or may not change with the tensile temperature. It is also noted that the measured yield stress at the  $M_s$  temperature was 375 MPa instead of zero, but this is similar to the behavior of binary films, because Hou measured the yield stress at  $M_s$  to be 100 MPa. The reason may be related to the high local lattice energy resulting from a phase transformation in a very small volume fraction. Imaginably SIM can not keep going at zero stress because the local lattice distortion works against it.

The tensile temperature also had influence on the ultimate strain. Figure 4.30 shows the relationship of the ultimate elongation and yield stress with temperature from 25°C to 250°C. The ultimate elongation ranged from about 6% to 11% and the yield stress ranged from 375 MPa to 690 MPa. The dependence of yield stress and ultimate elongation on test temperature may be divided into three regions. Region I (from 25°C to 150°C), Region II (from 150°C to 200°C) and Region III (from 200°C to 250°C). In Region I, the yield stress decreased with increased test temperature. In the meantime, the ultimate elongation was increased slightly. Considering that in this region the material was at least partially martensitic, decreasing of yield stresses suggested martensite reorientation became easier at higher temperature. Correspondingly, martensite reorientation may be more complete and gave better ductility. In Region II, the ductility remained near the maximum, and SIM stress increased linearly with temperature, which was discussed previously. In Region III, the yield stress decreased again with increased test temperature, and the ultimate elongation also decreased. This was related to the fact that materials strength was decreased at higher temperature. Thus, the amount of martensite formed by SIM transformation dramatically decreased, resulting a reduction of overall elongation.

### 4.2.3. Shape-Memory Properties

Shape-memory properties of *in-situ* crystallized  $\text{Ni}_{48.9}\text{Ti}_{36.6}\text{Hf}_{14.5}$  films were evaluated by both the constrained thermal cycling method and the free recovery method. Because most SMA applications are analogous to one of the two test methods, evaluation by both methods may provide information useful for application design of Ni-Ti-Hf SMA films.

**4.2.3.1. Free Recovery of Deformation in Martensite By Heating.** Figure 4.31 shows a series of room-temperature stress-strain curves for load-unloading of  $\text{Ni}_{48.9}\text{Ti}_{36.6}\text{Hf}_{14.5}$  films at overall pre-strain of about 2%, 3%, 4% and 5%. The remaining strain after unloading was measured at 0.9%, 1.8%, 2.7% and 3.5%, respectively, and they are plastic strains ( $\epsilon_p$ ). Recovery took place upon heating the sample to 250°C (65°C above  $A_f$ ), and residual strain was also measured. Figure 4.32 is a plot showing the recoverable strain as well as recovery rate as a function of the plastic pre-strain. The x-axis is the amount of pre-strain left after unloading ( $\epsilon_p$ ), the left-side y-axis is the amount of strain that is recovered ( $\epsilon_{rc}$ ), and the right-side y-axis is the recovery rate ( $RR$ ). It is indicated that the pre-strain at 25°C (147°C lower than the  $A_s$ , 100°C below  $M_f$ ) was partially recoverable when the material was heated to austenite. The magnitude of recoverable strain increased as the amount of pre-strain increased. Up to 2% of strain was recoverable when the sample was strained at 5% (which gave rise to a 3.5% plastic strain after unloading). The recovery rates ranged from about 55% to over 80%. Among the four different pre-strains of martensite at 25°C, the smaller recovery percentage was found at the lowest pre-strain and largest pre-strain. The maximum recovery rate was about 83% when the overall pre-strain was 3% (*i.e.*, plastic pre-strain was 1.8%). The difference of recovery rate at different pre-strain level suggested that slip occurred even at the very initial stage of plastic deformation. After an initial hardening, most strain resulted from martensite variant reorientation. When the (plastic) deformation went

beyond 3% or so, slip - mediated strain became more dominant.

The recovery rate measured in films presented above was generally less than those measured in melt-solidified bulk Ni-Ti-Hf SMAs [Pu *et al.* 1995; Wang *et al.* 1997], for which up to 3% fully recoverable strain was reported. However, that does not certify the properties of Ni-Ti-Hf films was much inferior to that of melt-solidified Ni-Ti-Hf SMAs, because the recovery rate measured in melt-solidified Ni-Ti-Hf alloys involved bending strain, while the strain for Ni-Ti-Hf films was uniaxial. SMAs usually recover far better from bending strain than from uniaxial strain.

Pre-straining of the martensite at higher temperatures and subsequently unloading and heating the material to austenite was carried out to determine the recoverability of the strain. Figure 4.33 shows the stress-strain curves of this series of experiments. In those experiments, samples were deformed at 25°C (147°C below the  $A_s$  temperature), 50°C (122°C below the  $A_s$  temperature), 100°C (72°C below the  $A_s$  temperature), and 150°C (22°C below the  $A_s$  temperature), respectively. At each of those temperatures the martensitic film was strained to about 4.3% ~ 4.5% elongation and the plastic strain after unloading was about 3%. The sample was then heated to 250°C (66°C above  $A_f$  temperature) so that the reverse martensitic transformation temperature was completed. Residual strain was measured after the sample was cooled down the test pre-straining temperature. Figure 4.34 shows the amount of strain recovered upon reverse transformation and the recovery rate as functions of deformation temperature of martensite. It is indicated that at fixed pre-strain, the strain recoverable by heating monotonically increased as the deformation temperature was approached  $A_s$ . The recovery rate also increased at the same time. Among the four tests at temperatures, deformation at 25°C (147°C below the  $A_s$  temperature) had the lowest recovery rate at 63%, and the deformation at 150°C (22°C below the  $A_s$  temperature) had the highest recovery rate at 83%.

4.2.3.2. *Transformational Superelasticity.* As presented previously, SIM related plateau-type stress-strain curve occurred when an initially austenitic sample was deformed. Figure 4.35 shows the stress-strain curves of the sample deformed at various temperatures (210°C, 200°C, 190°C and 180°C, which are 70°C, 60°C, 50°C and 40°C above the  $M_s$  temperature, respectively), to which the samples were cooled down from 250°C. The overall elongation was 4% at each of those temperatures, and both loading and unloading paths at the test temperature were also recorded. Although incomplete, isothermal recovery upon unloading was seen at different temperatures.<sup>29</sup> Figure 4.36 illustrates the recovery strain upon unloading as a function of the deformation temperature. It shows that best recovery occurs at 190°C (50°C above the  $M_s$ ) and 200°C (60°C above the  $M_s$ ), and the recovery rates were between 80% to 90%. At higher temperature (210°C) and lower temperature (180°C) the recovery rate fell to only 40% to 50%. It was noted that the recovery rates in superelastic deformation was typically higher than SME recovery of the strain imparted to martensite.

The isothermal recovery of tensile strain seen in this experiment demonstrates that the *in-situ* crystallized  $\text{Ni}_{48.9}\text{Ti}_{36.6}\text{Hf}_{14.5}$  films had superelastic properties. The dependence of superelastic recovery on test temperature was related to the transformation temperatures, and also to the dependence of material strength on temperature. At 200°C and 190°C (60°C and 50°C above the  $M_s$  temperature, respectively), a portion of the strain resulted from stress induced martensitic transformation, and reverse transformation upon unloading took place isothermally, giving rise to a recovery of the strain. However, the low strain recovery rate at high temperature and at low temperature occurred for different reasons. Lower recovery seen at higher temperature (210°C, 70°C above  $M_s$ ) may be because at this temperature, more strain resulted from slip related deformation. This is supported by the fact that the material yielded at lower stress at 210°C than at 200°C.

---

<sup>29</sup> For simplicity, in calculating the recovery rate in this set of experiments, the conventional elastic strain was included.

Lower recovery seen at lower temperature (180°C, 5°C below  $A_f$ ) was because the temperature was so low so that the reverse transformation was not completed. This is supported by the fact that the  $A_f$  temperature of this sample was above the tensile test temperature, and more recovery was observed when the sample was heated to higher temperature.

The effect of overall strain on isothermal recovery rate was also investigated. Figure 4.37 shows stress-strain curves of  $\text{Ni}_{48.9}\text{Ti}_{36.6}\text{Hf}_{14.5}$  SMA thin films deformed at 190°C (50°C above the  $M_s$  temperature and 6°C above the  $A_f$  temperature) to total initial strain of 2%, 3%, 4%, and 5% respectively. Isothermal recovery upon unloading was also shown in the figure. Figure 4.38 shows the recoverable strain upon isothermal unloading and recovery rate as functions of the initial strain. It is indicated that larger recovery strain was increased as the initial strain was increased. Up to about 4% strain was isothermally recovered upon unloading when the initial strain was 5%. In the meantime, the recovery rates range from about 80% to about 95%, but the strain recovery rate decreased monotonically as the initial strain was increased. This phenomenon may suggest that the transformational strain contributed less and less to the overall strain as the deformation continued.

**4.2.3.3. Thermal Cycling Under Constant Load.** Thermal cycling under various constant loads between 50°C and 300°C was conducted for *in-situ* crystallized  $\text{Ni}_{48.9}\text{Ti}_{36.6}\text{Hf}_{14.5}$  films. It was found that if the constrained thermal cycling started at temperature well below  $M_f$  temperature (such as room temperature which was about 100°C below  $M_f$ ), the first heating excursion showed little strain recovery while the second heating excursion had substantial strain recovery, the same phenomenon that was observed in the RTA crystallized  $\text{Ni}_{49.1}\text{Ti}_{36.2}\text{Hf}_{14.7}$  samples. This observation suggested that for *in-situ* crystallized  $\text{Ni}_{48.9}\text{Ti}_{36.6}\text{Hf}_{14.5}$  films, transformation strain can be most easily induced at temperature just above the  $M_s$  temperature via optimal variant formation.

Figure 4.39 shows a series of strain-temperature curves during thermal cycling starting from 300°C (115°C above  $A_f$ ) under different preset constant loads. It indicates that transformational strain was obtained when material was cooled down from high temperature and the strain may be completely or partially recovered upon re-heating the sample to high temperature, forming a hysteresis loop.

From each strain-temperature hysteresis loop at different biasing stresses, a number of data were taken including transformation temperatures, the strain resulting from cooling to martensite from austenite ( $\epsilon_c$ ), and stress recovered on heating from martensite to austenite ( $\epsilon_h$ ). The residual strain  $\epsilon_r$  was obtained by subtracting the recovered strain  $\epsilon_h$  (on heating) from the cooling induced strain  $\epsilon_c$ . Figure 4.40 shows the cooling induced strain and recovered strain (on heating) as functions of applied stress during thermal cycling. It is indicated that a small amount of transformational strain may be induced at biasing stress as little as 100 MPa. With increased applied stress during thermal cycling, the strain induced by cooling from high temperature (austenite) increased continuously. Under applied stress less than 250 MPa, the strain recovered by heating from low temperature equaled the strain generated on cooling from high temperature, indicating a full recovery, corresponding to a closed loop in strain-temperature curves. Under higher biasing stress during thermal cycling, the strain recovered on heating was less than that generated on cooling, resulting residual stress from each constrained thermal cycle. Therefore, 250 MPa was considered the maximum stress for perfect recovery during constrained thermal cycling, and the corresponding strain generated on cooling (which equaled the one recovered on heating), which was measured at 2.8%, was the maximum fully recoverable strain for this sample. Figure 4.40 also shows that, as the biasing stress during thermal cycling was increased beyond the maximum stress for complete recovery, more strain was obtained on cooling, and it reached nearly 5% as the biasing stress was increased to 500 MPa. At the same time, the recovered strain upon heating did not seem to be saturated at 3.6% (which was regarded

as maximum recoverable strain). Therefore, residual strain for a complete HT → LT → HT cycle was increased as the biasing stress as further increased beyond the maximum stress for full strain recovery.

The dependence of transformation temperatures ( $M_s$ ,  $M_f$ ,  $A_s$  and  $A_f$  temperatures) on biasing stress during thermal cycling is illustrated in Figure 4.41. As is shown, the transformation temperatures increased roughly linearly with increasing biasing stress during thermal cycling. Linear fitting <sup>30</sup> gave a number of  $dT/d\sigma$  slopes:  $dM_s/d\sigma = 0.152$  °C/MPa,  $dM_f/d\sigma = 0.098$  °C/MPa,  $dA_s/d\sigma = 0.157$  °C/MPa and  $dA_f/d\sigma = 0.243$  °C/MPa. Noticeably the slopes of  $dM_s/d\sigma$  and  $dA_s/d\sigma$  were very close to each other, which the other two slopes varied substantially.

In stress-induced martensitic transformation, Clapeyron's equation predicted a linear relationship between the transformation temperature and the applied stress. That was consistent with our experiments because the strain produced during cooling occurred at temperature above the  $M_s$  temperature measured when the material was stress-free. In addition, the values of  $dM_s/d\sigma$  and  $dA_s/d\sigma$  are in good agreement with the value of  $d\sigma_y/dT$  measured in Figure 4. 28 in the stress-strain curve at different temperature (= 6.23 MPa/°C which gives an inverse of 0.161 °C/MPa). Using the measured data of  $dM_s/d\sigma$  and  $dA_s/d\sigma$  and Clapeyron's equation (4.1), the theoretical transformation strain was estimated at from 4.9% to 5.1%. The difference between the measured value and predicted value may suggest the formation of martensite variant under stress was still not optimized for strain generation.

The linear fitting for the transformation finish temperatures with biasing stress did not go as well as that for transformation start temperatures with biasing stress. Furthermore, the values of  $dM_f/d\sigma$  and  $dA_f/d\sigma$  looked rather aberrant from the data from the values of  $dM_s/d\sigma$  and  $dA_s/d\sigma$ . Ironically, using the measured  $dM_f/d\sigma$  value and

---

<sup>30</sup> The last few data that were associated with high biasing stress were excluded in the linear fitting because at high biasing stress, deformation of the material relating to slip became more significant.

Clapeyron's equation, a 3.2% theoretical transformation strain was obtained which was fairly close to the measured value (3.6%). Nevertheless, the aberrance of  $dM_f/d\sigma$  and  $dA_f/d\sigma$  may be understandable if there exist components (such as fine precipitates) that can hinder the transformation significantly. In that case, one may see strain still creeping in at very low temperature at which a vast majority of austenite became martensite ("actual"  $M_f$  temperature was higher), and prolonged strain recovery at high temperature at which only very little austenite still existed ("actual" austenite  $A_f$  temperature was lower).

#### 4.2.4. Discussion on *In-situ* Crystallized Ni-Ti-Hf Films

In this section, as-deposited crystalline Ni-Ti-Hf SMA films that were produced by *in-situ* crystallization are discussed. High transformation temperatures as well as good mechanical properties were obtained. For films having 14.5% hafnium, the transformation temperatures ( $M_p = 135^\circ\text{C}$  and  $A_p = 180^\circ\text{C}$ ) were comparable with those for melt-solidified alloys with similar hafnium composition (Han *et al.*,  $M_p = 170^\circ\text{C}$ ,  $A_p = 235^\circ\text{C}$  for  $\text{Ni}_{49}\text{Ti}_{36}\text{Hf}_{15}$  alloy). The samples had good ductility (up to 10%) and high mechanical strength (Fracture stress over 1800 MPa at room temperature) that promise industrial applications.

For the first time, the mechanical properties of *in-situ* crystallized Ni-Ti-Hf films were studied at different temperatures. A side-by-side comparison was made between Ni-Ti-Hf films and binary Ni-Ti films. In general, the mechanical properties of the ternary films was affected by temperature in a way similar that for binary films. That is, the yield stress of martensite increased as the temperature decreased. The difference between binary and ternary films was that the ternary binary films typically had higher yield stress. In addition, strain-hardening rate for deformation associated with martensite reorientation in the ternary films was typically one order of magnitude higher that that in

the binary films. The strain-hardening rate for strain related to stress-induced martensitic transformation was even lower (0.32 GPa at 75°C). The ternary  $\text{Ni}_{48.9}\text{Ti}_{36.6}\text{Hf}_{14.5}$  films had much higher strain-hardening rate (3.7 ~ 14.2 GPa) in the deformation segment that was supposed to be associated with martensite reorientation or stress induced martensitic transformation. This result suggests that martensite reorientation encountered increasing resistance as deformation proceeded, especially when the deformation was done at temperatures substantially lower than the  $M_s$  temperature. When the stress was high enough, permanent strain resulting from slip was unavoidable. Similar to the results for binary Ni-Ti films, the strain-hardening rate associated with SIM in ternary  $\text{Ni}_{48.9}\text{Ti}_{36.6}\text{Hf}_{14.5}$  films seemed to be lower than that related to martensite reorientation, which suggested that SIM was a better way to obtain transformational strain. This observation was generally in agreement with the result from bulk Ni-Ti-Hf materials [Olier *et al.* 1995].

Shape memory properties were another major topic that was investigated for the *in-situ* crystallized Ni-Ti-Hf SMA films. The evaluation was done by two methods, free recovery method and thermal cycling. In the results obtained by the free-recovery tests, it was found that recovery rate of the strain imparted to martensite  $\text{Ni}_{48.9}\text{Ti}_{36.6}\text{Hf}_{14.5}$  films was higher when the deformation was done at higher temperature (closer to  $A_s$ ). That means more strain was generated from martensite reorientation. However, the strain recovery was never 100%, suggesting slip accompanied martensite reorientation all the time.

The results of SME evaluation using constant-load thermal cycling demonstrated a much better SME than that obtained from free-recovery tests. Nearly 3% of fully recoverable strain was observed at an applied stress of 250 MPa. The discrepancy may arise from the fact that the mechanisms of getting shape-memory strain are different in the two testing methods. Unlike the situation in the free-recovery test where the shape-memory strain resulted from reorientation and/or detwinning of existing martensite variants, the shape memory strain generated by cooling the austenite under stress was due

to the formation of preferred martensite variants that gave maximum strain in the stress direction. Apparently reorientation/detwinning of existing martensite variants may experience considerable lattice resistance so it required high applied stress, which may unavoidably activate other deformation mechanisms such as slip. Therefore, permanent strain may occur at the same time. Transformational strain generated from stressed thermal cycling required much smaller stress. It seemed that 100 MPa applied stress was adequate to affect the formation of martensite variants by SIM, and it was far below the critical stress for martensite variant reorientation. The maximum stress for a full recovery was as high as 250 MPa, indicating thermal cycling under such stress did not activate any deformation mechanisms that produced non-recoverable strain. Comparison between the results of the two SME testing methods suggests that stressed thermal cycling should be the optimal working condition of the Ni-Ti-Hf SMA thin films. However, if the material has to be deformed isothermally, it should take place at temperatures that are best for inducing the formation of preferred martensite variants, which corresponds to the temperature that is just above  $M_s$  temperature with the material still being austenitic.

Another interesting phenomenon worthy attention was that illustrated in Figure 4.17. That is, when Ni-Ti-Hf SMA films were stressed at room temperature (martensite state) and started cycling from there, there was little strain change in the first heating excursion. However, considerable amount of strain, depending on biasing stress, can be generated on cooling. This phenomenon was also related to the fact a strain by martensite reorientation was much harder to achieve than that by SIM. In design of an application, this characteristic of Ni-Ti-Hf SMA films needs to be considered. For example, in an actuator fabricated in a Si-etch process, thin film strip freed from the substrate is most likely under slightly tension at temperatures below  $M_f$  temperature. If one tries to deform the film in order to close a valve, it will need a great deal of stress and a permanent strain will occur. However, instead of stressing the material at room temperature, if one heats the SMA film to austenite then applies a biasing stress, much lower stress will be needed

to get the necessary strain, and because this strain is related to SIM, it will recover when the film is heated back to austenite.

In comparison between Ni-Ti SMA and Ni-Ti-Hf high-temperature SMA, one of the undesirable properties of the ternary material is that its austenite strength is low at high temperature. That accounts for absence of superelasticity in Ni-Ti-Hf high temperature SMA [Olier *et al.* 1995]. However, superelasticity was observed in Ni-Ti-Hf SMA thin films for the first time, even though perfect recovery has not been realized. This may result from high austenite strength of the Ni-Ti-Hf SMA thin film at temperature slightly above  $A_r$  temperature. The strengthening of the material may benefit from the fine-grain microstructure and also from the fact that the materials were made in the form of thin films.

## Chapter 5

### CONCLUSIONS

In this study, Ni-Ti-Hf high-temperature SMA films were produced by both post-annealing method and *in-situ* crystallization. For films crystallized by post-annealing, embrittlement occurred prior to the amorphous-to-crystalline phase transformation, even though the crystallized films still underwent martensitic transformation when the materials reached proper temperature range. By using a high heating rate for crystallization, the embrittlement was evidently alleviated. Rapid thermal annealing, which had ramp heating rate as high as 6000°C/min, produced crystalline films having better shape-memory and mechanical properties than conventional vacuum annealing with much lower ramp heating rate.

*In-situ* crystallized films exhibited much better properties than those produced by RTA treatment for the materials with the similar Hf composition. That was manifested by several facts: First, the transformation temperatures were about 20°C to 50°C higher in *in-situ* crystallized films and the transformation hysteresis was also lower (~45°C for *in-situ* crystallized films versus over 65°C for post-deposition annealed samples). Higher transformation temperatures and lower hysteresis are desired for actuators in MEMS systems. Secondly, the *in-situ* crystallized Ni-Ti-Hf films demonstrated better ductility than the RTA treated samples (~8.2% for *in-situ* crystallized films versus ~5.7% for post-deposition annealed samples at room temperature). Thirdly, the *in-situ* crystallized Ni-Ti-Hf films had larger fully recoverable strain (~2.8% for *in-situ* deposited crystalline films versus ~1.7% for post-deposition annealed samples) and higher maximum stress for perfect strain recovery thermal cycling (~250 MPa for *in-situ* crystallized films versus ~200 MPa for post-deposition annealed samples).

The difference of properties between *in-situ* crystallized samples and RTA treated samples may result from different microstructural characteristics. Both X-ray diffraction spectra and TEM micrograph indicated that the microstructure of RTA treated samples consisted in both martensite in very fine clusters of variants (~50 nm, see Figure 4.15(d)) and B2 phase at room temperature. In contrast, the microstructure of *in-situ* crystallized films was exclusively martensite with fine grain size at ~0.2 micron. While the martensite variant reorientation or the martensite induced by applied stress during a constrained cooling was responsible for the shape memory properties, the untransformed B2 phase in the RTA treated samples was expected to have a negative effect on the recoverable strain of the material. This was because the B2 phase, which did not reorient or transform under applied stress, did not contribute to the formation of a transformation strain. On the contrary, they may resist martensite reorientation or formation of martensite under influence of an applied stress. Therefore, the maximum transformation strain was decreased and higher biasing stress was needed to produce the same amount of transformation strain compared to the situation where fully martensitic microstructure may be obtained.

The transformation temperatures of RTA treated sample were apparently lower than the *in-situ* crystallized films. The reason may be fine grain structure and existence of the untransformed B2 phase in the RTA treated films. Very fine structure in martensites typically decreases the martensitic transformation temperature [Su *et al.* 1994, You *et al.* 1997]. The B2 phase may also suppress the transformation due to interfacial constraint, in the meantime, it is possible the composition of the matrix was altered because of the cubic phases.

In comparison, from the standing point of material properties, *in-situ* crystallization is the process of choice for making Ni-Ti-Hf high temperature SMA films. *In-situ* crystallization may offer advantages in other areas. For example, it is a one-step process, and contamination can be minimized. Also, the stress in the films may be

smaller because intrinsic stress (more likely compressive) and thermal stress (tensile stress for Ni-Ti-Hf on Si or on glass) are cancelled on cooling. However, RTA treatment is a fast process. In addition, the substrate is relatively cool compared to the film due to the unique means of heating in the RTA process. Therefore, thermal damage to the substrate could be minimized if appropriate parameters are selected, even though the film is heated to high temperature during the process.

The major conclusions of this research are highlighted as follows:

1. Two exothermic peaks appeared during isochronal heating of amorphous films prepared by sputtering. The first peak, which occurred at temperatures from 300°C to 450°C at heating rates from 5 °C/min to 40°C/min and had an activation energy of 162 kJ/mol, led to embrittlement of the amorphous films; the second peak, which occurred at temperature between 510°C to 560°C at heating rates from 5°C/min and had an activation energy of 347 kJ/mol, resulted from the amorphous-to-crystalline transformation.
2. Amorphous  $\text{Ni}_{49.1}\text{Ti}_{36.2}\text{Hf}_{14.7}$  films crystallized by conventional vacuum annealing showed martensitic transformation temperatures when cooled down to room temperature. The martensitic transformation temperatures were increased by substituting Hf for Ti but they were considerably lower than those in melt-solidified Ni-Ti-Hf alloys. Heating rate for post-deposition crystallization did not affect the transformation temperatures. However, the enthalpy for martensitic transformation in post-deposition crystallized  $\text{Ni}_{49.1}\text{Ti}_{36.2}\text{Hf}_{14.7}$  films, which in general was smaller than that for crystallized binary Ni-Ti films, increased as the heating rate was increased.

3. The films crystallized by vacuum annealing contained B19' martensite and B2 phases at room temperature even though the  $M_f$  temperature was typically over 80°C. The volume fraction of B2 phase decreased as the heating rate increased. The grain boundaries were irregular compared to classic metallographic microstructure.
4. Films crystallized by rapid thermal anneal at 650°C with a heating rate of 6000°C/min showed improved martensitic transformation characteristics compared to a conventional vacuum anneal that had heating rates from 5°C/min to 40°C/min. The RTA treated  $\text{Ni}_{49.1}\text{Ti}_{36.2}\text{Hf}_{14.7}$  films had room-temperature ductility of 5.8%, fully recoverable strain of 1.7%, recoverable strain of 1.95% and maximum stress for full strain recovery of 200 MPa. The microstructure of RTA treated samples displayed fine grains with a typical size less than 0.05  $\mu\text{m}$ .
5. *In-situ* crystallized  $\text{Ni}_{48.9}\text{Ti}_{36.6}\text{Hf}_{14.5}$  films exhibited better mechanical and shape-memory properties than the RTA treated films. The room-temperature ductility was 8.2% and fracture stress was 1820 MPa. The martensitic transformation temperatures were higher those in the RTA treated samples but still lower than those in melt-solidified alloys having same amount of hafnium addition. *In-situ* crystallized  $\text{Ni}_{48.9}\text{Ti}_{36.6}\text{Hf}_{14.5}$  films had fully recoverable strain of 2.8%, maximum recoverable strain of 3.6% and maximum stress for full strain recovery of 250 MPa.
6. The free-recovery method was used to evaluate shape-memory properties of the *in-situ* crystallized  $\text{Ni}_{48.9}\text{Ti}_{36.6}\text{Hf}_{14.5}$  films. The recovery rate was both pre-strain and temperature dependent, but 100% recovery was never observed. Transformational superelasticity was observed at temperature above  $A_f$  although the isothermal recovery was not perfect.

7. The martensitic transformation temperatures as well as mechanical properties in *in-situ* crystallized Ni-Ti-Hf films were affected by the hafnium composition. As hafnium composition in the films increased from 14.5at.% to 21.4at.%, the transformation temperature increased from 180°C to 245°C for  $A_p$ , and transformation hysteresis increased from 45°C to 63°C. At the same time, room-temperature ductility of the films was reduced from 8.2% to 5.1%.
8. The mechanical properties of as-sputtered crystalline thin film was highly temperature dependent and thermal history dependent. Higher ultimate elongation was obtained around reverse ( $M \rightarrow A$ ) transformation temperatures if the material was heated from martensite, and better ductility was obtained around forward ( $A \rightarrow M$ ) transformation temperatures if the material was cooled down from austenite. The yield stress of martensite decreased at higher temperatures.
9. The room-temperature microstructure of *in-situ* crystallized  $Ni_{48.9}Ti_{36.6}Hf_{14.5}$  films was fully martensitic with typical grain size on the order of 100 nm.. The martensite had a monoclinic structure with lattice parameters of  $a = 2.63 \text{ \AA}$ ,  $b = 4.01 \text{ \AA}$ ,  $c = 4.77 \text{ \AA}$  and  $\beta = 99.1^\circ$ . The microstructure of the RTA treated  $Ni_{49.1}Ti_{36.2}Hf_{14.7}$  films consisted in martensite having the same crystallographic structure as that in *in-situ* crystallized  $Ni_{48.9}Ti_{36.6}Hf_{14.5}$  films and a cubic phase having a lattice parameter  $a = 3.06 \text{ \AA}$ .
10. Considering mechanical properties, transformation temperature and shape memory properties, sputtering at elevated substrate temperature is the method of choice to make high-temperature Ni-Ti-Hf SMA thin films.

## **BIBLIOGRAPHY**

## BIBLIOGRAPHY

- AbuJdom, D.N., Thoma, P.E., Kao, M.-Y. and Angst, D.R., "High Transformation Temperature Shape Memory Alloy", US Patent # 5,114,504, May 19, 1992.
- Adachi, K. and Wayman, C.M., *Metall. Trans.*, **16A**, 1567, 1985.
- Adachi, K., Perkins, J. and Wayman, C.M., *Acta Metall.*, **36**, 1343, 1988.
- Angst, D.R., Thoma, P.E. and Kao, M., *J. de Physique IV*, **5**, pC8-747, 1995.
- Arbuzova, I.A. and Khandros, L.G., *Phys. Met. Metalloved*, **17**, 390, 1964.
- Barborini, E., Pieseri, P., Mutti, S., Milani, P., Biasioli, F., Iannotta, S. and Gialanella, S., *Nanostructured Materials*, **10**, 1023, 1998.
- Barth, E.P., Spaepen, F., Bye, R. and Das, S.K., *Acta Mater.*, **45**, 423, 1997.
- Bendahan, M., Canet, M., Seguin, J.-L. and Carchano, H., *Mater. Sci. & Eng.*, **B34**, 112, 1995.
- Bendahan, M., Seguin, J.-L., Canet, P. and Carchano, H., *Thin Solid Films*, **283**, 61, 1996.
- Besseghini, S., Villa, E. and Tuissi, A., *Mater. Sci. & Eng.*, **A273-275**, 390, 1999.
- Bodin, D., Moine P. and Eymery, J.P., *Nuclear Instruments and Methods in Physics Research, Section B: Beam Interactions with Materials*, **B23**, 337, 1987.
- Buchwitz, M., Adlwarth-Dieball, R. and Ryder, P.L., *Acta Metall. et Mater.*, **41**, 1885, 1993.
- Buehler, W.J. and Gilfrich, J.V. and Wiley, R.C., *J. Appl. Physics*, **34**, 1475, 1963
- Buehler, W.J. and Wang, F.E., *Ocean Eng.*, **1**, 105, 1968.
- Buehler, W.J. and Wiley, R.C., *Naval Ordnance Laboratory Report*, p61-75, 1961.
- Busch J.D. and Johnson, A.D., *IEEE' 90*, 40, 1990.
- Busch, J., Johnson, A.D., Lee, C.H., and Stevenson, D.A., *J. Appl. Physics.*, **68**, p6224, 1990.

- Busch, J.D., Johnson, A.D., Hodgson, D.E., Lee, C.H. and Stevenson, D.A., *Materials Science Forum*, **56-58**, 729, 1990; *J. Appl. Physics*, **68**, 6224, 1990.
- Buschow, K.H.J. and Bekmans, N.M., *J. Appl. Physics*, **50**, 6348, 1979.
- Buschow, K.H.J., *J. Appl. Phys.*, **56**, 304, 1984.
- Cesari, E., Ochin, P., Portier, R., Konomytsev, V., Koval Yu., Pasko, A. and Soolshenko, V., *Mater. Sci. & Eng.*, **A273-273**, 738, 1999.
- Chang, F.C. and Read, T.A., *Trans. AIME*, **49**, 191, 1951.
- Chang, L. and Grummon, D.S., *Materials Research Society Symposium Proceedings*, **246**, p141, Pittsburgh, PA, 1992.
- Chang, L. and Grummon, D.S., *Phil. Mag.*, **A76**, 163, 190, 1997.
- Chang, L., Ph.D. Dissertation, Michigan State University, East Lansing, MI, 1994.
- Chang, L.C. and Read, T.A., *Trans. AIME*, **49**, 191, 1951.
- Chen, H.S., *Mater. Sci. & Eng.*, **25**, 59, 1976.
- Chen, T., *Scripta Metall. et Mater.*, **31**, 1187, 1994.
- Cross, W., Kariotis, A. and Stimler, F., "Nitinol Characterization Study", NASA CR-1433, 1969.
- d'Heurle, F.M., *Metall. Trans.*, **1**, 725, 1970; *Inter. Mat. Rev.*, **A34**, 53, 1989.
- d'Heurle, F.M., Berenbaum, L. and Rosenburg, R., *Trans. AIME*, **242**, 502, 1968.
- Davis, L.A., *Metallic Glasses*, American Society of Metals, Metals Park, Ohio, 1978.
- Delaey, L., van Humbeeck, J., Chandrasekaran, M., Janssen, J., Andrade, A. and Mwamba, N., *Metals Forum*, **4**, 164, 1981.
- Ditman, J.B. and Bergman, L.A., in *Proc. of 2nd Inter Conference on Intelligent Materials*, ed. Rogers C.A. and Wallece, G.G., p450, Virginia, Technical Publishing Co. Inc., 1994.
- Donkersloot, H.C. and van Vucht, J.H.N., *J. of the Less-Common Metals*, **20**, 83, 1970.
- Enami, K., Martynov, V.V., Tomie, T., Khandros, L.G. and Nenno, S., *Trans. Japn. Inst. Metals*, **22**, 357, 1981.

- Filip, P. and Mazanex, K., *Scripta Mater.*, **35**, 349, 1996.
- Fonda, R.W. and Vandermeer R.A., *Phil. Mag. A.*, **76**, 119, 1997.
- Ford, D.S. and White, S.R., *Acta Mater.*, **44**, 2295, 1996.
- Fursenko, A.A., Galjukov, A.O., Makarov, Yu.N., Lutovinov, D.S. and Ramm, M.S., *J. Crystal Growth*, **148**, 155, 1995.
- George, J., *Preparation of Thin Films*, Marcel Dekker Inc., New York, 1992.
- Gisser, K.R.C., Busch, J.D., Johnson, A.D. and Ellis, A.B., *Appl. Physics Lett.*, **61**, 1632, 1992.
- Glezer, A.M., Molotilov, B.V. and Utevsckaya, O.L., *Physics of Metals and Metallography*, **58**, 147, 1984.
- Golberg, D.V., Otsuka, K., Horikawa, H. and Mitose, K., United States Patent #6,641,364, Jun. 24, 1997.
- Golberg, D., Xu, Y., Murakami, Y., Morito, S., Otsuka, K., Ueki, K. and Horikawa, H., *Scripta Metall. et Mater.*, **30**, 1349, 1994.
- Gong, F., Shen, H., Shen, G., Yang, Y., Yang, Z. and Wang, Y., *Shape Memory Materials '94, Proceedings of the International Symposium on Shape Memory Materials*, p272, International Academic Publishers, Beijing, 1994.
- Gruene, R., Oehring, M., Wagner, R. and Haasen, P., *Proceedings of the Fifth International Conference on Rapid Solidification*, p761-765, North-Holland, 1985.
- Grummon D.S. and Gotthardt, R., *Acta Mater.*, **48**, 635, 2000.
- Grummon, D.S., Hou, L., Zhao, Z. and Pence, T.J., *J. de Physique IV, Colloque C8*, 665, 1995.
- Grummon, D.S. and Zhang, J., *Phys. Stat. Sol.*, **186**, 17, 2001.
- Grummon, D.S., Zhang, J. and Pence, T.J., *Mater. Sci. & Eng. A*, **A273-275**, 722, 1999.
- Gu, H.D., You, L., Leung, K.M., Chuang, C.Y., Chan, K.S., and Lai, J.K.L., *Appl. Surface Science*, **127-129**, 579, 1996.
- Gyobu, A., Kawamura, Y., Horikawa, H. and Suburi, T., *Mater. Sci. & Eng.*, **A273-275**, 749, 1999.

- Haasen, P., *J. Non-Crystalline Solids*, **56**, 191, 1983.
- Han, S., Zou, W., Jin, S., Zhang, Z. and Yang, D., *Scripta Metall. et Mater.*, **32**, 1441, 1995.
- Han, X., Zou, W., Wang, R., Zhang, Z. and Yang, D.Z., *Acta Mater.*, **44**, 3711, 1996.
- Han, X.D., Zou, W.H., Wang, R., Zhang, Z., Yang, D.Z. and Wu, K.H., *J. De Physique IV*, **5**, C8-753, 1995.
- Hayashi, S., *Int. Progress in Urethanes*, **6**, 90, 1993.
- Hodgson, D.E. and Brown, J.W., “Using Nitinol Alloys”, Shape Memory Applications, Inc., San Jose, CA, 2000 (SMST-2000).
- Horikoshi, H. and Tamura, N., *Jpn J. Appl. Phys.*, **2**, 328, 1963.
- Hou, L. and Grummon, D.S., *Scripta Mater.*, **33**, 989, 1995.
- Hou, L., Pence, T.J. and Grummon, D.S., *Mat. Res. Soc. Proc.*, **360**, 369, 1995
- Hou, L., *Ph.D. Dissertation*, Michigan State University, East Lansing, MI, 1998.
- Hua, S., Su, C.M., and Wuttig, M., *MRS Symposium Proceedings*, **360**, p375, MRS Society, Pittsburgh, 1995.
- Humbrecht, J.V., *Trans. of ASME*, **121**, 98, 1999.
- Ikuta, K., Fujita, H., Ikeda, M. and Yamashita, S., *Micro Electro Mechanical Systems*, IEEE Proceedings No. 90CH2832-4, p38, IEEE, Piscataway, CA, 1990.
- Inoue, H., Miwa, N. and Inakazu, N., *Acta Mater.*, **44**, 4825, 1996.
- Ishida, A., Sato, M., Takei, A., Kase, Y. and Miyazaki, S., *J. de Physique IV*, **5**, C8-70, 1995.
- Ishida, A., Sato, M., Takei, A. and Miyazaki, S., *Mater. Trans., JIM*, **36**, 1349, 1995.
- Ishida, A., Sato, M., Takei, A., Nomura K. and Miyazaki, S., *Metall. and Mater. Trans*, **27A**, 3753, 1996.
- Ishida, A., Takei, A. and Miyazaki, S., *Thin Solid Films*, **228**, 210, 1993.
- Jardine, A.P., *Materials Research Society Symposium Proceedings*, **271**, p31, MRS, Pittsburgh, PA, 1990.

- Johnson, A.D., *J. MicroMech. Eng.*, **1**, 39, 1991.
- Johnson, A.D., Martynov, V.V. and Minners, R.S., *J. de Physique IV*, **5**, C8-783, 1995.
- Johnson, A.D., Martynov, V.V. and Shahoian, E.J., *Proceedings of SPIE*, **2441**, 165, 1995.
- Johnson, A.D. and Ray, C.A., "Shape memory alloy film actuated microvalve", US Patent #5,325,880, July 5, 1994.
- Kawamura, Y., Gyobu, A, Horikawa, H. and Saburi K., *J. de Physique IV*, **5**, C8-683, 1995; *J. Jap. Inst. of Metals*, **60**, 921, 1996.
- Khachin, V.N., Matveeva, N.A., Sivokha, V.P. and Chernov, D.V., *Doklod. Nauk SSSR*, **257**, 167, 1981.
- Kikuchi, T., Kajiwara, S. and Tomota, Y., *J. Physique IV*, **5**, C8-451, 1995.
- Kim, J.J., Moire, P. and Steveson, D.A., *Scripta Metall.*, **20**, 243, 1986.
- Kim, T., *Ph.D. Dissertation*, University of Maryland, 1994.
- Kim, Y., Katsurai, M. and Fujita, H., *Sensor and Actuator*, **20**, 33, 1989.
- Kim, Y.D. and Wayman, C.M., *Metall. Trans.*, **23A**, 2981, 1992.
- Kinuma, R., Matsumoto, M. and Honma, T., *Spring Meeting of Japan Institute of Metals*, Sedai, p221, 1986.
- Kissinger, H.E., *Anal. Chem.*, **29**, 1702, 1957.
- Knowles, K.M. and Smith, D.A., *Acta Metall.*, **29**, 101, 1981.
- Koval, Yu.N., Firstov, G.S. and Kotko, A.V., *Scripta Met. et Mat.*, **27**, 1611, 1992.
- Krulevitch, P., Lee, A. P., Ramsey, P. B., Trevino, J. C., Hamilton, J. and Northrup, M. A., *J. Microelectromechanical Systems*, **5**, 270, 1996.
- Krulevitch, P., Ramsey, P.B., Makowiecki, Lee, A.P., Northrup, M.A. and Johnson, G.C., *Thin Solid Films*, **274**, 101, 1996.
- Kuribayashi K., Yoshitake, M. and Ogawa, S., IEEE, p217, 1990.
- Lapin, V.B., Egorushkin, V.E., Shabalovshaya, S.A. and Ivanova, O.P., *Solid State Communications*, **73**, 471, 1990.

- Lee, A., Dino, R.C., Krulecitch, A.P., Lehew, S., Trwvino, J. and Northrup, M.A., *8th Int. Conf. on Solid-State Sensors and Actuators and Eurosensors IX*, Stockholm, p368, 1995.
- Lee, J., M.S. Thesis, Michigan State University, 1994.
- Li, D.Y. and Chen, L., *Acta Mater*, **45**, 471, 1997.
- Li, J.M., Quan, M.X. and Hu, Z.Q., *J. Mater. Sci. Lett.*, **16**, 921, 1997.
- Lin, H.C., Wu, S.K. and Chang, Y.C., in *Shape Memory Materials '94*, ed. Chu Y. and Tu, H., International Academic Publishers, Beijing, 1994.
- Lin, H.C., Wu, S.K. and Lin, J.C., *Materials Chemistry and Physics*, **37**, 184, 1994.
- Lindquist, P., Ph.D. Dissertation, University of Illinois, 1978.
- Lindquist, P. and Wayman, C.M., in "*Engineering Aspects of Shape Memory Alloys*", eds. Duerig T.W., Melton K.N., Stochel D. and Wayman C.M., Butterworth-Heinemann Ltd., Boston, 1990.
- Ling, C.H. and Kaplow, R., *Metall Trans*, **A11**, 77, 1981.
- Liu, Y. and McCormick, P.O., *Acta Metall. et Mater.*, **38**, 1321, 1990; *Materials Transactions, JIM*, **37**, 691, 1996.
- Lo, Y.C. and Wayman, C.M., *Scripta Metall. et Mater.*, **27**, 1097, 1992.
- Lo, Y.C., Wu, S.K. and Wayman, C.M., *Scripta Metall. et Mater*, **24**, 1571, 1990.
- Loirat, Y., Bocquet, J.L. and Limoge, Y., *J. Non-Crystalline Solids*, **265**, 252, 2000.
- Lotkov, A.I., Grishkov, V.N. and Fadin, V.V., *Phys Stat Sol*, **a(70)**, 513, 1982.
- Lu, S., in *Engineering Aspects of Shape Memory Alloys*, eds. Duerig, T.W., Melton, K.N., Stockel, D., and Wayman, C.M., Butterworth-Heinemann Ltd., Boston, 1990.
- Madsen, J.S. and Jardine, A.P., *MRS Proceedings*, **308**, 45, 1993.
- Massalski, T.B., (ed), *Binary Alloy Phase Diagrams*, **2**, p1768, American Metals Society, Metal Park, Ohio, 1987.
- Mathews, S.A., Wuttig, M. and Su., Q., *Metall. and Mater. Trans.*, **27A**, 2859, 1996.
- Matsumoto, O., Miyazaki, S., Otuka, K. and Tamira, H., *Acta Metall.*, **35**, 2137, 1987.

- Melton, K.N., *Proc. Inter. Conference on Martensitic Transformation*, p1054, 1986.
- Mercado, P.G. and Jardine A.P., *Proceedings of SPIE*, **2441**, 185, 1995.
- Mercier, O. and Melton, K.N., *Metall. Trans.*, **A10**, 387, 1979.
- Miura, S., Meada, S. and Nakanishi, N., *Phil. Mag.* **30**, 565, 1974.
- Miyazaki, S. and Ishida, A., *Mater. Trans., JIM*, **35**, 14, 1994; *Mater. Sci. & Eng.*, **A273-275**, 754, 1999.
- Miyazaki, S. and Otsuka, K., *Metall. Trans.*, **A17**, 53, 1986; *ISIJ Int.*, **29**, 353, 1989.
- Miyazaki, S., Hashinoga, T., Yumikura, K., Hirikawa, H., Ueki, T. and Ishida, A., *Proceedings of SPIE*, **2441**, 156, 1995.
- Miyazaki, S., Imai, T., Otsuka, K. and Suzuki, Y., *Scripta Metall.*, **15**, 853, 1981.
- Miyazaki, S., Nomura, K. and Ishida, A., *J. de Physique IV*, **5**, C8-677, 1995.
- Miyazaki, S., Sugaya, Y. and Otsuka, K., *MRS International Meeting on Advanced Materials*, **9**, 251, 1989.
- Moberly, W.J. and Melton, K.N., in *Engineering Aspects of Shape Memory Alloys*, eds. Duerig, T.W., Melton, K.N., Stockel, D., and Wayman, C.M., Butterworth-Heinemann Ltd., Boston, p46, 1990.
- Mrualeedharan, R.V., *Phy. Stat. Sol. (A) Appl. Research*, **125**, 83, 1991.
- Muddle, B.C. and Traill, R.M., in *Shape Memory Materials '94*, ed. Chu Y. and Tu, H., p689, International Academic Publishers, Beijing, 1994.
- Mueller, M.H. and Knott, H.W., *Trans. of the Metall. Society of AIME*, **227**, 674, 1963.
- Mulder, J.H., "Investigation of High Temperature Shape Memory Alloys from the Ni-Ti-Zr and Ni-Ti-Hf systems", Ph.D. thesis, Univ. Twente, Netherlands, 1995.
- Nakata, Y., Tadaki, T., Sakamoto, H., Tanaka, A. and Shimizu, K., *J. de Physique IV*, **5**, C8-671, 1995.
- Niikura, A., Tsai, A.P., Inoue, A. and Masumoto, T., *J. Non-Crystalline Solids*, **159**, 229, 1993.
- Nishida, M. and Honma, T., *Scripta Metall.*, **18**, 1293, 1984.
- Nishida, M. and Wayman, C. M., *Mater. Sci. & Eng.*, **93**, 191, 1987.

- Nishida, M., Wayman, C.M. and Honma, T., *Metall. Trans.*, **A17**, 1505, 1986; *Metall. Trans.*, **A18**, 785, 1987.
- Nishida, M., Wayman, C.M., Kainuma, R. and Honma, T., *Scripta Metall.*, **20**, 86, 899, 1986.
- Ogawa, K., Sato, K. and Miyazaki, S., *Metall. and Mater. Trans. A*, **28A**, 1985, 1997.
- Olier, P., Brachet, J.C., Bechade, J.L., Foucher, C. and Guenin, G., *Journal de Physique IV*, **5**, C8-741, 1995.
- Olson, R.R., King, M.E. and Wehner, G.K., *J. Appl. Physics*, **50**, 3677, 1979.
- Otsuka, K. and Shimizu, K., *Scripta Metall.*, **11**, 757, 1972; *Int. Met. Rev.*, **31**, 93, 1986.
- Otsuka, K., Oda, K., Ueno, Y. and Piao, M., *Scripta Metall. et Mater.*, **29**, 1355, 1993.
- Otsuka, K., Sawamura, T. and Shimizu, K., *Phys. Stat. Sol.*, **A5**, 457, 1971.
- Otsuka, K., in *Engineering Aspects of Shape Memory Alloys*, eds. Duerig, T.W., Melton, K.N., Stockel, D., and Wayman, C.M., Butterworth-Heinemann Ltd., Boston, 1990
- Perkins, J. and Sponholz, R.O., *Metall. Trans.*, **15A**, 313, 1984.
- Potapov, P.L., Poliakova, N.A. and Udovenko, V.A., *Scripta Mater.*, **35**, 423, 1996.
- Potapov, P.L., Shelyakov A.V., Gulyaev, A.A., Svistunova, E.L., Matveeva, N.M. and Hodgson, D., *Mater. Lett.*, **32**, 247, 1997.
- Pu, Z., Tseng, H.K., and Wu, K.H., *Proceedings of SPIE, Smart Materials*, **2189**, 289, 1994; *Proceeding of SPIE*, **2441**, 171, 1995.
- Qu, Z. and Xie, T., *Mater. Sci. & Eng.*, **A134**, 955, 1991.
- Quandt, E., Halene, C., Holleck, H., Feit, K., Kohl, M. and Schloßmacher, P., *Transducer'95 Euroensors*, 202, 1995.
- Quandt, E., Halene, C., Holleck, H., Feit, K., Kohl, M. and Schloßmacher, P., *the 8th Inter Conf on Solid-State Sensors and Actuators and Euroensors IX*, Stockholm, 282-PA11, 1995.
- Rai, A.K. and Bhaattacharya, R.S., *Mater. Sci. & Eng.*, **85**, 137, 1987.
- Ray, C.A., Sloan, C.L., Johnson, A.D., Busch, J.D. and Petty, B.R., *MRS proceedings*, **276**, 161, 1992.

Reed-Hill, R.E., and Abbaschian, R., *Physical Metallurgy Principles*, 3rd edition, PWS-KENT Publishing Company, Boston, 1992.

Rösner, H., Shelyakov, A.V., Glezer, A.M., Feit, K. and Schloßmacher, P., *Mater. Sci. & Eng.*, A273-275, 733, 1999.

Rostoker, W., *Trans. AIME*, **194**, 209, 1952.

Russell, S.M., Hodgson, D.E. and Basin F., in *Proceedings of 2<sup>nd</sup> International Conference on Shape Memory and Superelastic Technologies*, eds. Pelton, A., Hodgson, D., Russell S. and Duerig T., Pacific Grove, CA, p429, 1997.

Saburi, T. and Nenno, S., *Scripta Metall.*, **8**, 1362, 1974; in *Proceedings of the International Conference on Solid-State Phase Transformations*, eds. Aaronson, H.I., Langhlin, D.E., Sekera, R.F. and Wayman, C.M., p1455, The Metall. Soc. AIME, New York, New York, 1981.

Saburi, T., Nenno, S. and Fukuda, T., *J. the Less-Common Metals*, **125**, 157, 1986.

Sakamoto, H., Otsuka, K. and Shimizu, K., *Scripta Metall.*, **11**, 607, 1977.

Schloßmacher, P., *Materials Letters*, **31**, 119, 1997.

Schroeder, T.A., and Wayman, C.M., *Scripta Metall.*, **11**, 225, 1977; *Acta Metall.*, **27**, 405, 1979.

Shimizu, S., Xu, Y., Okunishi, E., Tanaka, S., Otsuka, K. and Mitose, K., *Mater. Lett.*, **34**, 23, 1998.

Sivokha, V.P., Savvinov, A.S., Voronin, V.P. and Khachin, V.N., *Phys. Met. Metall.*, **56**, 112, 1983.

Smialek, J.L. and Hehemann, R.F., *Metall. Trans.*, **4A**, 1571, 1973.

Sonius, S.E., Thijsse, B.J. and van den Beukel, A., *Scripta Metall.*, **17**, 545, 1983.

Su, Q., Hua, S.Z. and Wuttig, M., *Proceedings of SPIE*, **2189**, 409, 1994.

Su, Q., Kim, T., Zheng, Y. and Wuttig, M., *Proceedings of SPIE*, **2441**, 179, 1995.

Sun, L. and Wu, K.H., *Proceedings of SPIE*, **2189**, 298, 1994.

Suzuki, Y., Xu, Y., Morito, S., Otsuka, K. and Mitose, K., *Mater. Lett.*, **36**, 85, 1998.

Takahara, Y., *Mater. Sci. & Eng. A*, **A231**, 128, 1997.

Thoma, P., Blok, A. and Kao, M., in *Fundamental Aspects and Applications of SMA*, ed. Liu, C.T., Kunsmann, H., Otsuka, K. and Wuttig, M., *MRS proceedings*, **321**, 1991.

Thoma, P.E. and Boehm, J. J., *Mater. Sci. & Eng.*, **A273-275**, 385, 1999.

Thoma, P.E., AbuJdom, D.N. and Fariabi, S., US Patent #4,881,981, 1989.

Thornton, J.A. and Hoffman, D.W., *J. Vac. Sci. Technol.*, **A3**, 576, 1985.

Thornton, J.A., *Ann. Rev. of Mater. Sci.*, **7**, 239, 1977.

Tsuchiya, K. and Davies, S.T., *Nanotechnology*, **9**, 67, 1998.

Tuominen S.M. and Biermann R.J., *J. Metals*, February Issue, 32, 1998.

Ullakko, K., Huang, J.K., Kokorin, V.V. and O'Handley, R.C., *Scripta Mater*, **36**, 1133, 1997.

van den Beukel, A. and Huizer, E., *Scripta Metall.*, **19**, 1327, 1985.

van den Beukel, A., *Rapidly Solidified Materials*, Proceedings of an International Conference, San Diego, CA, USA, p193, ASM, Metals Park, Ohio, 1985.

van Vucht, J.H.N., *J. the Less-Common Metals*, **11**, 308, 1966.

Walker, J.A., Gabriel, K.J. and Mehaegany, M., *5th Int. Conf. on Solid State Sensors & Actuators*, Montreanx, Swiss, p123, 1989; *Sensors & Actuators*, **A21-A23**, p243, 1990.

Wang, L., Ma, L., Chen, M., Kimura, H. and Inoue, A., *Mater. Sci. & Eng.*, **A325**, 182, 2002.

Wang, Y.Q., Cai, W., Zhu, W.H. and Zhao, L.C., *Proceedings of the 2<sup>nd</sup> Int. Conf. on Shape Memory and Superelastic Technologies*, eds. Pelton, A., Hodgson, D., Russel, S. and Duerig, T., Pacific Grove, CA, USA, p77, 1997.

Wang, Z., Cai, W., Gao, Z.Y., Huang, L.Q. and Zhao, L.C., *Proceedings of the 2<sup>nd</sup> Int. Conf. on Shape Memory and Superelastic Technologies*, eds. Pelton, A., Hodgson, D., Russel, S. and Duerig, T., Pacific Grove, CA, USA, p113, 1997.

Wasilewski, R., *Scripta Metall.*, **4**, 127, 1971; *NASA Technical Report*, 1972.

Wasilewski, R., Betler, S.R., Hanlon, J.E. and Worden D., *Metall. Trans.*, **2**, 229, 1971.

Wayman, C.M. and Duerig, T.W., in “*Engineering Aspects of Shape Memory Alloys*”, eds. Duerig T.W., Melton K.N., Stochel D. and Wayman C.M., Butterworth-Heinemann Ltd., Boston, 1990.

Wayman, C.M., *The Int. Symp. on Shape Memory Alloys*, ed. Chu, Y.Y., Guilin, China, p59, 1986; *Progress in Materials Sciences*, **36**, 203, 1992.

Winzek, B. and Quandt, E., *Z. Metallkd.*, **90**, 10, 1999.

Wollants, P., DeBonte M. and Roos, J.R., *Z. Metallkd.*, **70**, 113, 1979.

Wollants, P., Roos, J.R. and Delaey L., *Progress in Materials Science*, **37**, 227, 1993.

Wu, K.H. and Ma, J.L., *SMST Proceedings*, 2000.

Wu, K.H., Liu, Y.Q., March, M. and Tseng, H.K., *Proceedings of SPIE*, **2198**, 306, 1994.

Wu, S.K. and Wayman, C.M., *Metallography*, **20**, 359, 1987; *Acta Metall.*, **37**, 2085, 1989.

Wu, S.K., Khachaturyan, A.G. and Wayman, C.M., *Acta Metall.*, **36**, 2065, 1988.

Wu, S.K., Lin, H.C. and Chou, T.S., *Acta Metall. et Mater.*, **38**, 95, 1990.

Wu, T.W. and Spaepen, F., *Acta Metall.*, **33**, 2185, 1985; *Phil. Mag.*, **B61**, 739, 1990.

Xie, C., Zhao, L. and Lei, T., *Scripta Metall.*, **24**, 1753, 1990.

Xie, C., Zhao, L., Duerig, T.W. and Wayman, C.M., *Scripta Metall.*, **24**, 1807, 1990.

Xu, Y., Shimizu, S., Suzuki, Y., Otsuka, K., Ueki, T. and Mitose K., *Acta Mater.*, **45**, 1503, 1997.

Yamasaki, T. and Ogino, Y., *Journal of Jap. Inst. of Metals*, **50**, 595, 1986.

Yang J.H. and Wayman C.M., *Materials Lett.*, **16**, 254, 1993.

Yang, W.S. and Mikkola, D.E., *Scripta Metall. et Mater.*, **28**, 161, 1993.

Yawny, A.A., Sade, M. and Lovey, M., *Materials Research Society Symposium Proceeding*, **459**, p369, MRS, Pittsburgh, PA, 1997; *Mater. Sci. & Eng.*, **A273-275**, 789, 1999.

Yi, H.C., Moore, J.J. and Petric, A., *Metall. Trans. A*, **23A**, 59, 1992.

You, L., Chung, C.Y., Han, X.D. and Gu, H.D., *Proceedings of the 2<sup>nd</sup> International Conference on Shape Memory and Superelastic Technologies*, Asilomar Conference Center, eds. Pelton, A., Hodgson, D., Russel, S. and Duerig, T., Pacific Grove, CA, USA, 189, 1997

Yurko, G.A., Barton, J.W. and Parr, J.G., *Acta Cryst.*, **12**, 909, 1959.

Zhang, C., Zhao, L, Duerig, T.W. and Wayman, C.M., *Scripta Metall.*, **24**, 1807, 1990.

Zhang, J., M.S. Thesis, Michigan State University, East Lansing, MI, 1997.

Zhang, J. and Grummon, D.S., *Mat. Res. Soc. Symp. Proc.*, **459**, 281, 1997.

Zhang, J. and Grummon, D.S., unpublished work, Michigan State University, 1998.

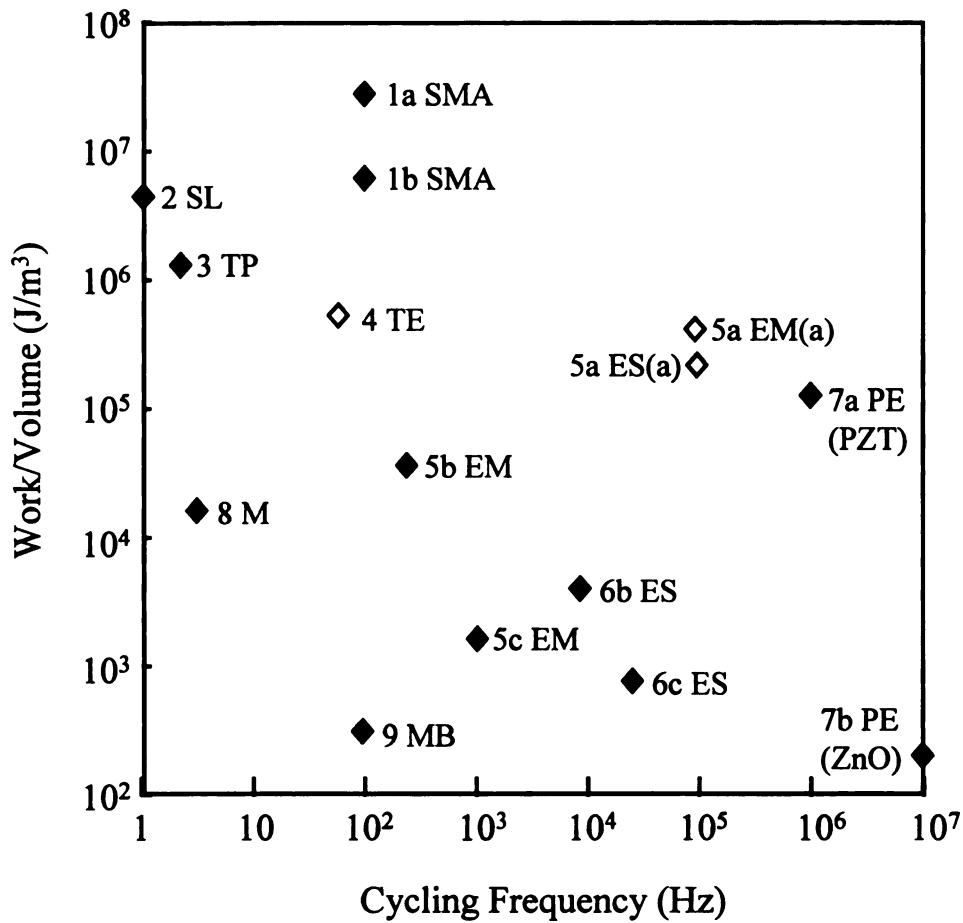


Figure 1.1. Work per volume versus cycling frequency for various microactuator.

1a: Ni-Ti SMA with the maximum one-time output ( $\sigma = 500$  MPa,  $\epsilon = 5\%$ );

1b: Ni-Ti SMA with thousand of cycles ( $\sigma = 300$  MPa,  $\epsilon = 2\%$ );

2: Solid-liquid phase change (SL);

3: Thermo-pneumatic (TP);

4: Thermal expansion (TE) (nickel on silicon);

5: Electro-magnetic (EM);

6: Electrostatic (ES);

7: Piezoelectric (PE) (PZT);

8: Muscle (M);

9: Microbubble (MB).

◇: ideal value; ◆: measured value [Kruevitch *et al.* 1996].

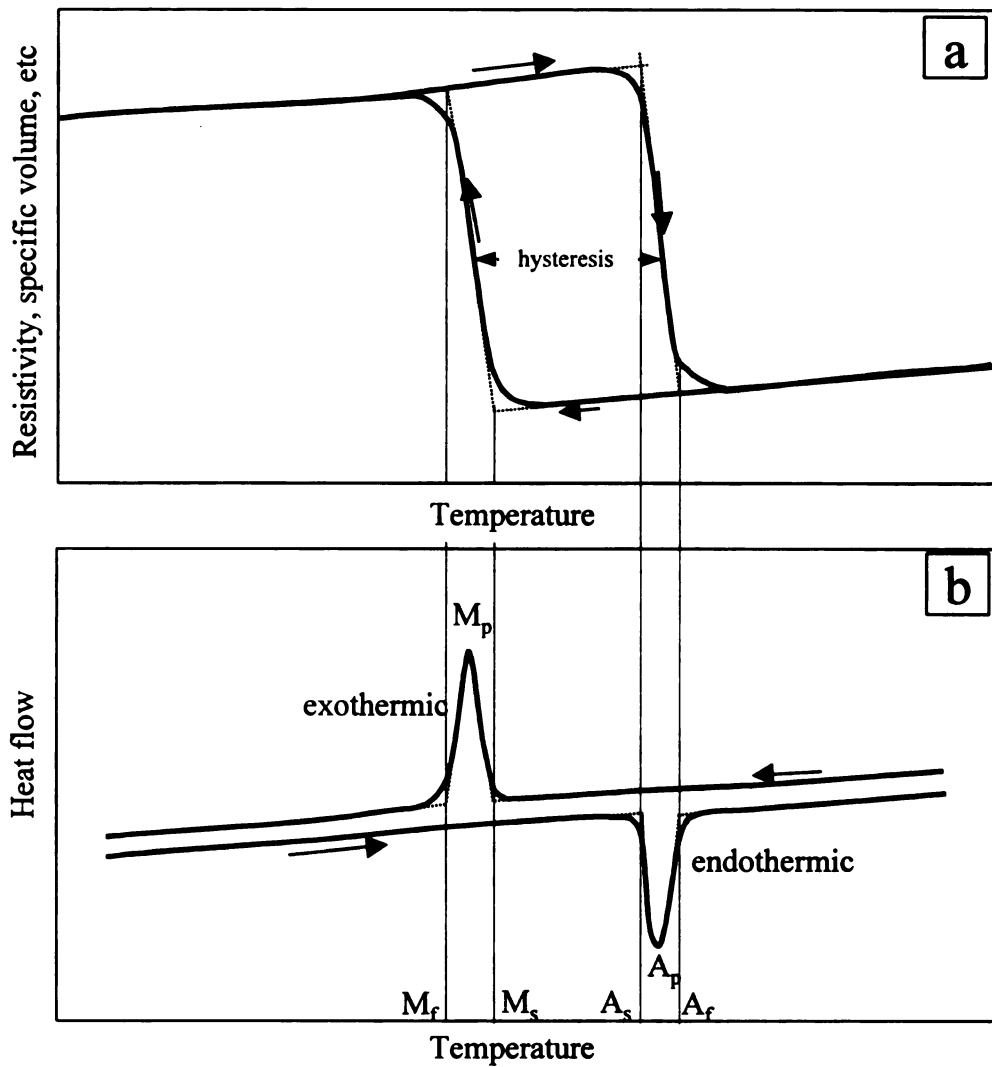


Figure 2.1. A schematic showing physical property changes (a) and endothermic/exothermic effects (b) during reversible martensitic phase transformation. Transformation temperatures are determined by the tangent - intercept method.

$M_s$ : martensite start temperature;  $M_f$ : martensite finish temperature;

$A_s$ : austenite start temperature;  $A_f$ : austenite finish temperature;

$M_p$ : martensite peak temperature;  $A_p$ : austenite peak temperature.

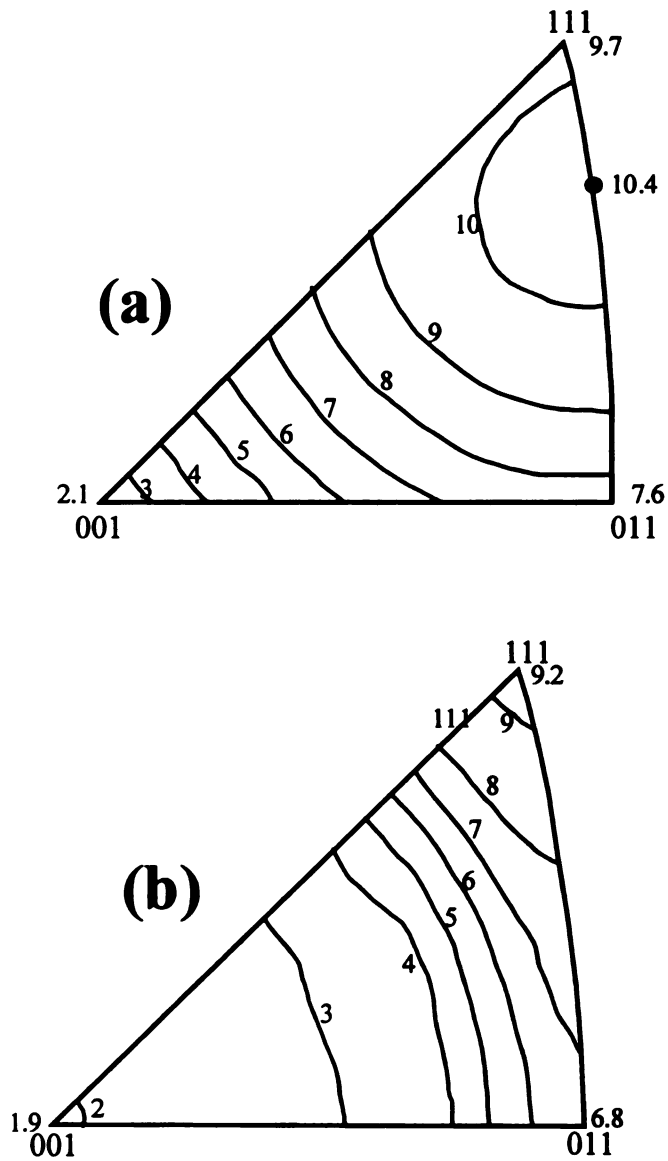


Figure 2.2. Theoretical recoverable strain of single-crystal Ni-Ti SMA as functions of crystal direction developed by (a) Saburi *et al.* [1981], (b) Inoue *et al.* [1996].

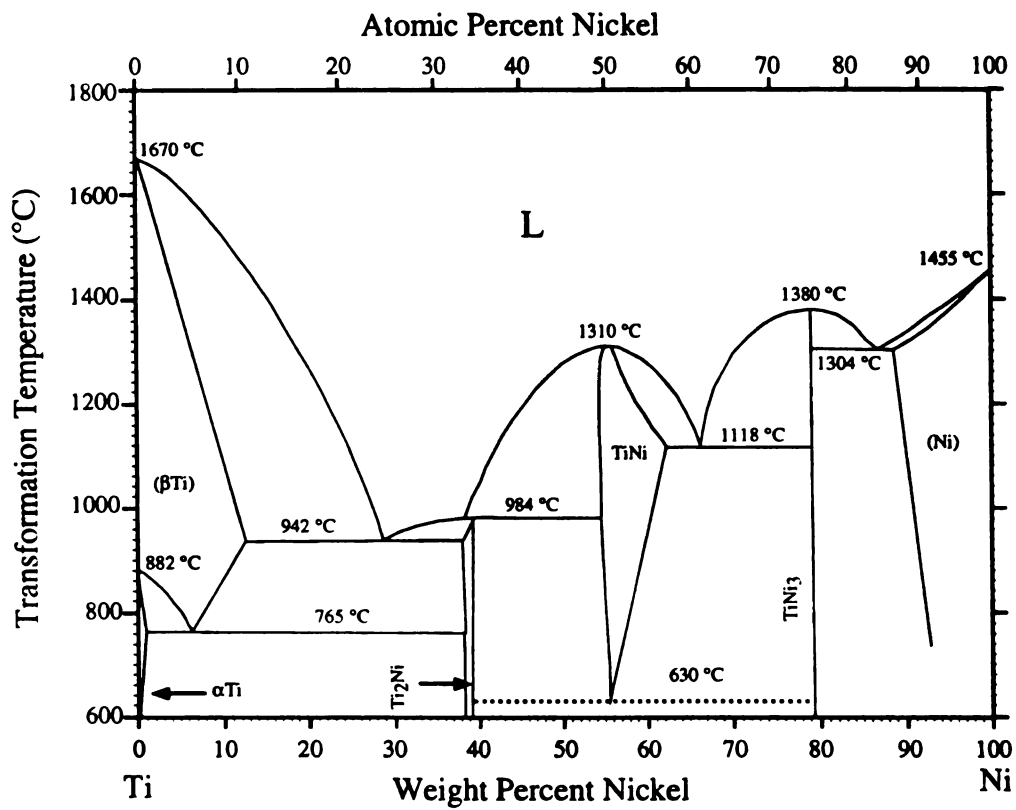


Figure 2.3. Equilibrium phase diagram of Ti-Ni alloy [Massalski 1987].

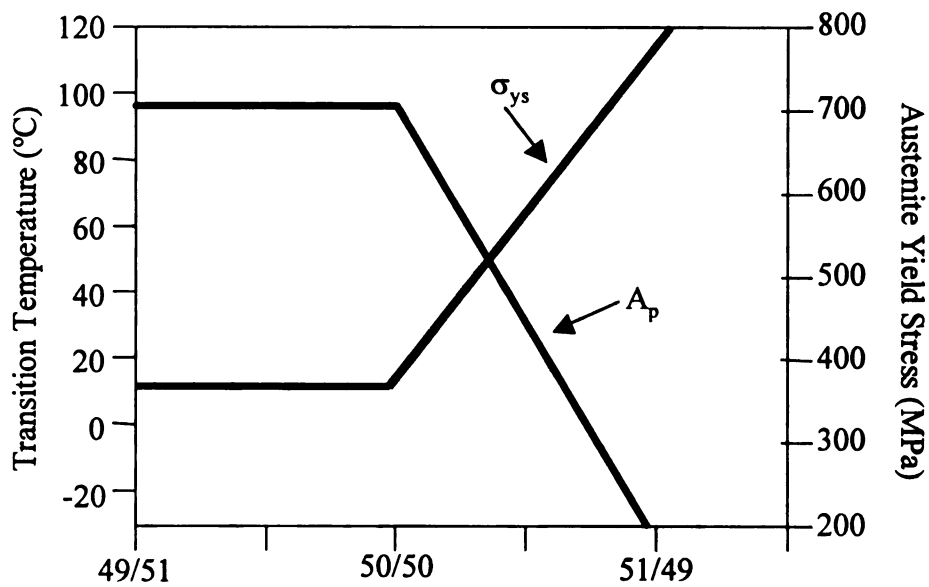


Figure 2.4. Schematic showing the dependence of austenite yield stress and reverse transformation peak temperature of Ni-Ti alloy on the composition of the material [Hodgson and Brown [2000]].

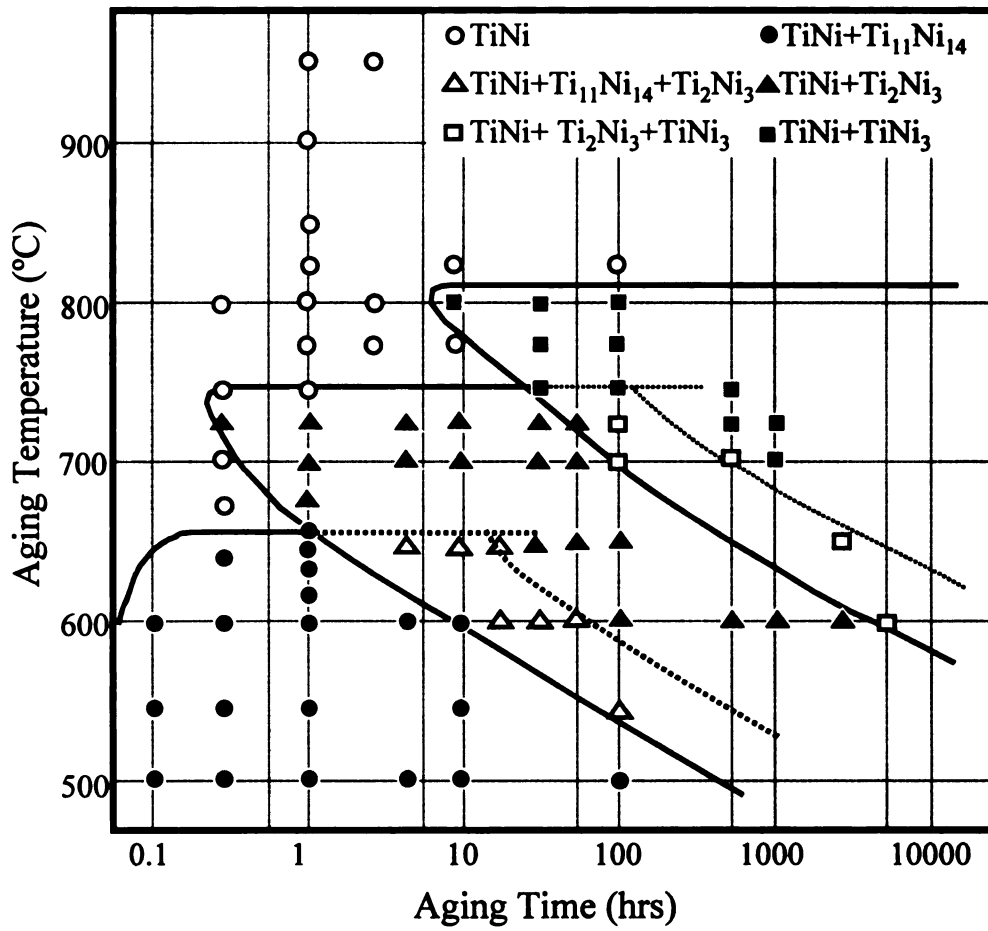


Figure 2.5. Isothermal time-temperature-transformation (TTT) diagram for Ti-52at.%Ni alloy [Nishida *et al.* 1986].

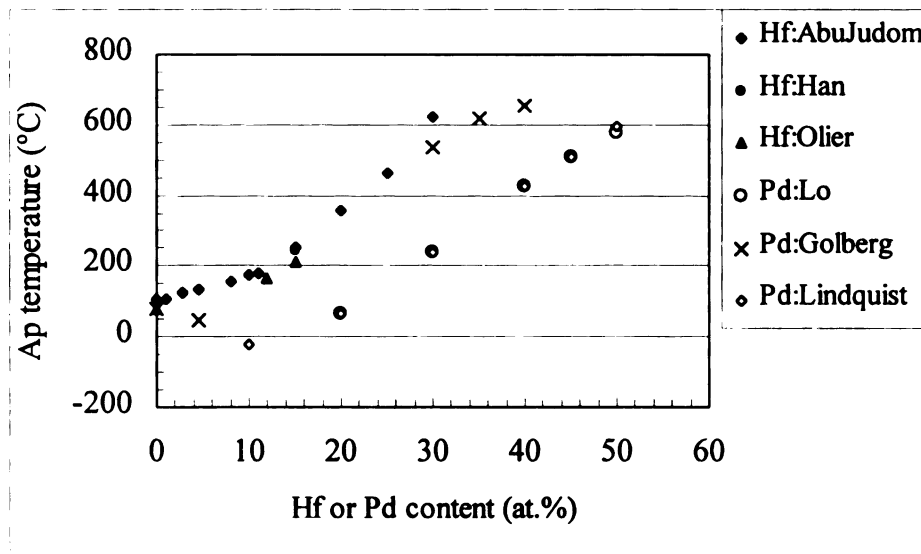


Figure 2.6. Effect of Pd and Hf composition on reverse martensitic transformation temperature of NiTi-base ternary alloys summarized from the literature.

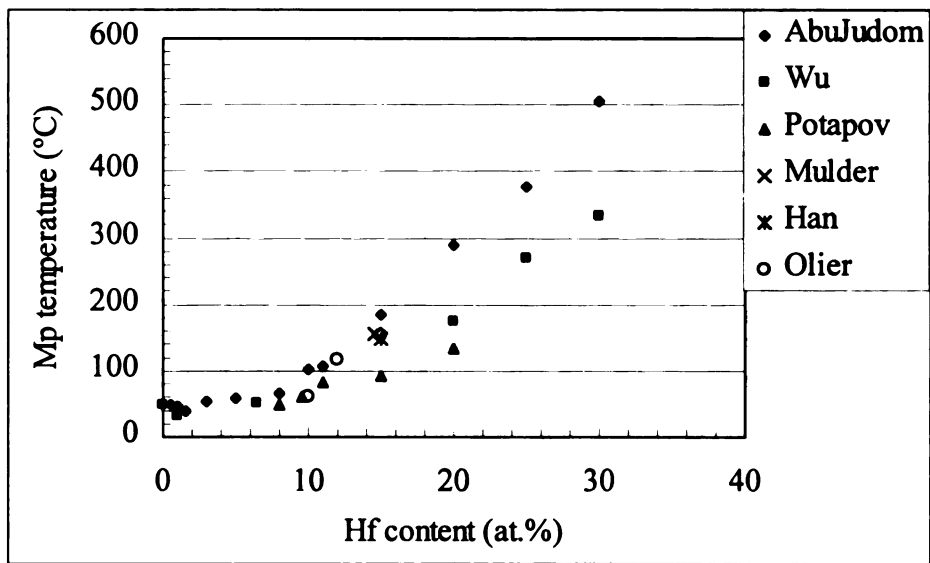


Figure 2.7. Effect of Hf composition on transformation temperature of Ni-Ti-Hf alloys summarized from the literature.

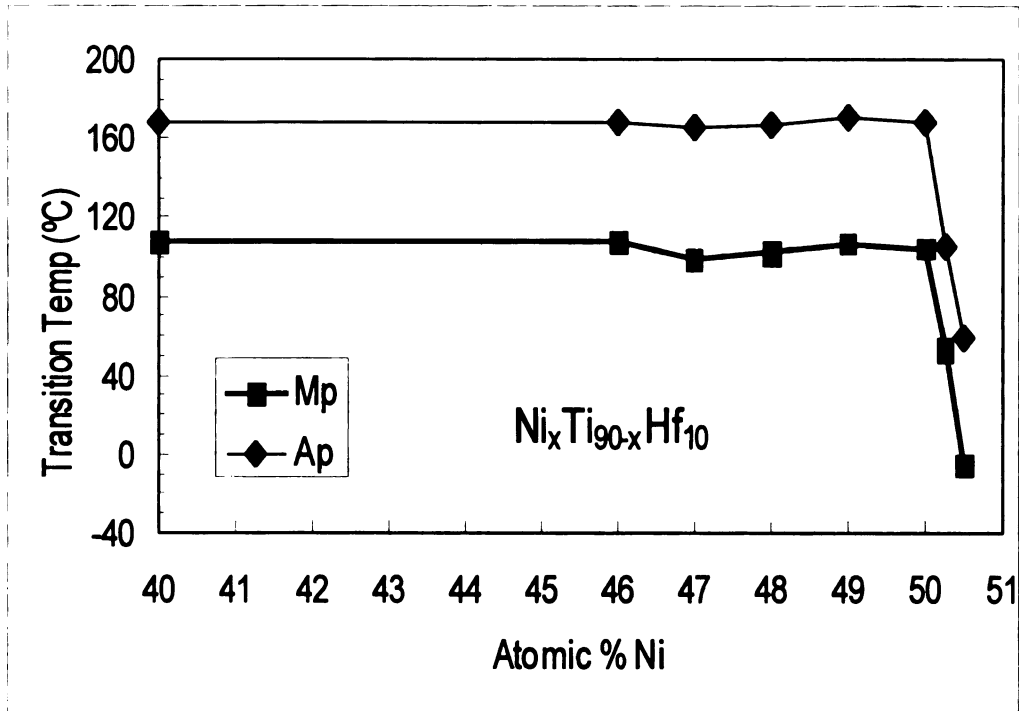


Figure 2.8. Effect of Ni composition on the transformation temperatures of Ni-Ti-Hf shape memory alloy [Augst *et al.* 1995].

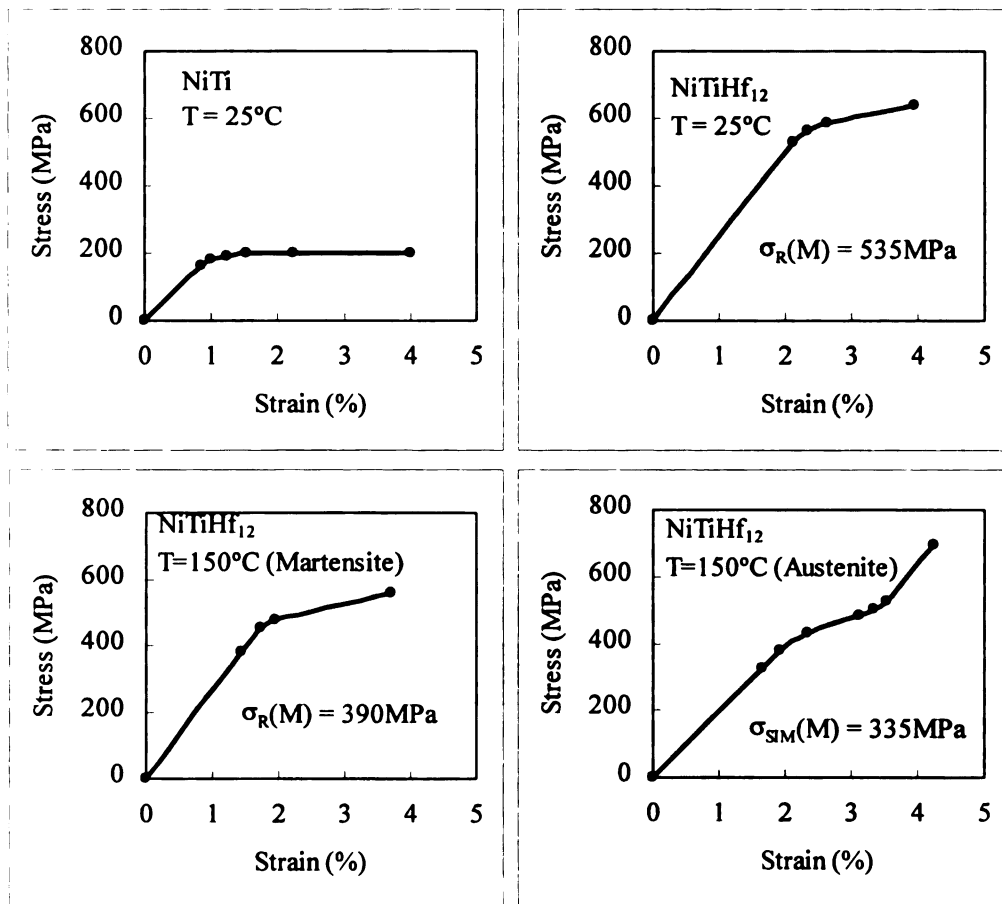


Figure 2.9. Deformation Behavior of Ni-Ti-Hf alloys at different test temperatures [ Olier *et al.* 1995].

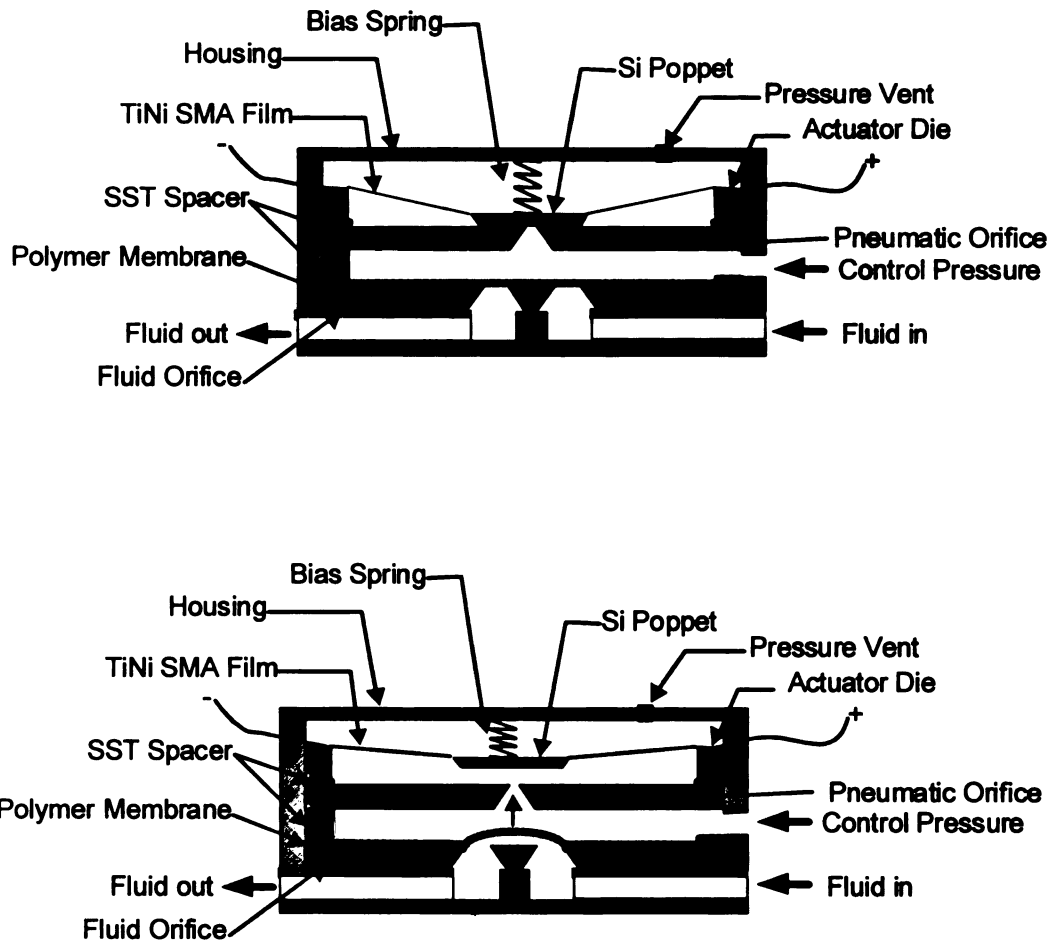


Figure 2.10. Structure of Si-based microvalve actuated using SMA Thin film.  
 Upper: close position when the SMA film is powered off;  
 Lower: open position when the SMA film is powered on.  
 [Johnson *et al.* 1994].

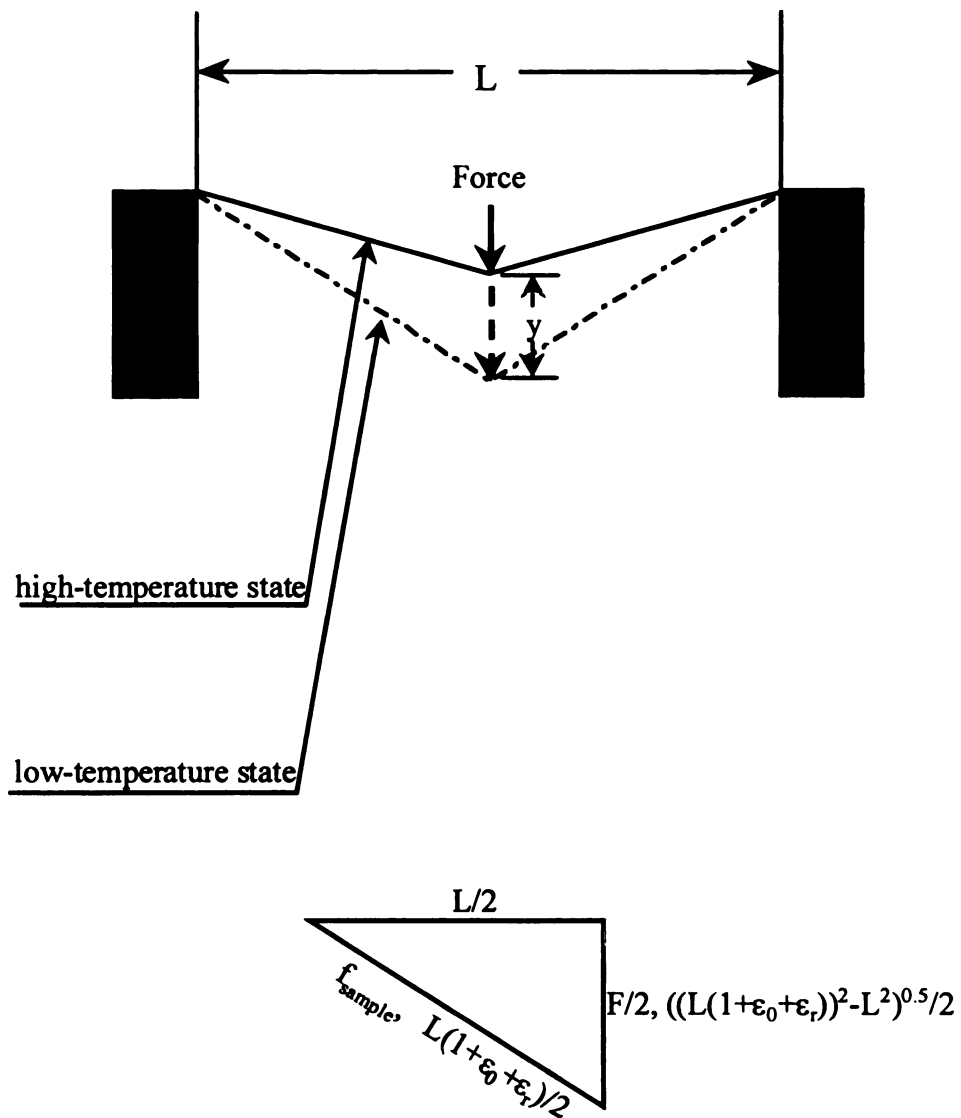


Figure 2.11. Schematic showing realization of vertical cyclic displacement from a horizontal SMA component under an applied force. The stress may also be calculated using similar triangular principle.

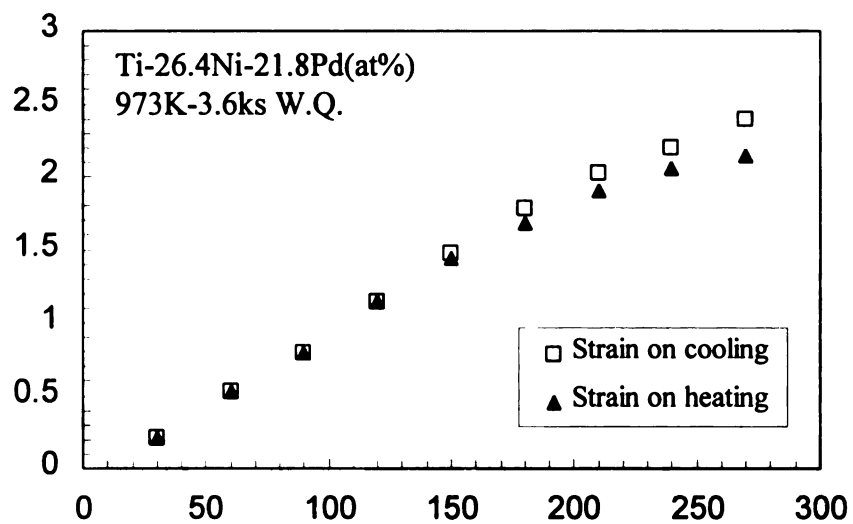


Figure 2.12. Shape-memory properties of sputtered Ni-Ti-Pd SMA thin films during thermal cycles under different applies stresses [Miyazaki *et al.* 1995].

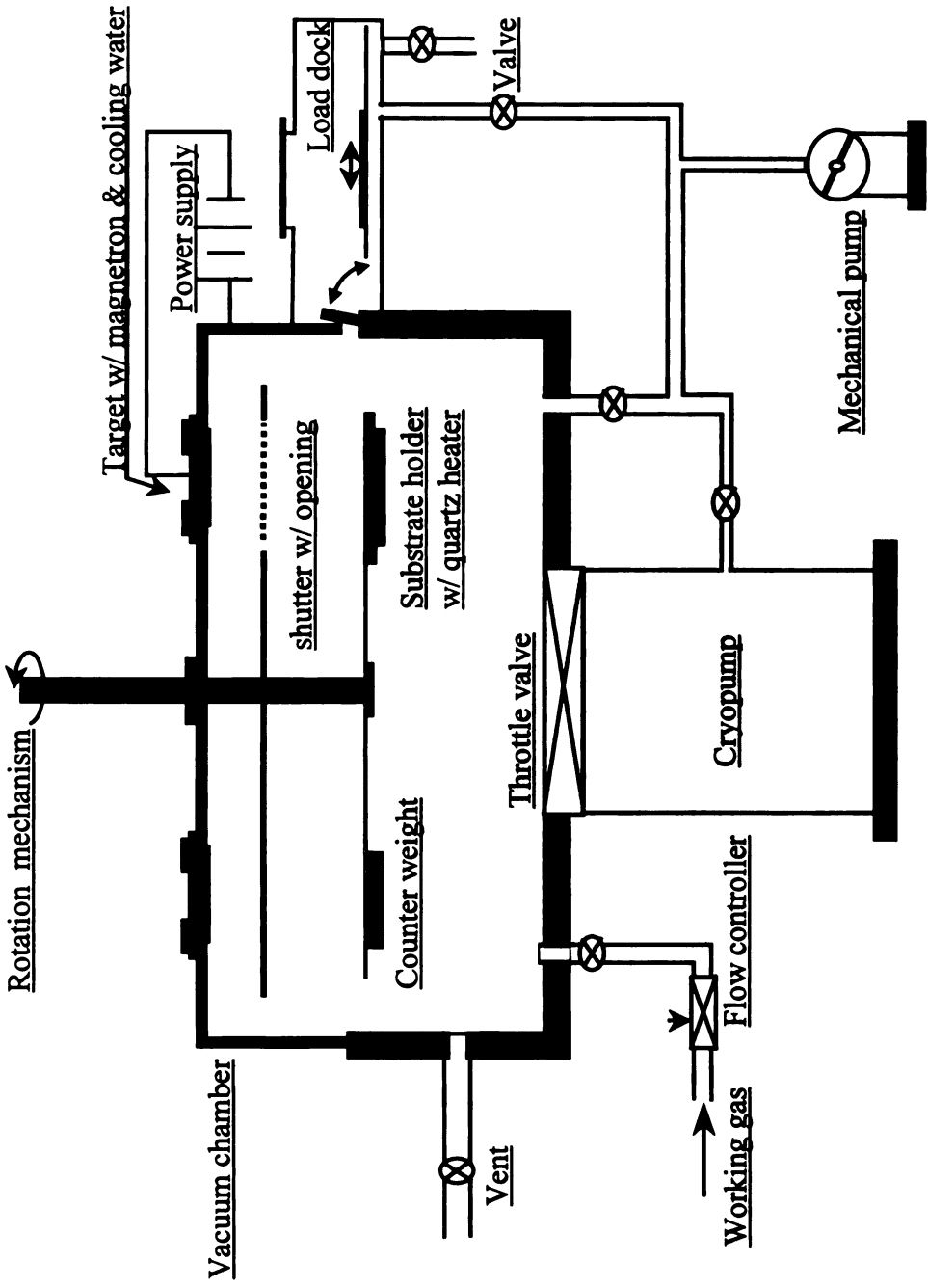


Figure 3.1 Schematic of the sputtering unit for Ni-Ti-Hf SMA film deposition.

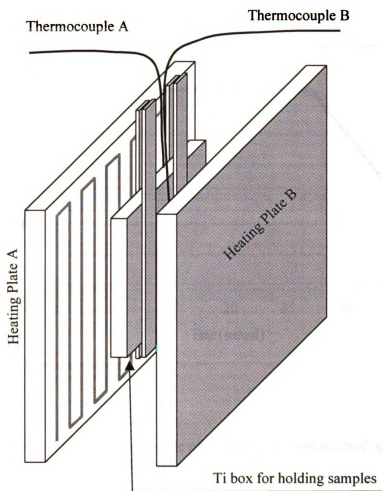


Figure 3.2. Schematic of apparatus for conducting heating treatment for Ni-Ti-Hf thin film.

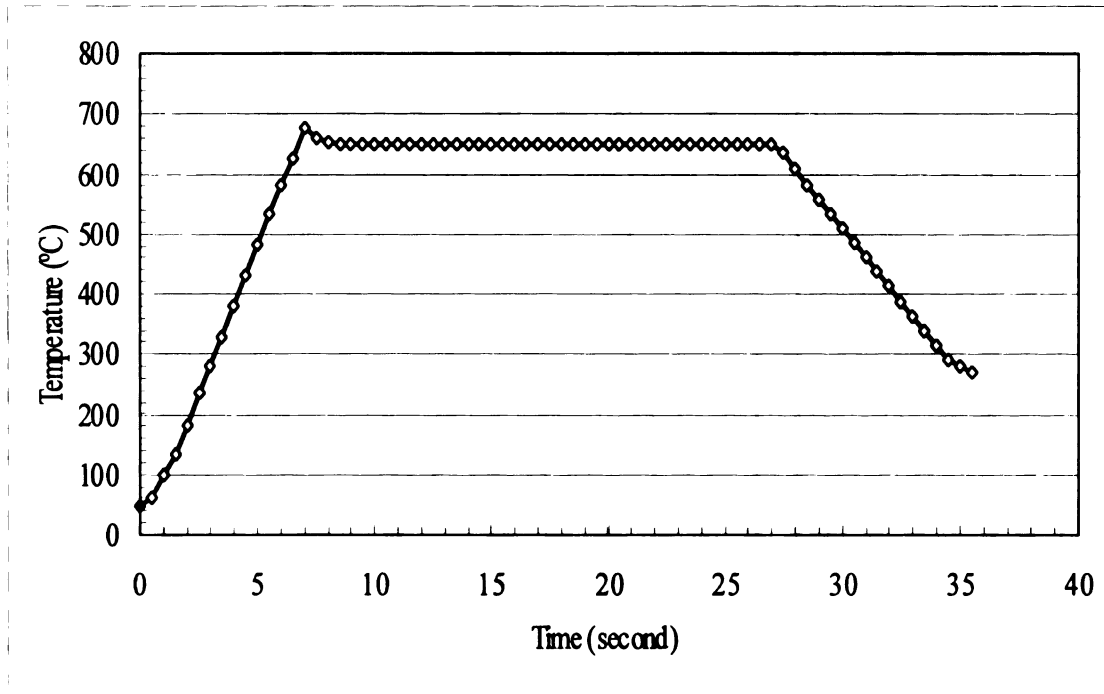


Figure 3.3. Typical temperature profile of sample in a rapid thermal anneal treatment for crystallization of Ni-Ti-Hf thin films.

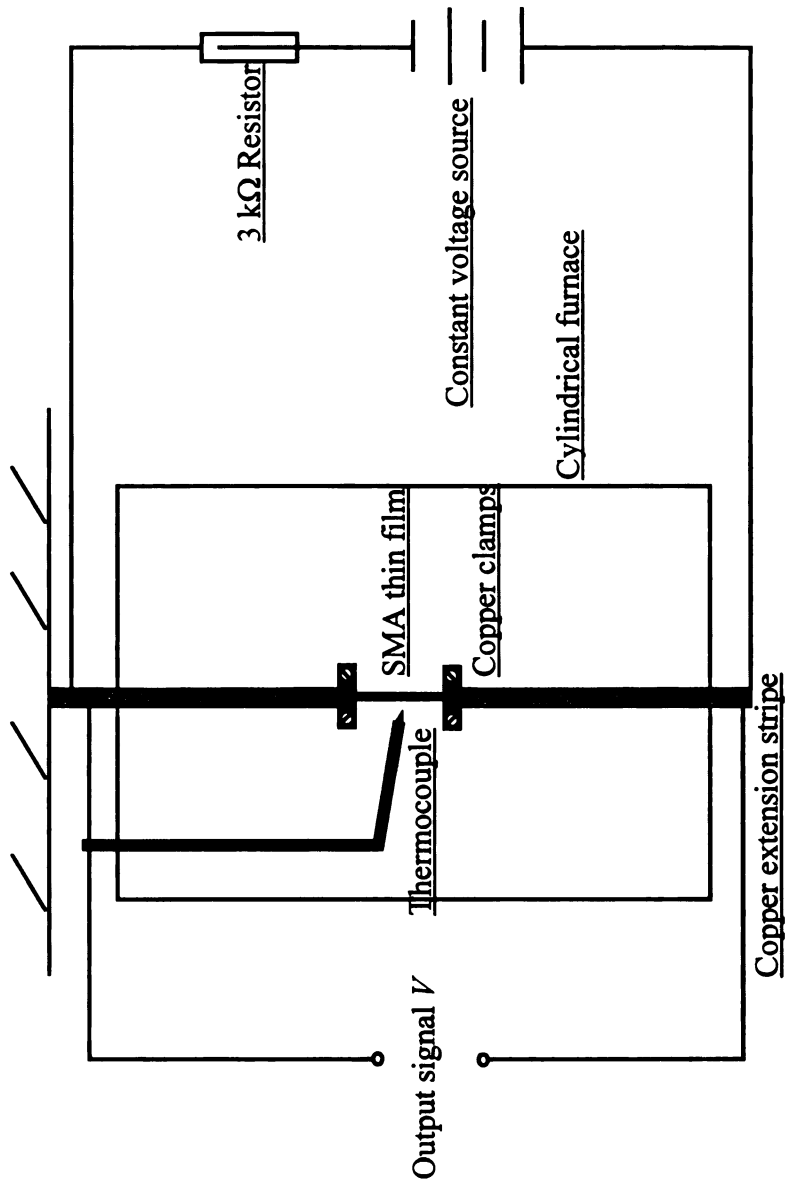


Figure 3.4. Schematic of the apparatus for measuring resistance of the thin film sample to determine phase transformation temperature in this study.

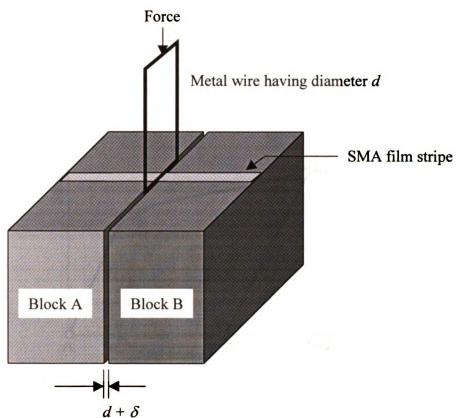


Figure 3.5. Schematic of the experimental setup of semi-quantitatively determining the ductility of Ni-Ti-Hf thin films using bending test.

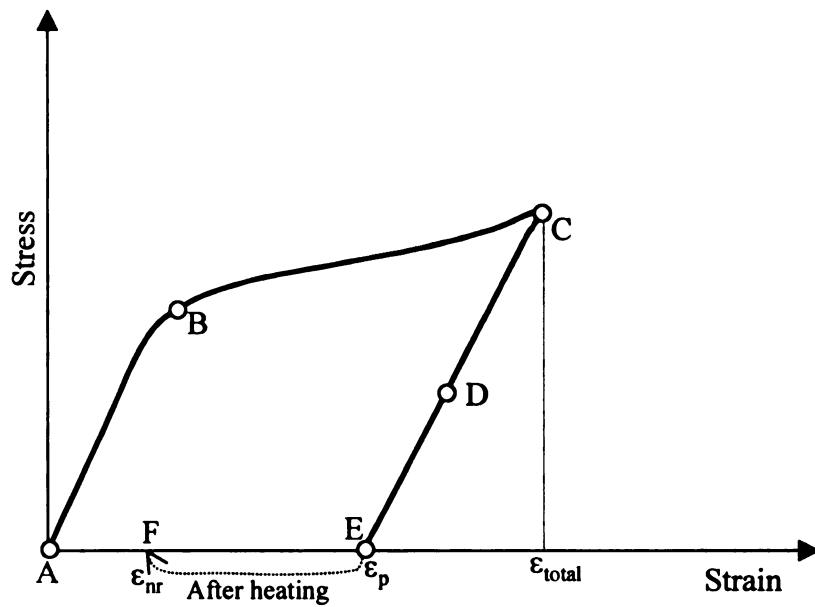


Figure 3.6. Schematic of the method measuring recoverability of a pre-strain put to Ni-Ti-Hf martensite.

A-B-C: loading curve of the sample;

C-D-E: unloading curve of the sample;

F: position that after sample was heated to  $>A_f$  then cooled down to test temperature.

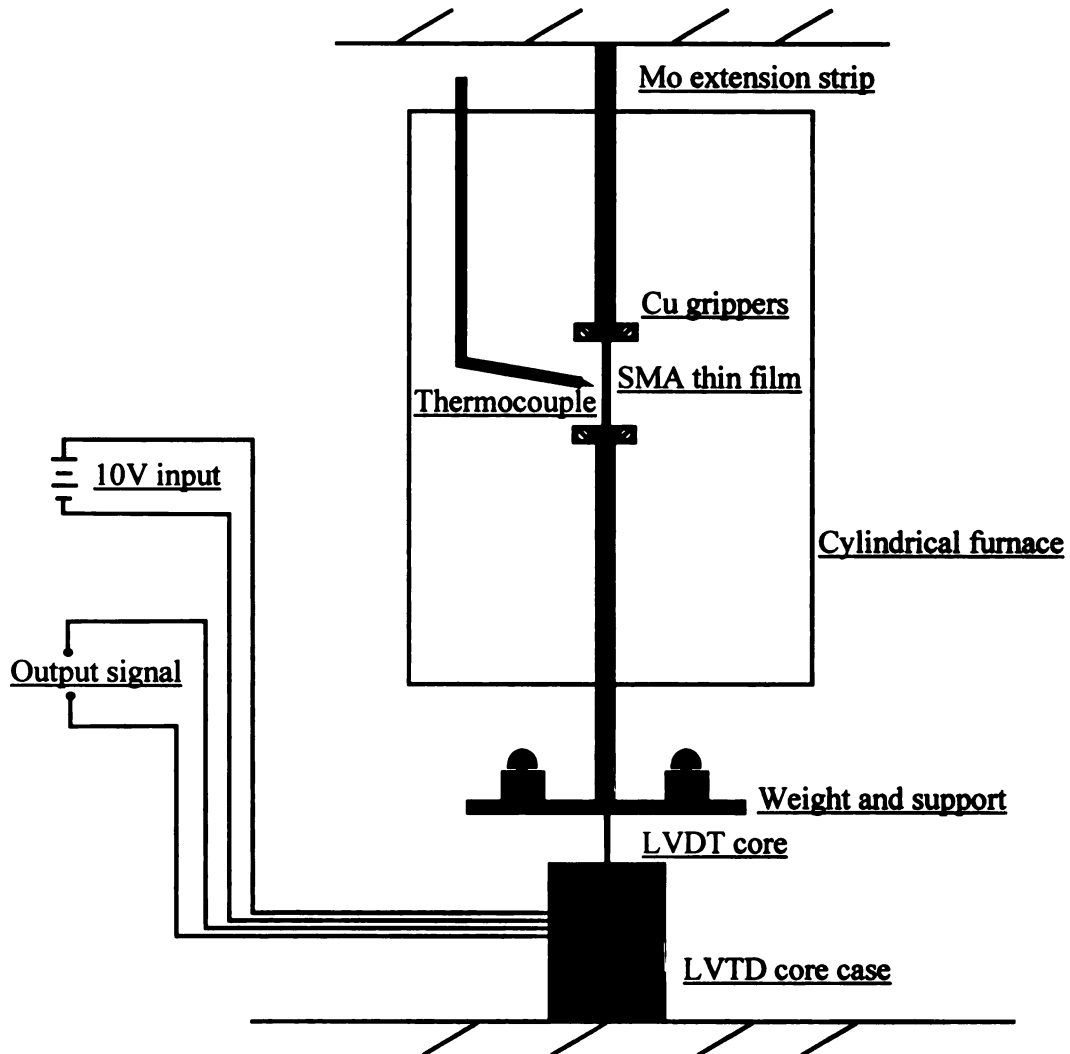


Figure 3.7. Schematic of the apparatus measuring shape memory properties of Ni-Ti-Hf thin film in constrained thermal cycles.

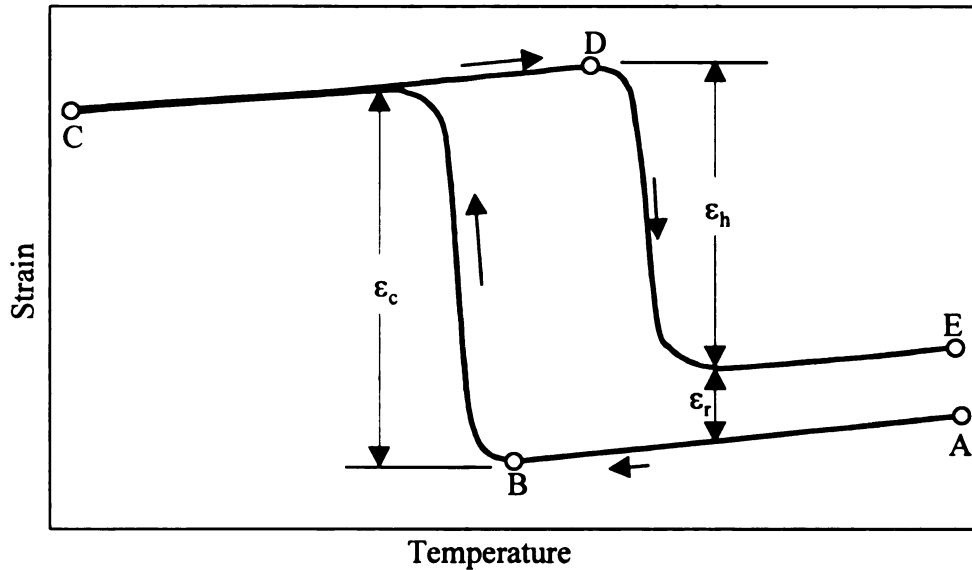


Figure 3.8. Typical hysteresis in a strain-temperature curve for measuring shape memory properties of Ni-Ti-Hf SMA thin films.

A-B-C: First cooling curve, slope A-B results from thermal contraction of the sample;

C-D-E: First heating up curve, slope C-D results from thermal expansion.

$\epsilon_c$ : strain induced by cooling the austenite to martensite;

$\epsilon_h$ : strain recovered by heating the martensite to austenite;

$\epsilon_r$ : residual strain during a complete constrained thermal cycle.

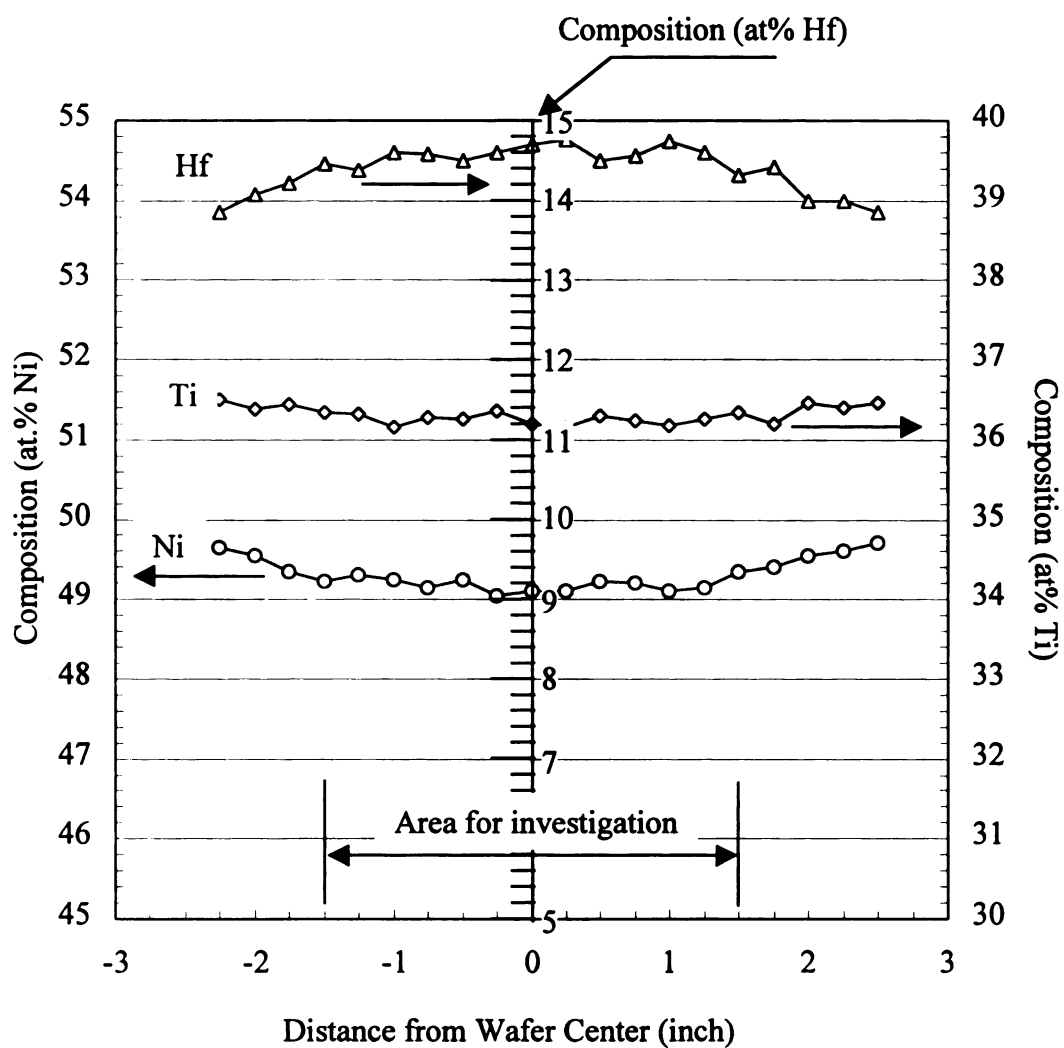


Figure 4.1. Composition uniformity of the thin films deposited from an 8"-diameter  $\text{Ni}_{48.5}\text{Ti}_{37.5}\text{Hf}_{14}$  target. Deposition parameters: working gas Kr 1.0 mTorr, deposition power 1 kW, working distance 81mm, substrate temperature  $200 \pm 15^\circ\text{C}$ , target life 20 kW·Hr.

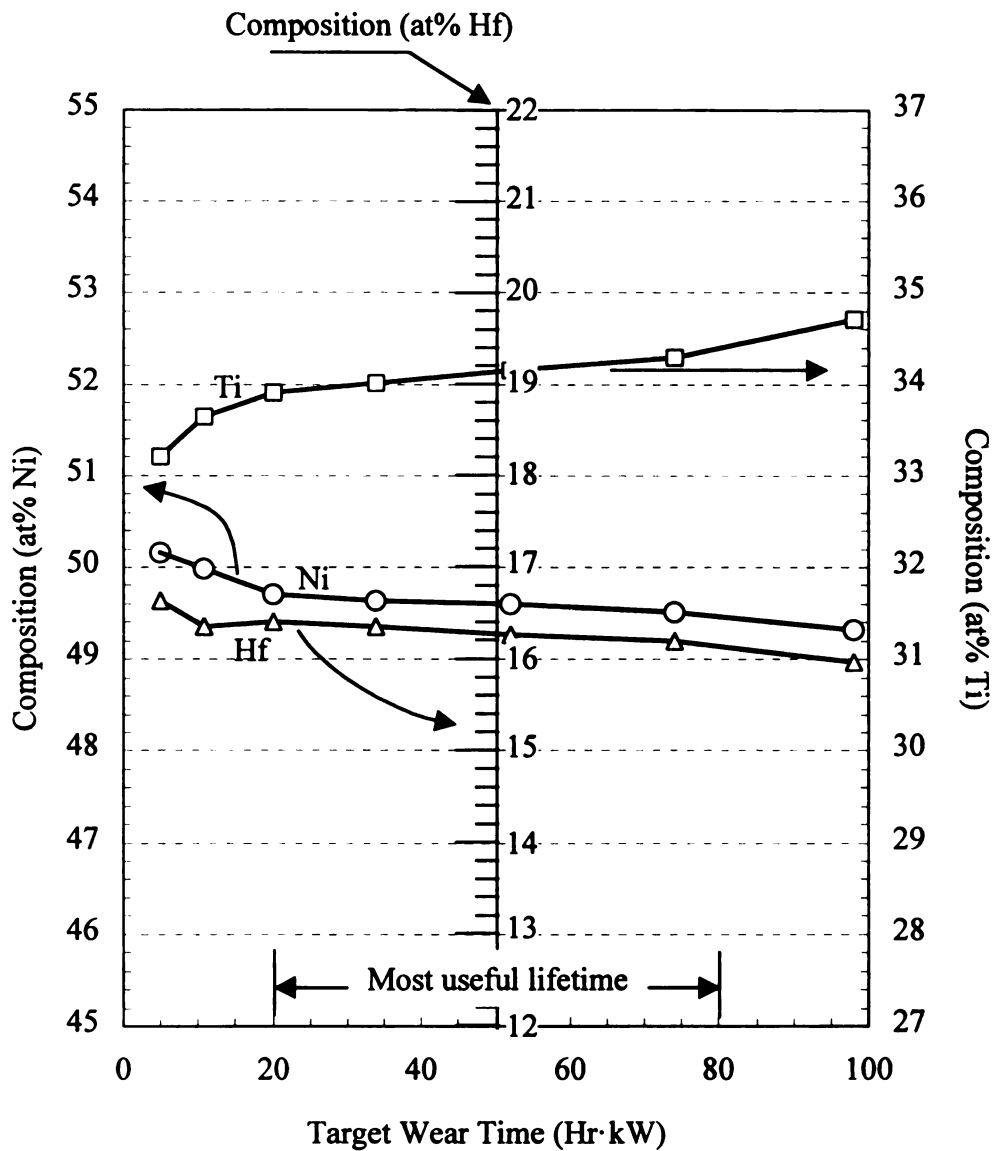


Figure 4.2. Composition variation of films at central area with continuous wearing of the  $\text{Ni}_{48.5}\text{Ti}_{35.5}\text{Hf}_{16}$  target. Deposition parameter: working gas Kr 1.0 mTorr, deposition power 1 kW, working distance 81 mm, substrate temperature  $200 \pm 15^\circ\text{C}$ .

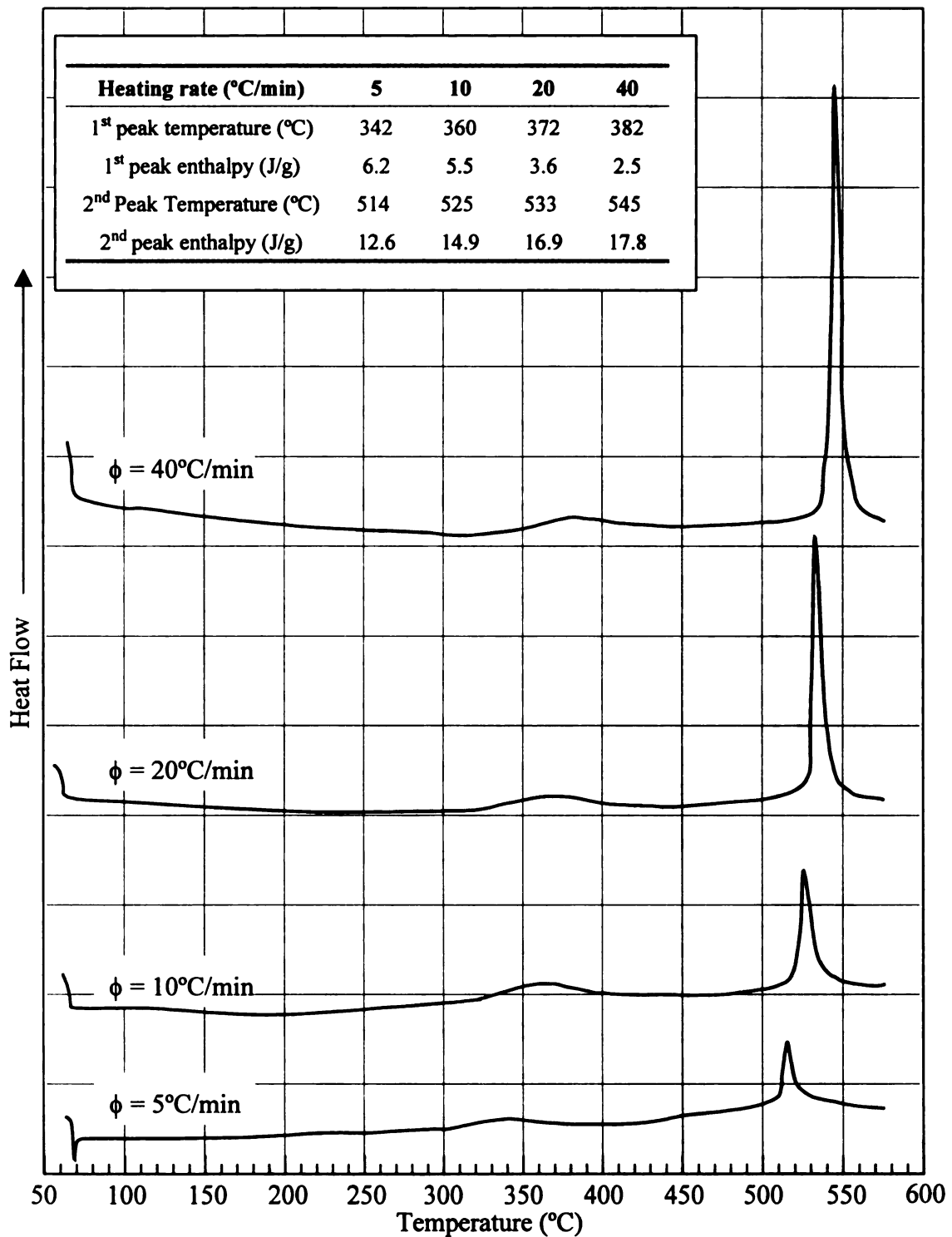


Figure 4.3. DSC curves of as-deposited amorphous  $\text{Ni}_{49.1}\text{Ti}_{36.2}\text{Hf}_{14.7}$  films during isochronal heating from room temperature to 575°C at different heating rates.

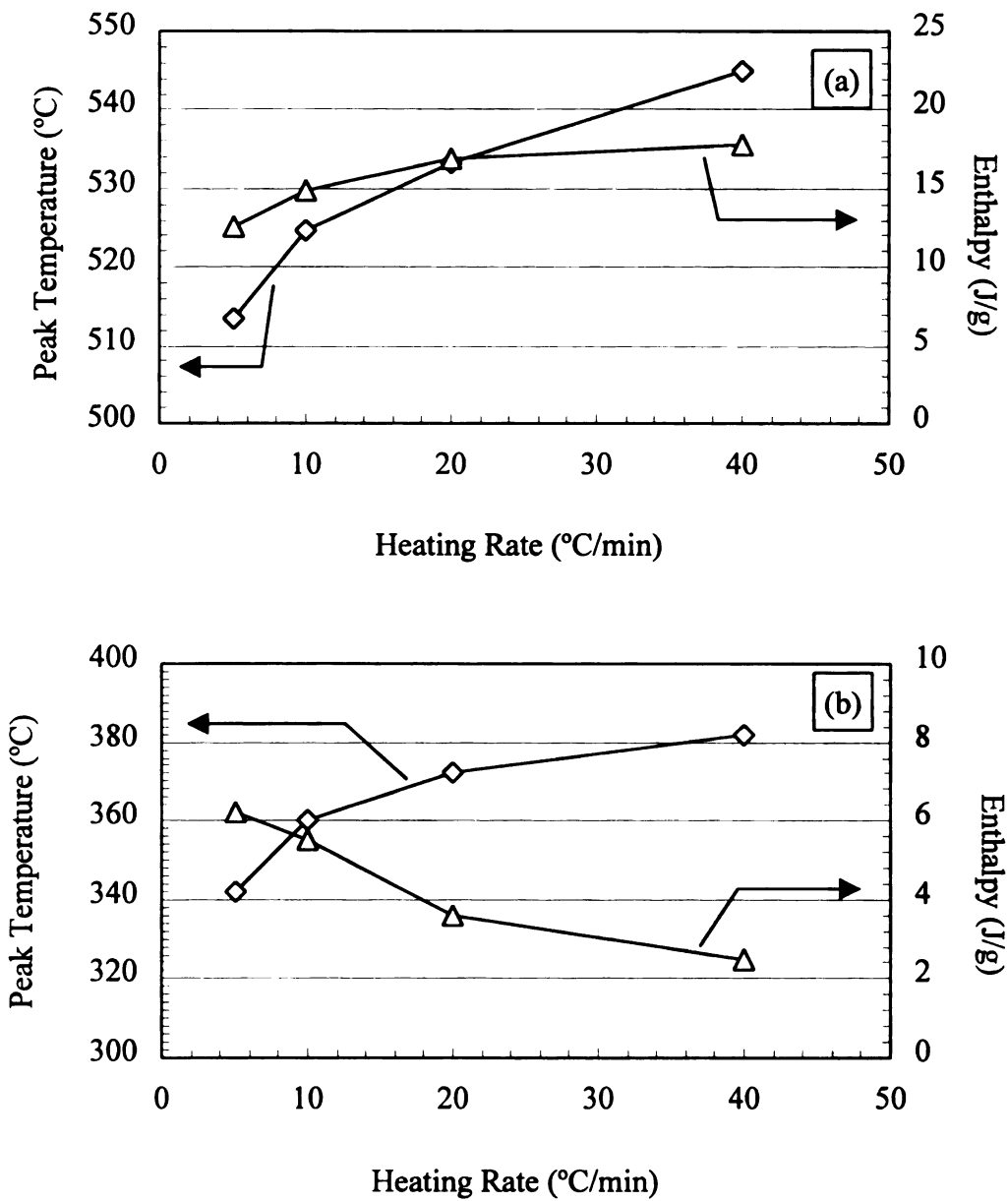


Figure 4.4. Dependence of exothermic peak temperatures and enthalpies on heating rate during heating as-deposited amorphous  $\text{Ni}_{49.1}\text{Ti}_{36.2}\text{Hf}_{14.7}$  films in DSC instrument. (a) high-temperature peak (2nd peak); (b) Low-temperature peak (1st peak).

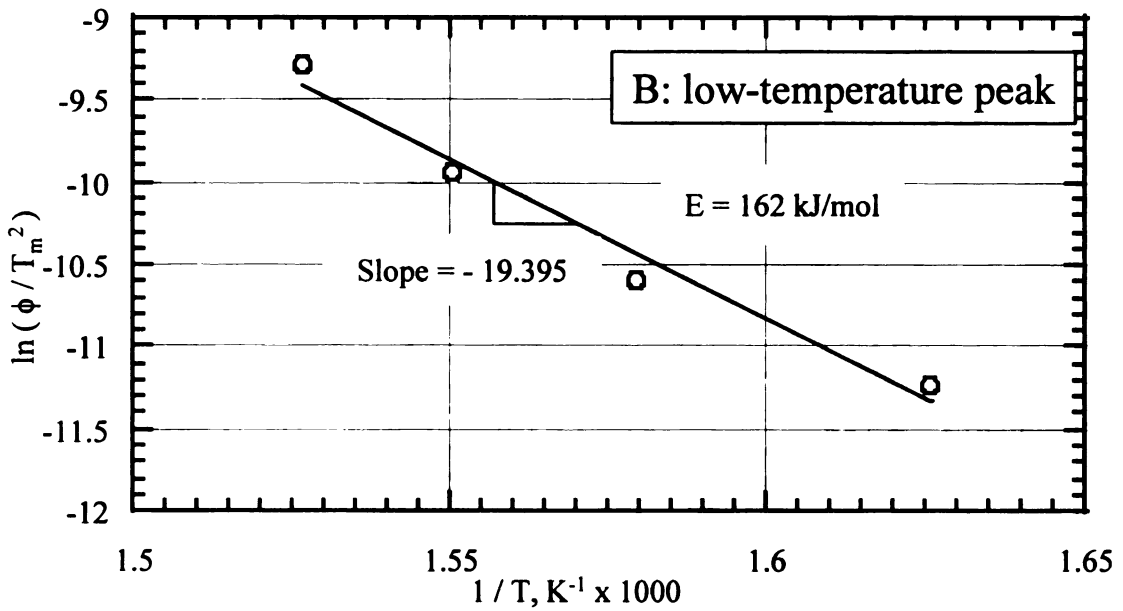
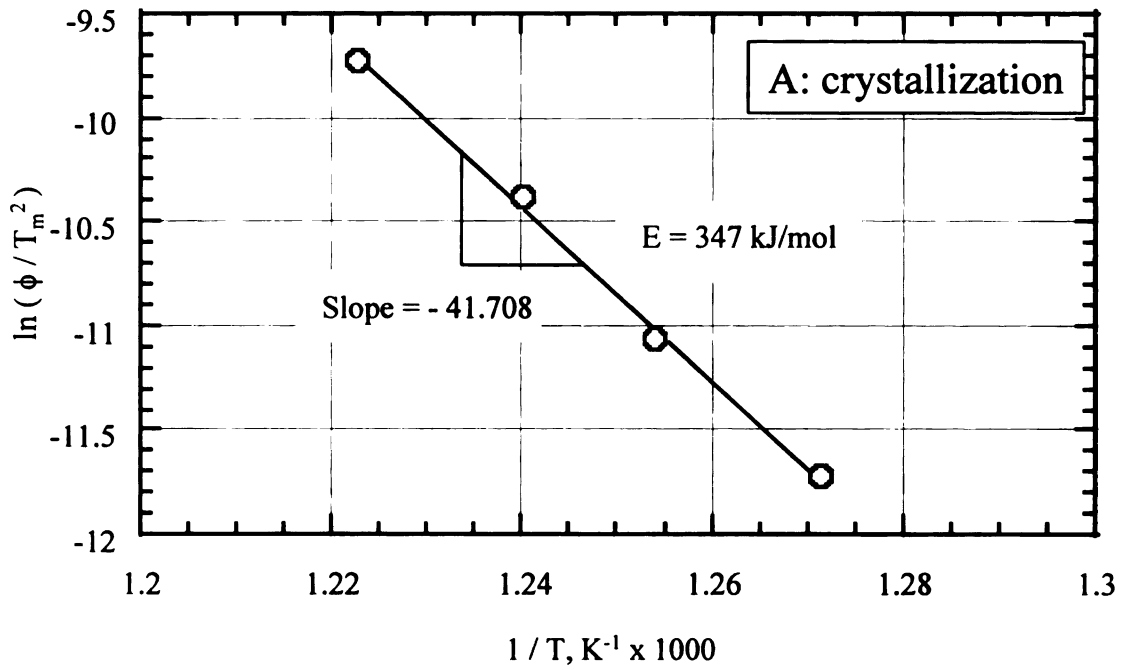


Figure 4.5. Estimation of activation energy for crystallization transformation (2nd peak, or the peak at higher temperature) and the transformation associated with the low-temperature exothermic peak (1st peak on DSC curve) using Kissinger's method.

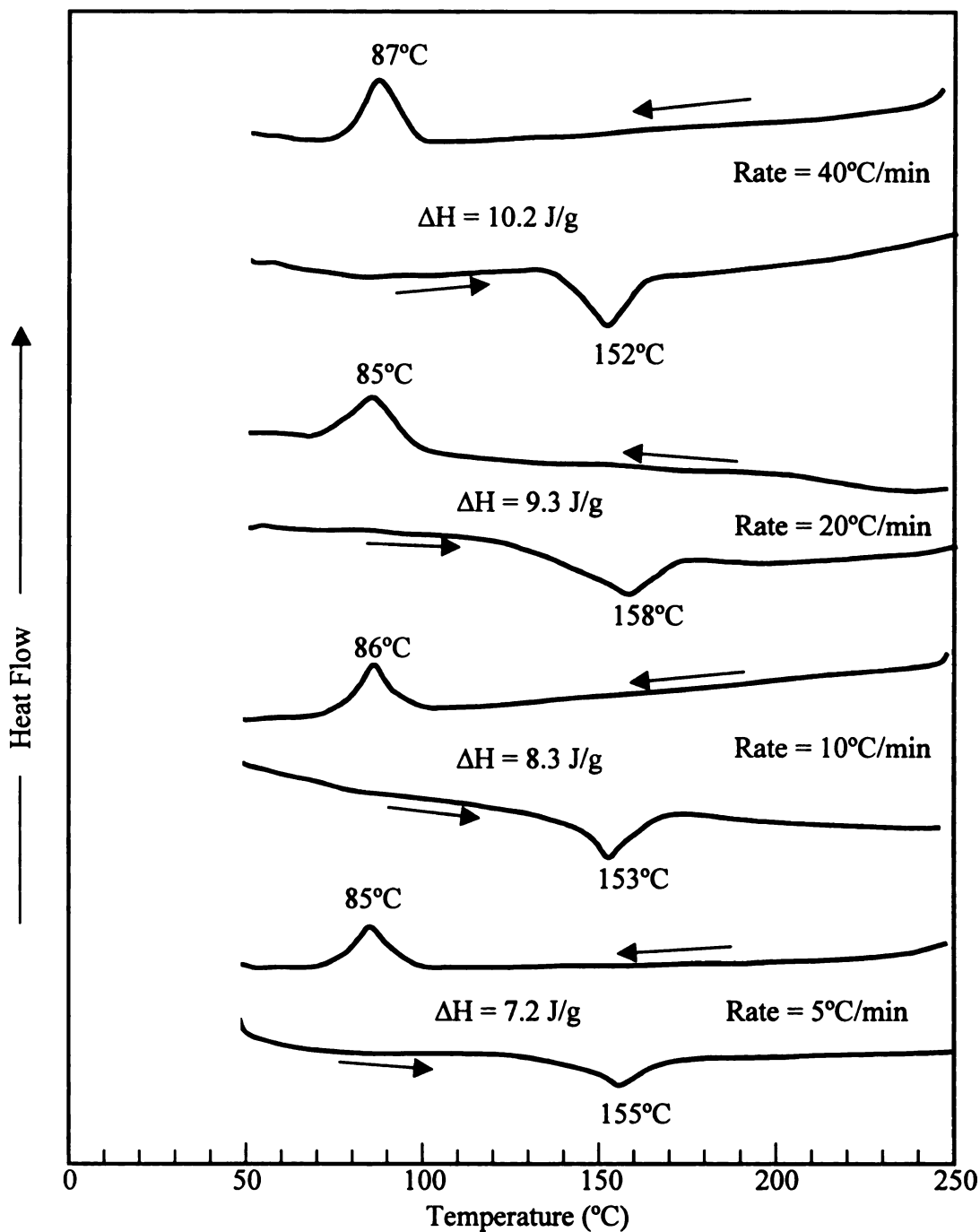


Figure 4.6. DSC curves of  $\text{Ni}_{49.1}\text{Ti}_{36.2}\text{Hf}_{14.7}$  films crystallized by isochronal anneal at different heating rates showing reversible martensitic transformation during thermal cycling between 50°C and 250°C.

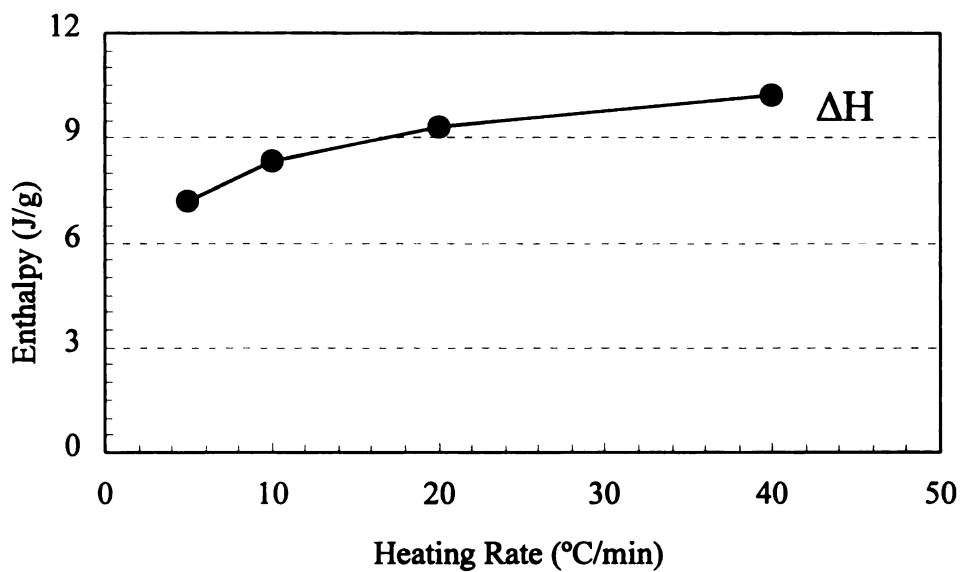
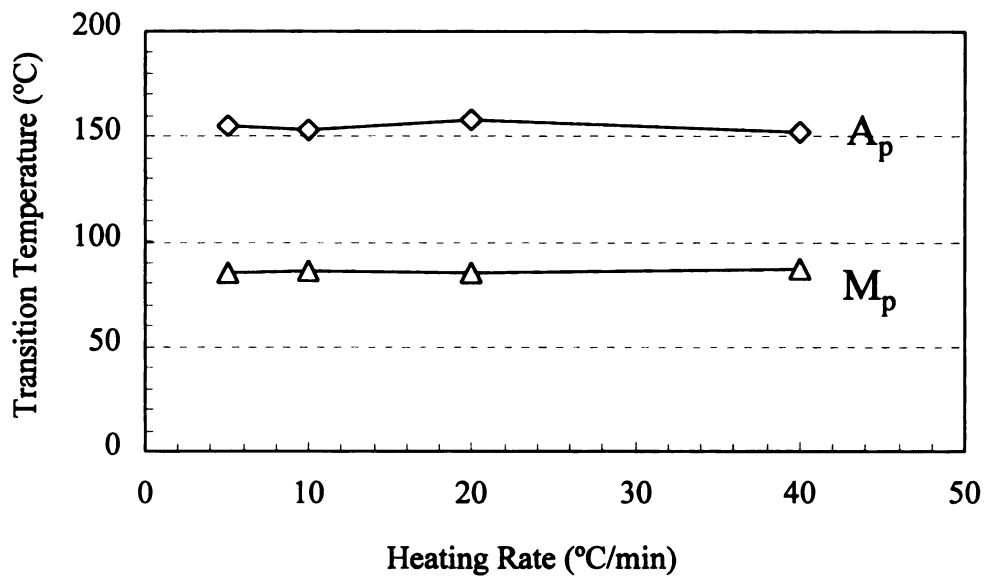


Figure 4.7. Martensitic transformation temperatures ( $A_p$  and  $M_p$ ) of annealed  $Ni_{49.1}Ti_{36.2}Hf_{14.7}$  films as functions of heating rates during isochronal heating for crystallization.

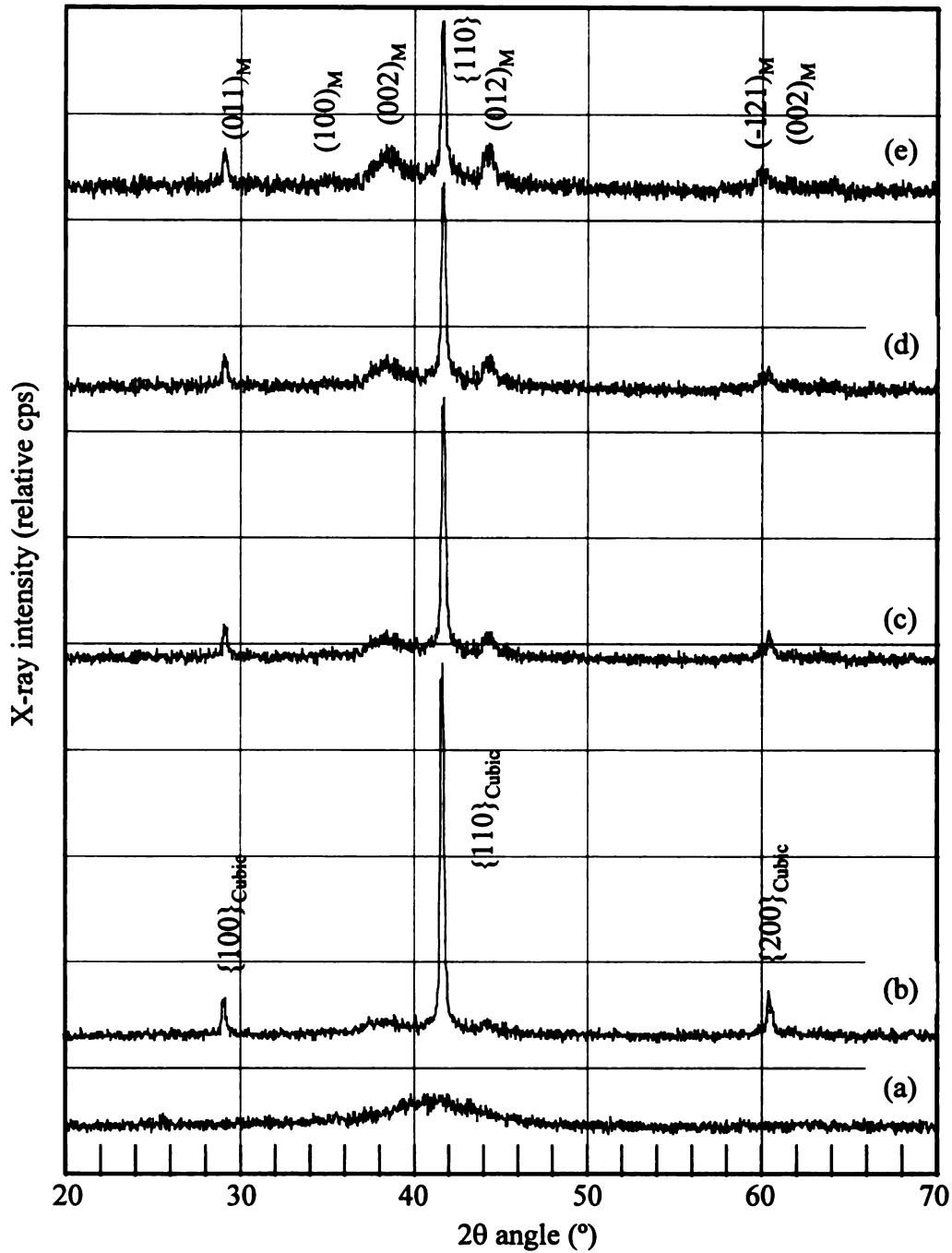


Figure 4.8. Room-temperature XRD spectra of as-deposited amorphous  $\text{Ni}_{49.1}\text{Ti}_{36.2}\text{Hf}_{14.7}$  films and the samples crystallized by isochronal heating to  $575^\circ\text{C}$  at different rates.

(a) as-deposited amorphous; (b),  $\phi = 5^\circ\text{C}/\text{min}$ ; (c)  $\phi = 10^\circ\text{C}/\text{min}$ ;  
 (d)  $\phi = 20^\circ\text{C}/\text{min}$ ; (e)  $\phi = 40^\circ\text{C}/\text{min}$ .

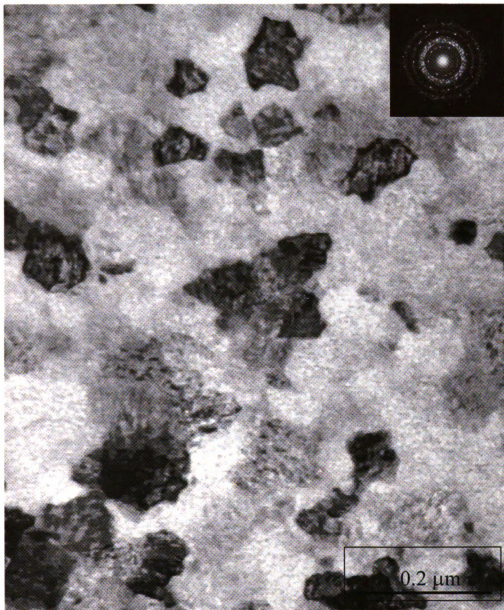


Figure 4.9(a). TEM micrograph and SAED pattern of as-deposited amorphous  $\text{Ni}_{49.1}\text{Ti}_{36.2}\text{Hf}_{14.7}$  thin films after crystallized by isochronal heating to  $575^\circ\text{C}$  at  $5^\circ\text{C}/\text{min}$  heating rate.

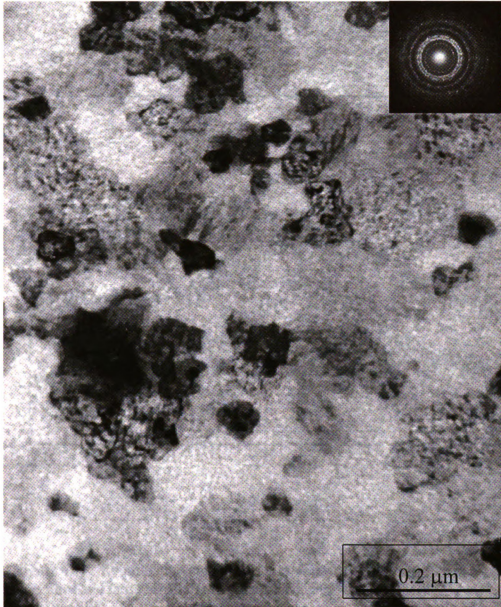


Figure 4.9(b). TEM micrograph and SAED pattern of as-deposited amorphous  $\text{Ni}_{49.1}\text{Ti}_{36.2}\text{Hf}_{14.7}$  thin films after crystallized by isochronal heating to 575°C at 40°C/min heating rate.

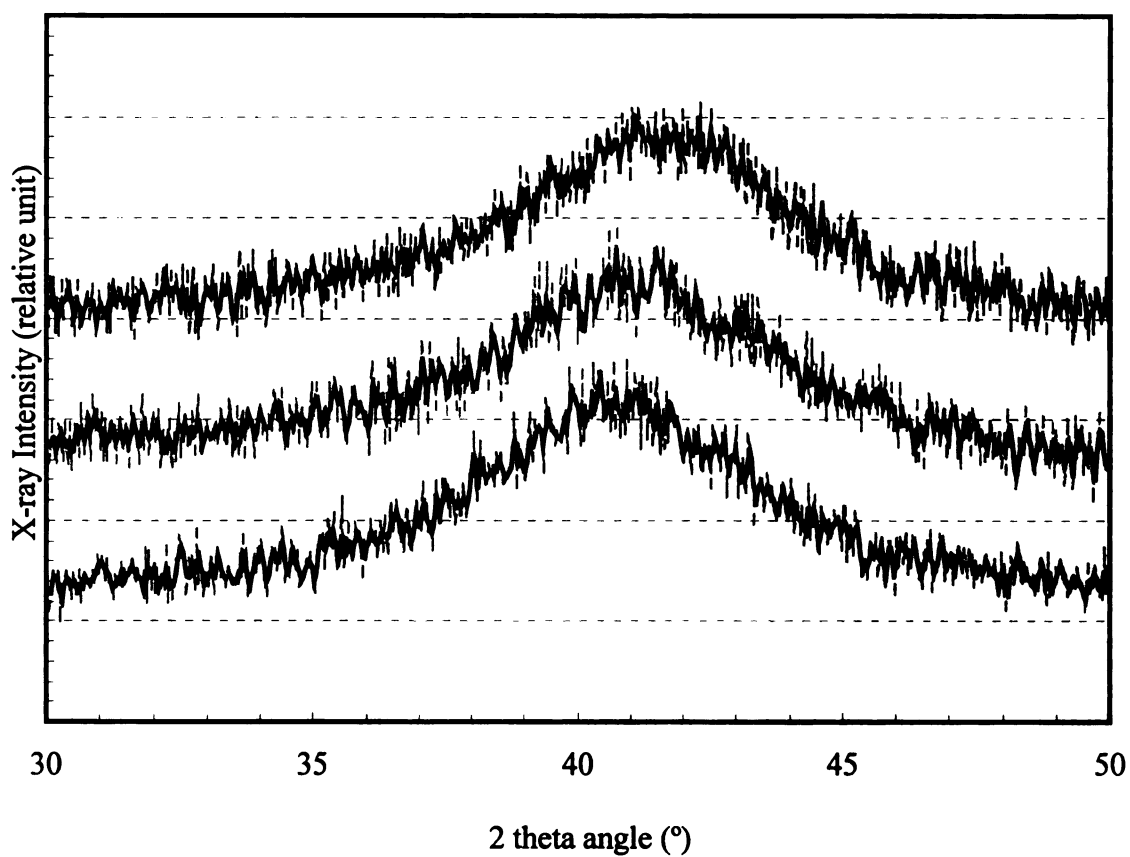


Figure 4.10. Room-temperature XRD of as-deposited amorphous  $\text{Ni}_{49.1}\text{Ti}_{36.2}\text{Hf}_{14.7}$  thin films and those for films after annealed at 300°C and 350°C for 1 hour, respectively.

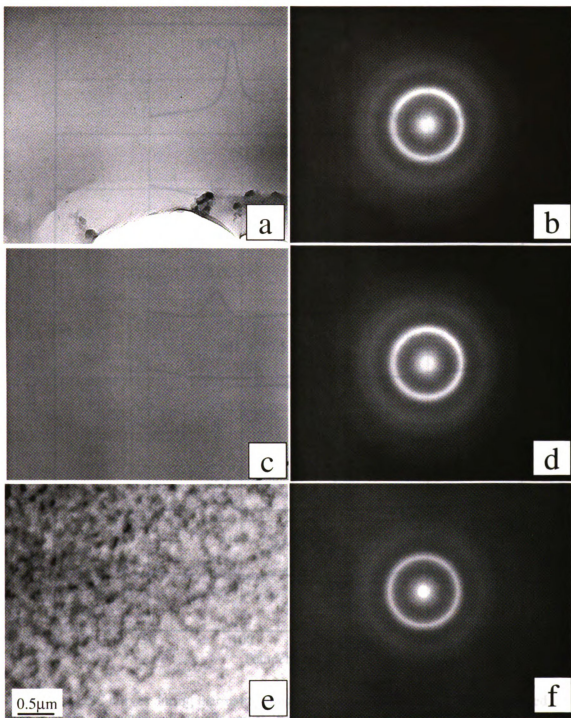


Figure 4.11. TEM micrograph and SAED pattern of as-deposited amorphous  $\text{Ni}_{49.1}\text{Ti}_{36.2}\text{Hf}_{14.7}$  films and those for films after annealed for 1 hour at low temperatures. (a) and (b): as-deposited amorphous; (c) and (d): after 1 hr anneal at  $300^\circ\text{C}$ ; (e) and (f): after 1 hr anneal at  $350^\circ\text{C}$ .

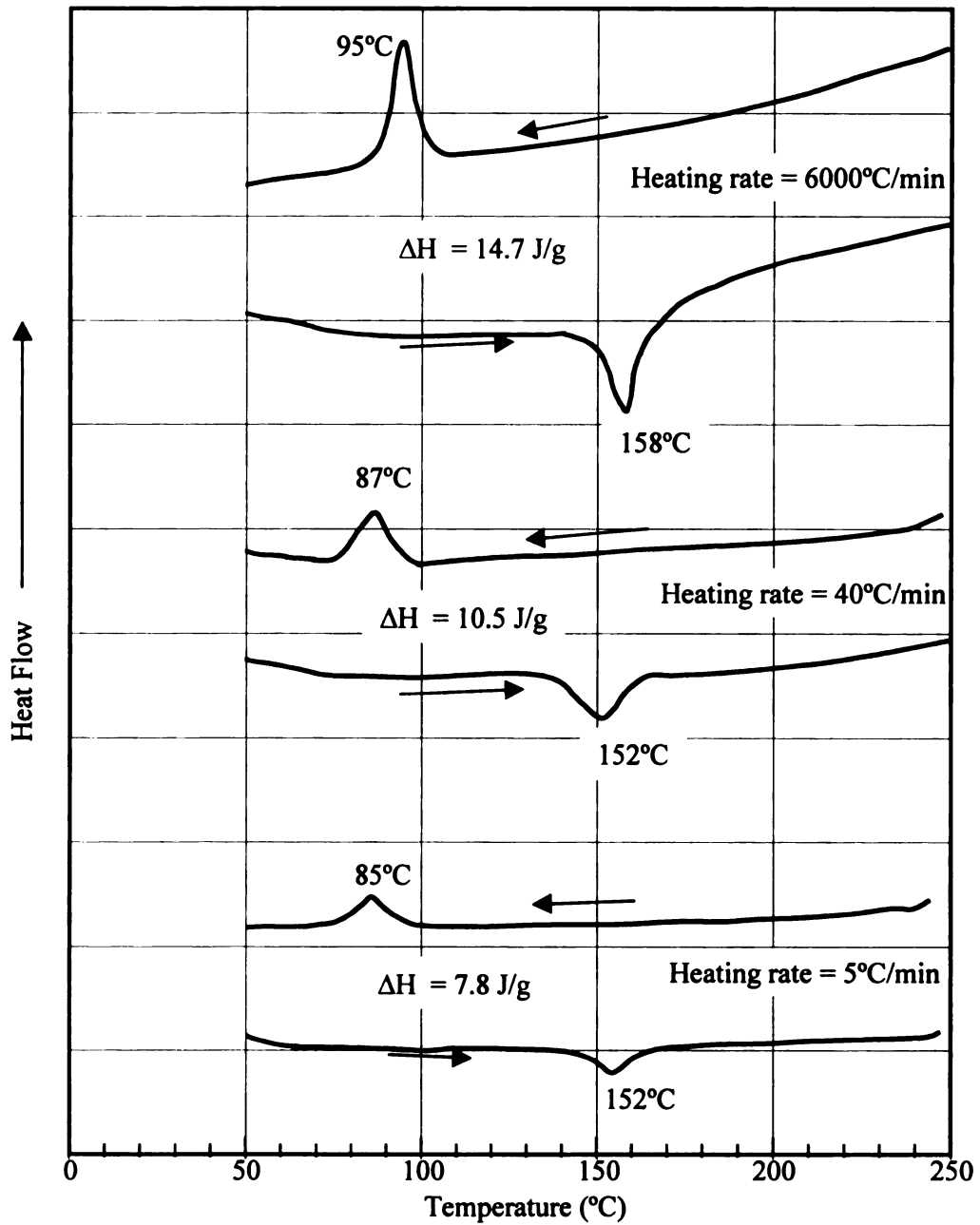


Figure 4.12. DSC curves during thermal cycling between 50°C and 250°C of as-deposited amorphous  $\text{Ni}_{49.1}\text{Ti}_{36.2}\text{Hf}_{14.7}$  films after crystallized by isothermal annealing at different heating rates.

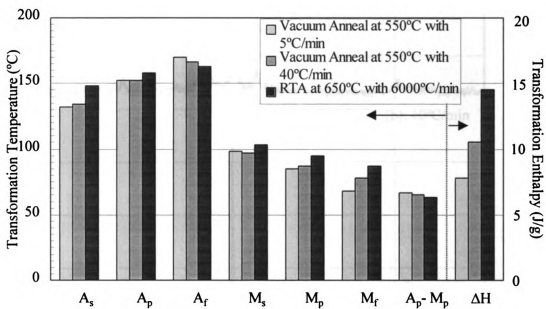


Figure 4.13. Transformation temperatures and transformation enthalpy of  $\text{Ni}_{49.1}\text{Ti}_{36.2}\text{Hf}_{14.7}$  films isothermally annealed by different procedures (conventional vacuum anneal and RTA).

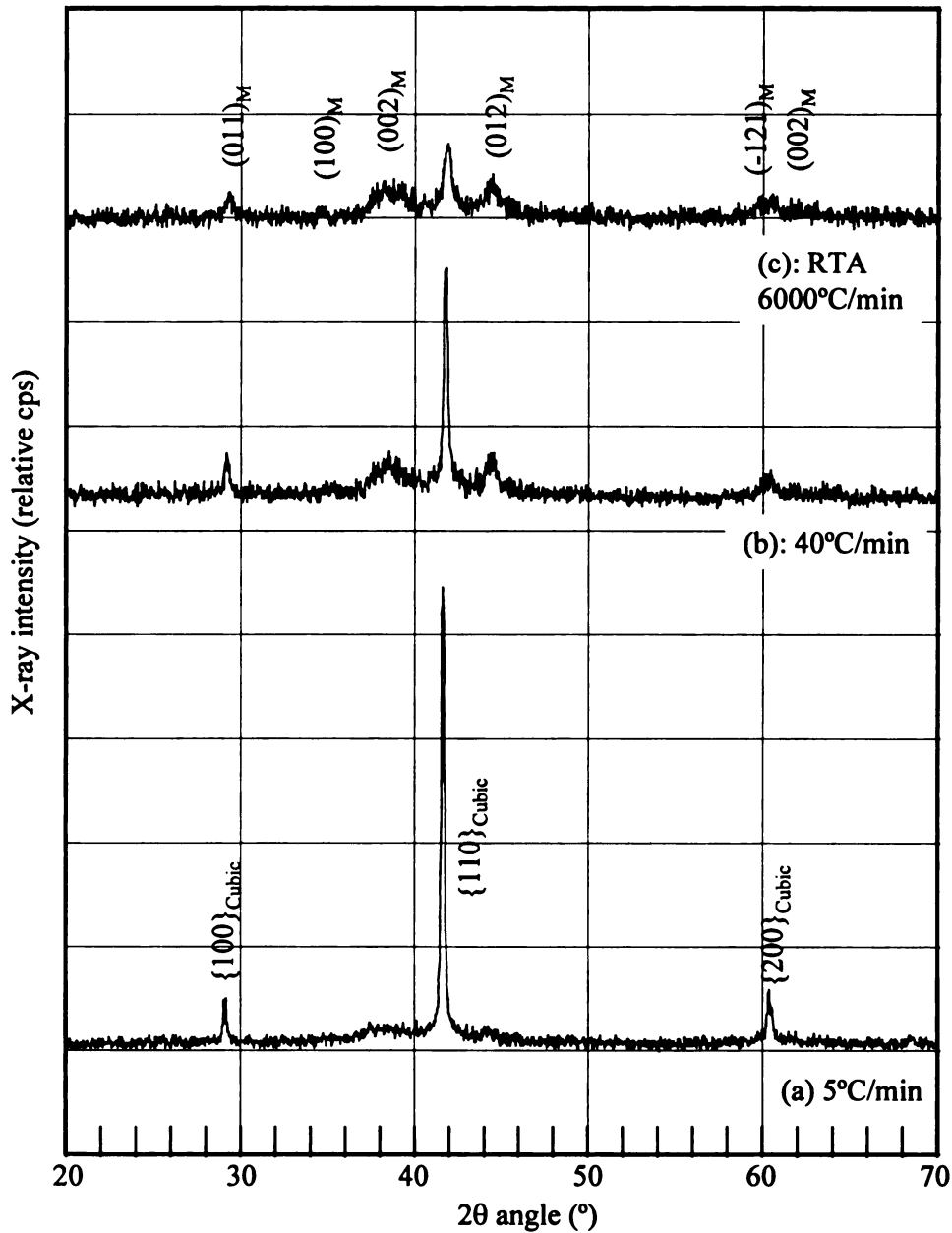


Figure 4.14. Room-temperature XRD spectra of as-deposited amorphous  $\text{Ni}_{49.1}\text{Ti}_{36.2}\text{Hf}_{14.7}$  thin films after crystallized by isothermal annealing via different ramp rates from room temperature to the annealing temperature.  
 (a) vacuum annealing at 550°C for 1 hour with a ramp rate of 5°C/min;  
 (b) vacuum annealing at 550°C for 1 hour with a ramp rate of 40°C/min;  
 (c) rapid thermal annealing at 650°C for 20 seconds with a ramp rate of 6000°C/min.

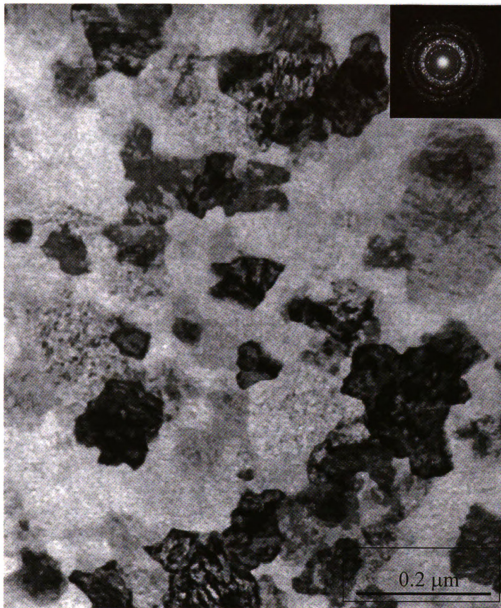


Figure 4.15 (a). TEM micrograph and SAED patterns of as-deposited amorphous  $\text{Ni}_{49.1}\text{Ti}_{36.2}\text{Hf}_{14.7}$  films after crystallized by isothermal annealing at  $550^\circ\text{C}$  for 1 hour with a ramp rate of  $5^\circ\text{C}/\text{min}$  from room temperature to  $550^\circ\text{C}$ .

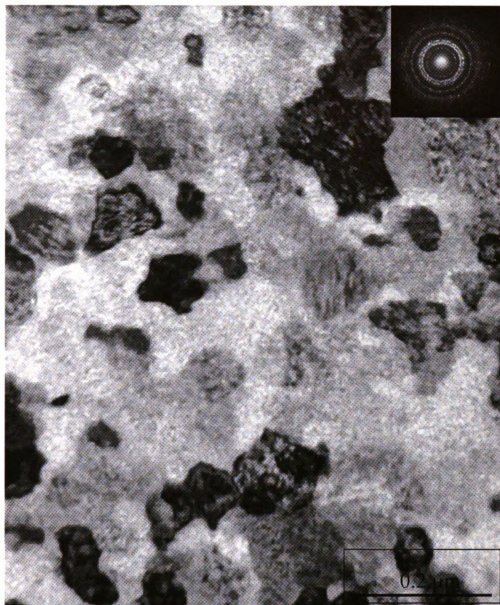


Figure 4.15 (b). TEM micrograph and SAED patterns of as-deposited amorphous  $\text{Ni}_{49.1}\text{Ti}_{36.2}\text{Hf}_{14.7}$  films after crystallized by isothermal annealing at  $550^\circ\text{C}$  for 1 hour with a ramp rate of  $40^\circ\text{C}/\text{min}$  from room temperature to  $550^\circ\text{C}$ .

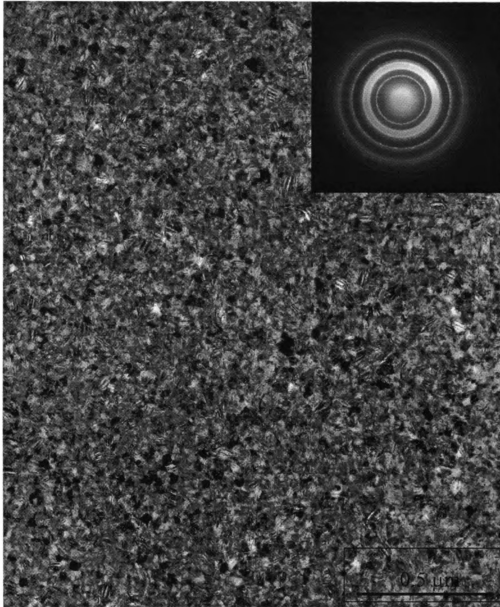


Figure 4.15 (c). TEM micrograph and SAED patterns of as-deposited amorphous  $\text{Ni}_{49.1}\text{Ti}_{36.2}\text{Hf}_{14.7}$  films after crystallized by rapid thermal annealing at  $650^\circ\text{C}$  for 20 secs with a ramp rate of  $6000^\circ\text{C}/\text{min}$ .

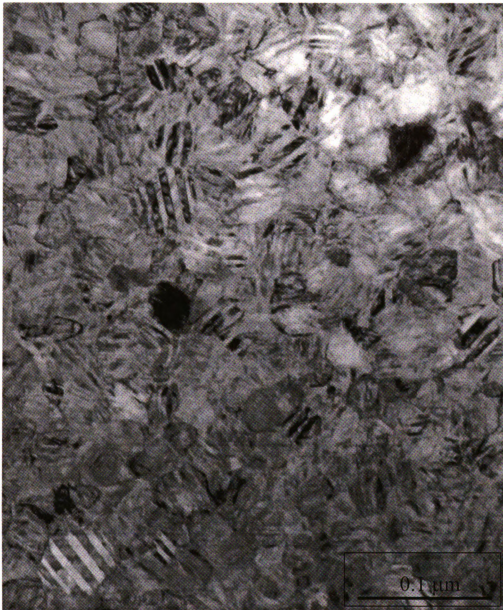


Figure 4.15 (d), TEM micrograph (higher magnification) of as-deposited amorphous  $\text{Ni}_{49.1}\text{Ti}_{36.2}\text{Hf}_{14.7}$  films after crystallized by rapid thermal annealing at  $650^\circ\text{C}$  for 20 secs with a ramp rate of  $6000^\circ\text{C}/\text{min}$ .

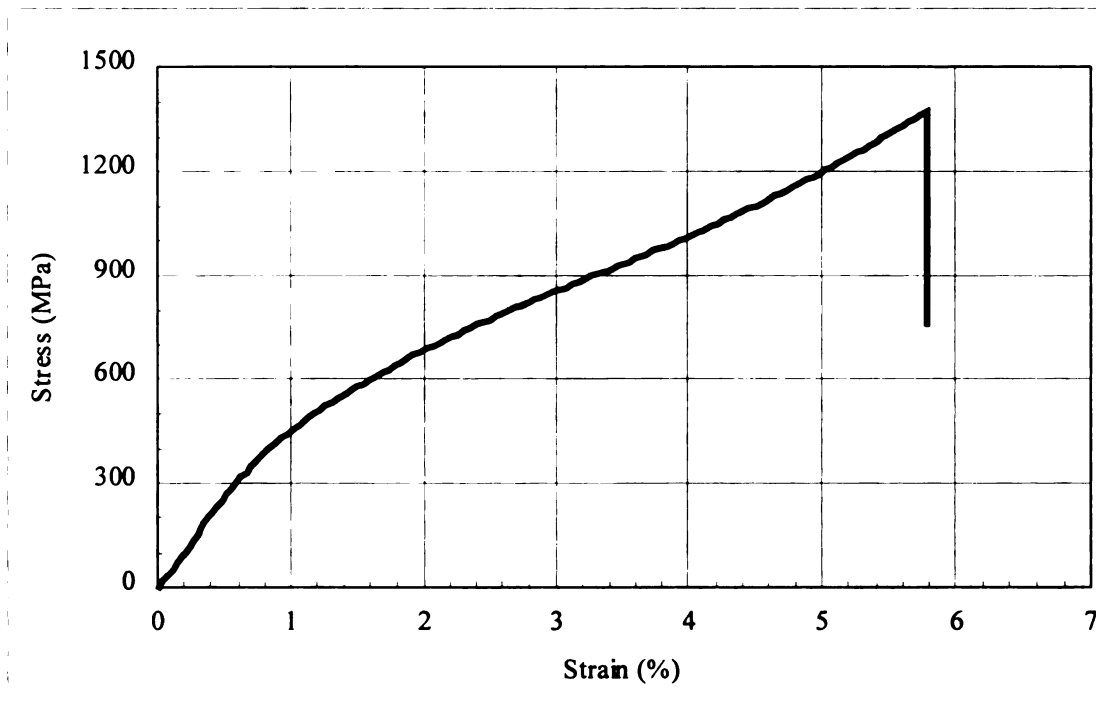


Figure 4.16. Room-temperature stress-strain curve of as-deposited amorphous  $\text{Ni}_{49.1}\text{Ti}_{36.2}\text{Hf}_{14.7}$  films after rapid thermal annealing at  $650^\circ\text{C}$  for 20 seconds with heating rate of  $100^\circ\text{C}/\text{sec}$ .

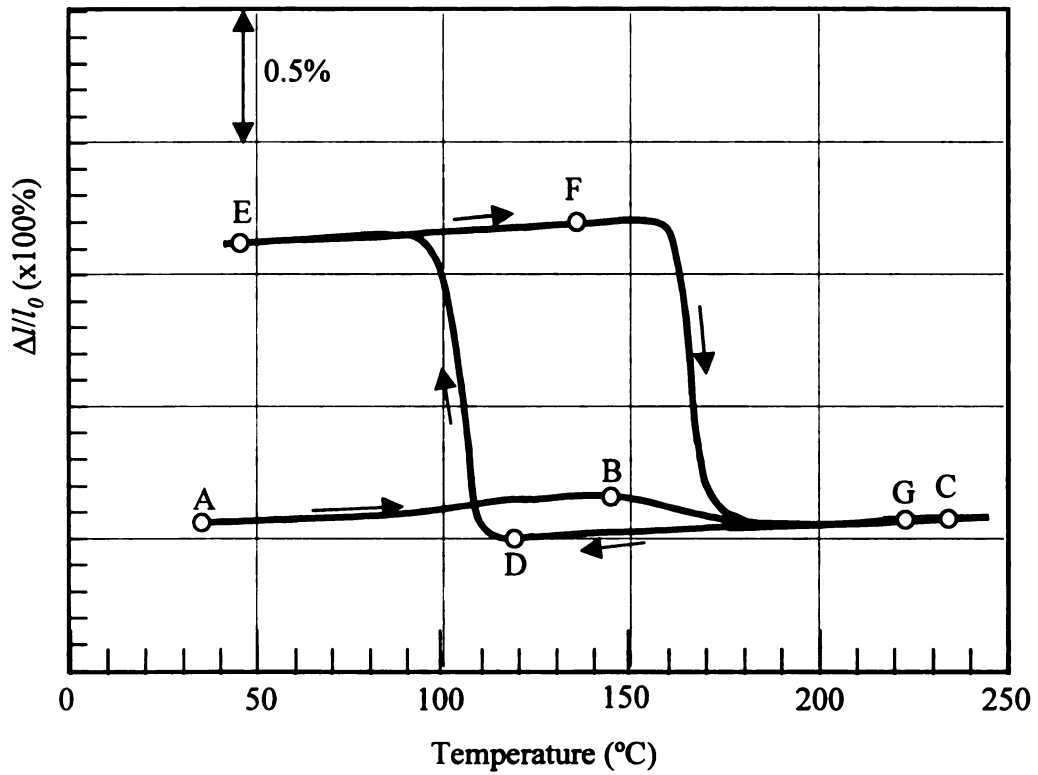


Figure 4.17. Schematic strain-temperature curve of RTA crystallized  $\text{Ni}_{49.1}\text{Ti}_{36.2}\text{Hf}_{14.7}$  films during constrained thermal cycling starting from room temperature (fully martensitic microstructure).

1st heating excursion: A  $\rightarrow$  B  $\rightarrow$  C;

1st cooling excursion: C  $\rightarrow$  D  $\rightarrow$  E;

2nd heating excursion: E  $\rightarrow$  F  $\rightarrow$  G.

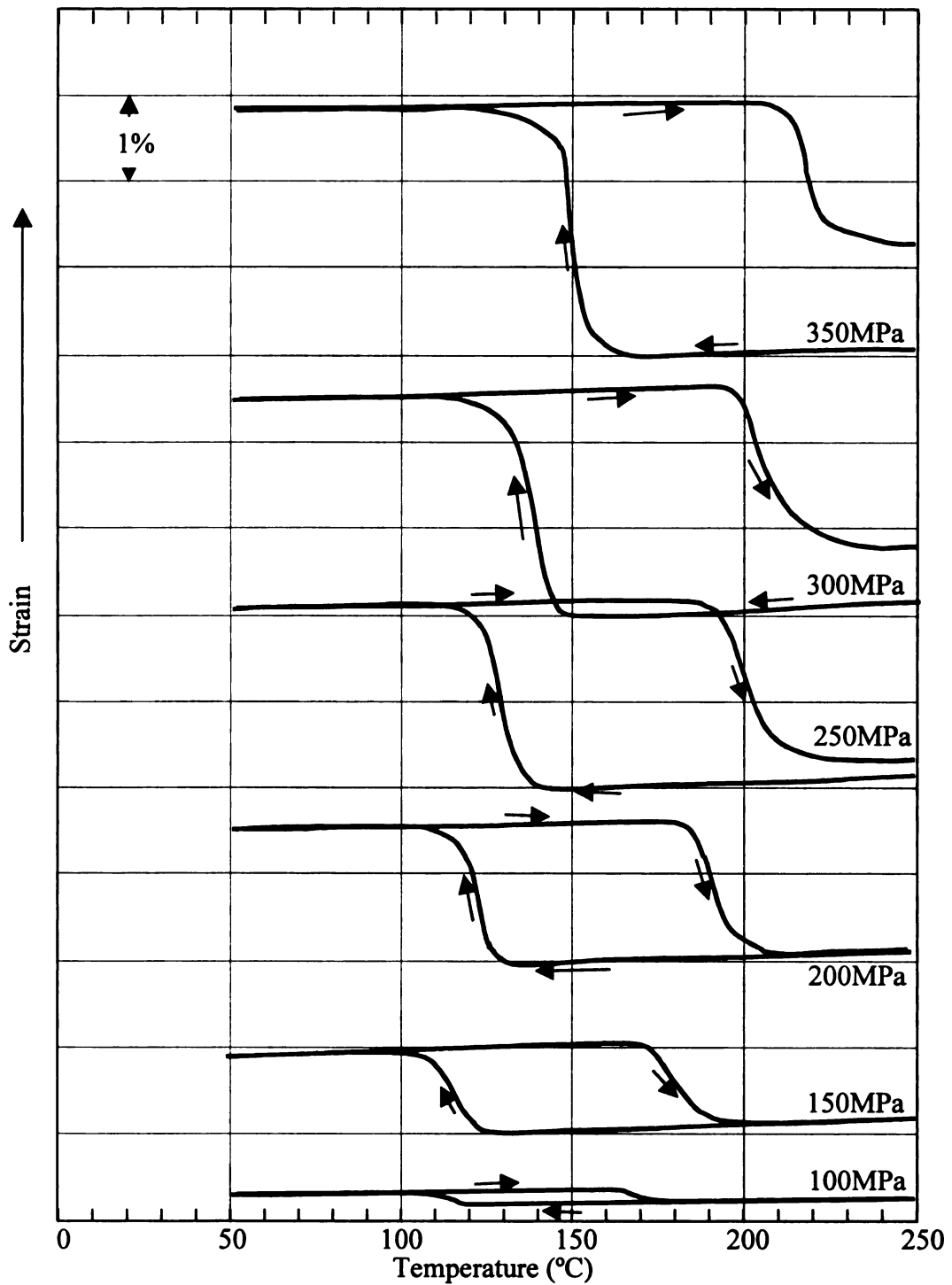


Figure 4.18. Strain-temperature curves of as-deposited amorphous  $\text{Ni}_{49.1}\text{Ti}_{36.2}\text{Hf}_{14.7}$  thin films crystallized by RTA anneal at  $650^{\circ}\text{C}$  for 20 seconds during thermal cycling under different loads.

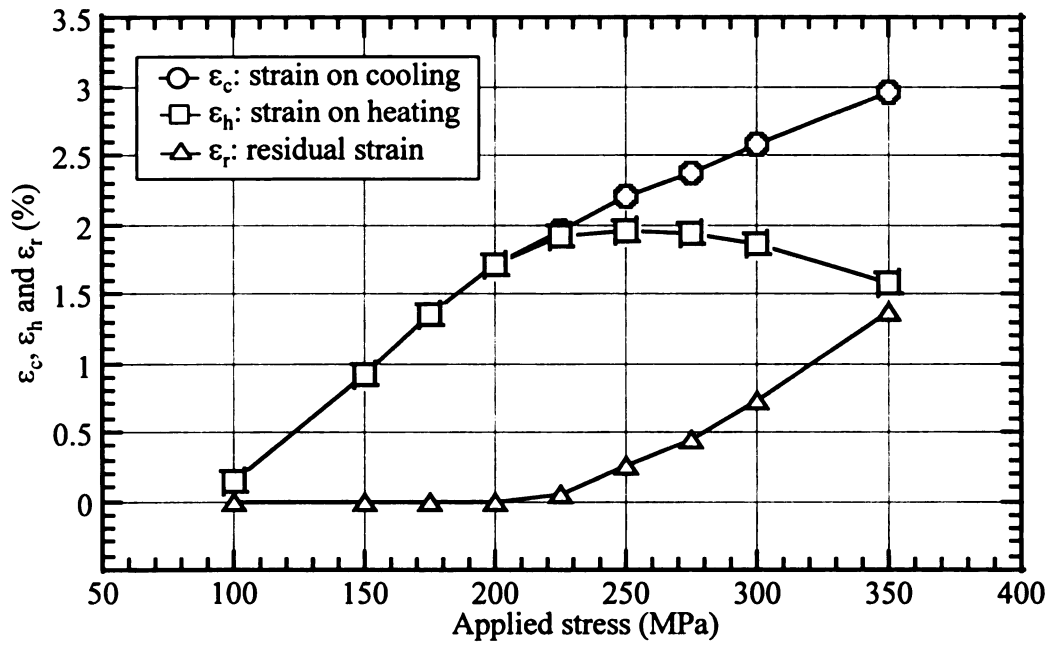


Figure 4.19. Dependence of strain induced by cooling from austenite to martensite and that recovered by heating from martensite to austenite of RTA treated as-deposited amorphous  $\text{Ni}_{49.1}\text{Ti}_{36.2}\text{Hf}_{14.7}$  SMA thin films on applied stress during thermal cycling.

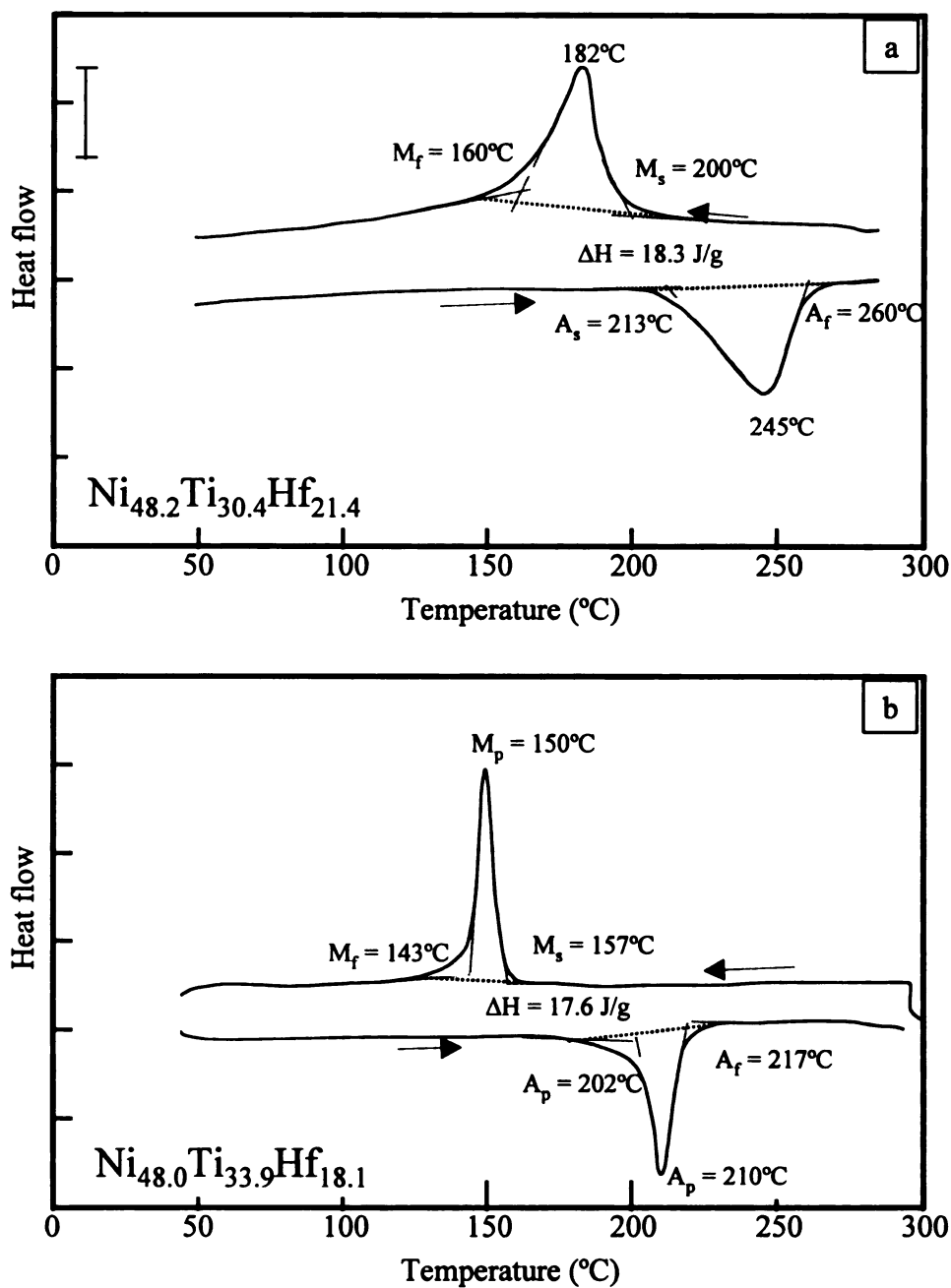
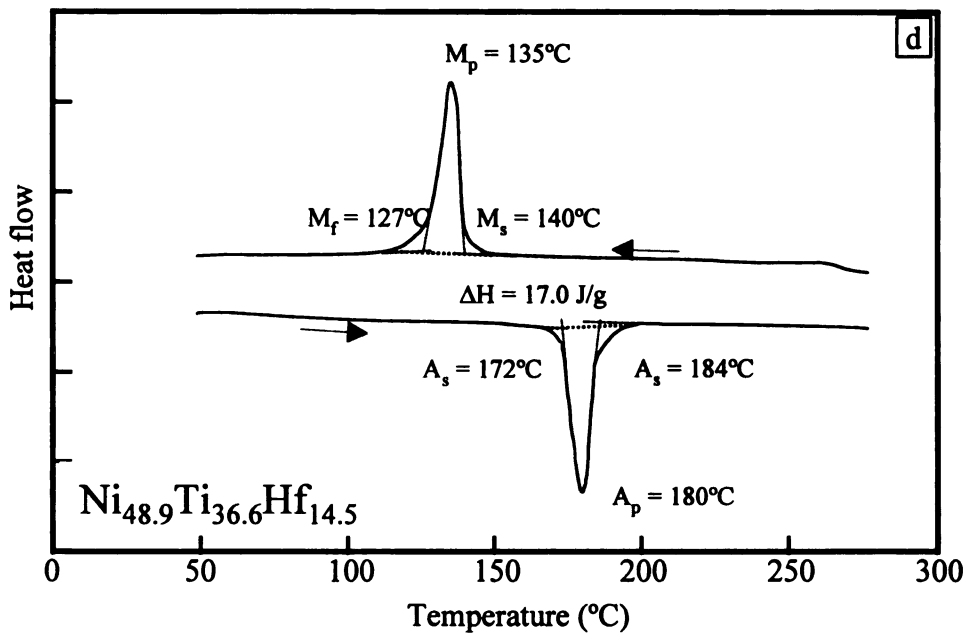
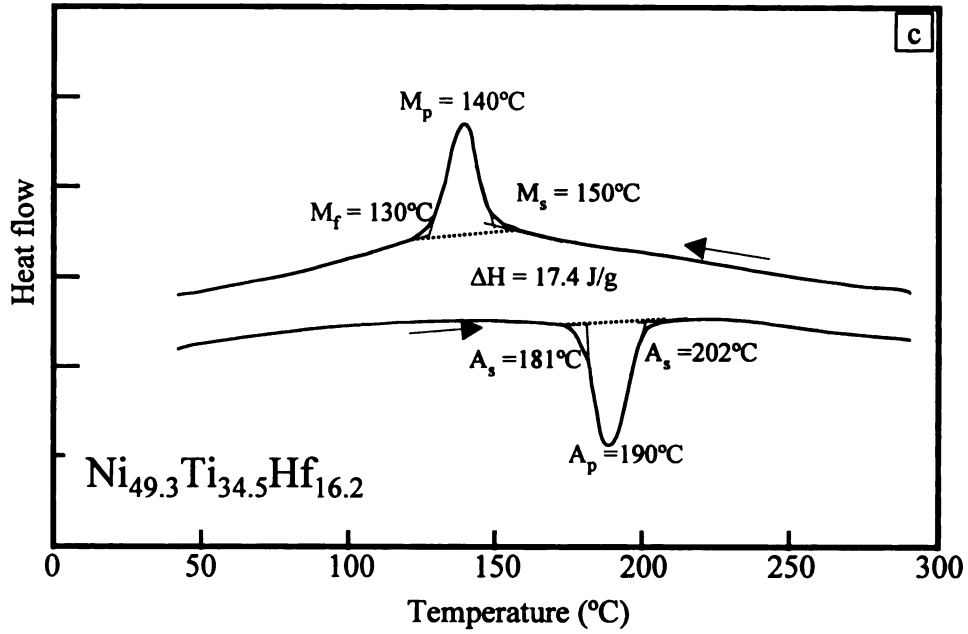


Figure 4.20. DSC curves of *in-situ* crystallized Ni-Ti-Hf thin films with different hafnium content during thermal cycling between 50°C and 300°C.  
 (a)  $\text{Ni}_{48.2}\text{Ti}_{30.4}\text{Hf}_{21.4}$ ; (b)  $\text{Ni}_{48.0}\text{Ti}_{33.9}\text{Hf}_{18.1}$ ; (c)  $\text{Ni}_{49.3}\text{Ti}_{34.5}\text{Hf}_{16.2}$ ; (d)  $\text{Ni}_{48.9}\text{Ti}_{36.6}\text{Hf}_{14.5}$

Figure 4.20 (continued)



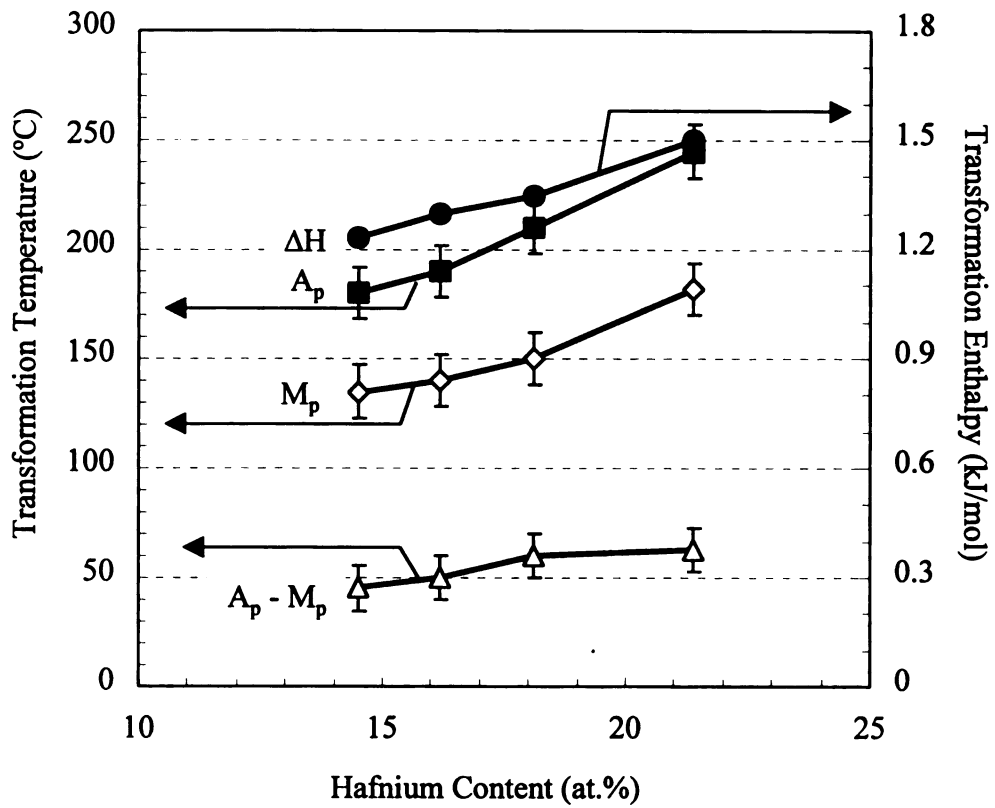


Figure 4.21. Dependence of transformation temperatures ( $M_p$ ,  $A_p$ ), transformational hysteresis ( $A_p - M_p$ ) and transformational enthalpy ( $\Delta H$ ) on hafnium content in *in-situ* crystallized Ni-Ti-Hf films.

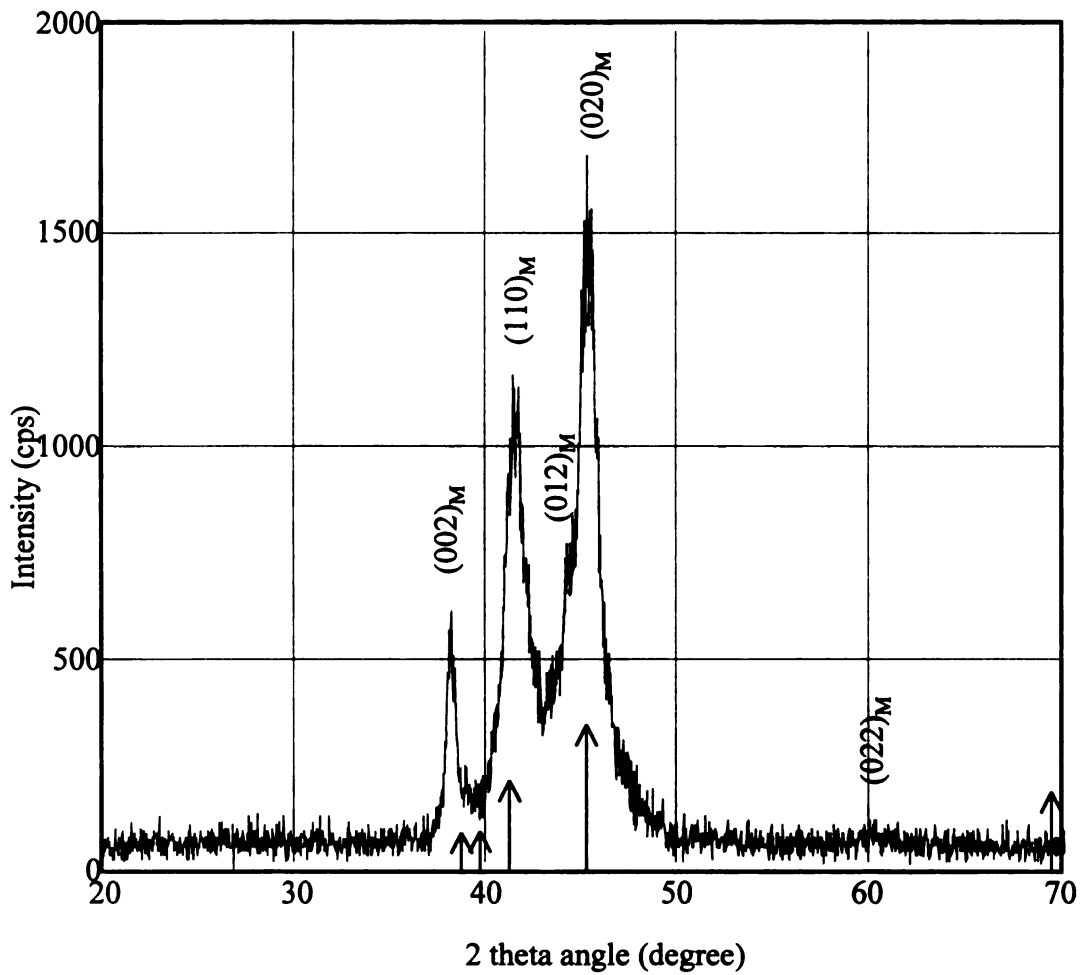


Figure 4.22. Room-temperature XRD of the *in-situ* crystallized Ni<sub>48.9</sub>Ti<sub>36.6</sub>Hf<sub>14.5</sub> SMA film. The bars with arrows show the peak locations for Ti<sub>2</sub>Ni or Ti<sub>4</sub>Ni<sub>2</sub>O<sub>x</sub> phases from powder diffraction data.

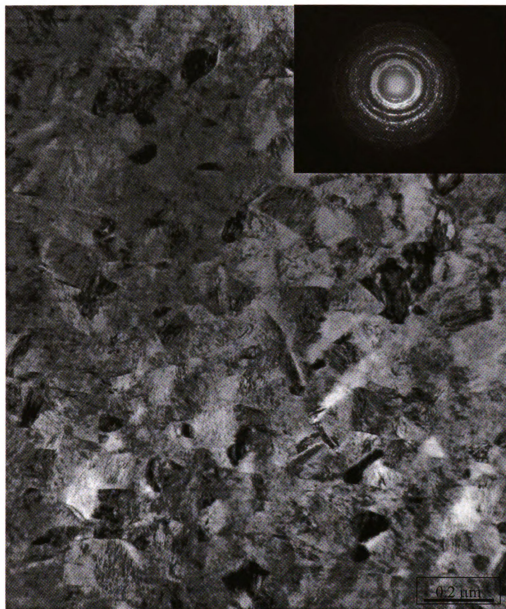


Figure 4.23(a). TEM micrograph and SAED pattern of *in-situ* crystallized  $\text{Ni}_{48.9}\text{Ti}_{36.6}\text{Hf}_{14.5}$  SMA films taken at ambient temperature.



Figure 4.23(b). TEM micrograph (higher magnification) of *in-situ* crystallized  $\text{Ni}_{48.9}\text{Ti}_{36.6}\text{Hf}_{14.5}$  SMA films taken at ambient temperature.

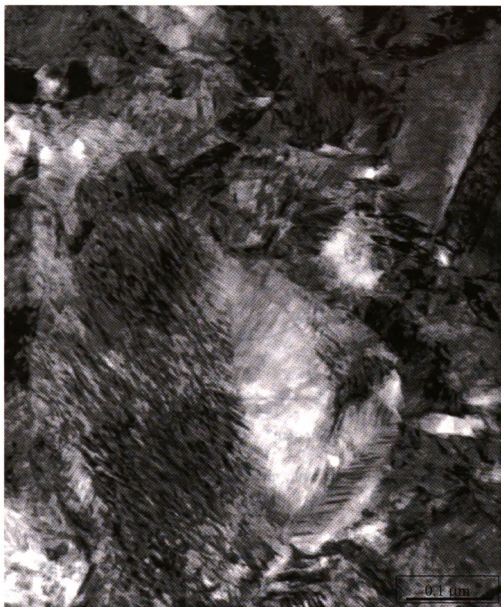


Figure 4.23(c) TEM micrograph (high magnification) of *in-situ* crystallized  $\text{Ni}_{48.9}\text{Ti}_{36.6}\text{Hf}_{14.5}$  SMA films taken at ambient temperature.

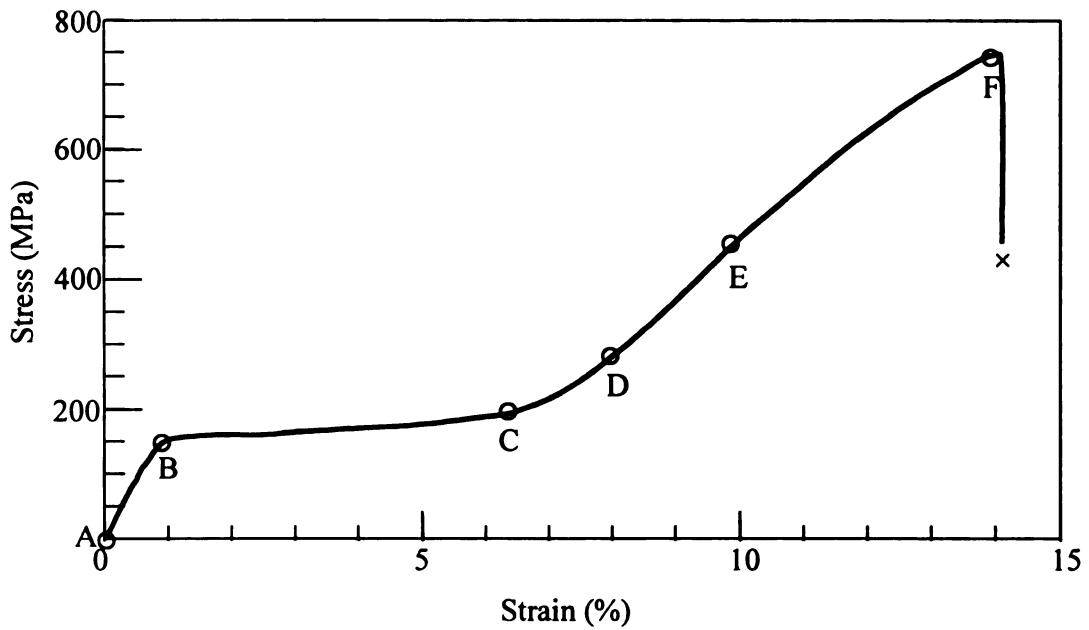


Figure 4.24. Room-temperature stress-strain curve of an *in-situ* crystallized  $\text{Ti}_{50.5}\text{Ni}_{49.5}$  SMA thin film.

- A-B: Conventional elastic region;
- B-C: Martensite reorientation and detwinning region;
- C-D: Transition region;
- D-E: 2nd elastic region accompanied by partial plastic deformation;
- E-F: Conventional yield region.

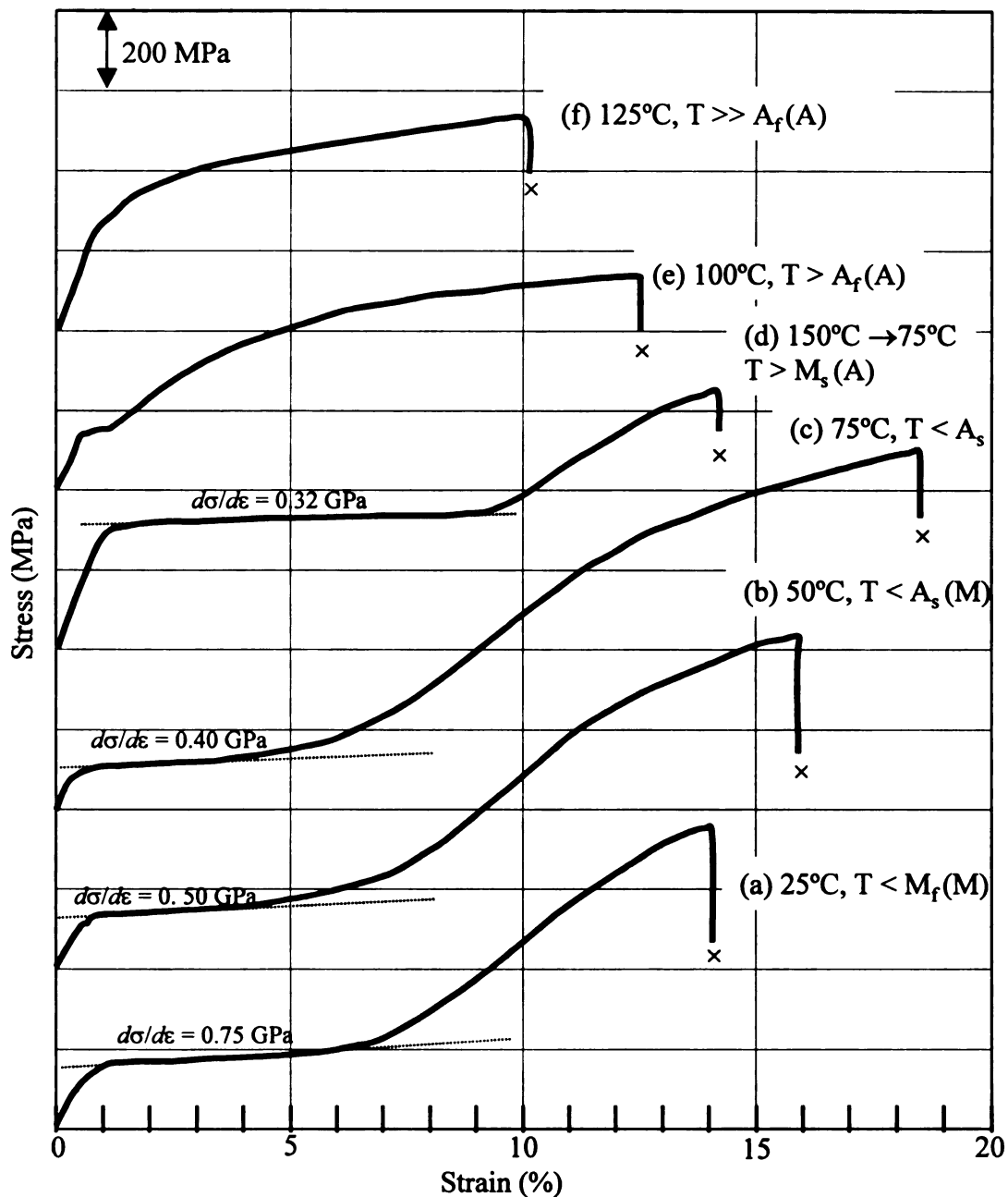


Figure 4.25. Stress-strain curves of an *in-situ* crystallized binary  $\text{Ti}_{50.5}\text{Ni}_{49.5}$  SMA ( $M_f = 55^\circ\text{C}$ ,  $M_s = 37^\circ\text{C}$ ,  $A_s = 78^\circ\text{C}$ ,  $A_f = 90^\circ\text{C}$ ) at different temperatures. (a)  $T = 25^\circ\text{C}$ ; (b)  $T = 50^\circ\text{C}$ ; (c)  $T = 75^\circ\text{C}$ , (d)  $T = 75^\circ\text{C}$  but this temperature was cooled from  $150^\circ\text{C}$  ( $53^\circ\text{C}$  above  $A_f$ ); (e)  $T = 100^\circ\text{C}$ ; and (f)  $T = 125^\circ\text{C}$ .

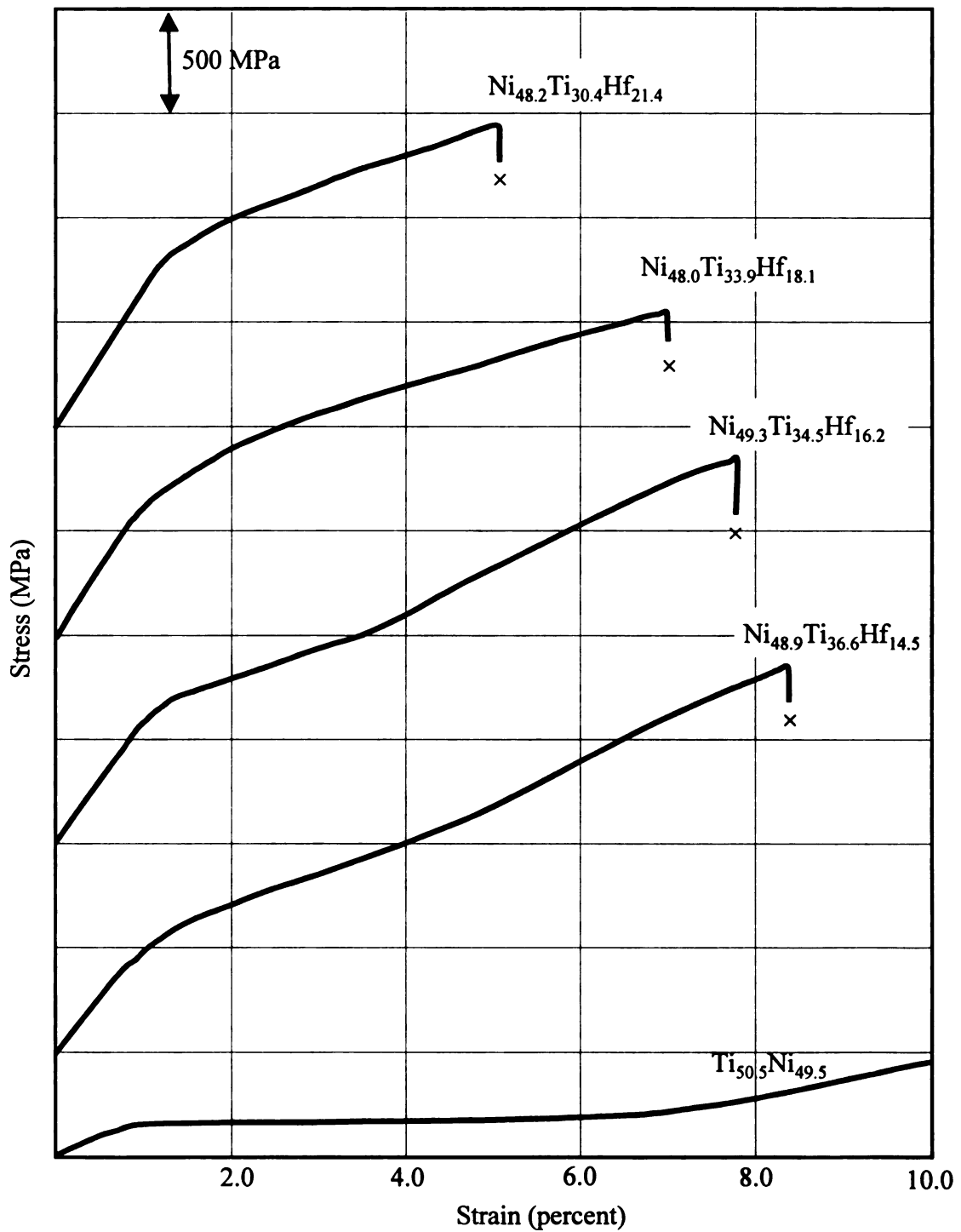


Figure 4.26. Room-temperature stress-strain curves of *in-situ* crystallized Ni-Ti-Hf thin films with different hafnium content.

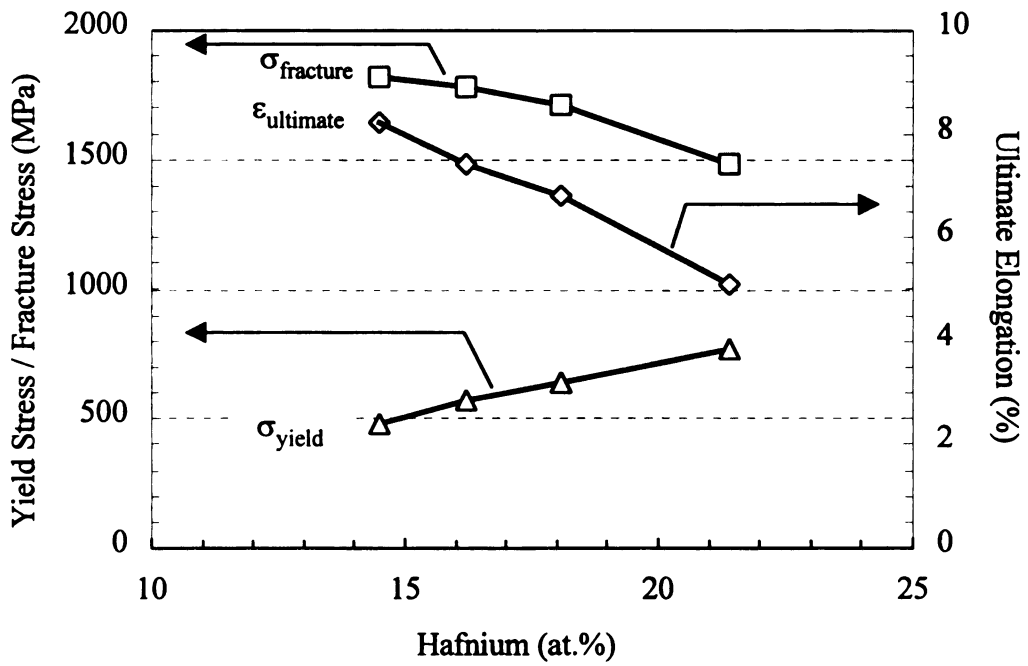


Figure 4.27. Dependence of room-temperature yield stress, fracture stress and ultimate elongation on hafnium content in *in-situ* crystallized Ni-Ti-Hf films.

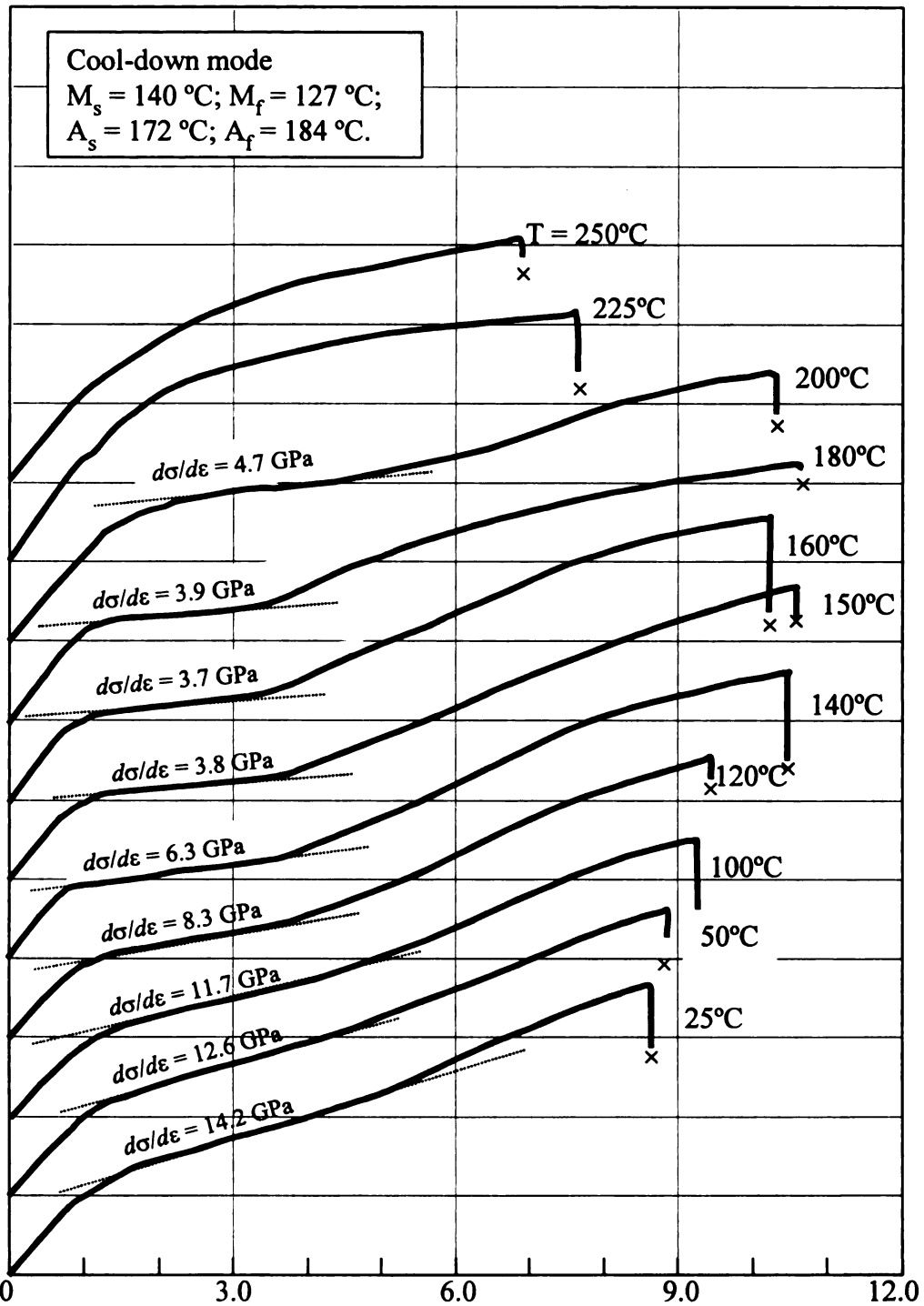


Figure 4.28. Stress-strain curves of *in-situ* crystallized  $\text{Ni}_{48.9}\text{Ti}_{36.6}\text{Hf}_{14.5}$  SMA thin films at different test temperatures using cooling-down routine.

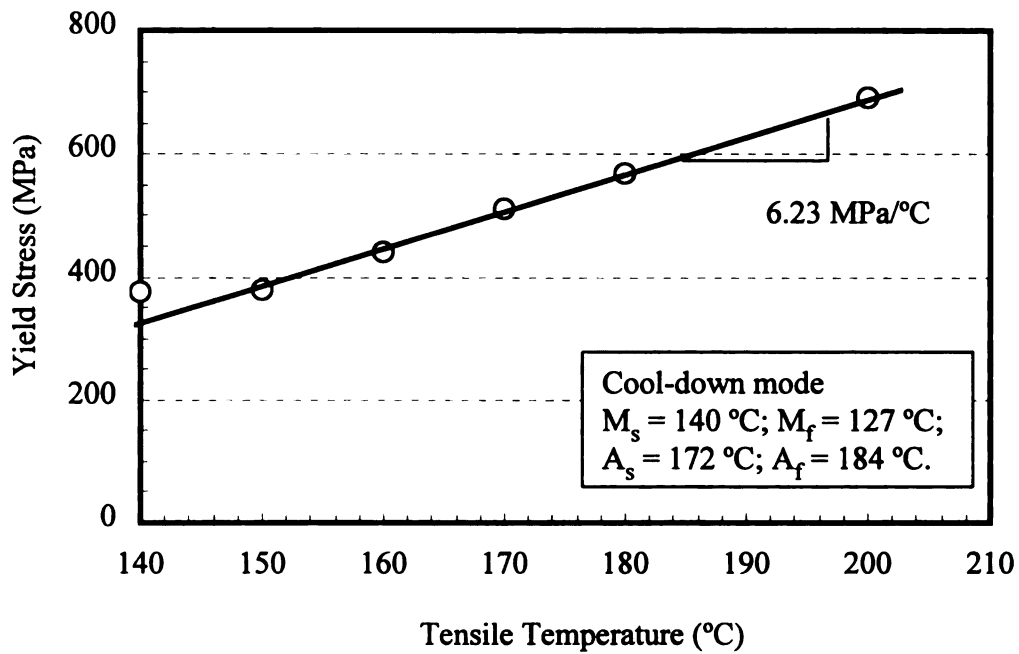


Figure 4.29. Dependence of yield stress of *in-situ* crystallized Ni<sub>48.9</sub>Ti<sub>36.6</sub>Hf<sub>14.5</sub> SMA on tensile test temperatures between 200°C and 140°C using cool-down procedure.

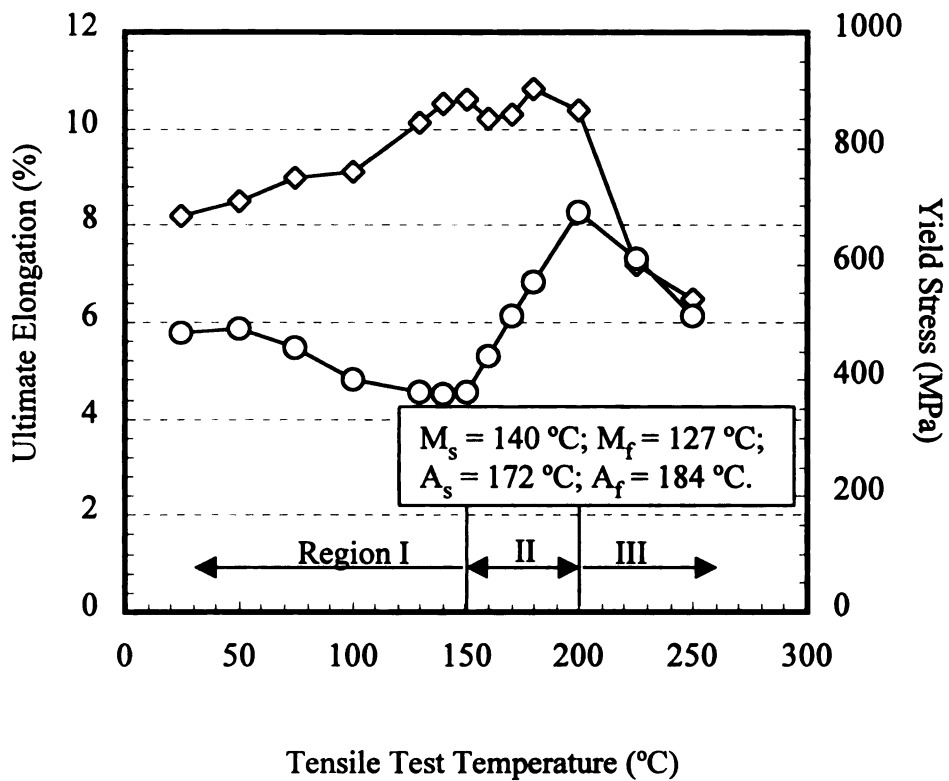


Figure 4.30. Dependence of ultimate elongation and yield stress on test temperature of *in-situ* crystallized  $\text{Ni}_{48.9}\text{Ti}_{36.6}\text{Hf}_{14.5}$  SMA thin films using cool-down mode.

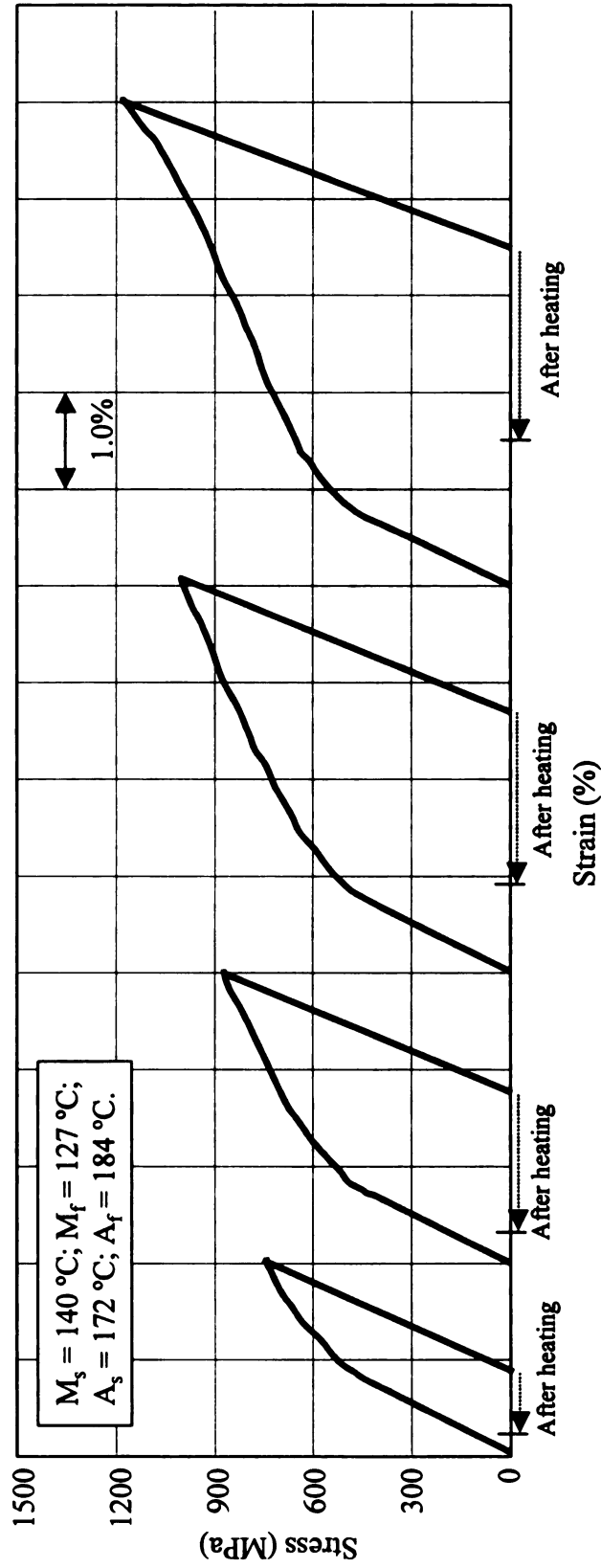


Figure 4.31. Stress-strain curves of *in-situ* crystallized  $\text{Ni}_{4.89}\text{Ti}_{3.66}\text{Hf}_{14.5}$  thin films elongated at room-temperature upon loading, unloading and subsequent heating.

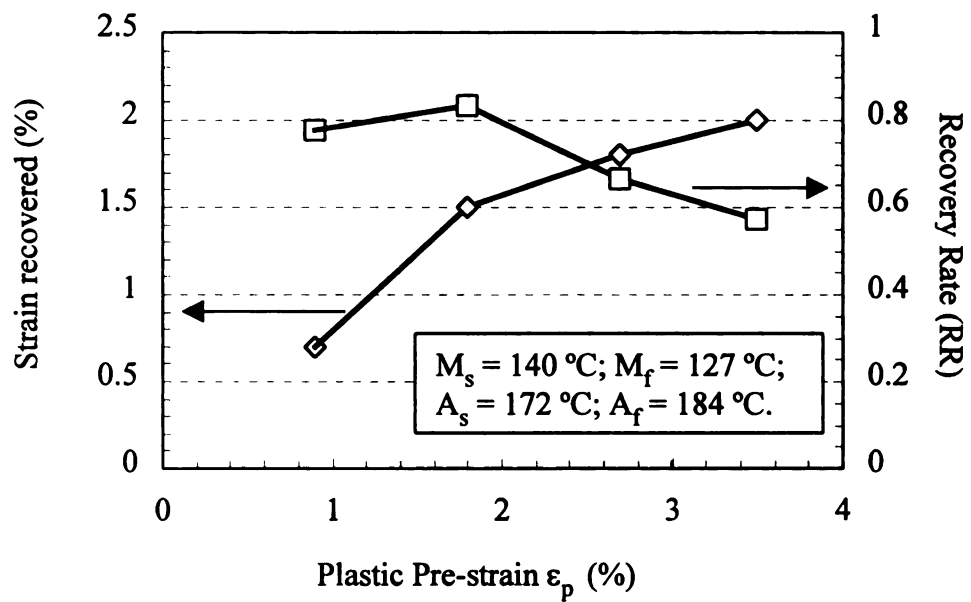


Figure 4.32. Recoverable strain and recovery rate of *in-situ* crystallized  $\text{Ni}_{48.9}\text{Ti}_{36.6}\text{Hf}_{14.5}$  films with different amount of pre-strain introduced at room temperature.

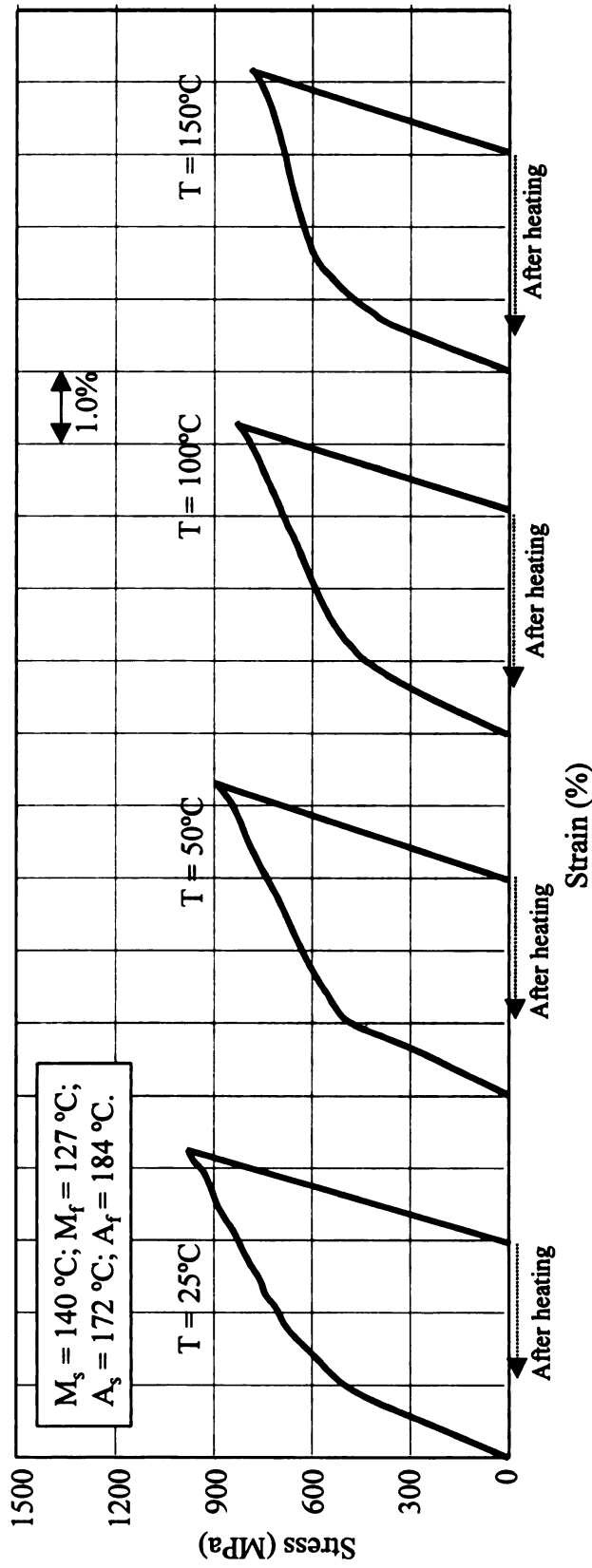


Figure 4.33. Stress-strain curves of *in-situ* crystallized  $\text{Ni}_{48.9}\text{Ti}_{36.6}\text{Hf}_{14.5}$  thin films elongated at different temperatures upon loading, unloading and subsequent heating. The strain upon unloading was fixed at about 3%, and the direct-heating routine was used.

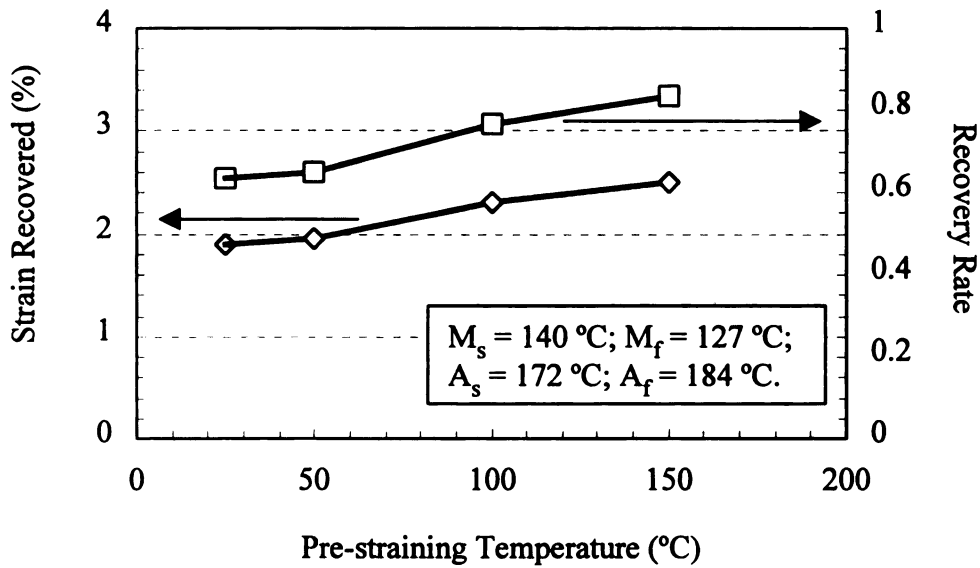


Figure 4.34. Dependence of recoverable strain and recovery rate on deformation temperature of *in-situ* crystallized  $\text{Ni}_{48.9}\text{Ti}_{36.6}\text{Hf}_{14.5}$  martensite films at a fixed pre-strain of about 3%. The samples were heated from room temperature to the test temperature before elongation.

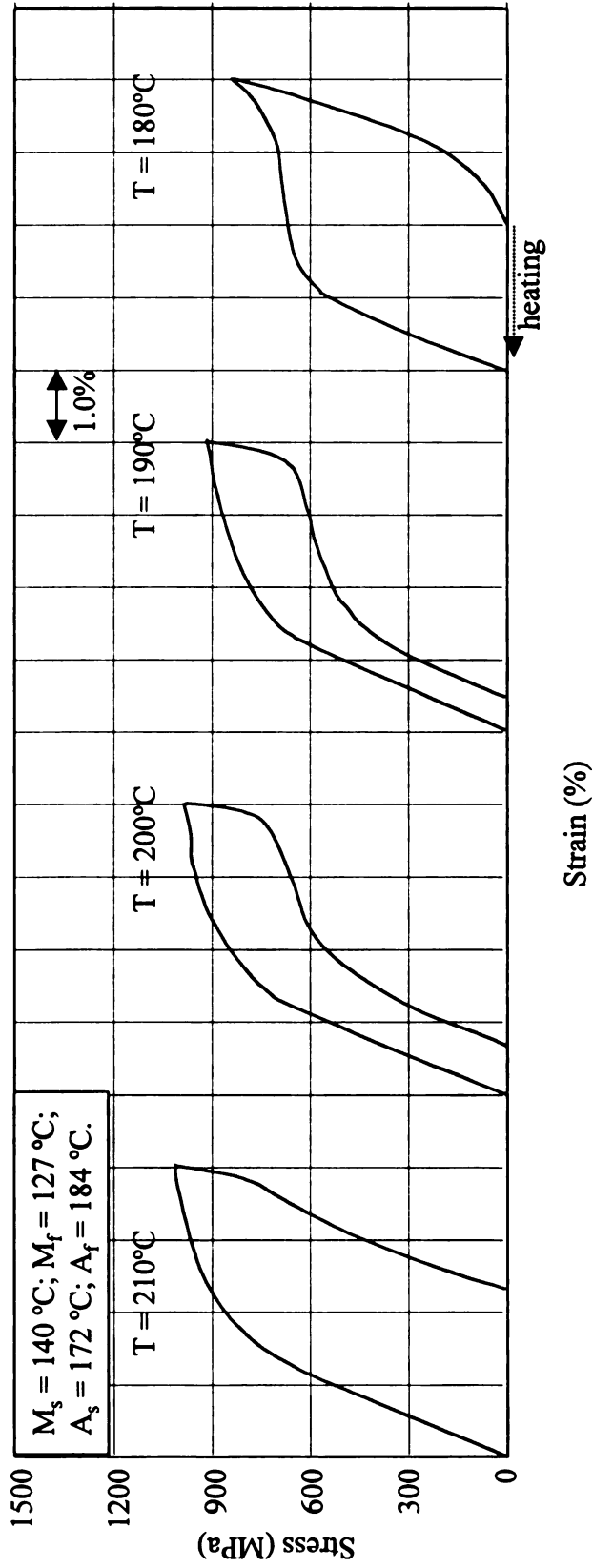


Figure 4.35. Strain-stress curves of *in-situ* crystallized  $\text{Ni}_{48}\text{Ti}_{36.6}\text{Hf}_{14.5}$  elongated at different temperatures (in the initially austenitic condition) during loading and unloading. Before test, samples were heated to 250°C and then cooled to various test temperatures.

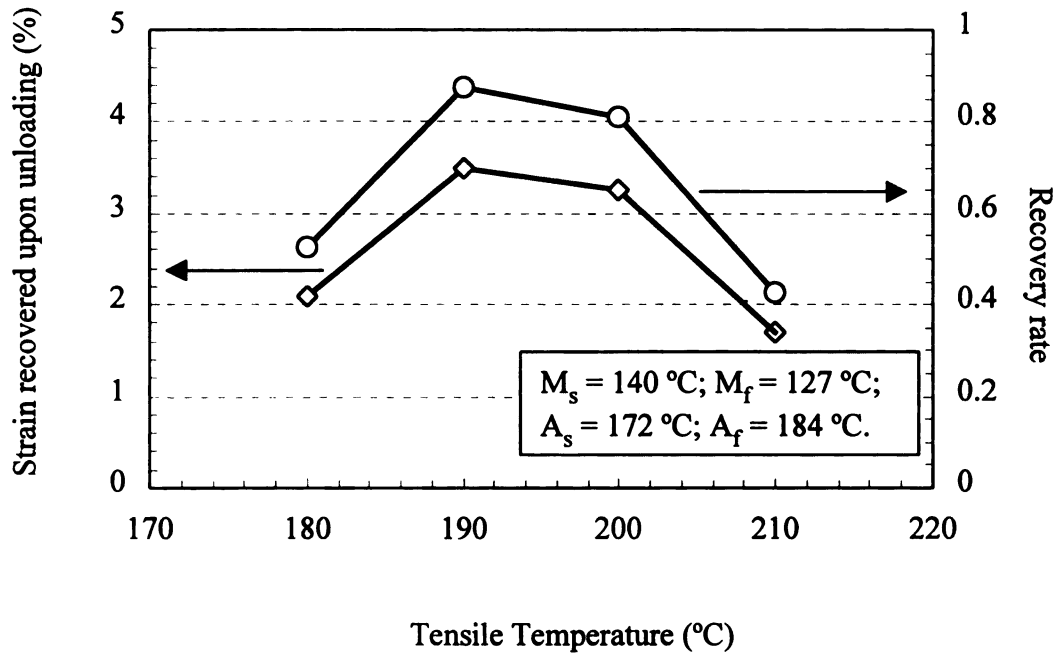


Figure 4.36. Dependence of isothermal strain recovery on deformation temperature for *in-situ* crystallized Ni<sub>48.9</sub>Ti<sub>36.6</sub>Hf<sub>14.5</sub> SMA thin film at fixed total tensile strain of 4%. The samples were cooled from 250°C to the test temperature before elongation.

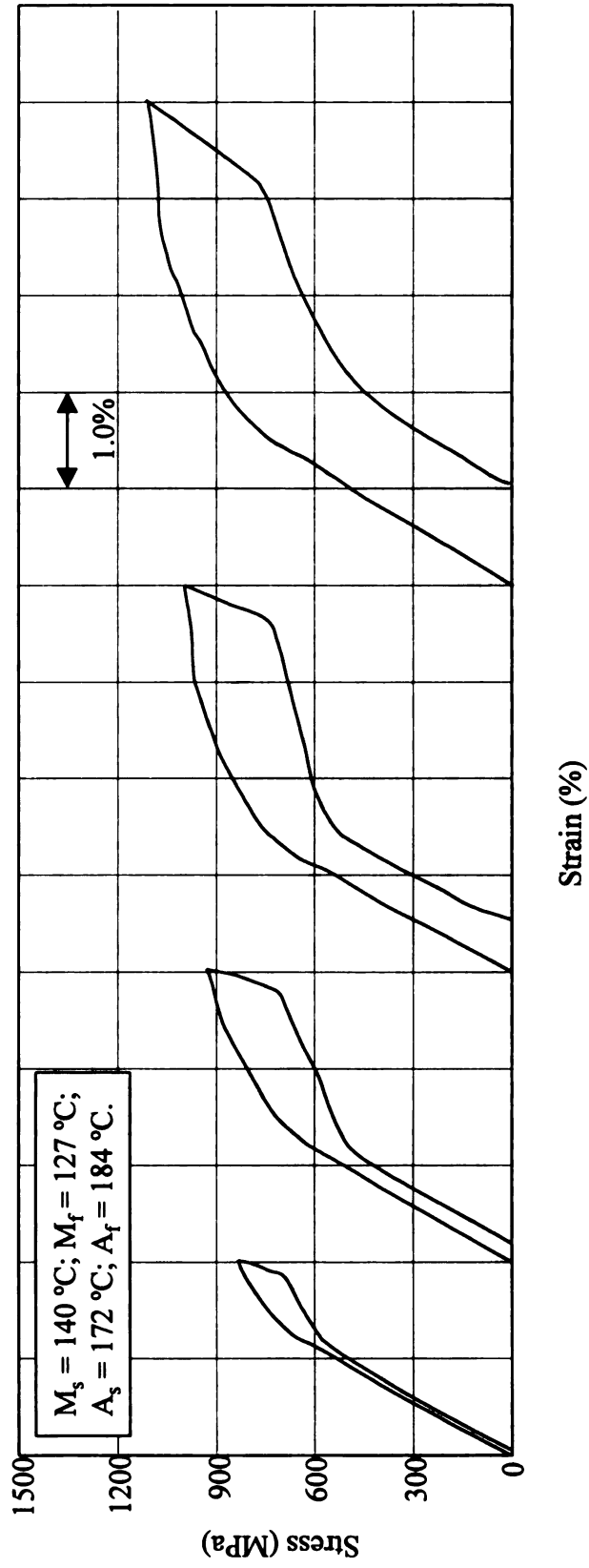


Figure 4.37. Stress-strain curves of *in-situ* crystallized  $\text{Ni}_{48.9}\text{Ti}_{36.6}\text{Hf}_{14.5}$  thin films loaded and unloaded at  $190^\circ\text{C}$  for different amounts of total strain.

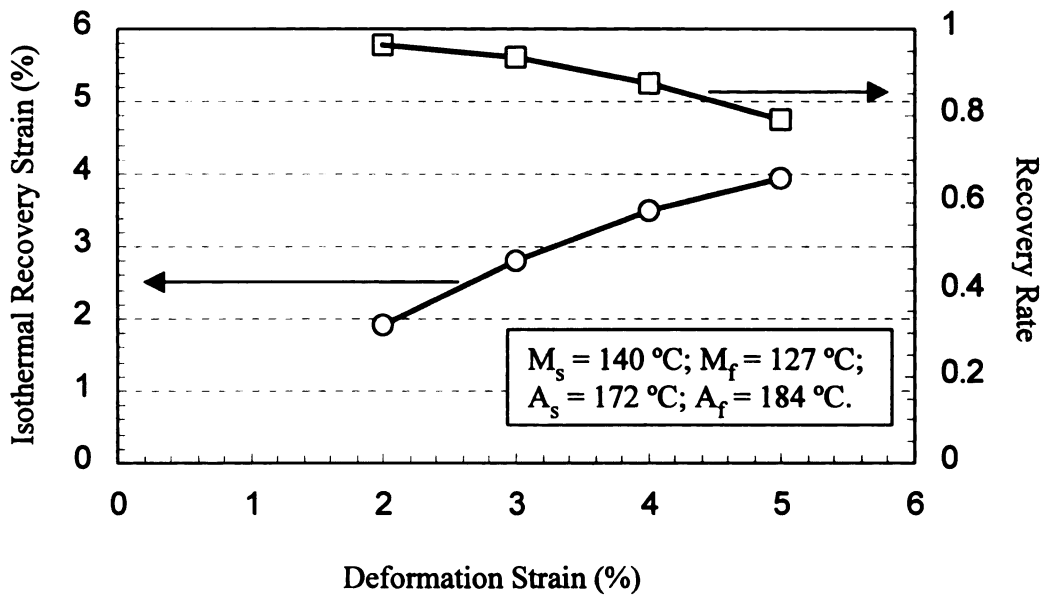


Figure 4.38. Dependence of recoverable strain and recovery rate on initial strain of *in-situ* crystallized Ni<sub>48.9</sub>Ti<sub>36.6</sub>Hf<sub>14.5</sub> SMA thin films when elongation was done at 190°C.

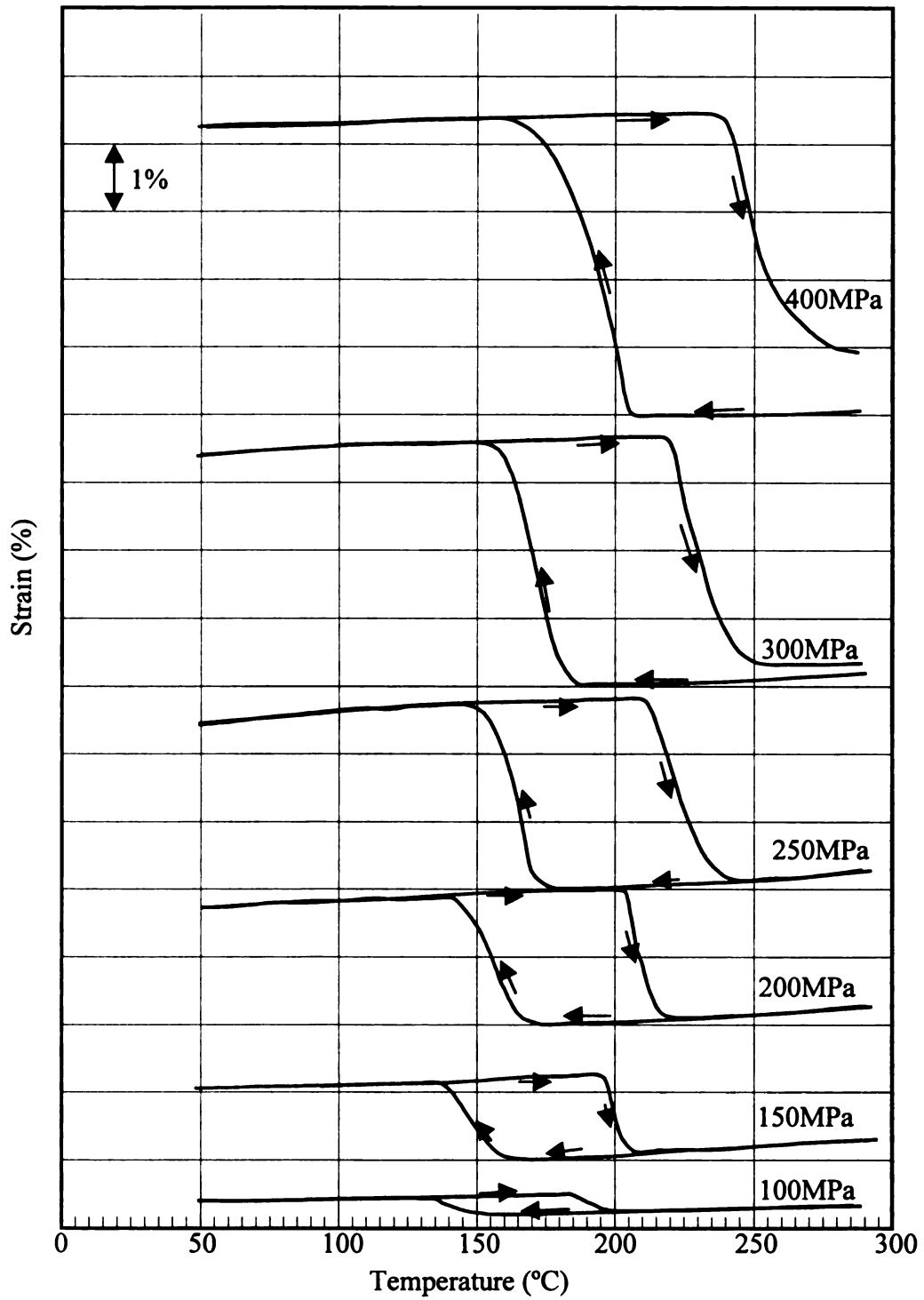


Figure 4.39. Strain-temperature curves of *in-situ* crystallized  $\text{Ni}_{48.9}\text{Ti}_{36.6}\text{Hf}_{14.5}$  thin film during thermal cycling under various constant stresses.

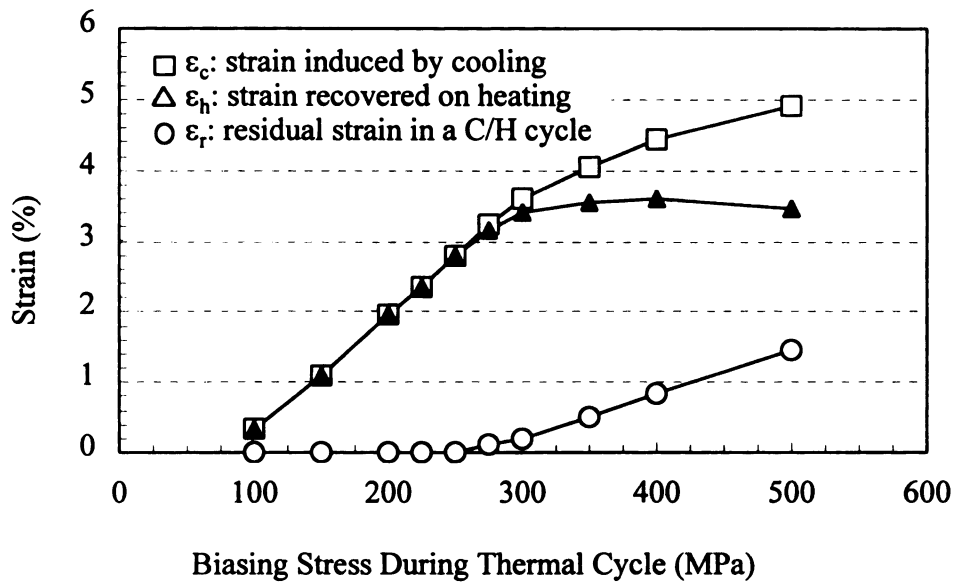


Figure 4.40. Dependence of strain induced by cooling from austenite to martensite and that recovered by heating from martensite to austenite of *in-situ* crystallized  $\text{Ni}_{48.9}\text{Ti}_{36.6}\text{Hf}_{14.5}$  SMA thin films on biasing stress during thermal cycling.

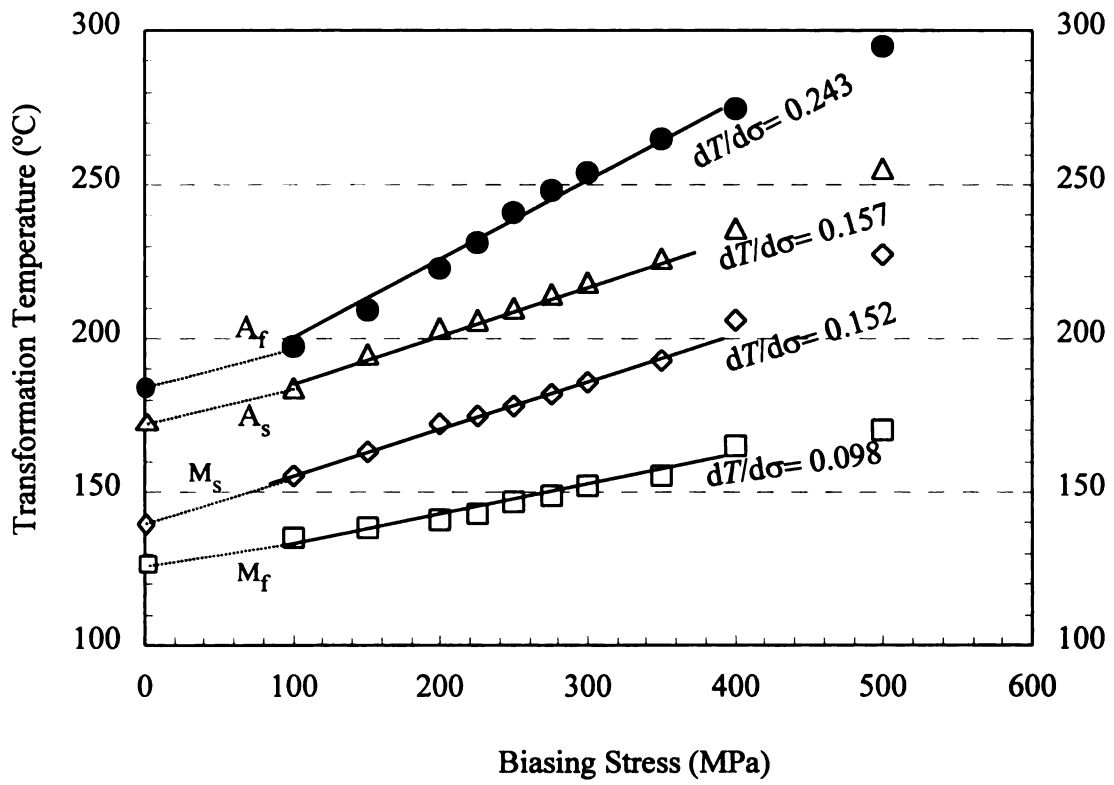


Figure 4.41. Dependence of transformation temperatures on applied stress during thermal cycling of *in-situ* crystallized  $\text{Ni}_{48.9}\text{Ti}_{36.6}\text{Hf}_{14.5}$  SMA thin films.

MICHIGAN STATE UNIVERSITY LIBRARIES



3 1293 02327 0907